The Heat Capacity of Superfluid ^{4}He in the Presence of a Constant Heat Flux Near T_λ

Thesis by

Alexa Welsh Harter

In Partial Fulfillment of the Requirements
for the Degree of
Doctor of Philosophy

California Institute of Technology
Pasadena, California

2001
(Defended July 20, 2000)

Acknowledgements

There are a number of people without whom this thesis could not have been completed. I owe a great deal to my thesis advisor, David Goodstein, who not only shared his scientific ideas, enthusiasm, and uncommon ability to sort out the essential, but also demonstrated much patience and understanding. I would like to thank Talso Chui, Richard Lee, and Peter Day, who taught me a number of experimental techniques and provided invaluable assistance in the laboratory. I am indebted also to Peter Weichman, who gave me considerable insight into my experiment and proofread my thesis with a theorist's careful eye.

Bill Weber, my fellow sub-basement dweller, was a tremendous scientific sounding board, friend, and team mate during my days at Caltech. Mike Lilly and Kalyani Sukhatme have my gratitude for offering me their counsel, commiseration, friendship, and most importantly for making sure that I was properly caffeinated. Roian Egnor, Anthony Leonardo, and Michael Murphy provided me with homes away from home during the week of my defense. Xinkai Wu and Andrew Chatto deserve my thanks for taking over this project so that, unlike others, I can cut the cord without regret.

There are a number of other members of the low temperature community who provided helpful advice and assistance over the years. Among them are Rob Duncan, Nils Asplund, Keith Schwab, John Hartman, David Rowe, Yury Mukharsky, Dave Pearson, John Lipa, Rudolph Haussmann, and Guenter Ahlers.

My parents deserve a great deal of credit for not believing my fourth grade teacher when she told them I would never be good at math and for giving me much encouragement along the way. I am also grateful to Reinaldo Román, who left Ann Arbor to join me in Pasadena, endured my crazy hours, but most of all, was always there for me.

My first few years at Caltech would not have been the same without Tom Murphy, Bill Weber, Laura Grego, Chris Fassnacht, and Arthur Street, who helped keep me awake and inspired during many late night problem sessions. I owe them, Hideo Mabuchi, Babra Akmal, and others a debt of gratitude. And thanks to all who joined me on my various adventures and activities: random potlucks and cookfests, late night excursions to collect bruises on the ice slopes of Wrightwood, expeditions to Mammoth, biking at the crack of dawn through God's country, thawing out at the Yonomono, getting rescued by BMW test drivers in the middle of an asteroid shower in the Angeles National Forest, and playing soccer with the Phys. Rev. Netters.

I would also like to acknowledge Richard Lee for preparing a few figures that eventually got incorporated in some form or another into this thesis and for taking notes with meticulous detail; and Xinkai Wu for lending a hand with data analysis.

Abstract

We present the first experimental evidence that the heat capacity of superfluid ^{4}He, at temperatures very close to the lambda transition temperature, T_λ, is enhanced by a constant heat flux, Q. The heat capacity at constant Q, C_Q, is predicted to diverge at a temperature $T_c(Q) < T_\lambda$ at which superflow becomes unstable. In agreement with previous measurements, we find that dissipation enters our cell at a temperature, $T_{\rm DAS}(Q)$, below the theoretical value, $T_c(Q)$. Our measurements of C_Q were taken using the discrete pulse method at fourteen different heat flux values in the range $1\ \mu{\rm W/cm}^2 \leq {\rm Q} \leq 4\ \mu{\rm W/cm}^2$. The excess heat capacity ΔC_Q we measure has the predicted scaling behavior as a function of T and Q: $\Delta C_Q \cdot t^\alpha \propto (Q/Q_c)^2$, where $Q_c(T) \sim t^{2\nu}$ is the critical heat current that results from the inversion of the equation for $T_c(Q)$. We find that if the theoretical value of $T_c(Q)$ is correct, then ΔC_Q is considerably larger than anticipated. On the other hand, if $T_c(Q) \approx T_{\rm DAS}(Q)$, then ΔC_Q is the same magnitude as the theoretically predicted enhancement.

Contents

List of Figures

List of Tables

Chapter 1 Introduction

The superfluid transition in ^{4}He is an ideal testing ground for studies of critical phenomena. It is uniquely suited for this enterprise: it is a transition in the liquid state, so it is not affected by strains or defects that affect transitions in solids; it occurs at low temperature, so most impurities in the sample are frozen out; and finally, because helium has a large thermal conductivity, particularly in the superfluid phase, its thermal relaxation times are extremely short, making it possible to obtain measurements at equilibrium on reasonable time scales. The lambda transition is, in fact, the sharpest cooperative transition discovered so far [1]. As a result, it is probably the best characterized phase transition on earth. And in space: experiments to measure finite size effects (Confined Helium Experiment—CHEX) and the heat capacity of ^{4}He (Lambda Point Experiment—LPE) [2] were recently flown aboard the space shuttle, removing the one inhomogeneity encountered in earth-bound samples—the gravitationally induced pressure dependence of the local transition temperature. The results of this experiment were in remarkable agreement with theoretical predictions.

Above the superfluid transition temperature, T_λ, ^{4}He is a normal fluid with a finite thermal conductivity, so the application of a heat flux creates a nonequilibrium state in which there is a temperature gradient in the sample. Below T_λ, ^{4}He is a superfluid with near-infinite thermal conductivity. On this side of the transition it is therefore possible to apply a heat flux while maintaining a uniform temperature throughout the sample. This turns out to create an unusual situation in which thermodynamics may be used to describe a system that is not in equilibrium. The heat flux therefore creates an excellent system in which to explore the effects of dynamical conditions on phase transitions.

There have been a number of predictions about the way that a constant heat flux will affect the superfluid transition. It is expected that Q will depress the transition temperature [3–7], and that it will significantly change the thermodynamic properties

in the vicinity of the transition. In particular, it has been predicted that a constant heat flux will cause the heat capacity to diverge at the depressed transition temperature [8, 9]. It is expected that it will diverge far more strongly than its near-logrithmic behavior in the absence of a heat current, and that this divergence occurs while the superfluid density remains finite.

Although there has been a considerable amount of theoretical work on this topic in recent years [4, 6, 9–18], the physics in the vicinity of the non-equilibrium transition is far from understood. Experimental measurements [19] indicate that the temperature at which superfluidity vanishes is, indeed, depressed by Q, although the magnitude of the depression differs significantly from that predicted by current theories [12, 18]. The first measurements of the heat capacity comprise the work of this thesis.

One might well ask why such a strong divergence has only now been observed. After all, over the course of the past sixty years, there have been numerous experiments investigating the physics of helium under heat flow, and it would seem that if there were a huge anomaly in the specific heat, one of these experiments might well have stumbled upon it. There are two main reasons why this did not happen:

1. Although the heat capacity divergence is expected to be quite strong, the temperature range over which it is predicted to be different from that of the usual static transition is extremely small. For example, for a heat current of 10 μW/cm^2, the transition temperature, $T_c(Q)$, should be depressed by only 1.1 μK, and the heat capacity should only be measureably enhanced in the region within approximately 1 μK below $T_c(Q)$. Therefore, in order to conclusively observe the effect of a heat current on the heat capacity, extremely sensitive thermometry is essential. Thermometers of this caliber were only developed in recent years [20, 21] for LPE. These instruments have evolved to the point where they are now limited only by the thermal fluctuations intrinsic to any finite sample in contact with a heat reservoir [21, 22].

2. Under most conditions, the heat capacity enhancement is masked by various other phenomena. When high heat currents are applied to ^{4}He, it becomes

dissipative, and thermal gradients appear that interfere with a measurement of the heat capacity [23, 24]. When low heat currents are applied to superfluid ^{4}He, the temperature range of the effect becomes smaller than the variation of the transition temperature throughout the cell due to gravity.

Therefore, in order to see evidence of the predicted 'strong divergence', it was necessary to take our data [25] in an experimental cell that was less than 1 mm high, over a very specific range of Q, with thermometers that have a resolution better than 10^{-10} K [26].

Before proceeding to the specific theoretical predictions and experiments that both motivated and composed this project, I will first outline a few of the essential relations and concepts that will be used in subsequent derivations and discussions.

1.1 Superfluidity and the two-fluid model

Soon after helium was liquified in 1908 by Heike Kamerlingh Onnes, it became clear that it had a number of strange properties that are not shared by other substances [27]. For one, helium refuses to freeze under its saturated vapor pressure. In fact, it is the only substance that remains a liquid all the way down to absolute zero. It is necessary to apply pressures in excess of 25 atmospheres to produce the solid phase (see Fig. 1.1).

Under a pressure of 1 atmosphere, ^{4}He liquifies at 4.21 K. When it is cooled further, it undergoes another phase transformation from one liquid state to another. This transition is accompanied by a near-logrithmic divergence in the specific heat that resembles the Greek letter λ. This curve, shown at various reduced temperatures in Fig. 1.2, is what gives the transition its name. The transition occurs at a temperature $T_\lambda = 2.1768$ K[1] under saturated vapor pressure. The state above T_λ is known as He I and the state below T_λ as He II.

While He I is a normal viscous fluid, He II is a superfluid that exhibits a number of unusual characteristics. It has the peculiar ability to flow without dissipation, and it

[1] $T_\lambda = 2.1768$ K on the T_{90} temperature scale. Many references quoted in this thesis use the T_{58} value of $T_\lambda = 2.1720$ K. Reference [30] has compiled all measurements of the equilibrium and transport properties of ^{4}He known at the time of publication, and converted them to the T_{90} scale.

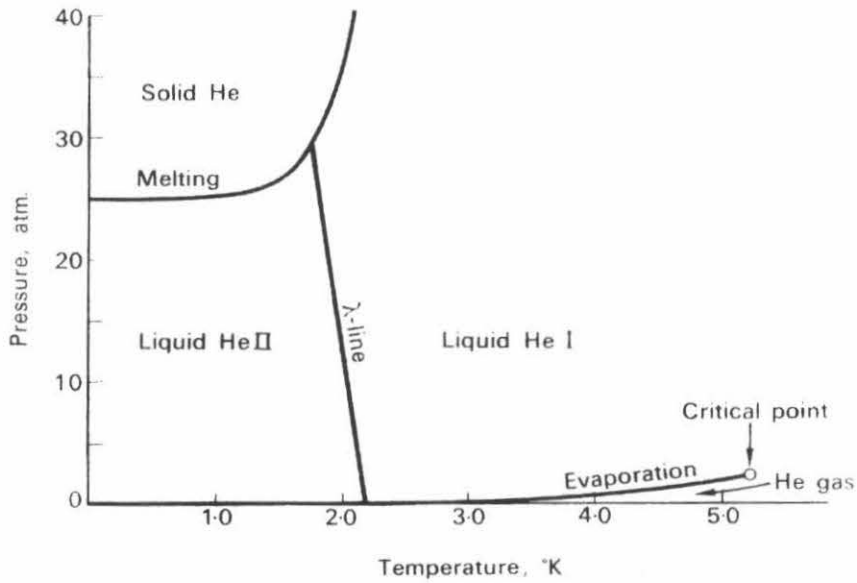

Figure 1.1: The phase diagram of ^{4}He. (From Galasiewicz [28], page 7 — after London [29].)

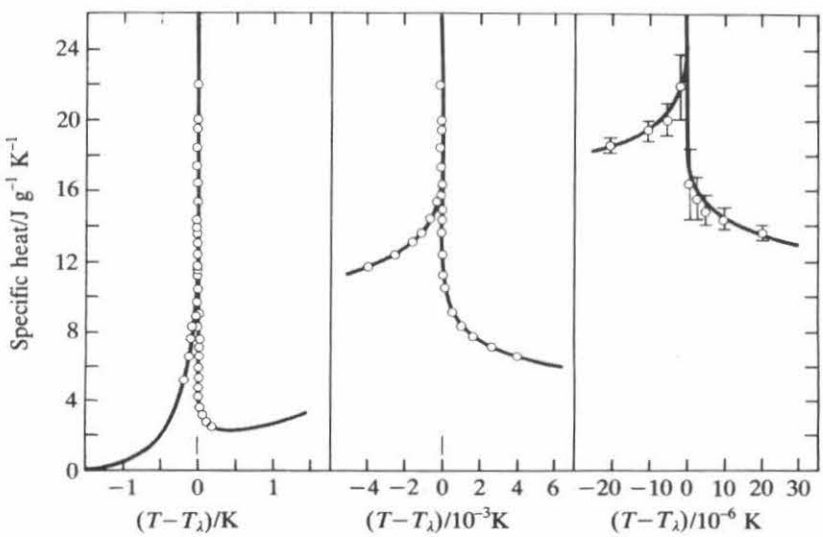

Figure 1.2: The specific heat of ^{4}He under the saturated vapor pressure as a function of $T-T_\lambda$. (From Wilks and Betts [31], page 169 — after Buckingham and Fairbank [32].)

has an extremely large thermal conductivity. In addition, experiments investigating the viscosity of He II give different results depending on the way in which they are performed. Measurements indicate that it can flow through capillaries or small holes without resistance and therefore has no viscosity at all. However, if an object is dragged through the liquid, it encounters a small resistance that changes as a function of temperature, implying that it has a finite, albeit small, viscosity.

This strange inconsistency can be explained by the two-fluid model that was first introduced in 1938 by Tisza [33], and considerably modified several years later by Landau [34, 35]. In this empirical description of superfluidity, He II is composed of two completely interpenetrating, inseparable fluids. One, the normal fluid, possesses an ordinary viscosity, and the other, the so-called superfluid, has no viscosity at all. The normal fluid has density ρ_n, velocity $\mathbf{v}_n$, and entropy S. The superfluid has density ρ_s and velocity $\mathbf{v}_s$, but carries no entropy. The total density ρ of the helium is simply the sum of its two separate densities,

$$\rho = \rho_n + \rho_s. \tag{1.1}$$

While the total density is more or less independent of temperature, and is equal to 0.145 g/cm^3 [30], the superfluid and normal fluid densities change as a function of temperature. The total mass current density of the helium, $\mathbf{j}$, can be expressed in terms of the currents of the two fluids

$$\mathbf{j} = \rho\, \mathbf{v} = \rho_n \mathbf{v}_n + \rho_s \mathbf{v}_s. \tag{1.2}$$

When helium is forced to flow through small channels, the normal fluid is held to the walls by its viscosity, while the superfluid flows through without impedence. An object dragged through the helium, however, encounters the resistance of the normal fluid. Experiments of the second kind can therefore be performed to determine the dependence of ρ_n and ρ_s on temperature. A torsional oscillator experiment of this sort, performed by Andronikashvili [36], indicates that the normal fluid fraction, ρ_n/ρ, is equal to unity at the superfluid transition, but decreases to zero at absolute

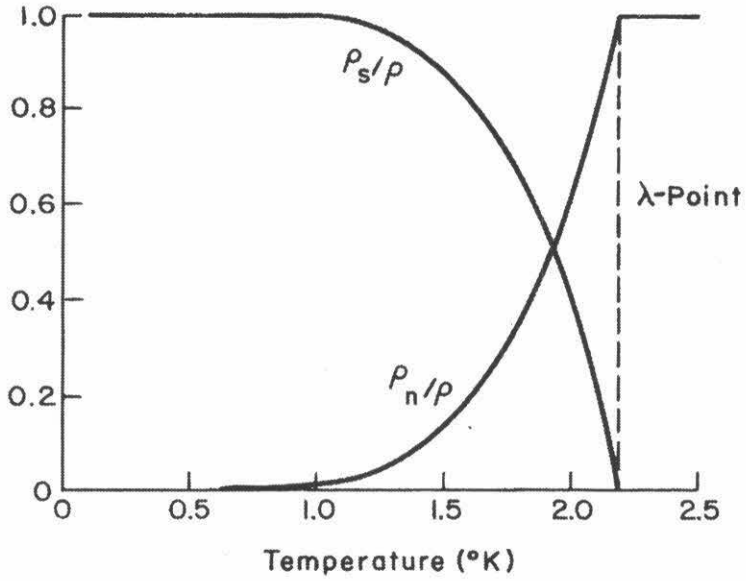

Figure 1.3: The superfluid and normal fluid densities as measured in Andronikashvili's experiment. (From Donnelly [37], page 17.)

zero. The results of this experiment are shown in Fig. 1.3. Near the lambda point, the superfluid density vanishes as

$$\rho_s = \rho_0 \, t^{\zeta}, \tag{1.3}$$

where $\zeta = 0.671$ is a universal exponent, $\rho_0 = 0.38$ g/cm^3, and t is the reduced temperature,

$$t \equiv \frac{T_\lambda - T}{T_\lambda}. \tag{1.4}$$

A theoretical basis for the two-fluid model was provided in 1941 by Landau [34, 35]. He described superfluid helium as a weakly excited quantum system, in which a gas of excitations, or quasiparticles, moves within a background fluid that lies in an unexcited state. At absolute zero, the helium consists entirely of this perfect background fluid and flows without dissipation. At higher temperatures, excitations are created that can collide with each other and with the walls of the container, causing the fluid to exhibit some of the properties of a normal fluid, such as viscosity. These excita-

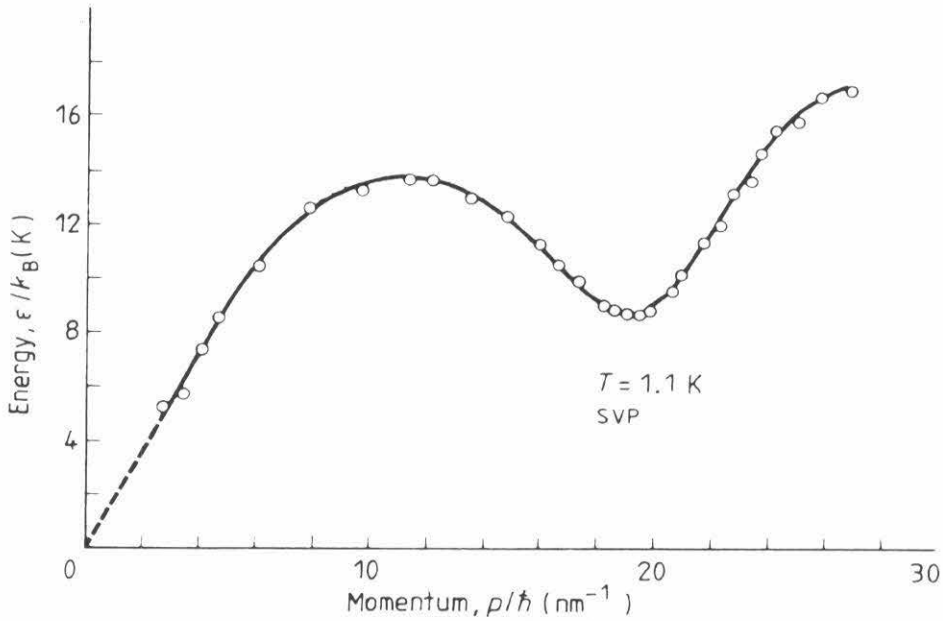

Figure 1.4: He II excitation spectrum obtained from neutron scattering experiments. (From Tilley and Tilley [41], page 44 — after Henshaw and Woods [40].)

tions are collective excitations of the system, rather than individual excited particles. In the two fluid model, the normal fluid is identified with the gas of quasiparticles, while the superfluid is identified with the perfect background fluid.

Landau also presented the essential features of the quasiparticle energy spectrum, shown in Fig. 1.4, based on phenomenological arguments. He showed that at low energies the dispersion curve is a straight line and the excitations are phonons. At higher energies, the curve reaches a local maximum before dipping down to a local minimum. The excitations in the region of the minimum are called rotons, and they are the only other major contribution to the thermodynamic behavior of superfluid helium. The thermodynamic functions can be calculated very accurately for this distribution, except in the vicinity of the lambda point, where the quasiparticle density becomes extremely high [37]. Landau's spectrum was later confirmed by neutron-scattering experiments [38–40].

1.2 Heat transport in superfluid ^{4}He

As previously mentioned, superfluid ^{4}He has an extremely large thermal conductivity. When applied heat currents are small, it is impossible to set up any temperature gradients whatsoever within the bulk liquid. In this limit, its thermal conductivity is effectively infinite. Heat flow of this kind must clearly be attributed to a different process than standard conduction. It can, in fact, be explained by the two-fluid model.

When heat is applied to helium, the normal fluid, which carries all the entropy, flows from the heated end of the cell to the cold end. Because the total density of the liquid remains constant, the superfluid component flows in the opposite direction, towards the heater. When it reaches the hot end of the cell, it heats up, converts to normal fluid, and then returns once again to the cold end. The heat current density is

$$\mathbf{Q} = \rho \, ST \, \mathbf{v}_n. \tag{1.5}$$

When there is no net mass flow, $\mathbf{j} = 0$, and so according to (1.2), $\rho_n \mathbf{v}_n = -\rho_s \mathbf{v}_s$. This implies that

$$\mathbf{Q} = (\rho_n + \rho_s) \, ST \, \mathbf{v}_n = \rho_s \, ST \, (\mathbf{v}_n - \mathbf{v}_s). \tag{1.6}$$

A heat current therefore sets up a counterflow, $\mathbf{W} = \mathbf{v}_n - \mathbf{v}_s$, between the superfluid and the normal fluid velocities (see Fig. 1.5).

1.3 The static superfluid transition

When it was first discovered, the superfluid transtion was compared to the condensation of an ideal Bose gas [29]. It was thought that below T_λ, the helium atoms start to populate the ground state of the system, forming a condensate. It was this comparison that lead to Tizsa's development of the two-fluid model. The atoms in

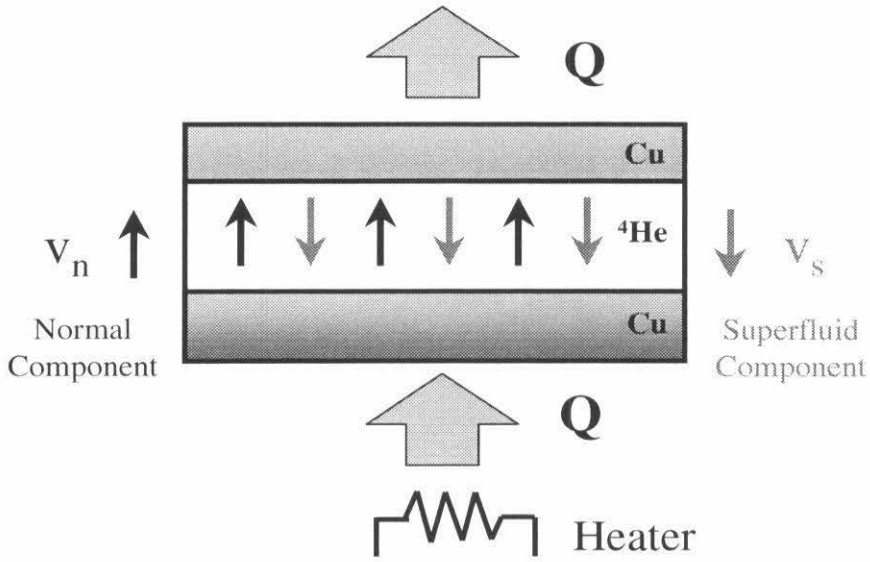

Figure 1.5: Heat is supplied at the bottom of a cell of He II, establishing a counterflow $W = v_n - v_s$ in the superfluid.

the condensate are in a single quantum state, so all that is needed to describe them is a single 'condensate wave-function',

$$\psi = \langle \Psi \rangle = \psi_0 \, e^{i\phi}. \tag{1.7}$$

Where Ψ is the Bose field operator and $n_0 = \psi_0^2$ gives the number density of atoms in the condensate.

Although this was a compelling suggestion, the lambda transition is clearly not a direct manifestation of the condensation of an ideal Bose gas. In helium, the forces between the atoms have a significant effect on the behavior of the fluid, and cannot be ignored. Theory indicates that these interactions deplete the condensate, so that even at absolute zero only about ten percent of the helium atoms occupy the zero momentum state [42, 43].

Because the lambda transition is second order, it can be described, at least qualitatively, by the Landau theory of phase transitions [44]. Its change in state can be

described in terms of an order parameter that characterizes its distance from criticality. For the lambda transition, the order parameter is identified to be the condensate wave-function defined by (1.7).

The superfluid motion is a response to order parameter phase twists, and one has the relation:

$$\mathbf{v}_s = \frac{\hbar}{m_4}\nabla\phi, \tag{1.8}$$

where m_4 is the ^{4}He atomic mass. The change in free energy $\Delta F = \frac{1}{2}\rho_s \mathbf{v}_s^2$ for small v_s then serves to *define* the equilibrium ρ_s. On the other hand, the condensate density n_0 is in general an independent thermodynamic quantity, unrelated to ρ_s.

Many of the elements of the transition can be derived by the application of Landau mean-field-theory (MFT) in the form of a power-law expansion of ψ and its gradients. This description assumes that the system can be accurately described by the average value of the order parameter, and neglects any fluctuations about this mean value. In superfluid helium, fluctuations are always important, and there is no temperature range for which the MFT is strictly valid. As with other critical point transitions, these fluctuations lead to singularities in many properties of the system near the lambda point, and must be treated through proper application of critical scaling laws, renormalization group (RG) theory, and other theoretical tools.

1.4 Heat flow and the superfluid transition

The application of a heat flux significantly alters the lambda transition. As was previously mentioned, the most outstanding observable changes are predicted to be a depression of the transition temperature and a strong divergence of the specific heat. The qualitative features of these two effects can be derived from extremely simple arguments.

1.4.1 The depressed temperature of superfluid breakdown

If a heat flux, Q, is applied to the bottom of a cell of superfluid helium, and heat is removed from the top at an equal rate, the helium remains isothermal, and a counterflow is created between the superfluid and the normal fluid. For a closed cell there is no net mass flow, so according to (1.6), $\mathbf{Q} = \rho_s \, ST\mathbf{W}$. We can henceforth drop the vector notation without ambiguity, since all of the motion in this particular case is only in one direction (see Fig. 1.5).

The presence of a counterflow gives the system an extra degree of thermodynamic freedom, so it is therefore expected that the superfluid density, ρ_s, should be a function of W (at least at larger W) as well as of temperature and pressure. There is little experimental data to elucidate the dependence of ρ_s on W. The only experiment to date is a measurement by Hess [45] that took place well below T_λ. His results are consistent with a calculation of the dependence of ρ_n (and by extension ρ_s) on W derived from the spectrum of elementary excitations [34, 46, 47]. In the vicinity of the lambda transition, where no experimental measurements exist and elementary excitation theory is expected to fail, we must rely on phase transition theory. Both MFT [48] and RG theory [6] predict[2] that ρ_s will be sufficiently depressed by W that the quantity $q \equiv \rho_s(W)W$ will eventually decrease with increasing W (see Figs. 1.6 and 1.8). Because S and T are more or less constant in the vicinity of the transition, $Q \propto q$ according to (1.6). This implies that for any given temperature, there is a maximum heat current beyond which superflow becomes unstable. This heat current occurs at the peak, when $(\partial Q/\partial W)_T = 0$. We may therefore define a set of points in the $T - Q$ plane that acts as a boundary beyond which superfluidity cannot exist. We label this curve as $T_c(Q)$, or $Q_c(T)$. The fact that $T_c(Q) < T_\lambda$ follows because $\rho_s(W) > 0$ at this point.

For experiments in which the heat flux, Q, is held constant, the instability occurs in the following way. Far below T_λ, the superfluid fraction is relatively large, so an applied heat flux results in a small counterflow velocity. As the temperature of

[2]The form of $\rho_s(W)$ for these theories will be explicitly discussed in Sec. 1.6.1.

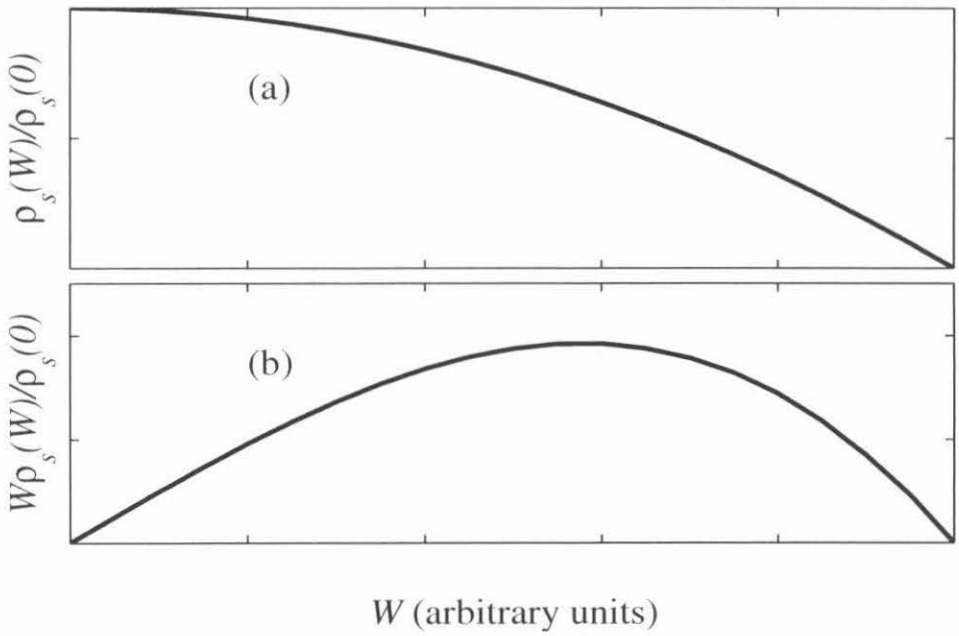

Figure 1.6: (a) ρ_s depressed by W, calculated using mean-field theory; (b) the resulting value of $q \equiv \rho_s(W)W$.

.

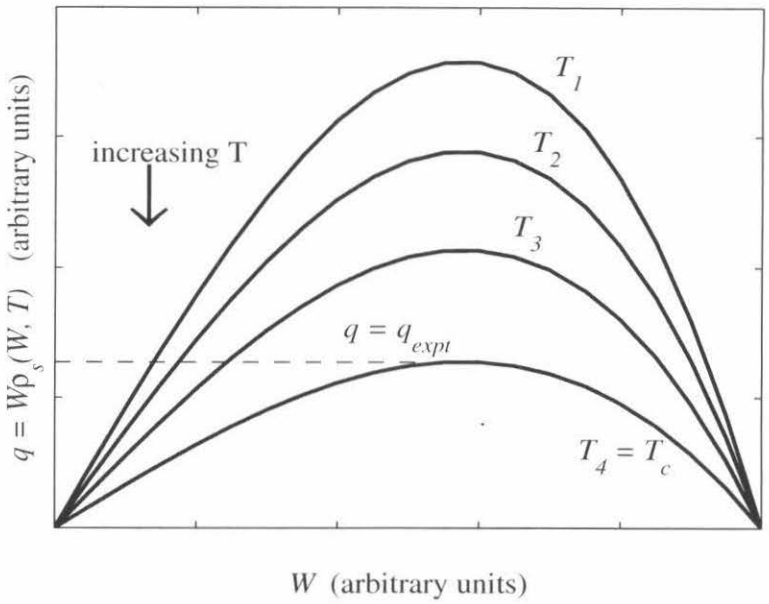

Figure 1.7: Fixed Q, changing T. Thick solid lines: the function $q = \rho_s(W,T)W$ for various values of T. Dashed line: The value of $q = q_{\rm expt} = Q/ST$ fixed in the experiment. The intersection of a given $q(T)$ curve and $q_{\rm expt}$ gives the counterflow velocity induced by the applied heat flux Q at that temperature T. When $T > T_c$, no value of W satisfies $Q = ST\rho_s(W)W$, and superflow breaks down.

the helium is raised, the system will react by decreasing the superfluid density and increasing the counterflow velocity. Because Q is fixed, it must do this in such a way that the product of the two remains constant. When the temperature is raised to $T_c(Q)$, the system reaches a point where it will not be able to increase W while keeping Q constant. This happens when ρ_s is sufficiently depressed by the counterflow that any further increase in W will cause the product $\rho_s(W)W$ to decrease (see Fig. 1.7). At $T_c(Q)$ the heat flux can no longer be carried by a counterflow, and superfluidity will break down.

1.4.2 Heat capacity divergence

The divergence of the heat capacity can be understood in similar terms. As the temperature is raised, the superfluid density decreases, and the counterflow velocity

must increase in order to carry the heat current. The kinetic energy associated with this counterflow is equal to $\frac{1}{2}\rho_s W^2 = (\rho_s W)^2/2\rho_s$. Since the quantity $\rho_s W$ is held fixed in any experiment in which Q is fixed, any decrease in ρ_s leads to an increase in the kinetic energy. Therefore, an increase in the temperature of the system is accompanied by an increase in the kinetic energy. Since the heat capacity, C_Q, is simply the amount of energy that must be added to raise the temperature of the fluid at fixed Q, there is an enhancement of the heat capacity. In fact, because ρ_s is depressed by W, the counterflow velocity must increase by more and more to keep Q steady as the temperature is incrementally raised towards $T_c(Q)$. An increasing amount of energy is therefore required to raise the temperature, and the heat capacity ultimately diverges at the instability.

The necessity of the divergence in the heat capacity can be put on a bit firmer ground with the help of thermodynamics [8]. The presence of a counterflow in superfluid helium introduces a new pair of conjugate variables to the thermodynamic description of the system. This new pair consists of W and q, where W is the counterflow velocity, and $q = \rho_s W$ is the superfluid momentum in the normal fluid frame. The free energy at constant density can then be written

$$dF = -sdT + qdW, \tag{1.9}$$

where s is the entropy density.

As we have seen before, keeping $Q = ST\rho_s W$ constant is equivalent to keeping q constant. At constant q, the proper free energy to use is $\Phi(T, q) = F(T, W) - Wq$, yielding $d\Phi = -sdT - Wdq$. The molar heat capacity at constant Q is:

$$C_Q = -TV\left(\frac{\partial^2 \Phi}{\partial T^2}\right)_Q, \tag{1.10}$$

where $V = 27.38$ cm^3/mol is the molar volume.

In order to see why this quantity necessarily diverges, we can employ a proof that is identical to the one that relates C_P and C_V, shown in all standard thermodynamics texts [49]. We start with the entropy density $s(T, W)$, and find that

$$ds = \left(\frac{\partial s}{\partial T}\right)_W dT + \left(\frac{\partial s}{\partial W}\right)_T dW. \tag{1.11}$$

Therefore,

$$C_Q = TV\left(\frac{\partial s}{\partial T}\right)_Q = C_W + TV\left(\frac{\partial s}{\partial W}\right)_T \left(\frac{\partial W}{\partial T}\right)_Q. \tag{1.12}$$

From (1.9), we obtain the Maxwell relation

$$\left(\frac{\partial q}{\partial T}\right)_W = -\left(\frac{\partial s}{\partial W}\right)_T, \tag{1.13}$$

and the expression for the heat capacity becomes

$$C_Q = C_W - TV\left(\frac{\partial q}{\partial T}\right)_W \left(\frac{\partial W}{\partial T}\right)_q, \tag{1.14}$$

where we have used the fact that fixing Q is equivalent to fixing q. We now simply employ the identity,

$$\left(\frac{\partial q}{\partial T}\right)_W \left(\frac{\partial T}{\partial W}\right)_q \left(\frac{\partial W}{\partial q}\right)_T = -1, \tag{1.15}$$

to find

$$C_Q = C_W + TV\frac{(\partial q/\partial T)_W^2}{(\partial q/\partial W)_T}. \tag{1.16}$$

We have already seen that superflow breaks down when $(\partial q/\partial W)_T = 0$. The fact that this quantity appears in the denominator of (1.16) implies that C_Q also diverges at this point. This result will be true so long as ρ_s is depressed sufficiently by W that $q = \rho_s(W)W$ eventually decreases with W [see Figs. 1.6(b) and 1.8(b)].

1.5 The exponents related to the superfluid transition under heat flow

1.5.1 The exponent of the transition temperature depression

For finite values of Q, $T_c(Q)$ lies below T_λ.[3] As Q approaches zero, $T_c(Q)$ approaches $T_\lambda(Q = 0)$. In order to determine a more precise relationship between these two temperatures, we can employ scaling arguments to determine the singular behavior of the heat flux [7]. The idea behind the scaling hypothesis is that all singularities that occur in the vicinity of the critical point are caused by fluctuations that are correlated over a length of order ξ. As the system approaches the transition, and $\xi \to \infty$, microscopic length scales are no longer important. The only length that matters is ξ.

Near T_λ, $Q = \rho_s WST \simeq -\rho_s v_s ST$. Since S and T are constants, the only terms that exhibit singular behavior are ρ_s and v_s. For the purpose of calculating exponents, we may therefore write $Q_c \sim (\rho_{sc} v_{sc}^2)/v_{sc}$. The numerator is a singular term in the free energy density that is inversely proportional to the correlation volume,

$$f \sim \frac{\rho_{sc} v_{sc}^2}{2} \sim \xi^{-d}. \tag{1.17}$$

The scaling properties of the denominator can be determined from the properties of the superfluid order parameter. According to (1.8) and (1.7),

$$v_{sc} \sim \nabla\phi \sim \frac{\nabla\psi}{\psi}. \tag{1.18}$$

Therefore, v_{sc} has the character of an inverse length. Since the correlation length is the only relevant length near the critical point, $v_{sc} \sim \xi^{-1}$. Putting all these relations together, we find $Q_c \sim \xi^{-d}\xi^1$. The correlation length diverges as $t^{-\nu}$, where $\nu = 0.6705$ [50, 51] is the correlation length exponent and t is the reduced temperature. Therefore, $Q_c \sim t^{\nu(d-1)}$. Inverting this equation and substituting $d = 3$, we find that

[3] Some of the text in this section appears in Goodstein, Chui, and Harter [7].

$$t_c = \frac{T_\lambda - T_c(Q)}{T_\lambda} \sim Q^{\frac{1}{2\nu}}. \tag{1.19}$$

1.5.2 The exponent of the heat capacity divergence

In the vicinity of the divergence, (1.16) indicates that $C_Q \sim 1/\left(\partial q/\partial W\right)_T$. We can expand q about q_c, the value of q at the transition:

$$q = q_c + \left(\frac{\partial q}{\partial W}\right)_{W_c}(W - W_c) + \frac{1}{2}\left(\frac{\partial^2 q}{\partial W^2}\right)_{W_c}(W - W_c)^2 + ... \tag{1.20}$$

Since $(\partial q/\partial W)_{W_c} = 0$, and $(\partial^2 q/\partial W^2)_{W_c} < 0$, this implies that $q_c - q \sim (W_c - W)^2$, and $(\partial q/\partial W)_T \sim W_c - W$. Therefore, for measurements at fixed $T < T_\lambda$,

$$C_Q(T) \sim \frac{1}{W_c - W} \sim \frac{1}{\sqrt{q_c - q}} \sim [Q_c(T) - Q]^{-\frac{1}{2}}. \tag{1.21}$$

For measurements at fixed $Q > 0$, with $T_c(Q)$ defined by $Q_c(T_c) = Q$, one has

$$Q_c(T) = Q_c(T_c) + \left(\frac{\partial Q_c}{\partial T}\right)_{T=T_c}(T - T_c) + \ldots \tag{1.22}$$

Since $\partial Q_c/\partial T$ is finite at $T = T_c$, $Q_c - Q \sim T_c - T$ to leading order, and

$$C_Q \sim \theta^{-\frac{1}{2}}, \tag{1.23}$$

where θ is the reduced temperature with respect to $T_c(Q)$,

$$\theta \equiv \frac{T_c - T}{T_c}. \tag{1.24}$$

The heat capacity divergence at fixed Q is therefore considerably stronger than its near-logrithmic behavior with no heat current.

This analysis neglects the fluctuations in W, which are predicted to diverge at $T_c(Q)$. The exponent will be influenced by these fluctuations.

1.6 Predictions for the magnitude of the heat capacity enhancement

The magnitude of the heat capacity enhancement can be derived from the expression for the free energy.[4] From (1.9), in experiments where the counterflow velocity is held constant, the change in the free energy is

$$\Delta F = F(T,W) - F(T,0) = \int_0^W \rho_s(W')W'\,dW'. \tag{1.25}$$

Likewise, when Q is held constant, the change in the relevant free energy is

$$\Delta\Phi = \Phi(T,q) - \Phi(T,0) = -\int_0^q W\,dq' = -\int_0^q \frac{q'}{\rho_s}\,dq'. \tag{1.26}$$

In order to use these two expressions to calculate the change in the heat capacity, we need to know the dependance of ρ_s on W.

1.6.1 The depression of ρ_s with W

We will calculate $\rho_s(T,W)$ using three different theories: the MFT [48], which we modify by using empirical exponents, the ψ theory [52], and RG theory.[5] These theories all start from a mean-field expansion,

$$F_{\rm mf} = \alpha|\psi|^2 + \beta|\psi|^4 + J|\nabla\psi|^2 + M|\psi|^6, \tag{1.27}$$

which is written in the frame of reference of the normal fluid. Here α, β, J and M are expansion coefficients, M is zero except in the ψ theory, the macroscopic wave function is given by $\psi = \psi_0\, e^{i\phi}$, and $v_s = (\hbar/m)\nabla\phi$ (equal to the laboratory frame $W = v_s - v_n$), and m is the mass of a ^{4}He atom. The parameter α plays the role of the reduced temperature, with the equilibrium mean field transition to superfluidity

[4] Some of the text in the next section appear in Chui, Goodstein, Harter, and Mukhopadhyay [8].

[5] We will explicitly use the results of HD [6] in this discussion. More recently, Haussmann has modified this theory to obtain another prediction for C_Q that includes the effects of vortices. The results of Haussmann's theory will also be compared to our data.

occurring when α become negative. For a uniform v_s one obtains

$$F_{\rm mf} = (\alpha + Jk_0^2)\psi_0^2 + \beta\psi_0^4 + M\psi_0^6, \tag{1.28}$$

where $k_0 = mv_s/\hbar$.

The expression for $\psi_0(W)$ is obtained by minimizing $F_{\rm mf}$ with respect to ψ_0. The superfluid density is obtained by substituting $\psi_0(W)$ back into $F_{\rm mf}$ and computing $\rho_s = (1/v_s)(\partial F_{\rm mf}/\partial v_s)$ All three theories give $\rho_s(W,T)$ in the form

$$\rho_s(W,T) = \rho_s(W=0,T)\, f(\kappa), \tag{1.29}$$

where $\kappa = W/W_t$ and W_t is a characteristic velocity given by $W_t = \hbar/m\xi$. Within mean field theory, for $\alpha < 0$, one has $\xi = \sqrt{-J/2\alpha}$. For comparison with experimental data we will use the substitutions $\xi = \xi_0(2t)^{-\nu}$, where $\xi_0 = 1.43 \times 10^{-8}$ cm [53]. The characteristic velocity W_t can be expressed as $W_t = W_0\, t^{\nu}$, where $W_0 = \hbar 2^{\nu}/m\xi_0 = 175.4$ m/sec.

We find that for MFT, $\rho_s(W=0) = 2\alpha^2 m^2\xi^2/\hbar^2\beta$, $f(\kappa) = 1 - 2\kappa^2$, and, using this same form for $\rho_s(W=0)$, for ψ theory,

$$f(\kappa) = \frac{2(1-\kappa^2)}{1+\sqrt{1-\mu(1-2\kappa^2)}} - \frac{2\mu(1-2\kappa^2)^2}{\sqrt{1-\mu(1-2\kappa^2)}[1+\sqrt{1-\mu(1-2\kappa^2)}]^2}, \tag{1.30}$$

where $\mu = -3M\alpha/\beta^2$ is the scaling combination for M which vanishes as $\alpha \to 0$, indicating that M plays no role near the transition.

For HD theory, $f(\kappa)$ is given by equations (5.12), (C11), and (C3) in [6], and is shown in Fig. 1.8. All three theories predict that ρ_s is sufficiently depressed to cause superflow to break down.

1.6.2 The calculation of C_W

Next we compute the heat capacity enhancement using these expressions for $\rho_s(W)$. We first treat the case where the counterflow velocity, W, is *held constant*. This

(a)

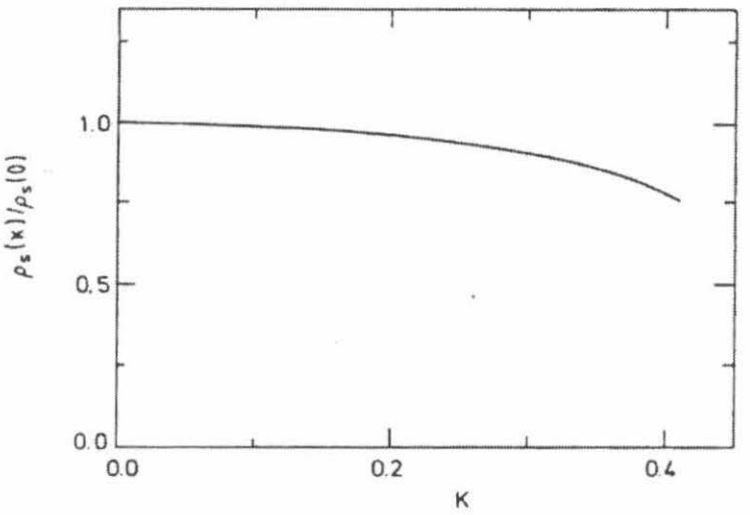

(b)

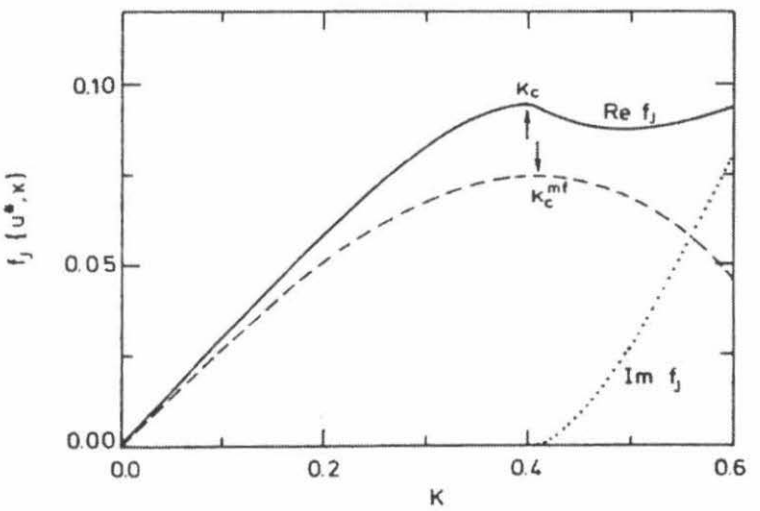

Figure 1.8: (a) The depression of ρ_s with $\kappa \equiv W/W_t$, where W_t is a characteristic velocity given by $W_t = \hbar/m\xi$, calculated using renormalization group theory. (From Haussmann and Dohm [6], Fig. 5.) (b) The amplitude of the superfluid current density, $J_s \equiv -\rho_s v_s$ versus κ. Solid line: Renormalization group theory. Dashed line: Mean field theory. (From Haussmann and Dohm [6], Fig. 4.)

experiment has not yet been performed, but the expression for C_W is embedded within the expression for C_Q, the quantity measured in our experiment. From (1.25), the change in the free energy due to the presence of a counterflow is:

$$\Delta F = \rho_s(0) W_t^2 \int_0^\kappa x f(x)\, dx. \tag{1.31}$$

The heat capacity is changed by

$$\Delta C_W = -TV \left(\frac{\partial^2 \Delta F(T,W)}{\partial T^2} \right)_W, \tag{1.32}$$

where $V = 27.38$ cm^3/mol is the molar volume. Using $\rho_s(0) = \rho_0\, t^\zeta$, where $\rho_0 = 0.370$ g/cm^3 [54], together with the scaling relation $\zeta = \nu = (2-\alpha)/3$, we obtain

$$\Delta C_W\, t^\alpha = -C_0 \nu \left[3\,(3\nu - 1) \int_0^\kappa x f(x)\, dx - (4\nu - 1)\, \kappa^2 f(\kappa) + \nu \kappa^3 \frac{\partial f(\kappa)}{\partial \kappa} \right], \tag{1.33}$$

where $C_0 = V \rho_0 W_0^2 / T_\lambda = 143$ J/mol K. For MFT, this reduces to

$$\Delta C_W\, t^\alpha = \frac{C_0 \nu \kappa^2}{2} \left[(1-\nu) + (1+\nu)\, \kappa^2 \right]. \tag{1.34}$$

For ψ theory and for HD theory, (1.33) is evaluated using numerical differentiation and integration. The results are shown in Fig. 1.9(a). C_W approaches a finite constant at $\kappa_c = W_c/W_t$ in all three theories.

1.6.3 The calculation of C_Q

The divergence of C_Q occurs because ρ_s is depressed by W. However, the heat capacity would still be enhanced by the presence of a heat flux even if ρ_s were not depressed at all. In this limit, $\rho_s = \rho_0\, t^\zeta$, and

$$\Delta\Phi = -\frac{1}{2}\rho_s W^2 = -\frac{1}{2\rho_s}\left(\frac{Q}{ST}\right)^2 = -\frac{1}{2\rho_0}\left(\frac{Q}{ST}\right)^2 t^{-\zeta}. \tag{1.35}$$

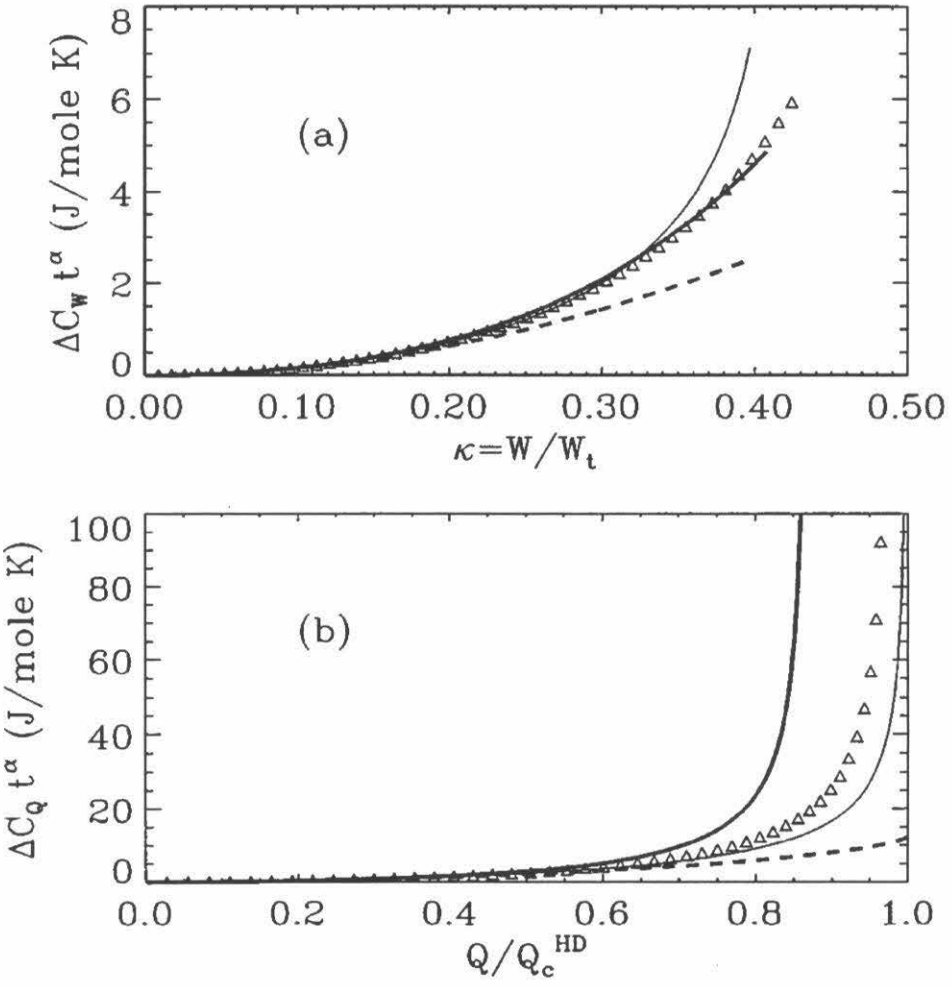

Figure 1.9: Thin line: HD theory. Thick line: MFT. Triangles: ψ theory with $M = 1$. Dashed line: no ρ_s depression. (a) C_W (b) C_Q. (From Chui *et al.* [8], Fig. 2.)

	Mean field	HD theory	H theory
κ_c	$1/\sqrt{6}$	0.397	?
$f(\kappa_c)$	2/3	0.790	?
$Q_0 = Q_c/t^{2\nu}$ (W/cm^2)	6082	7395	6571

Table 1.1: A summary of κ_c, $f(\kappa_c)$, and $Q_c/t^{2\nu}$.

Therefore,

$$\Delta C_Q = -TV\left(\frac{\partial^2 \Delta\Phi}{\partial T^2}\right)_Q = \frac{Q^2\zeta(\zeta+1)V}{2\rho_0 S^2 T_\lambda^3}\, t^{-(\zeta+2)}. \tag{1.36}$$

Since $Q_c = Q_0\, t^{2\nu}$, $\zeta = \nu$, and $\alpha = 2 - 3\nu$, we can rewrite this expression as

$$t^\alpha \Delta C_Q = \frac{\nu(\nu+1)VQ_0^2}{2\rho_0 S^2 T_\lambda^3}\left(\frac{Q}{Q_c}\right)^2, \tag{1.37}$$

which gives a finite enhancement for all $Q < Q_c(T)$ or all $T < T_c(Q)$.

When ρ_s is depressed by W, the heat capacity is given by (1.16), and the heat capacity enhancement is

$$\Delta C_Q = \Delta C_W + TV\frac{(\partial q/\partial T)_W^2}{(\partial q/\partial W)_T}. \tag{1.38}$$

Substituting the expression defined in (1.29) for $\rho_s(W)$, $q = \rho_s W = \rho_0 f(\kappa) W t^\nu$, the heat capacity enhancement becomes:

$$\Delta C_Q = \Delta C_W + C_0\, t^{-\alpha}\nu^2\kappa^2\left[\frac{\kappa\partial f(\kappa)}{\partial\kappa} - f(\kappa)\right]^2 \Big/ \frac{\partial\, \kappa f(\kappa)}{\partial\kappa}. \tag{1.39}$$

These results can be expressed in terms of the variable $\varrho \equiv Q/Q_c$, by using the relation $\varrho = \kappa f(\kappa)/[\kappa_c f(\kappa_c)]$ obtained from the expression $Q = \rho_s(W)WST$. The values for κ_c, $f(\kappa_c)$, and $Q_c/t^{2\nu}$ are listed in Table 1.1.

For the mean-field theory,

$$t^\alpha\, \Delta C_Q = C_0\nu\kappa^2\left[\frac{(\nu+1) + 5(\nu-1)\kappa^2 + 2(\nu-3)\kappa^4}{2(1-6\kappa^2)}\right]. \tag{1.40}$$

At small ϱ, this reduces to:

$$t^{\alpha}\,\Delta C = \frac{C_0}{2}\nu(\nu+1)\kappa_c^2 f^2(\kappa_c)\varrho^2\left[1+0.965\varrho^2+O(\varrho^4)\right]. \tag{1.41}$$

By comparing this expression to (1.36), we see that the first term in this expansion is the enhancement in C_Q that would result from a counterflow if ρ_s were not depressed by W. Figure 1.9(b) shows that all three theories give a divergent C_Q. Again, the results for the ψ theory and the HD theory are obtained numerically. Because Q_c is different for the three theories, we have used Q/Q_c^{HD} as the x axis, so that all three theories can be plotted on the same scale. Here Q_c^{HD} is the critical heat current given by HD. Figure 1.10 shows the divergence based on HD theory as a function of t for various values of Q.

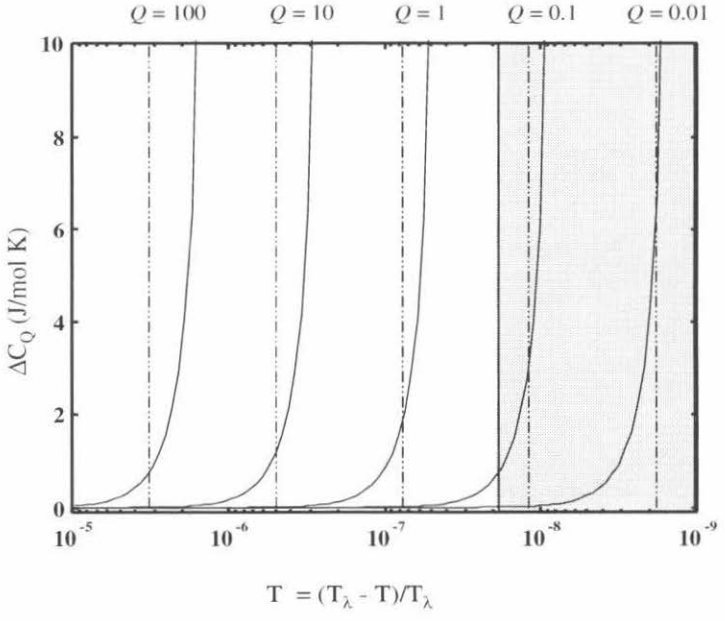

Figure 1.10: Solid lines: ΔC_Q, as calculated for HD theory [6, 8], for various values of Q. The units of Q are $\mu\mathrm{W/cm}^2$. Dotted-dashed lines: the temperatures at which superflow was *observed* to break down at these Q values by Duncan, Ahlers, and Steinberg [19] [This temperature will be called $t_{\mathrm{DAS}}(Q)$]. These lines indicate how much of the enhancement our experiment expected to measure. Shaded region: the area cut off by the gravity width of our 0.064 cm high cell.

Haussmann's theory

Haussmann recently performed another RG calculation based on model F. His approach permits the order parameter $\langle\psi\rangle$ to equal zero both above and below T_λ, and includes the effect of vortices [18]. He found $T_c(Q)$ to be at a slightly lower temperature than the value calculated previously by Haussmann and Dohm [6]. He also found a stronger enhancement of C_Q. His function reaches a maximum at $T_c(Q)$ instead of showing a divergence[6] (see Fig. 1.11).

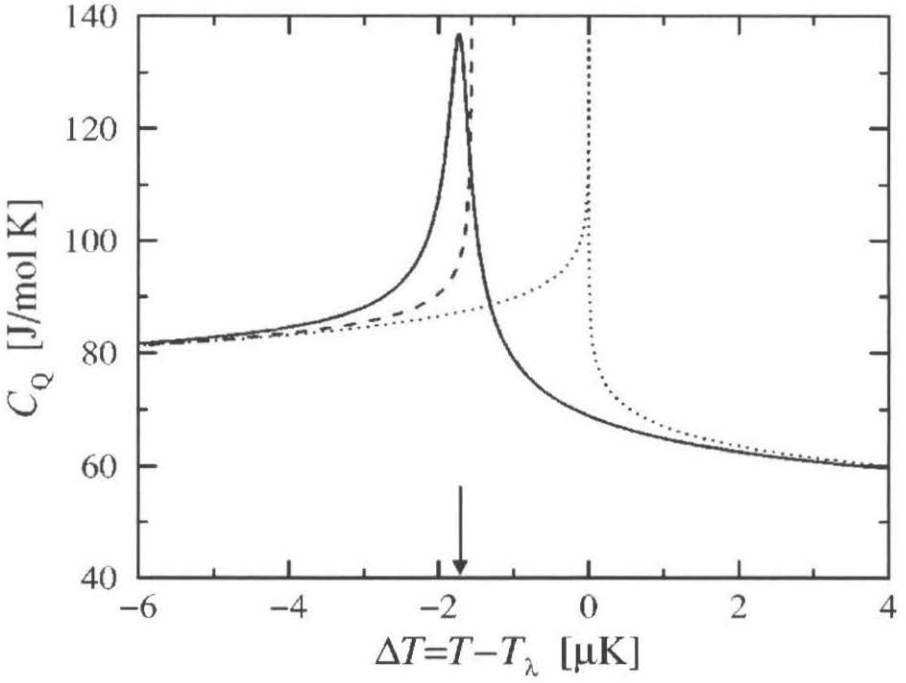

Figure 1.11: C_Q for $Q = 42.9\ \mu\mathrm{W/cm}^2$. Solid line: theory of Haussmann [18]. Dashed line: previous theories [8, 9], where vortices were neglected. Dotted line: specific heat with $Q = 0$. The arrow indicates $\Delta T_c(Q)$. (From Haussmann [18], Fig. 7.)

[6]Since the divergence of C_Q is predicted by thermodynamics, Haussmann's failure to predict a divergence is due to the fact that his calculation takes into account dissipative effects, and therefore smears out the transition in much the same way as gravity smears out the zero Q transition. In particular his calculation accounts for a finite temperature gradient in the superfluid phase.

1.7 The nature of the superfluid transition under heat flow

The critical heat flux, Q_c, reflects a thermodynamic instability in the counterflow velocity. It is the point at which convective heat transport can no longer be supported by the fluid, and superfluidity must break down. This transition is clearly not the same as the ordinary superfluid transition, since the superfluid density ρ_s is not equal to zero at $T_c(Q)$. It has been considered to be analogous to the spinodal line of a first order phase transition, where a homogeneous metastable state becomes unstable at a finite value of the order parameter (and the superfluid density) [4, 6]. The singular objects produced by this instability are vortices [14]. This transition also bears some resemblance to a distinct phase transformation, even though thermal gradients preclude there from being an equilibrium normal phase of finite Q on the other side of the transition [8]. When a system is characterized by a pair of conjugate variables (pressure-volume, concentration-chemical potential, magnetization-magnetic field), a phase transition usually occurs when the generalized susceptibility diverges (gas-liquid critical point, binary mixture phase separation, Curie point). In this particular case, q and W are a new conjugate pair whose susceptibility, $(\partial W/\partial q)_T \sim (\partial q/\partial W)_T^{-1}$, diverges at $T_c(Q)$. By analogy to other cases, W, instead of ρ_s, might be the order parameter for this transition, and q the conjugate field.

According to the fluctuation-dissipation relation [55], the mean square fluctuations in W are equal to $\langle \Delta W^2 \rangle = k_B T (\partial W/\partial q)_T$, and therefore diverge at $T_c(Q)$. It is these fluctuations that must spontaneously generate vortices, and hence temperature gradients, before one actually reaches $T_c(Q)$, leading to a breakdown of the thermodynamic approximation to nonequilibrium superfluidity and smearing the transition. It is yet to be determined how close to $T_c(Q)$ one can approach before this happens, and hence exactly how sharp the critical singularities discussed in this thesis really are.

Chapter 2 The Superfluid Transition in the Q-T Plane

This chapter presents a review of many of the experiments and theories that investigate the physics of ^{4}He in the presence of a heat flux. It is comprised of the complete text of an article written for *Reviews of Modern Physics* by Peter Weichman, David Goodstein, and myself [56]. It should provide the necessary background and relevant context for this project. The article concludes with a brief review of the experiment described in the remaining chapters of this thesis. Although most of the information in this section will be repeated later on, it is included here in order to maintain the integrity of the original text. Perhaps it should be considered as a preview of things to come.

Some of the symbols used in this article are different than those used for the other chapters of this thesis. A few of the differences result from the fact that this experiment is performed extremely near T_λ, where the superfluid density ρ_s and the normal fluid velocity $\mathbf{v}_n$ are both extremely small. This implies that in our range of interest, $\mathbf{W} \equiv \mathbf{v}_n - \mathbf{v}_s \approx -\mathbf{v}_s$, and $q \equiv \rho_s \mathbf{W} \approx -\mathbf{J}_s \equiv -\rho_s \mathbf{v}_s$.

Most of the other discrepancies are simply due to differences in notation. Unfortunately, this is symptomatic of the field in general, where there are a plethora of notational conventions floating around in the literature. One of the more disturbing (and confusing) differences is the terminology used for the temperature of superfluid breakdown: a number of papers refer to the *theoretical* temperature of superfluid breakdown as $T_c(Q)$ and the experimental temperature as $T_{\rm DAS}(Q)$, while others refer to the *experimentally measured* temperature of superfluid breakdown as $T_c(Q)$, and the theoretical temperature as $T_\lambda(Q)$.[1] The most significant notation differences

[1] This entire thesis, and all of the papers published out of our research group, sticks to the first convention. It is our belief that since the transition under heatflow is of a very different nature, it should be distinguished in a significant way from the traditional transition at T_λ.

are summarized in Table 2.1.

Abstract

The behavior of liquid ^{4}He in a heat flux, Q, close to the superfluid transition, can be represented by a phase diagram in the Q-T plane and described by means of a new set of critical point exponents, which we introduce. We review a striking array of recent experiments and their theoretical interpretations. The excitement that surrounds this field arises from the fact that advanced thermometry and the future availability of a microgravity experimental platform aboard the International Space Station will soon open to experimental exploration a new frontier of decades of reduced temperatures that were previously inaccessible.

2.1 Introduction

Due to its extraordinary purity and insensitivity to external perturbations, superfluid ^{4}He has long been the best system for accurate, detailed experimental investigations of phase transitions and critical phenomena. The essence of superfluidity, however, lies in the dynamics of flowing helium, rather than in equilibrium properties such as the specific heat and the superfluid density. In recent years, considerable experimental attention has been focused on the behavior of liquid helium, near the lambda transition temperature, T_λ, when a flux of heat, $\mathbf{Q}$, is passed through it [19, 25, 57–59]. This article reviews the wealth of exciting new physical phenomena uncovered by these experiments and by the parallel theoretical investigations [4, 11, 12, 17, 60, 61].

At sufficiently small $\mathbf{Q}$, superfluid ^{4}He transports heat essentially without dissipation, by means of superfluid-normal fluid counterflow. At higher $\mathbf{Q}$, or as T approaches T_λ, this transport mode breaks down. In Sec. 2.2 we discuss the phase diagram of helium in the Q-T plane. In this plane, the superfluid state is bounded by a transition curve, $Q_c(T)$, outside of which dissipative flow takes over. We also introduce and evaluate a new set of critical exponents that arise as a consequence of superflow.

	A	B	C	D	E	F	G
This chapter	$-\epsilon$	NA	$-\mathbf{u}_s$ $-\mathbf{U}_s \equiv \mathbf{W}$	$T_{DAS}(Q)$	$T_c(Q)$	$-\mathbf{J}_s \equiv -\rho_s \mathbf{v}_s$	Q_0^c
Other chapters	t	θ	$\mathbf{W}$	$T_{DAS}(Q)$	$T_c(Q)$	$\mathbf{q} \equiv \rho_s \mathbf{W}$	Q_0
Group α	t $-\epsilon$	θ	$\mathbf{W}$ $-\mathbf{v}_s$	$T_{DAS}(Q)$	$T_c(Q)$	$\mathbf{P} \equiv \rho_s \mathbf{W}$ q	Q_0
Group β	t	NA	$\mathbf{w}$ $-\mathbf{u}_s$	$T_c(Q)$	$T_\lambda(Q)$	$-\mathbf{J}_s$	Q_0

Table 2.1: A list of the different notation conventions used in this thesis and the literature. Group α: The notation convention used in the papers of D. L. Goodstein, P. B. Weichman, R. V. Duncan, and their collaborators. Group β: The notation convention used in the papers of G. Ahlers, R. Haussmann, V. Dohm and their collaborators. NA: not applicable.

The above table headings:	**What they refer to:**
A	The reduced temperature with respect to the static transition temperature: $(T_\lambda - T)/T_\lambda$
B	The reduced temperature with respect to the dynamic transition temperature: $(T_c - T)/T_c$
C	The counterflow velocity
D	The experimentally measured temperature of superfluid breakdown [19]
E	The theoretically predicted temperature of superfluid breakdown [6, 18]
F	The superfluid momentum density
G	The amplitude of the critical heat current

In Sec. 2.3 we describe an inhomogeneous phase where the heat flows through both normal and superfluid regions, separated by an interface region that is neither normal nor superfluid. In the normal region the heat flux produces a static temperature gradient. In the superfluid region, the heat flows at constant temperature. In the interface region, a transition between these types of behavior is mediated by fluctuations in a way that is not yet accessible either to experiment or to theory.

A recurring theme throughout the article is the fundamental limitation imposed by the Earth's acceleration due to gravity, g_e, on the resolution of Earth-based experiments. Gravity produces a pressure gradient across the sample, leading to a variation in the local lambda transition temperature $T_\lambda(z)$ with height z according to

$$\partial_z T_\lambda(z) = -\gamma \frac{g}{g_e}, \quad \gamma \simeq 1.27 \ \frac{\mu\mathrm{K}}{\mathrm{cm}}. \tag{2.1}$$

For generality, the possibility of gravity g different from that on Earth is included. For $g = g_e$ the transition temperature therefore decreases by 1.27 μK per centimeter of column height. If T is tuned so that, say, the center of the cell is at the local lambda point, the upper region will be superfluid while the lower region will be normal fluid. The interface between, defined as the region over which the local properties differ significantly from those of a bulk system at the same local temperature and pressure, is about 0.1 mm wide on Earth [62]. This figure also estimates the maximum possible critical correlation length in the system.

The inhomogeneity induced by g_e causes the critical singularities to be rounded on a scale set by the height of the cell. Balancing gravity effects against finite size effects, which enter if the cell is too small, the optimal cell height is about 0.3 mm, leading to rounding on a scale $\epsilon \equiv (T - T_\lambda)/T_\lambda \sim 10^{-7}$. Present thermometry [2, 59] is capable of resolving reduced temperatures ϵ 3-4 orders of magnitude smaller than this. In essence there is a new frontier, consisting of decades of previously unavailable reduced temperature around T_λ, that can only be explored in microgravity. Experiments measuring equilibrium specific heat (Lambda Point Experiment—LPE) [2] and finite size effects (Confined Helium Experiment—CHEX) have recently flown aboard the

space shuttle.

Gravity also has a strong effect on the interface region discussed in Sec. 2.3. As we have seen above, the interface is compressed by gravity to a width of about 0.1 mm, too small to be studied experimentally. The interface region will be studied in an experiment (Critical Dynamics Experiment—DYNAMX) presently being prepared for a low temperature microgravity platform (Low Temperature Microgravity Physics Facility—LTMPF) that is to be part of the International Space Station (ISS).

Although gravity is detrimental to some measurements, there can also be interesting new physics when both gravity and heat current are present. In Sec. 2.4 we describe the so-called *self-organized critical* (SOC) state, in which g and Q conspire to produce a new, essentially homogeneous, nonequilibrium state where the temperature $T(z)$ precisely parallels $T_\lambda(z)$ at a fixed Q-dependent distance. At larger Q, this state undergoes a transition from normal to superfluid, with the temperature gradient supported by a stream of vortices in the latter.

Finally, in Sec. 2.5 we discuss the specific heats under heat flow, predicted [8, 9, 12], and subsequently confirmed [25], to be *enhanced* above the equilibrium form, with a singularity predicted at the phase boundary $Q_c(T)$. This experiment too ultimately needs to be performed at very low Q, and the required microgravity version is currently being proposed.

2.2 Nonequilibrium critical phenomena and scaling

Under conditions where a uniform heat flux $\mathbf{Q}$ is applied to superfluid ^{4}He, a thermal counterflow is created in which the normal fluid moves along with $\mathbf{Q}$ at velocity $\mathbf{u}_n$, and the superfluid moves oppositely with velocity $\mathbf{u}_s$. For sufficiently small heat current not too close to T_λ [more precisely, one requires $Q < Q_c(T)$, with $Q_c(T)$ defined in Fig. 2.2 and (2.21) below] the temperature $T < T_\lambda$ is essentially uniform

and the heat flux is

$$\mathbf{Q} = TS\rho\mathbf{u}_n, \tag{2.2}$$

where S is the entropy per unit mass, $\rho = \rho_s + \rho_n$ is the total mass density, composed of superfluid and normal fluid parts, and $\mathbf{u}_n$ is the normal fluid velocity. Since there is no net mass flow, one has $\mathbf{j}_n = -\mathbf{j}_s$, where $\mathbf{j}_s = \rho_s\mathbf{u}_s$ and $\mathbf{j}_n = \rho_n\mathbf{u}_n$ are, respectively, the superfluid and normal fluid mass current densities, and $\mathbf{u}_s$ is the superfluid velocity. Close to T_λ one finds experimentally $S \simeq S_\lambda \equiv 1.58$ J/gK, $\rho_s \approx \rho_0|\epsilon|^\zeta$, with $\rho_0 \simeq 0.37$ g/cm^3, critical exponent $\zeta \simeq 0.671$, and $\rho_n \simeq \rho \simeq 0.14$ g/cm^3. Thus, in experimentally motivated units,

$$u_s \approx 7.9 \times 10^{-3} \frac{Q}{1\mu\mathrm{W/cm}^2} \left(\frac{10^{-6}}{|\epsilon|}\right)^\zeta \mathrm{cm/s} \tag{2.3}$$

$$u_n \approx 2.1 \times 10^{-6} \frac{Q}{1\mu\mathrm{W/cm}^2} \mathrm{cm/s}. \tag{2.4}$$

At experimentally accessible values $Q = 1$ μW/cm^2 and $|\epsilon| = 10^{-6}$, u_s is a modest 80 μm/s and u_n is nearly four orders of magnitude smaller.

2.2.1 Thermodynamic formalism

The isothermal condition allows an effective thermodynamic description of the finite $\mathbf{Q}$ state [63]. Although nonequilibrium scaling does not rely on this, a more intuitive description of a number of phenomena special to superfluidity results, and so it is worthwhile presenting the theory in this context.

In the frame of reference moving with the normal fluid (in which there is no heat flow), the differential of the free energy density $F(T, \mathbf{U}_s)$ may be written,

$$dF = -SdT + \mathbf{J}_s \cdot d\mathbf{U}_s, \tag{2.5}$$

in which $\mathbf{U}_s = \mathbf{u}_s - \mathbf{u}_n$ and

$$\mathbf{J}_s = \left(\frac{\partial F}{\partial \mathbf{U}_s}\right)_T = \rho_s\mathbf{U}_s, \tag{2.6}$$

with the second equality serving as a *definition* of $\rho_s(T, U_s)$ when U_s is not small. Near T_λ the smallness of $\mathbf{u}_n$ implies that $\mathbf{U}_s \simeq \mathbf{u}_s$ and $\mathbf{J}_s \simeq \mathbf{j}_s$. In this frame one has the defining relation $\mathbf{U}_s = (\hbar/m)\nabla\phi$, where m is the ^{4}He atomic mass, and

$$\phi(\mathbf{r}) = \frac{m}{\hbar}\mathbf{U}_s \cdot \mathbf{r} \tag{2.7}$$

is the phase of the superfluid order parameter $\psi = |\psi|e^{i\phi}$, yielding the usual helical structure of ψ aligned along $\mathbf{U}_s$. The effective thermodynamic description (2.5) relies on the existence of a time-independent ψ in the presence of a finite phase gradient. In fact, thermally nucleated phase slips in the helical structure (interpreted as tunneling between different metastable local minima of the free energy) lead to small temperature gradients and decay of superflow. However, the decay time is extremely large at low heat currents and temperatures not too close to T_λ [64]. The thermodynamic description (2.5) is valid on time scales smaller than this. As $\mathbf{U}_s$ increases, both the order parameter magnitude $|\psi(U_s, T)|$ and the superfluid density are suppressed relative to their equilibrium values at $U_s = 0$, $Q = 0$.

Variations at constant $\mathbf{Q} = -TS\mathbf{J}_s$ are most conveniently performed by defining the Legendre transformed free energy $\Phi(T, \mathbf{J}_s) = F - \mathbf{J}_s \cdot \mathbf{U}_s$ with differential

$$d\Phi = -SdT - \mathbf{U}_s \cdot d\mathbf{J}_s. \tag{2.8}$$

Close to T_λ, where $TS \simeq T_\lambda S_\lambda$ is essentially constant, variations at constant $\mathbf{Q}$ are asymptotically the same as those at constant $\mathbf{J}_s$. For example, the specific heat at fixed $\mathbf{Q}$ may be taken as

$$C_Q = T\left(\frac{\partial S}{\partial T}\right)_{J_S}, \tag{2.9}$$

where $S(T, \mathbf{J}_S) = -(\partial\Phi/\partial T)_{J_S}$. With the above observation in mind, we shall henceforth treat $\mathbf{J}_s$ and $\mathbf{Q}$ as differing only by a constant factor.

2.2.2 Nonequilibrium scaling

The fact that $\mathbf{U}_s$ and $\mathbf{J}_s$ (or $\mathbf{Q}$) may be treated as thermodynamically conjugate variables has important consequences for the structure of the thermodynamic functions near T_λ [65]. We proceed by analogy with the conjugate variables h and m at conventional critical points, where h is the external magnetic field and m the magnetization at a Curie point, or h is the difference from critical pressure and m the difference from critical density at a liquid-vapor critical point. There the free energy $A(T,h)$, analogous to Φ, has differential $dA = -SdT - mdh$ and its singular part A_s obeys an *asymptotic scaling form* [see, e.g., [66]],

$$A_s(T,h) = E_0|\epsilon|^{2-\alpha}\mathcal{A}\left(\frac{D_0 h}{|\epsilon|^\Delta}\right), \tag{2.10}$$

in which α is the specific heat exponent, Δ is the "gap exponent," $\mathcal{A}(x)$ is a universal scaling function, and E_0, D_0 are nonuniversal scale factors, specified uniquely via, say, the normalizations $\mathcal{A}(0) = \mathcal{A}'(0) = 1$. There are actually two scaling functions, $\mathcal{A}_\pm(x)$ for $\pm\epsilon > 0$, but we shall primarily be interested in the ordered phase $\epsilon < 0$ and consider only $\mathcal{A}_- \equiv \mathcal{A}$.

Similarly, the singular part of the superfluid free energy, Φ_s, is expected to obey the scaling form,

$$\Phi_s(T,Q) = A_0|\epsilon|^{2-\alpha}\Upsilon\left(\frac{Q}{Q_0|\epsilon|^{\Delta_Q}}\right), \tag{2.11}$$

in which $\alpha \simeq -0.013$ [2] is again the usual equilibrium specific heat exponent, Δ_Q is the gap exponent for Q, $\Upsilon(y)$ is the $\epsilon < 0$ universal scaling function, and A_0, Q_0 are nonuniversal scale factors, specified uniquely via, say, the normalizations $\Upsilon(0) = \Upsilon''(0) = 1$ [$\Upsilon(y)$ must be an even function of y due to the obvious symmetry under sign reversal of Q].

The derivative of (2.10) with respect to h yields

$$m(T,h) = -E_0 D_0|\epsilon|^\beta \mathcal{A}'\left(\frac{D_0 h}{|\epsilon|^\Delta}\right) \tag{2.12}$$

where the prime denotes derivative with respect to argument and the order parameter

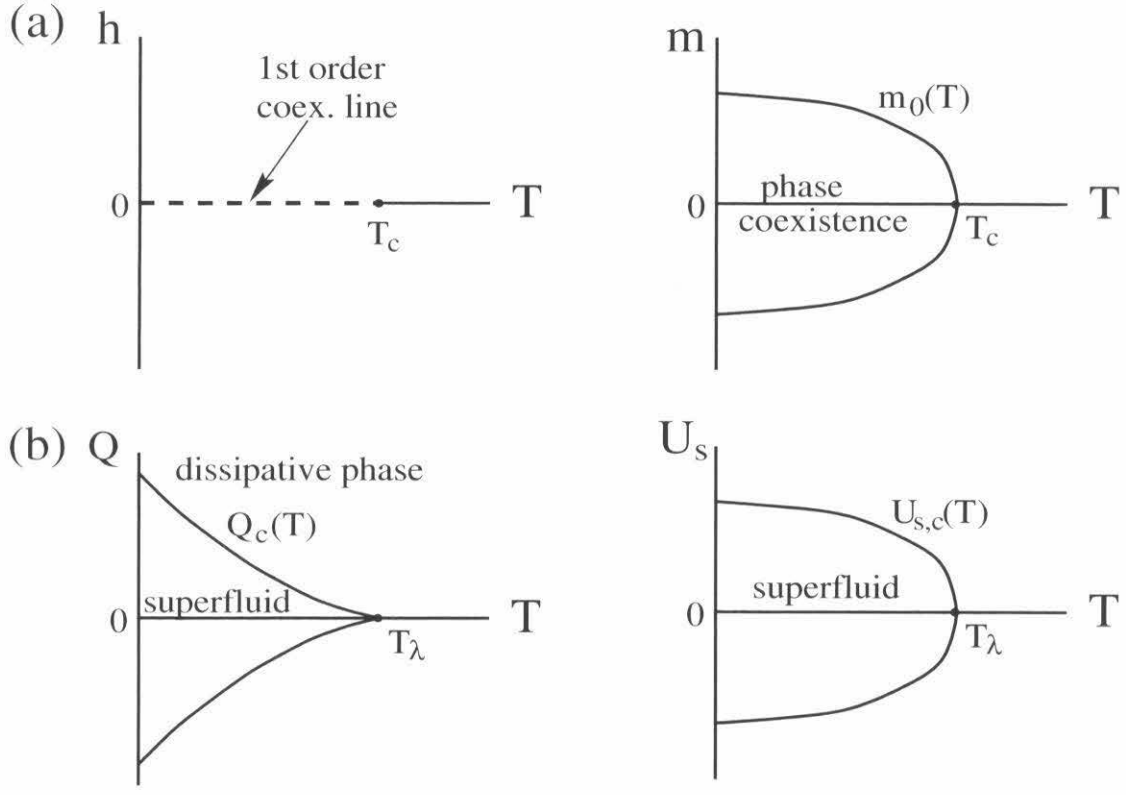

Figure 2.1: Comparison of phase diagrams in (a) conventional T-h and T-m spaces and (b) superfluid T-Q and T-U_s spaces. Here, $m_0(T)$ is the spontaneous magnetization, or the liquid density minus the critical density. The critical lines $Q_c(T)$ and $U_{s,c}(T)$, enclose the region of stable superflow, which corresponds also to the region of validity of the thermodynamic description, and like the thermodynamic description itself are sharp only in the absence of phase slips. The different shapes of these curves near T_λ are determined by the fact that $\Delta_Q > 1$, while $\beta_Q < 1$ [see equations (2.19)–(2.22) below]. The nature of the critical behavior as Q approaches Q_c from below, and the nature of the inhomogeneous dissipative phase for $Q > Q_c$, will be discussed in later sections. A major difference between (a) and (b) is the lack of a first order line below T_λ in the latter. Thus, h vanishes throughout the phase coexistence region in the T-m plane, whereas $Q \propto J_s = \rho_s U_s$ varies continuously throughout the superfluid phase in the T-U_s plane.

exponent β obeys the scaling relation $\beta = 2-\alpha-\Delta$. The second h derivative yields the order parameter susceptibility (compressibility, in the case of a liquid-vapor critical point)

$$\chi(T,h) = -E_0 D_0^2 |\epsilon|^{-\gamma} \mathcal{A}'' \left(\frac{D_0 h}{|\epsilon|^{\Delta}} \right) \tag{2.13}$$

with $\gamma = \alpha + 2\Delta - 2$, which then yields the famous Essam-Fisher scaling law $\alpha + 2\beta + \gamma = 2$ [66].

Similarly, the derivative of Φ_s with respect to J_s yields U_s in the form

$$U_s(T,Q) = -B_0 |\epsilon|^{\beta_Q} Y' \left(\frac{Q}{Q_0 |\epsilon|^{\Delta_Q}} \right), \tag{2.14}$$

where $B_0 = A_0 T_\lambda S_\lambda / Q_0$, and one has the generalized order parameter exponent scaling relation

$$\beta_Q = 2 - \alpha - \Delta_Q. \tag{2.15}$$

The equilibrium superfluid density enters the free energy F via a term $\Delta F_s = \frac{1}{2}\rho_s U_s^2$ for small U_s. The Legendre transform yields a term $\Delta\Phi_s = -J_s^2/2\rho_s$ for small J_s, and the inverse of the superfluid density now appears in the theory as a generalized susceptibility:

$$\begin{aligned} \frac{1}{\rho_s(T, Q=0)} &= -\left(\frac{\partial^2 \Phi_s}{\partial J_s^2} \right)_{T, J_s = 0} = \left(\frac{\partial U_s}{\partial J_s} \right)_{T, J_s = 0} \\ &= -\frac{R_0 Y''(0)}{|\epsilon|^{\gamma_Q}} \end{aligned} \tag{2.16}$$

where $R_0 = A_0 (T_\lambda S_\lambda / Q_0)^2$ and the generalized susceptibility exponent γ_Q obeys the Essam-Fisher relation [66],

$$\gamma_Q = \zeta = 2\Delta_Q + \alpha - 2 \tag{2.17}$$

$$\alpha + 2\beta_Q + \gamma_Q = 2 \tag{2.18}$$

Generally the gap exponent is independent of α and must be separately determined. However, in the superfluid problem the Josephson relation [see, e.g., [67] and refer-

ences therein] yields $\zeta = 2 - \alpha - 2\nu = (d-2)\nu$. Here $\xi \approx \xi_0/|\epsilon|^\nu$ with, in dimension $d = 3$, $\nu = \zeta \simeq 0.671$ and $\xi_0 \simeq 3.4$ Å [68], describes the divergence of the superfluid coherence length, $\xi = (m^2 k_B T/\hbar^2 \rho_s)^{1/(d-2)}$, and the second equality follows from the hyperscaling relation $2 - \alpha = d\nu$ [65, 66]. We therefore identify

$$\Delta_Q = 2 - \alpha - \nu = (d-1)\nu. \tag{2.19}$$

This scaling law implies that Q scales with the cross-sectional area ξ^{d-1} of a correlation volume ξ^d: Q becomes significant when the power incident on a correlation area is of order $Q_0 \xi_0^{d-1}$.[2] From (2.15) one obtains

$$\beta_Q = \nu. \tag{2.20}$$

This relation has the interpretation that $(m/\hbar)\mathbf{U}_s$, which has dimensions of inverse length, scales with the inverse correlation length ξ^{-1}: the phase gradient has a significant effect when its wavelength $2\pi\hbar/mU_s$ becomes comparable to ξ. Note that, more typically, one begins with the latter assumption and reverses the above argument to *derive* the Josephson relation.

Just as arbitrarily small h smears the singular behavior near a Curie point, one expects an arbitrarily small Q to either smear or drastically alter the lambda point critical behavior. This is consistent with $\Delta_Q > 0$, implying that the scaling argument y diverges as $|\epsilon| \to 0$ at any finite Q, serving to define Q as a *relevant perturbation* to the lambda point [65]. In Fig. 2.1 a schematic of the expected phase diagram is shown, contrasting it with that for a conventional critical point. The lines $Q_c(T)$ and $U_{s,c}(T)$ are the boundaries beyond which superfluidity breaks down: for $Q > Q_c$, due

[2] One may estimate Q_0 as follows. Two scale factor universality yields a form $C_s = k_B(R_\xi/\xi)^d/\alpha|\epsilon|^2$ for the singular part of the equilibrium specific heat below T_λ, where the hyperuniversal ratio $R_\xi \simeq 0.90$ in $d = 3$ [69]. This must match the scaling form (2.11) at $Q = 0$ and determines $A_0|\epsilon|^{2-\alpha} = [k_B T_\lambda/\alpha(1-\alpha)(2-\alpha)](R_\xi/\xi)^d$ [with the choice $Y(0) = 1$]. Equating the quadratic terms $A_0|\epsilon|^{2-\alpha}(Q/Q_0|\epsilon|^{\Delta_Q})^2 = -J_s^2/\rho_s$ [with the choice $Y''(0) = 1$], one obtains finally $Q_0 = T_\lambda S_\lambda \sqrt{-A_0\rho_0}$, and $Q_0\xi_0^{d-1} = mk_B T_\lambda^2 S_\lambda R_\xi^{d/2}/\hbar\sqrt{-\alpha(1-\alpha)(2-\alpha)}$ (using $\rho_0 = m^2 k_B T_\lambda/\hbar^2\xi_0^{d-2}$). Substitution of experimental numbers yields $A_0 \simeq -21$ J/cm^3 and $Q_0 \simeq 30$ kW/cm^2.

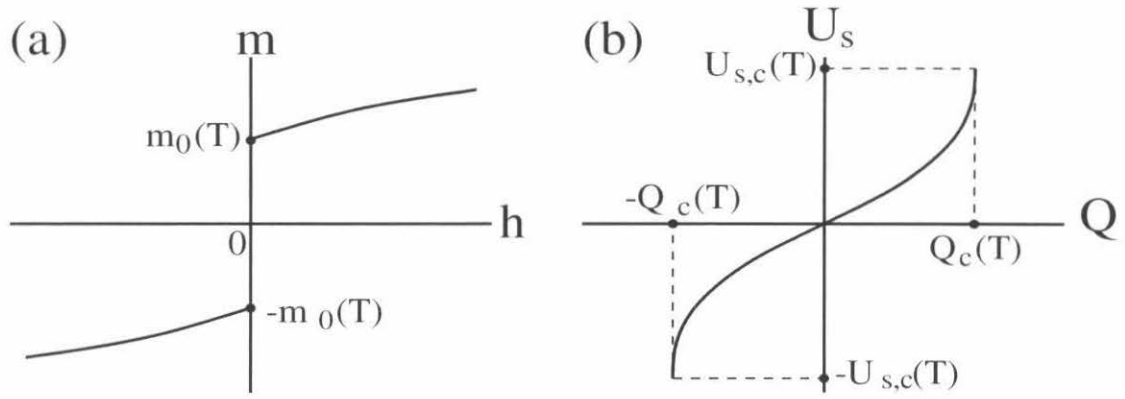

Figure 2.2: Comparison of the isothermal equation of state (a) in the conventional h-m plane and (b) in the superfluid Q-U_s plane. At $h = 0$ there is a first order transition between up and down magnetized states, or between liquid and vapor states. As $|h|$ increases, $|m(T,h)|$ increases as well. As $|Q|$ increases $|U_s|$ increases until the superfluid breaks down at $|Q| = Q_c(T)$, at which point $U_s(Q,T)$ has a square root cusp. At this same point the specific heat at constant U_s also has a square root cusp [12], while the specific heat at constant Q has an inverse square root divergence [8].

to suppression of the order parameter and superfluid density, the heat current is too large for the superfluid to support isothermal heat transport, and a nonequilibrium phase transition to a new dissipative phase occurs. The nature of this phase will be discussed in Sec. 2.3 below. In Fig. 2.2 we sketch the isothermal equations of state for the conventional and superfluid systems. At a fixed subcritical temperature the conventional system displays the usual first order jump in m at $h = 0$ between up and down magnetized states, or between liquid and vapor states. The superfluid system displays a continuous variation of U_s with Q, but at $|Q| = Q_c(T)$ encounters the boundary between superfluid and dissipative phases. At this point $U_s(Q)$ has a square root cusp [12], corresponding to a strong suppression of ρ_s and a divergent susceptibility $(\partial U_s/\partial J_s)_T$. This singularity is exhibited in the scaling form (2.11) as square root cusps in $Y(y)$ at some finite value $y = \pm y_c$. This yields the predictions

$$Q_c(T) \approx Q_0 y_c |\epsilon|^{\Delta_Q} \tag{2.21}$$

$$U_{s,c}(T) \approx B_0 Y'(y_c) |\epsilon|^{\beta_Q} \propto Q_c(T)^{1/\delta_Q}, \tag{2.22}$$

in which

$$\delta_Q = \Delta_Q/\beta_Q = 1 + \gamma_Q/\beta_Q. \tag{2.23}$$

The latter relation generalizes the Widom scaling law $m(T_c, h) \propto h^{1/\delta}$ with $\delta = \Delta/\beta = 1 + \gamma/\beta$ which follows from (2.12) in the limit $\epsilon \to 0$ [the asymptotic behavior $\mathcal{A}'(x) \sim x^{\beta/\Delta}$ as $x \to \infty$ is required for consistency] [66]. From (2.17) and (2.20) one obtains explicitly $\delta_Q = d - 1$. As will be discussed in Sec. 2.5, the specific heats at constant U_s and Q are also singular at $U_{s,c}(T)$ and $Q_c(T)$ [8, 9, 12].

The coherence length itself obeys a scaling form

$$\xi(T, Q) = \xi_0 |\epsilon|^{-\nu} \Xi\left(\frac{Q}{Q_0 |\epsilon|^{\Delta_Q}}\right), \tag{2.24}$$

with $\Xi(0) = 1$. Considering variations of ξ at a fixed value of $y = Q/Q_0|\epsilon|^{\Delta_Q}$, one may write

$$\xi = \xi_0 (Q/Q_0)^{-\nu_Q} y^{\nu_Q} \Xi(y) \tag{2.25}$$

$$\nu_Q \equiv \nu/\Delta_Q = 1/(d-1), \tag{2.26}$$

serving to define an exponent describing the characteristic variation of ξ with $\mathbf{Q}$. Attempts to verify the scaling relations (2.21) and (2.26), with $\Delta_Q = 2\nu$ and $\nu_Q = 1/2$ in $d = 3$, will be discussed in later sections.

In Table 2.2 we summarize the various critical exponents we have defined, along with their values in general dimension d and in $d = 3$.

As a final comment, we note that verifications of certain dynamical scaling laws in ^{4}He are complicated by a fundamental problem associated with the smallness of the exponent α. Scaling forms like (2.11) implicitly assume that $|\epsilon|$ is sufficiently small that all *irrelevant* scaling variables may be ignored. It turns out that α controls the relevance of *mass and heat diffusion* to the dynamic critical behavior [70] through an additional scaling variable $w \equiv \gamma_0 |\epsilon|^{-\alpha}$, where γ_0 is a parameter of order unity in the Model F equations [70] (describing the near-critical dynamics of ^{4}He) which couples entropy and density fluctuations to order parameter fluctuations. The variable w

exponent	general d	$d = 3$
ν	$1/2 \leq \nu(d) \leq \infty$	0.671
α	$2 - d\nu$	-0.013
ζ	$2 - \alpha - 2\nu = (d-2)\nu$	0.671
Δ_Q	$2 - \alpha - \nu = (d-1)\nu$	1.342
β_Q	ν	0.671
γ_Q	ζ	0.671
δ_Q	$1 + \gamma_Q/\beta_Q = d - 1$	2
ν_Q	$\nu/\Delta_Q = 1/(d-1)$	1/2

Table 2.2: Equilbrium and nonequilibrium critical exponents and their values. Note that no exact expression for the correlation length exponent $\nu(d)$ is known, aside from the boundary values $\nu(2) = \infty$ and $\nu(d \geq 4) = \frac{1}{2}$, but all other exponents are either given exactly or in terms of ν. There are other independent exponents (e.g., the critical correlation exponent $\eta \simeq 0.02$), but they happen not to be involved in any of the experiments we discuss. Expressions in the center column involving d explicitly require hyperscaling, and are therefore valid only for $d \leq 4$. For $d \geq 4$ the exponents all stick at their mean field values, and may be determined by substituting $\nu = \frac{1}{2}$, $\alpha = 0$ into the non-explicitly d-dependent forms of the scaling relations.

does not appear in any equilibrium scaling function (where such fluctuations may be completely "integrated out" of the partition function), but does appear in those involving dissipative transport, e.g., that of the thermal conductivity [11]. Since $\alpha < 0$ this variable vanishes as $|\epsilon| \to 0$ but extremely slowly: $\epsilon = 10^{-75}$ leads only to $|\epsilon|^{-\alpha} \simeq 0.1$. The scaling function then has a very slow parametric dependence on w, leading to "quasi-scaling" [11] of the heat conductivity, and hence to an apparent slow variation of the associated critical exponent with w. Measured dynamic critical exponents affected in this way may typically be expected to differ from their true asymptotic values by 10-20% [19].

The scaling phenomena considered here, however, are mainly those associated with properties of isothermal superfluids, which though out of equilibrium, are nevertheless argued to behave as equilibrium thermodynamic systems. To the extent that this is true (i.e., to the extent that vortex excitations can be ignored), the Model F equations again produce a thermodynamic-type partition function with entropy/density fluctuations integrated out, and finite $\mathbf{Q}$ enforced by an imposed uniform helical twist in the order parameter [12]. The scaling variable w will again not appear, and one

expects that quasi-scaling will be absent in (2.11) and from all quantities derived from it, and hence that the exponents in Table 2.2 will exhibit experimentally their predicted values. On the other hand, the phase boundaries in Fig. 2.1(b) are defined by the *onset* of dissipative transport, with divergent fluctuations in the local heat current as they are approached. Such fluctuations lead to vortex creation, decay of superflow, breakdown of the effective equilibrium description, and the reappearance of the variable w. In some sense w must control the "fuzziness" of the boundary $Q_c(T)$, and an experimental test of the relations (2.21) may exhibit quasi-scaling even if, for y sufficiently less than y_c, the scaling function $Y(y)$ does not. This issue is potentially testable by the specific heat measurements discussed in Sec. 2.5. Unfortunately, as exhibited in Fig. 2.9 below, present data are constrained to lie sufficiently far below $Q_c(T)$ that both asymptotic and nonasymptotic forms fit equally well.

2.3 The nonequilibrium superfluid-normal interface

2.3.1 Interface statics

Consider a cylindrical cell with a heat current $\mathbf{Q}$ driven along its axis, labeled by coordinate z, in which the up-stream endwall, $z = 0$, has $T(0) > T_\lambda$. In the normal phase heat is transported by thermal conduction, which at sufficiently small Q is described by the Fourier law

$$Q = -\kappa \partial_z T, \tag{2.27}$$

where $\kappa(T) \approx \kappa_0 \epsilon^{-\mu}$ is the thermal conductivity, predicted to diverge at T_λ, consistent with its infinite value at all $T < T_\lambda$. Experimentally one finds [53, 58, 71] $\kappa_0 \simeq 12\ \mu\mathrm{W/cm}^2$ and $\mu \simeq 0.44$. In a very tall cell in which T varies substantially along its length, one may view (2.27) as locally valid with $\kappa(z) = \kappa[T(z)]$ so long as $T(z)$ remains sufficiently far above T_λ. "Sufficiently far above T_λ" may be quantified by the condition that the temperature drop across a coherence length be much smaller

than the deviation from T_λ:

$$\xi|\nabla T| \ll T - T_\lambda \quad \Rightarrow \quad \frac{Q\xi}{\kappa\epsilon T_\lambda} \ll 1. \tag{2.28}$$

Putting in ^{4}He parameters, this requires

$$\epsilon \gg 6 \times 10^{-8} \left(\frac{Q}{1\ \mu\mathrm{W/cm}^2} \right)^r, \quad r \equiv \frac{1}{1+\nu-\mu} \simeq 0.81. \tag{2.29}$$

As z increases, $T(z)$ will eventually violate (2.29), and one enters a region of *nonlinear heat transport*. In effect, κ becomes a strong function of Q in this region. Moreover, as illustrated in Fig. 2.3, at some position z_0, $T(z_0) = T_\lambda$, and the system enters the superfluid phase for $z > z_0$: a nonequilibrium superfluid–normal fluid interface is generated. Far downstream from this interface, $T(z)$ levels out at a temperature $T_\infty(Q)$, one of the nonequilibrium thermodynamic states discussed in Sec. 2.2 above. Correspondingly, the order parameter magnitude $|\psi(z)|$, which effectively vanishes for $z < z_0$, grows in the interface region and saturates at a value $|\psi_\infty(Q)|$ for $z \gg z_0$.[3]

The interface is the region over which the mode of heat transport converts from conduction to superfluid counterflow. Its characteristic width $\xi(Q)$, through which T and $|\psi|$ vary substantially (Fig. 2.3), is expected to scale according to (2.25). We may estimate this width semi-quantitatively by defining a reduced temperature scale ϵ_Q through equality in (2.28) and (2.29), and defining

$$\xi(Q) \equiv \xi(\epsilon_Q) \approx 24 \left(\frac{Q}{1\ \mu\mathrm{W/cm}^2} \right)^{-r\nu} \mu\mathrm{m}, \quad r\nu \simeq 0.54. \tag{2.30}$$

The scaling relation (2.26) predicts $r\nu = \nu_Q$ ($= 1/2$ in $d = 3$), requiring the scaling relation $\mu = 1 - \zeta$ ($\simeq \frac{1}{3}$ in $d = 3$) [70]. The difference between experimental and theoretical values is presumably due to the quasi-scaling effect described at the end of Sec. 2.2. Quantitative renormalization group based predictions for the full temperature profile $T(z, Q)$, explicitly including the quasi-scaling phenomenon [11, 72], are

[3] In fact $T(z)$ continues to decrease slowly with z in the superfluid phase due to rare phase slip events [17, 18], so $T_\infty(Q)$ and $|\psi_\infty(Q)|$ are not sharply defined, but we shall not dwell on this complication here.

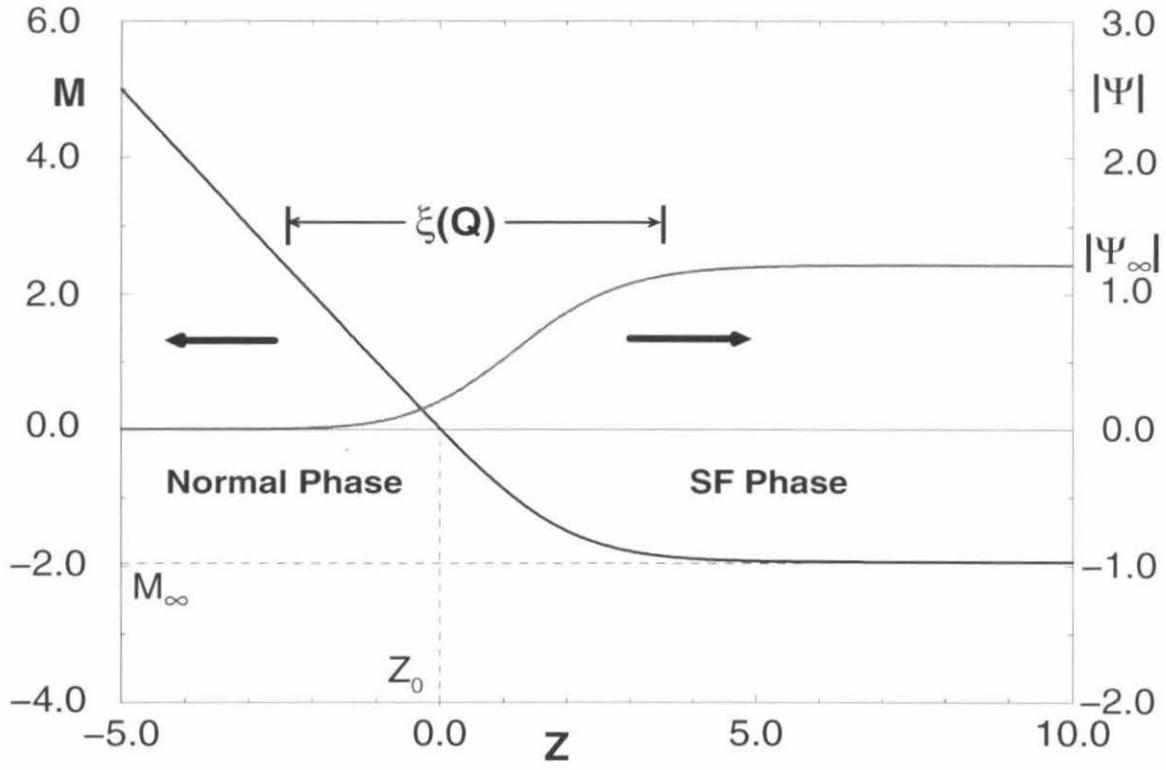

Figure 2.3: Scaled temperature and order parameter profiles $M(Z)$ and $\Psi(Z)$, computed within the mean field approximation [4, 60]. Here $Z = z/l(Q)$, $|\Psi| \propto |\psi| l(Q)$ and $M \propto (T - T_0) l^2(Q)$, where T_0 is the mean field transition temperature and $l(Q) \propto Q^{-1/3}$ is essentially the correlation length (2.25) in the mean field approximation. With these scalings the profiles are independent of Q.

limited to the normal fluid region $z < z_0$ where the vanishing of ψ greatly simplifies the calculations. Less quantitative predictions for the entire profile are limited to mean field [4] (which ignores critical fluctuations) or large-N [17, 18] (which replaces the single complex order parameter with an N-component vector) approximations.

An experimental measurement of the temperature profile $T(z, Q)$ within the interface region for a sequence of different Q would allow a detailed exploration of near-critical, nonlinear heat transport. It would also provide an experimental test of the scaling prediction (2.26). Such a measurement requires a regime in which $\xi(Q)$ is larger than the width W of the thermometer. Present technology places a limit $W > 50$ μm. From (2.30), heat currents below 1 μW/cm^2 are required. Present technology allows controlled heat currents down to about 1 nW/cm^2, leading to $\xi \approx 1$ mm, so at first sight such an experiment appears feasible.

In fact, Earth's gravity g_e places a fundamental limit on the maximum possible interface width. As described in Sec. 2.1, gravity produces an equilibrium ($Q = 0$) superfluid-normal fluid interface with width of order $\xi(g_e) = 100$ μm. From (2.30), $\xi(Q) = \xi(g_e)$ for $Q \simeq Q_g \equiv 70$ nW/cm^2. For Q of order Q_g, gravity will begin to have a strong effect on the nonequilibrium interface [59], and for $Q \ll Q_g$ the heat current will be a small perturbation on the equilibrium interface. Thus $\xi(Q)$ will saturate at $\xi(g_e)$ as $Q \to 0$ and the regime $\xi(Q) \gg W$ is unattainable on Earth.

For this reason the critical dynamics experiment (DYNAMX) is currently being prepared for the microgravity environment of the International Space Station, with flight planned for 2004. Heat currents as low as 5 nW/cm^2 will be used. The temperature profile $T(z, Q)$ will be measured to subnanoKelvin resolution by slowly moving the interface past a fixed thermometer. The latter is accomplished by removing heat from the downstream end of the cell slightly more slowly than it enters the upstream end, with the effect that the normal phase slowly invades the cell, thus translating the interface.

2.3.2 Transition from thermodynamic to interface state

We have discussed three possible classes of steady nonequilibrium states: (a) conducting normal states with static temperature profile determined by (2.27); (b) isothermal thermodynamic states with steady superfluid counterflow determined by (2.2); and (c) states with a nonequilibrium interface forming a "conversion boundary" between states of type (a) and (b). Transitions between (a) and (c) occur continuously: if state (a) is cooled to the point where the downstream endwall temperature passes through T_λ, an interface will form out of that endwall and steadily move upstream. Conversely, as heat is added to state (c), the interface will move downstream until the interface disappears into the endwall.

Similarly, the transition from (c) to (b) is continuous. The interface will disappear into the upstream endwall as heat is extracted, yielding an isothermal thermodynamic state at temperature $T_\infty(Q)$. Further extraction of heat will cause the temperature to drop below $T_\infty(Q)$.

The nature of the transition from (b) to (c) is less clear. At issue is whether the bulk superfluid, in the absence of an interface, recognizes $T_\infty(Q)$ as a special temperature. Within the mean field approximation, the answer is no [4]: the thermodynamic state is stable up to a temperature $T_c(Q)$, with $T_\lambda > T_c(Q) > T_\infty(Q)$, whose functional inverse $Q_c(T)$ we might identify with the boundary in Fig. 2.1(b), at which the superfluid density is suppressed to the point where it is incapable of supporting the heat current. As shown in Fig. 2.4, when the thermodynamic state is heated above $T_c(Q)$ a complicated dynamics results, with the system finally settling down into a state with an interface. Since $T_\infty(Q) < T_c(Q)$, the superfluid side actually *cools*, with a compensatory heating of the normal side. The final position of the interface is determined from energy conservation.

The question of whether or not a first order transition from (b) to (c) survives in some form beyond the mean field approximation is subtle, and is probably a question of time scale. The same thermal nucleation of vortices that leads to a small temperature gradient in the superfluid phase presumably also leads to a continuous (b) to

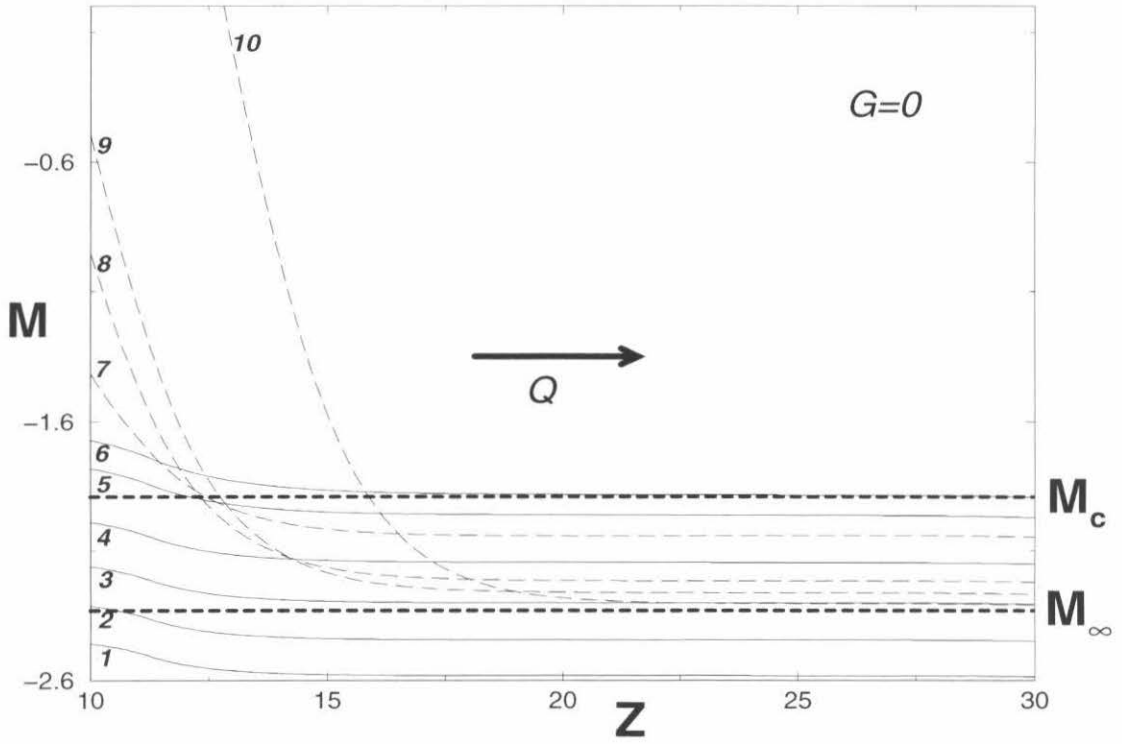

Figure 2.4: For bulk scaled temperature (see caption to Fig. 2.3) $M > M_c$ the uniform superfluid state becomes unstable to a state with an interface [61]. Curves 1-6 (solid) show consecutive *stable* (time independent) superfluid temperature profiles obtained in the mean field approximation upon slowly varying the right-hand wall temperature. Curves 7-10 show snapshots of the time evolution, computed within a simple one-dimensional model, initiated by a series of phase slips (not shown) after the right-hand wall temperature is raised slightly above that of curve 6. The key feature is the net temperature drop (from M_c to M_∞) observed in the bulk superfluid. (From Weichman and Miller [61].)

(c) transition, with the interface entering continuously from the upstream endwall, if the experimental heating rate is infinitesimally slow. Any finite heating rate may, however, allow a "superheating" of (b), inducing an apparent first order transition to (c) nucleated by a random vortex creation event. Such an effect would be analogous to superheating and supercooling effects at conventional first order transitions, the boundary $Q_c(T)$ being analogous to a spinodal line at which a local free energy barrier separating the superheated or supercooled state from the true equlibrium state disappears.

Experimental investigation of the (b) to (c) transition is complicated by boundary effects. The singular Kapitza resistance leads to an additional heating of the upstream endwall, which then acts as a nucleation point for vortices even when the temperature of the bulk superfluid is still below $T_\infty(Q)$ [25]. Clever cell designs that reduce the heat current near the endwall below that in the bulk may eventually allow experimental observation of a superheating effect.

2.3.3 Interface dynamics

Despite the greatly reduced gravity, the Space Station environment is less than ideal for other reasons. Vibrational noise ("g-gitter") exists at a level of about $10^{-3}\ g_e$, and one might worry that such noise might couple strongly to the interface, and perhaps destabilize it. Understanding the effects of acceleration noise requires an understanding of (a) the *free dynamics* of the interface when it is perturbed away from its steady state, e.g., whether or not the interface is even dynamically stable, or whether small perturbations might undergo some kind of "dendritic growth," and (b) the manner in which vibration, or other perturbations, couple to, and perhaps amplify this motion [60].

Suppose that a slow variation, $z_0 = z_0(\mathbf{r})$, with the transverse coordinates $\mathbf{r} = (x, y)$, is applied to the interface position and is subsequently released. The problem is to derive an equation of motion for $z_0(\mathbf{r}, t)$. In order to motivate the interesting physical questions, it is useful to consider first the analogous problem of the motion of

an *equilibrium* interface between up and down domains of an Ising ferromagnet, with diffusive "Model A" dynamics [70]. *Surface tension* acts as a restoring force against perturbations away from a flat interface, and one may derive a *diffusion equation* for the relaxation of long wavelength perturbations of the interface position:

$$(\partial_t - D\nabla^2) z_0(\mathbf{r}, t) = \eta(\mathbf{r}, t), \tag{2.31}$$

in which the value of D depends on the microscopic parameters in the model, and the driving term η, vanishing for free relaxation, has been included for completeness. *Thermal fluctuations* in the spins lead to a Gaussian white noise form for η with correlator $\langle \eta(\mathbf{r}, t)\eta(\mathbf{r}', t')\rangle = \zeta_0 \delta(\mathbf{r} - \mathbf{r}')\delta(t - t')$ where ζ_0 depends on microscopic parameters and on temperature. Using this form one may compute the equal time variance in the interface position

$$\begin{aligned} C(\mathbf{r} - \mathbf{r}') &\equiv \langle [z_0(\mathbf{r}, t) - z_0(\mathbf{r}', t)]^2 \rangle \\ &= \frac{\zeta_0}{4\pi D} \ln\left(\frac{|\mathbf{r} - \mathbf{r}'|}{a_0}\right), \end{aligned} \tag{2.32}$$

where a_0 is an atomic length scale. One sees that fluctuations in the interface position *diverge* logarithmically with separation: a famous result known as *interface roughness*, encountered most frequently in discussions of crystal facet shapes. The interface is locally stable and flat, but globally wanders arbitrarily large distances.

The result (2.32) shows that there are subtle physical issues, lying beyond the much simpler question of stability, arising because the interface breaks the continuous translation invariance of the system. Whenever a continuous symmetry is broken, a Goldstone mode is generated, corresponding in this case to very slow relaxation of long wavelength perturbations of the interface position, $z_0 \propto e^{i\mathbf{k}\cdot\mathbf{r} - \lambda(k)t}$, with (2.31) yielding $\lambda = Dk^2$. Such long wavelength "modes" are highly susceptible to thermal or externally generated noise spectrum $\zeta(k)$, and it is the convergence at small k of the integral

$$\langle z_0(\mathbf{r}, t)^2 \rangle = \int \frac{d^2k}{(2\pi)^2} \frac{\zeta(\mathbf{k})}{\mathrm{Re}\lambda(\mathbf{k})}, \tag{2.33}$$

that determines whether or not the interface is rough. For the case $\zeta(k) \equiv \zeta_0$, (2.33) diverges logarithmically, which same divergence is reflected in the correlator (2.32).

The physics of the nonequilibrium superfluid-normal interface is very different from that of the equilibrium magnetic interface. Transport on the normal side of the interface is diffusive, but transport on the superfluid side is essentially ballistic, and the dynamics of the interface itself involves a very intricate coupling of the two. To leading order one finds an equation of motion [60]

$$(\partial_t^2 - c^2\nabla^2)z_0(\mathbf{r},t) = \eta(\mathbf{r},t), \tag{2.34}$$

so that the interface supports *traveling wave* excitations, with a well defined speed $c(Q)$ of the same order as the bulk second sound speed. At next-to-leading order one finds that these excitations are *singularly damped*, with $\lambda = ick + Dk^{3/2}$, so that $\mathrm{Re}\lambda \propto k^{3/2}$ rather than k^2 (as for bulk second sound waves) at small k. Positivity of $\mathrm{Re}D$ establishes intrinsic dynamical stability of the interface. One may interpret the enhanced damping as arising from the waves on the interface "rubbing" up against the normal phase. Moreover, one finds that thermal fluctuations enter via a spectrum $\zeta(k) \propto k^{5/2}$ for η, vanishing strongly as $k \to 0$. The physics of this result is related to the fact that interface motion is a *cooperative* phenomenon, involving evanescent dynamics of the superfluid order parameter to a depth $\sim k^{-3/2}$ scaling as the $\frac{3}{2}$ power of the wavelength.[4] The microscopic thermal noise, which is white, must then be averaged over a similar volume to obtain its net effect on the mode, leading eventually to the greatly reduced $\zeta(k)$ above. In contrast, the Ising interface moves by local spin flips and the microscopic noise is averaged only over a microscopic region of width a_0 and ζ remains white.

The net result of the analysis is that the integral (2.33) is strongly convergent at $k = 0$, and the superfluid-normal interface is globally flat. This is good news for DYNAMX, where a rough interface would have led to substantial smearing of the temperature profile on a scale varying as the logarithm of the cell cross-section.

[4]The evanscent depth on the normal side is much smaller, scaling as $k^{-1/2}$. For comparison, gravity waves on fluid surfaces yield fluid motion to a depth $\sim k^{-1}$ proportional to the wavelength.

Vibrational acceleration noise couples to the interface in the same way that Earth's gravity does, through the variation in the local T_λ with pressure. A slight change in T_λ will cause the interface to translate (for accleration normal to the interface) or tilt (for acceleration parallel to the interface) slightly, but if the change is *oscillatory* it could resonate with one of the interfacial second sound modes, leading to a rapid growth in the interface motion. A detailed examination of the expected frequency spectrum of the Space Station g-gitter, together with the discrete spectrum of standing wave modes allowed in the experimental cell within the planned temperature and heat current range, shows that such resonances may indeed occur, but that the singular damping is sufficiently strong that the interface oscillation amplitude should saturate at acceptably low levels [73].

The existence of the interfacial second sound mode has yet to be tested experimentally. This might be accomplished by applying a sequence of heat pulses to the cell sidewall near the interface and detecting a response at the opposite sidewall. Scattering of bulk second sound pulses off the interface, with detection of the reflected pulses, might also provide interesting information about the coupling of bulk and interface modes.

2.4 The self-organized critical state

We have so far discussed phenomena in which optimal conditions occur in the absence of gravity. It transpires that there is a very interesting phenomenon in which gravity and heat current *combine* to produce a new type of dynamical state. The so-called *self-organized critical* (SOC) state occurs in a cell which is heated from above, so that $\mathbf{g}$ and $\mathbf{Q}$ are parallel.[5]

Gravity depresses the lambda point $T_\lambda(z)$ with increasing depth according to

[5]When Q and g are antiparallel (heat from below) they cooperate to simply produce a sharper interface. The name SOC is motivated by nonequilibrium states found in "sandpile" models displaying critical power law "avalanche" behavior with no apparent tuning parameter [74]. Although the "SO" part of SOC is justified for the ^{4}He state, the "C" part is not since analogous critical power laws have yet to be demonstrated either theoretically or experimentally. The name, however, has stuck and we will not attempt to alter convention here.

(2.1), while heat current leads to decreasing temperature $T(z)$ with depth according to (2.27). The reduced temperature $\epsilon(z) \equiv [T(z) - T_\lambda(z)]/T_{\lambda,0}$, where $T_{\lambda,0}$ is, say, the bulk transition temperature if gravity were absent (and hence approximately the transition temperature at the top of the cell), contains a *competition* between these two effects. One might, in fact, imagine tuning Q in such a way that $\epsilon(z)$ is independent of z [10]: the sample would apparently exist in an essentially homogeneous near-critical state. In fact, it was argued [75, 76] that the system actually "self-organizes" $T(z)$ in order to enforce a uniform ϵ. Assuming the validity of the Fourier law (2.27), ϵ must be uniquely defined by

$$\kappa(\epsilon_{\rm SOC}) = Q/|\partial_z T_\lambda|, \tag{2.35}$$

where $\epsilon_{\rm SOC}$, a function of the ratio Q/g, is the reduced temperature of the new state. This state has recently been observed experimentally [58].

The fact that κ increases with decreasing T ensures stability of the SOC state to small perturbations [75, 76]. More specifically, an analysis of the heat diffusion equation in the normal phase [61] shows that a perturbation $\epsilon(\mathbf{x}) = \epsilon_{\rm SOC} + \delta\epsilon(\mathbf{x})$ obeys an equation of motion whose solutions are decaying plane waves of the form

$$\delta\epsilon(\mathbf{x}, t) = \delta\epsilon(\mathbf{q}) e^{-D_{SOC} q^2 t} e^{i\mathbf{q}\cdot(x + c_{\rm SOC}\hat{z}t)}, \tag{2.36}$$

with $D_{\rm SOC} = \kappa(\epsilon_{\rm SOC})/C_p(\epsilon_{\rm SOC})$ and $c_{\rm SOC} = -|\partial_z T_\lambda|\kappa'(\epsilon_{\rm SOC})/T_{\lambda,0}C_p(\epsilon_{\rm SOC})$, where C_p is the equilibrium specific heat at constant pressure. Thus, in addition to the decay controlled by the diffusion constant $D_{\rm SOC}$, there is an unexpected anisotropic propagation effect where the perturbation moves upstream at speed $c_{\rm SOC}$. For the reasonable value $Q = 50$ nW/cm^2 (see below), one finds $c_{\rm SOC} \simeq 2.8$ mm/s, and the propagation effect should be experimentally observable for reasonable cell geometries [61].

Since κ diverges as $\epsilon \to 0$, (2.35) implies that $\epsilon_{\rm SOC} \to 0$ as $Q \to \infty$. However, for large Q the Fourier law breaks down. In particular $\kappa(T_\lambda, Q)$ is finite for $Q > 0$ [11], and the SOC state must therefore lie below $T_\lambda(z)$ for sufficiently large $Q > Q_{SOC}$. This is consistent with experimental data [58], reproduced in the inset to Fig. 2.5,

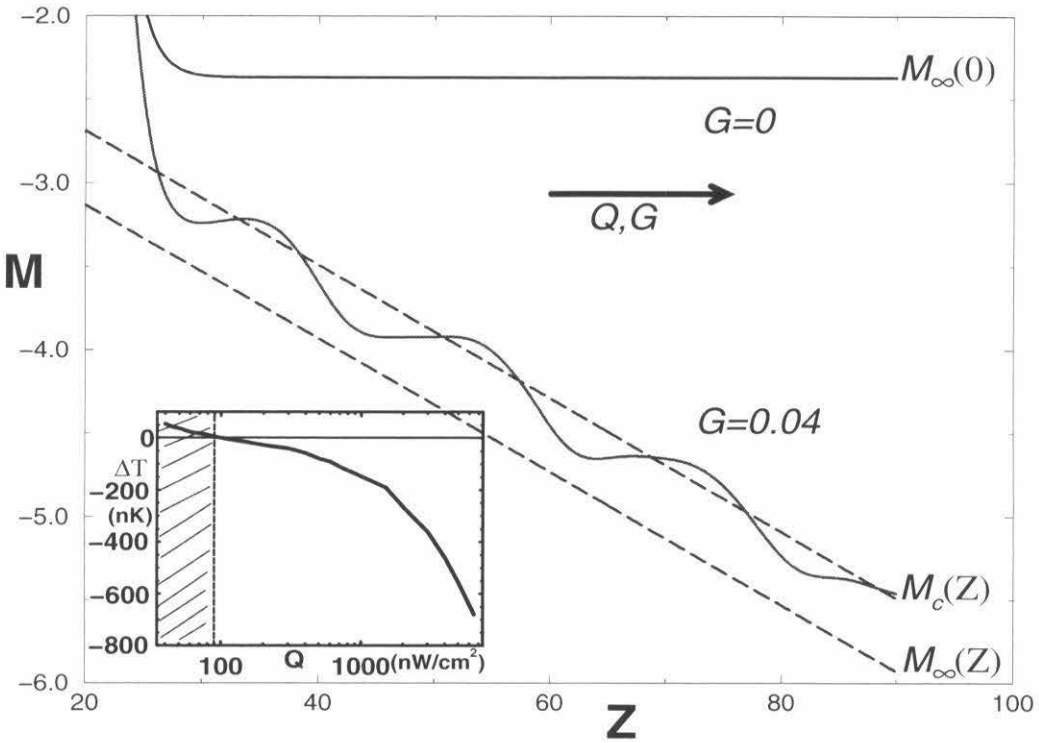

Figure 2.5: Simulation of the SOC state using the same simplified 1-d model as in Fig. 2.4. For $G \propto g/Q = 0$ the temperature gradient in the normal phase ($Z < 20$) gives way to an asymptotically isothermal superfluid phase ($Z > 30$) with temperature $T_\infty(Q) < T_{\lambda,0}$. For $G > 0$ the superfluid phase develops phase slips (vortices in 3-d), and a corresponding dynamic staircase structure in $T(z)$, roughly bounded between $T_\infty(z)$ and $T_c(z)$, to produce the SOC state. The density of phase slips increases with G. Inset: experimental data replotted from Fig. 4 of [58] showing the self-organization temperature, $\Delta T(Q) = T(Q, z) - T_\lambda(z)$. Only for $Q < 100$ nW/cm^2 (small shaded region) is the SOC state in the normal phase. (From Weichman and Miller [61].)

which shows that $\epsilon_{\rm SOC} < 0$ for $Q > 100$ nW/cm^2. Using (2.35), along with (2.28) defining the validity of the Fourier law, one may show that the previous theory is valid for [14, 61]

$$6.1 \left(\frac{Q}{100\text{nW/cm}^2}\right)^{(1+\nu)/\mu} \left(\frac{g}{g_e}\right)^{1-(1+\nu)/\mu} \ll 1. \tag{2.37}$$

Equality in (2.37) serves an estimate for $Q_{\rm SOC}$ and yields $Q_{\rm SOC} \simeq 60$ nW/cm^2 under Earth's gravity, in very reasonable agreement with the experimental result.

The question now remains as to the nature of the SOC state below T_λ. The state must undergo some kind of transition to superfluidity, but the fact that it continues to support a finite temperature gradient appears inconsistent with the isothermal nature of a superfluid. The resolution of this paradox is shown in Fig. 2.5. Let $T_\infty(z) = T_\lambda(z) - \Delta T_\infty(Q)$ and $T_c(z) = T_\lambda(z) - \Delta T_c(Q)$ define local values of the interface and instability temperatures discussed in Sec. 2.3.2, where $\Delta T_c = T_{\lambda,0} - T_c(Q)$ and $\Delta T_\infty = T_{\lambda,0} - T_\infty(Q)$ are the deviations from T_λ in zero gravity. For $g = 0$ an interface state, represented by the upper curve in Fig. 2.5, is formed. For $g > 0$, $T(z)$ first drops below the local transition at a point z_0, and attempts to asymptote to an isothermal superfluid at a temperature close to $T_\infty(z_0)$. However, at a point $z_1 > z_0$, the descending line $T_c(z_1)$ meets $T_\infty(z_0)$ and the superfluid becomes unstable. A vortex is generated and crosses the cell, leading to dissipation and a finite temperature drop across it. By this mechanism the temperature is able to drop below the instability temperature and asymptote once again to an isothermal superfluid at a temperature close to $T_\infty(z_1)$. The entire scenario then repeats itself approximately periodically at a sequence of points z_n, $n = 1, 2, 3, \ldots$, where $T_c(z_n)$ meets $T_\infty(z_{n-1})$. The result is a dynamic staircase structure, a snapshot of which is represented by the lower curve in Fig. 2.5. This structure fluctuates in time as vortices form and annihilate, but is found numerically to slowly move escalator fashion upstream [61].

The time resolution of present thermometry is far too poor to detect fluctuations in the temperature profile, whose mean would correspond to a straight line parallel

to and somewhere between $T_\infty(z)$ and $T_c(z)$.[6] Experiments to detect the predicted stream of vortices, via the second sound noise they generate, are in the planning stages. A simple calculation shows that the distances between vortices must scale as $z_n - z_{n-1} \approx [\Delta T_\infty(Q) - \Delta T_c(Q)]g_e/\gamma g$, increasing with larger Q and smaller g. Although the SOC state requires finite gravity, the regime of widely separated vortices may in the future prove sufficiently interesting that a controlled low gravity experiment will become desirable.

2.5 Specific heat at constant heat current

2.5.1 Enhanced specific heat

The presence of a heat current is predicted to enhance the specific heat of superfluid ^{4}He above its equilibrium value, C_0. This can easily be seen at low Q, sufficiently far below T_λ, where the free energy enhancements are $\Delta F(T, \mathbf{U}_s) = \frac{1}{2}\rho_s \mathbf{U}_s^2$ and $\Delta\Phi(T, \mathbf{J}_s) = -\mathbf{J}_s^2/2\rho_s$, in which $\rho_s(T) \approx \rho_0|\epsilon|^\zeta$ is the equilibrium superfluid density. Thus, at fixed superfluid velocity $\mathbf{U}_s$,

$$\Delta C_{U_s} \equiv C_{U_s} - C_0 \approx T\rho_s \mathbf{U}_s^2 \zeta(1-\zeta)/2T_\lambda^2|\epsilon|^2 > 0, \tag{2.38}$$

while at fixed heat current $\mathbf{Q}$,

$$\Delta C_Q \equiv C_Q - C_0 \approx T\mathbf{J}_s^2 \zeta(1+\zeta)/2T_\lambda^2 \rho_s|\epsilon|^2 > 0. \tag{2.39}$$

Closer to T_λ the superfluid density depends strongly on heat current and the apparent divergences at T_λ in (2.38) and (2.39) are replaced by new singularities at the phase boundary $T_c(U_s)$ shown in Fig. 2.1(b). It is predicted that ΔC_{U_s} will remain finite, rising to a cusp at the phase boundary [12], while ΔC_Q is predicted to diverge [8, 9]. The latter result follows on very general grounds from the thermodynamic con-

[6] A renormalization group calculation of this mean profile as a function of Q in the large-N limit is described in [17, 18].

jugacy of $\mathbf{U}_s$ and $\mathbf{J}_s$ discussed in Sec. 2.2. The usual thermodynamic manipulations imply the relation

$$C_Q = C_{U_s} + T \left(\frac{\partial J_s}{\partial T} \right)_{U_s}^2 \left(\frac{\partial U_s}{\partial J_s} \right)_T . \tag{2.40}$$

Since the susceptibility, $(\partial U_s/\partial J_s)_T$ [proportional to the slope of the curve in Fig. 2.2(b)] is expected to diverge at the phase boundary, while $(\partial J_s/\partial T)_{U_s} = U_s(\partial \rho_s/\partial T)_{U_s}$ remains finite, C_Q will exhibit a *divergent* enhancement.

There have been no measurements of C_{U_s} to date, but an experiment of this kind might be performed in the presence of a persistent current flowing around a loop, similar to the superfluid gyroscope experiment [77], where in the absence of vortices $\mathbf{U}_s$ indeed remains fixed as T is varied. A measurement could prove difficult due to the small magnitude of the enhancement and the challenge of holding $\mathbf{U}_s$ constant while measuring the specific heat. However, it has been suggested that with very fast thermometry, a measurement of C_{U_s} might be obtained through a second-sound measurement where the second-sound waves are propagated perpendicular to $\mathbf{U}_s$ [16].

Measurement of C_Q is more straightforward. The predicted divergence of ΔC_Q, together with the fact that $\mathbf{Q}$ can be experimentally controlled with great precision, implies a much more visible experimental signature. The first experimental measurements of this quantity were recently reported [25]. As will be discussed below, they indicate that the heat capacity is indeed enhanced, but with a magnitude that is significantly larger than theoretical predictions.

2.5.2 The superfluid breakdown temperature

Experiments performed at constant Q should find that C_Q diverges at a temperature $T_c(Q) < T_\lambda$, defined by inverting (2.21):

$$|\epsilon_c(Q)| = \frac{T_\lambda - T_c(Q)}{T_\lambda} = \left(\frac{Q}{Q_0^c} \right)^x , \tag{2.41}$$

where $Q_0^c = Q_0 y_c$ and $x = 1/\Delta_Q = 1/2\nu \simeq 0.746$ [5, 7, 72]. Based on a renormalization group analysis of the Model F equations [70], in an approximation neglecting vortices

(and hence decay of superflow), the prediction $Q_0^c \approx 7.4$ kW/cm^2 was obtained [6]. More recently, using an extension of this theory, accounting for dissipation within a large-N approximation, the value $Q_0^c \approx 6.6$ kW/cm^2 was obtained [18].

These theoretical results disagree with the results of thermal conductivity experiments [19]. The onset of thermal resistance was found to occur at a temperature, which we call $T_{\rm DAS}(Q)$, that obeys (2.41), but with $x = 0.813 \pm 0.012$ and $Q_0^c = 568 \pm 200$ W/cm^2. This is a curve in the T-Q plane that falls below the theoretically estimated $T_c(Q)$ for all experimentally accessible temperatures (see Fig. 2.6). A number of explanations have been proposed for the discrepancy: (a) the transition at $T_{DAS}(Q)$ may be caused by a temperature instability at the cell wall associated with the singular Kapitza resistance [which raises the temperature near the bottom (heated) end plate above that of the bulk, which therefore could serve as a vortex nucleation center], and hence lies below $T_c(Q)$ [25]; (b) $T_{\rm DAS}$ may be related to a gravity-dependent transition, again lying below $T_c(Q)$, and will increase towards $T_c(Q)$ as gravity is reduced, e.g., by going into space [18]; (c) since the transition is only sharply defined in the absence of vortices, $T_{\rm DAS}(Q)$ might be analogous to a spinodal line in a first-order phase transition [57]: fluctuation-induced vortices nucleate the transition to the dissipative phase, and $T_{\rm DAS}(Q)$ will differ from experiment to experiment, depending on the heating rate used. Since any superfluid state above $T_\infty(Q)$ should be unstable by this mechanism, an infinitessimally slow experiment should find the transition at $T_\infty(Q)$.

It is possible that all of these effects (and perhaps others) are present. The real question, whose resolution clearly requires more experimental data, is which one imposes the most severe limitation on present experiments. The answer to this question has implications for the measurement of $C_Q(T)$. If effect (c) is dominant, then experiments have basically already reached the intrinsic limit on how close they can approach the divergence of $C_Q(T)$ (for the range of Q explored thus far), though it may be possible to design an experiment with faster heating rates and fast enough thermometers to reach $T_c(Q)$ before a vortex can nucleate. On the other hand, if proposal (b) is correct, a space-based microgravity measurement of $C_Q(T)$ should

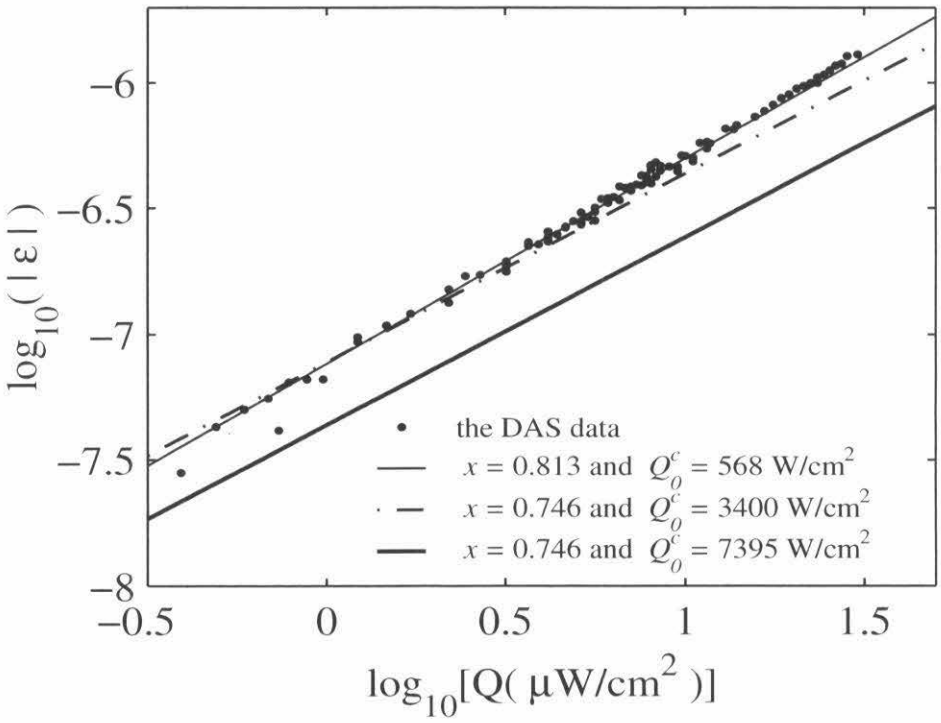

Figure 2.6: Thick solid line: $T_c(Q)$, the theoretically predicted temperature of superfluid breakdown [6]. Thin solid line: $T_{\rm DAS}(Q)$, where the exponent x and amplitude Q_0^c are chosen to best fit to the observed temperature of superfluid breakdown represented by the data points [19]. Dashed-dotted line: the value of Q_0^c that, along with the theoretical value $x = 1/2\nu$, makes the experimental heat capacity data match the more recent theoretical prediction for the scaling function [18] (see Fig. 2.9 below).

be able to get considerably closer to $T_c(Q)$ than one performed on the ground. If proposal (a) is correct, carefully designed ground-based experiments might be able to approach $T_c(Q)$ more closely: if $T_{\rm DAS}$ is due to a boundary effect, a cell constructed with a bottom plate that is much larger than the cross-sectional area of the bulk helium sample could decrease the singular Kapitza resistance sufficiently so that the bulk helium can reach $T_c(Q)$ without a boundary instability interfering. A cell of this configuration that maintains a reasonable geometry for heat flow would have to be fairly tall and might therefore be more susceptible to gravity effects.

2.5.3 Experimental measurements

The first experimental measurements of $C_Q(T)$ [25] confirm the predicted enhancement, but find that its magnitude is significantly larger than current predictions [8, 9, 18]. The data were taken over the range 1 μW/cm^2 $\leq Q \leq$ 4 μW/cm^2, and a representative set at $Q = 3.5$ μW/cm^2 is shown in Fig. 2.7.

The extent of the disagreement between theory and experiment can be observed more clearly when the data are plotted in scaled form. All theories predict that the enhancement should obey a scaling form

$$\Delta C_Q = |\epsilon|^{-\alpha} f_{J_s}\left[\frac{Q}{Q_c(T)}\right], \tag{2.42}$$

where $f_{J_s}(x)$ is a universal scaling function. From (2.39) and the scaling relations in Table 2.2, for $x \ll 1$ one has

$$\begin{aligned} f_{J_s}(x) &= f_2 x^2 + O(x^4) \\ f_2 &\equiv [\zeta(\zeta+1)(Q_0^c)^2/2\rho_0 T_\lambda^3 S_\lambda^2]. \end{aligned} \tag{2.43}$$

Using the theoretical estimates one obtains $f_2 = 8.9$ J/mol K for $Q_0^c = 7.4$ kW/cm^2 and $f_2 = 7.0$ J/mol K for $Q_0^c = 6.6$ kW/cm^2, where the molar volume 27.38 cm^3/mol has been used to obtain familiar units.

In Fig. 2.8 we show the heat capacity enhancement as a function of the scaling

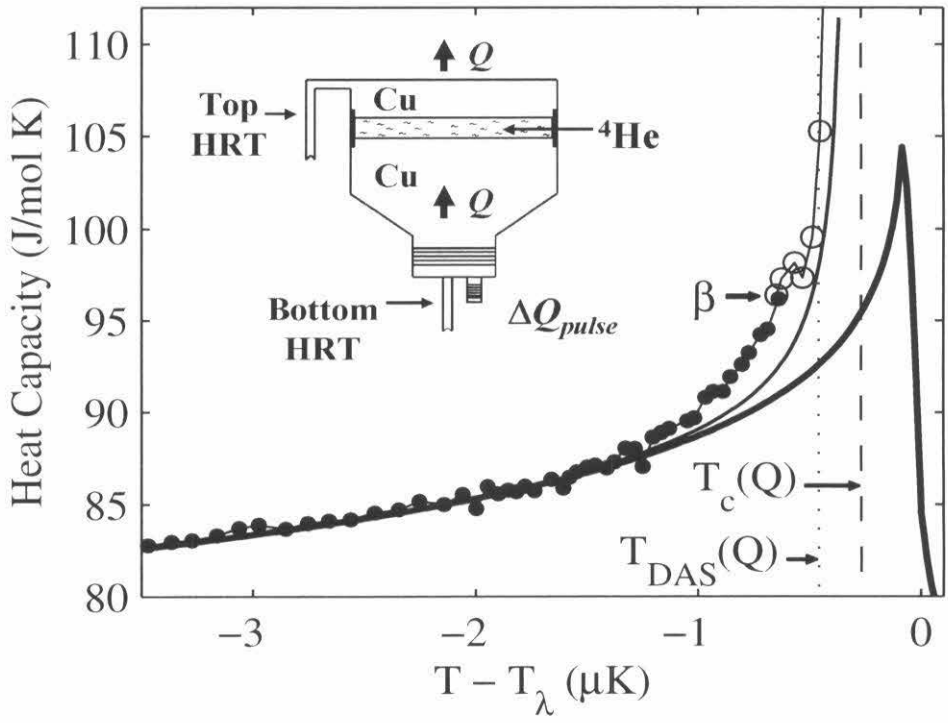

Figure 2.7: Sample heat capacity data for $Q = 3.5\ \mu\mathrm{W/cm}^2$ [25]. Thick solid line: equilibrium C_0 obtained from a fit to the LPE data [2] that is subsequently rounded for gravity. Thin solid line: theoretical prediction [18] that includes vortices (rounded for gravity). Solid circles: data from the average of the top and bottom thermometers. Open circles: data from the top thermometer only [beyond the point marked β, where the bottom (hotter) thermometer was found to change its behavior, perhaps as a result of a boundary heating effect]. The temperature T_{DAS} marks the onset of dissipation found in earlier thermal conductivity experiments [19], while $T_c(Q)$ is estimated from a certain theoretical fit to the data discussed later in the text. Inset: schematic diagram of the experimental cell. HRT stands for high resolution thermometer. (From Harter, Lee, Chatto, Wu, Chui, and Goodstein [25], Fig. 1.)

variable $(Q/Q_c)^2$. Since $Q_c(T)$ is not actually measured in the experiment, we scale the data using the theoretically predicted form $Q_c = Q_0^c|\epsilon|^{\Delta_Q}$ with $Q_0^c = 6.6$ kW/cm^2 and $\Delta_Q = 2\nu = 1.342$ [18]. As anticipated, the data for all $Q \geq 2$ μW/cm^2 collapse onto a single linear curve, verifying that the exponent Δ_Q is at least consistent with the data. However, the slope of the experimental line is $f_2^{\rm expt} = 69 \pm 4$ J/mol K, approximately ten times larger than the theoretical prediction.

An optimistic explanation for the discrepancy between theory and experiment is that the theories are producing reasonable estimates for the universal scaling function $f_{J_s}(x)$, but that the nonuniversal amplitude Q_0^c, depending on detailed properties of the ^{4}He system and therefore more difficult to compute, is estimated less accurately. As illustrated in Fig. 2.9(a), the choice[7] $Q_0^c = 3.4$ kW/cm^2 in fact places the experimental data on top of the more recent theoretical curve [18]. With this choice, $T_c(Q)$ lies somewhat above $T_{\rm DAS}(Q)$ (vertical dashed line in Fig. 2.6). A somewhat smaller choice for Q_0^c would provide an equally good fit to the earlier theory [6]. Unfortunately, all of the data lie at fairly small $(Q/Q_c)^2 \leq 0.3$ where the scaling function has little structure (essentially indistinguishable from linear within the scatter of the data). A true test would require data in the regime $(Q/Q_c)^2 \to 1$ where the scaling function diverges.

For completeness we also show in Fig. 2.9(b) an equally good scaling collapse based on the assumption that $T_c(Q) \approx T_{\rm DAS}(Q)$. Thus, we use $Q_c(T)$ derived from (2.41) using $x = 0.813$ (i.e., effectively $\nu = 0.615$) and $Q_0^c = 0.65$ kW/cm^2 [optimally chosen within the error bars quoted in [19]]. Since $T_{\rm DAS}$ places a lower bound on $T_c(Q)$, the sharpest conclusion we can make at this stage is that the data are consistent with the scaling hypothesis for a fairly broad range of experimentally and theoretically motivated parameter choices and that more data closer to $T_c(Q)$ will be required for a critical test of the theory.

The experimental measurements were taken in a cell that was only 0.64 mm high, about as close to the optimal height as practical considerations allow. Although the

[7] This value is in fact within the estimated margin of error for the amplitude calculation. The uncertainty of the theory is a factor < 2 (R. Haussmann, private communication), while the adjustment here is $\simeq 1.9$.

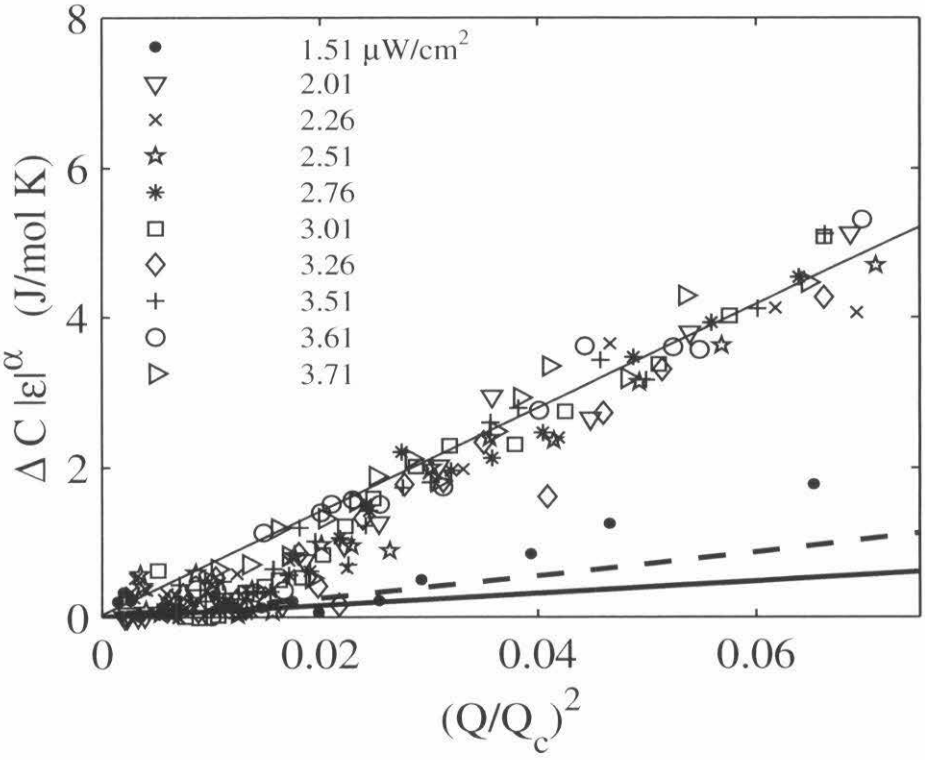

Figure 2.8: Scaling plot of the differential heat capacity measurements for various values of Q [25]. The experimental data are scaled using $Q_0^c = 6.6$ kW/cm^2, and terminated at the temperature indicated by β in Fig. 2.7. The predicted collapse of the data for different Q values onto nearly the same curve verifies the basic scaling hypothesis (2.42). Thin solid line: straight line fit to the data. Thick solid line: theoretical prediction neglecting dissipation [8, 9]. Dashed line: theoretical prediction including dissipation [18]. Neither theoretical curve is rounded for gravity. (From Harter, Lee, Chatto, Wu, Chui, and Goodstein [25], Fig. 3.)

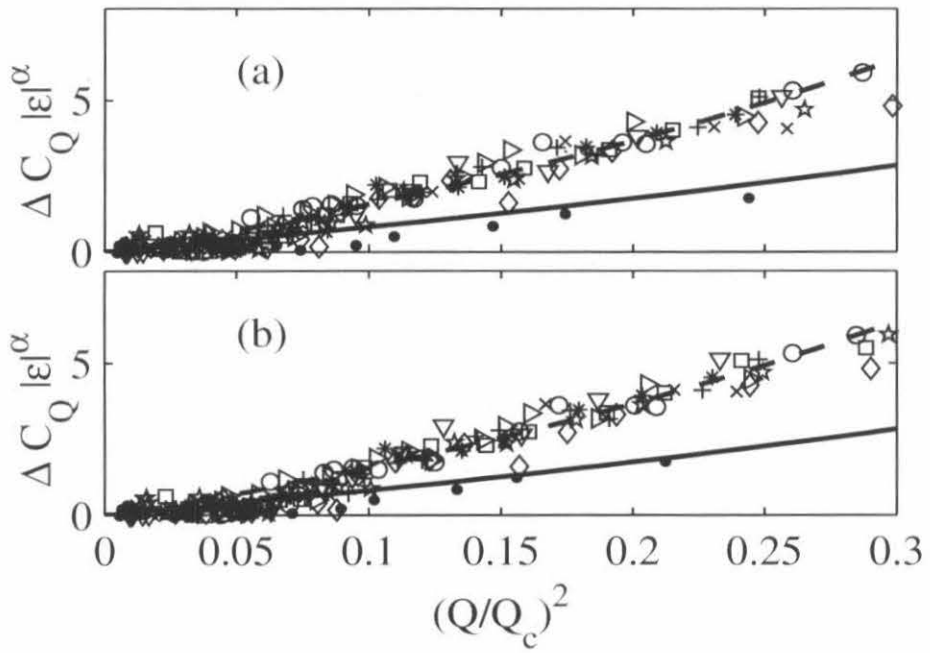

Figure 2.9: Alternative scaling plot of the differential heat capacity measurements for various values of Q [25]. The data symbols are the same as those used in Fig. 2.8. The experimental data are scaled using $Q_c(T)$ derived from (2.41) by (a) using the theoretical exponent value $x = 1/2\nu = 0.746$, but amplitude $Q_0^c = 3.4$ kW/cm^2 chosen to best match the theoretical scaling function; and by (b) assuming that $T_c(Q) \approx T_{DAS}(Q)$ with $Q_0^c = 0.65$ W/cm^2 and $x = 0.813$. For the Q-range of the experimental data, the two analyses are basically identical, with the lines completely overlapping to well within experimental resolution. Only for higher Q data would the two fits become distinguishable. Solid line: theoretical prediction neglecting dissipation [8, 9]; Dashed line: theoretical prediction including dissipation [18].

effects of gravitational rounding were therefore minimized, they were not entirely eliminated. The variation of T_λ across the cell due to gravity was $\delta T_\lambda \simeq 8 \times 10^{-8}$ K. A reasonable criterion for a data point to be unaffected by gravity is that one should have $|T - T_\lambda| \geq 10\,\delta T_\lambda$. This would restrict the temperature range of the experiment to more than about 1 μK below T_λ. Essentially none of the interesting data shown in Figs. 2.7–2.9 satisfy this criterion. In fact, because measurements [23] have shown that under a heat flux $Q > 4$ μW/cm^2, helium exhibits appreciable dissipation, there is no range of parameters for which this criterion can be satisfied under Earth's gravity in an isothermal experiment that measures C_Q close to $T_c(Q)$.

The small cell height used in the experiment precluded the use of side-wall thermometry. The helium temperature was measured using thermometers mounted on the cell end-plates and the data were corrected for the singular Kapitza resistance [78]. The temperature range of the measurements was limited because the bottom (hotter) thermometer changed its behavior before the bulk helium temperature reached $T_{DAS}(Q)$ [25]. It was proposed that this change was due to another boundary effect related to the Kapitza resistance. The temperature at which this phenomenon occurred is indicated by β in Fig. 2.7, and is the maximum temperature of the data shown in Figs. 2.8 and 2.9. As a result of the reduced range, the data in Fig. 2.9 do not reach high enough temperatures to encounter much curvature in the scaling function. Measurements that approach closer to the divergence are clearly needed. Data up to $T_{DAS}(Q)$ should be easily obtainable using a deeper cell constructed with a mid-plane thermometer. However, since rounding due to gravity will be even more of a detriment over the region where the scaling function has significant curvature, the ill-effects of the deeper cell height will obscure some of the benefit gained by the increased temperature range.

The only definitive way to circumvent the problems raised in the previous two paragraphs is to perform a space-based measurement of C_Q. An experiment in the absence of gravity would obtain data up to $T_{\rm DAS}(Q)$ without gravitational rounding, permitting an extension of the scaling data into a more revealing temperature range. This would allow a considerably improved estimate of where $T_c(Q)$ lies in relation

to $T_{\rm DAS}(Q)$ [in particular if ΔC_Q is still finite at $T_{\rm DAS}(Q)$ one would conclude that $T_c(Q) > T_{\rm DAS}(Q)$]. Furthermore, a space experiment would test the suggestion that $T_{\rm DAS}(Q)$ is a gravity artifact [18], and permit the construction of a deep cell with asymmetric endplates to test whether $T_{\rm DAS}(Q)$ is a boundary effect.

Chapter 3 Apparatus

This chapter discusses many aspects of the design of the experimental apparatus used to take our heat capacity measurements. It will outline the requirements needed to obtain successful measurements, the constraints imposed by external conditions, and the specifications of the final apparatus. A schematic diagram of the experimental setup is shown in Fig. 3.1.

3.1 Limitations on the experimental design

3.1.1 Cell height: gravity and finite size effects

In a laboratory on Earth, the dependence of T_λ on pressure is such that $dT_\lambda/dz \equiv \alpha = 1.27\ \mu\mathrm{K/cm}$ where z is the vertical distance in gravity. Below T_λ, superfluidity keeps helium isothermal, but the distance from the transition, $t \equiv (T_\lambda - T)/T_\lambda$, is nonuniform due to gravity (see Fig. 3.3). The span in reduced temperature in a cell of height l is $\delta t = \alpha l/T_\lambda$. In order to minimize the effects of gravity, it is therefore desirable to design an experimental cell to be as short as possible. However, if it is too small, finite-size effects will significantly alter the physics. In order to avoid this regime, it is reasonable to require that $l \geq 10\xi$, where ξ is the coherence length, $\xi = \xi_0\, t^{-2/3} \approx 2 \times 10^{-8}\, t^{-2/3}$ cm. Thus if we limit experiments to the range $t > \delta t$, we find an absolute lower limit for t given by

$$t \geq \left(\frac{10\ \xi_0\ \alpha}{T_\lambda}\right)^{\frac{3}{5}} \approx 2 \times 10^{-8}, \tag{3.1}$$

corresponding to an optimal cell height of $l \approx 0.3$ mm. However, a cell this small is rather difficult to construct. The calorimeter used for the experiment described in this thesis was designed to be approximately 1 mm tall. In actuality it was measured to be 0.640 mm high, corresponding to $\delta t = 4 \times 10^{-8}$ and an experimental temperature

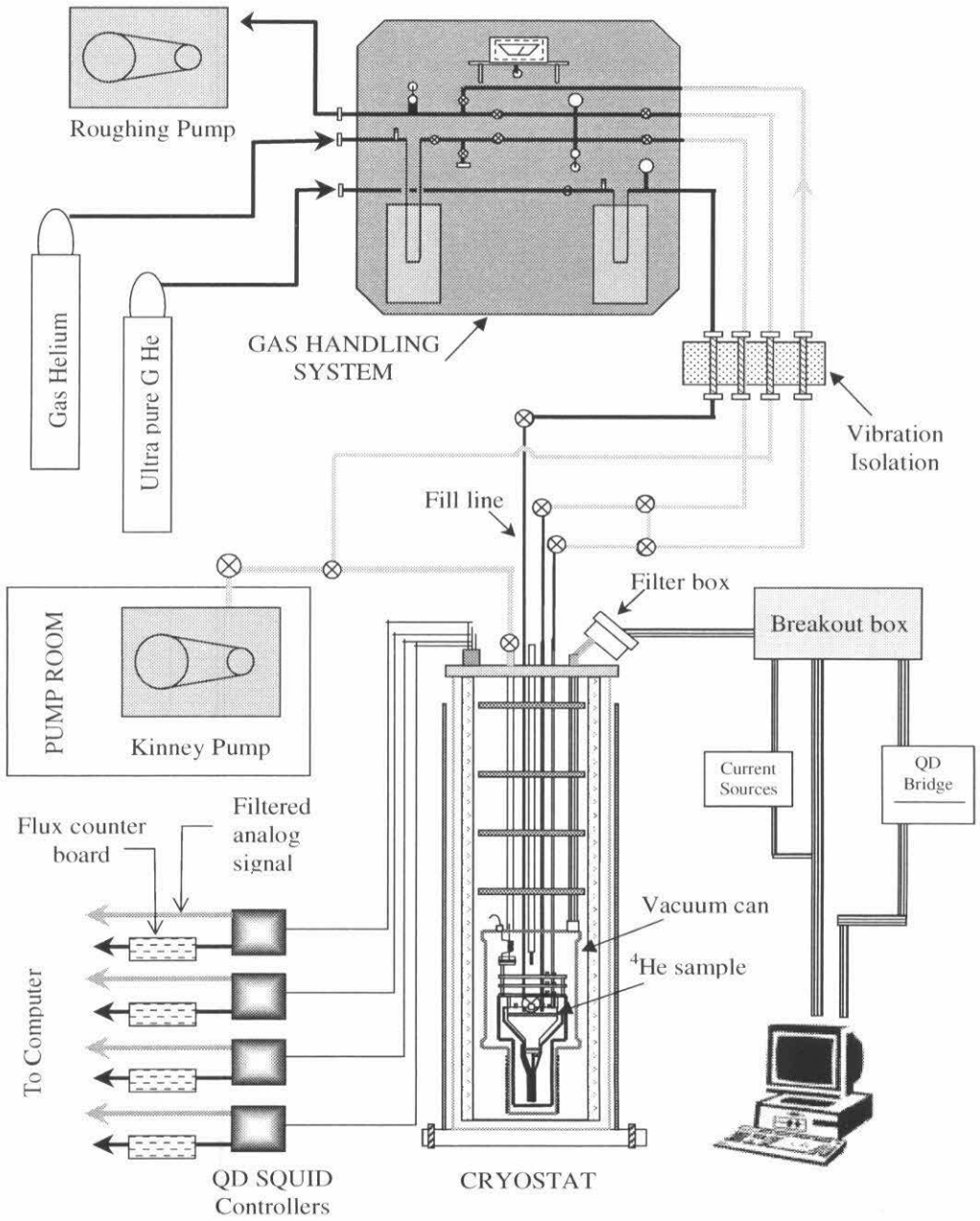

Figure 3.1: A schematic drawing of the complete experimental system.

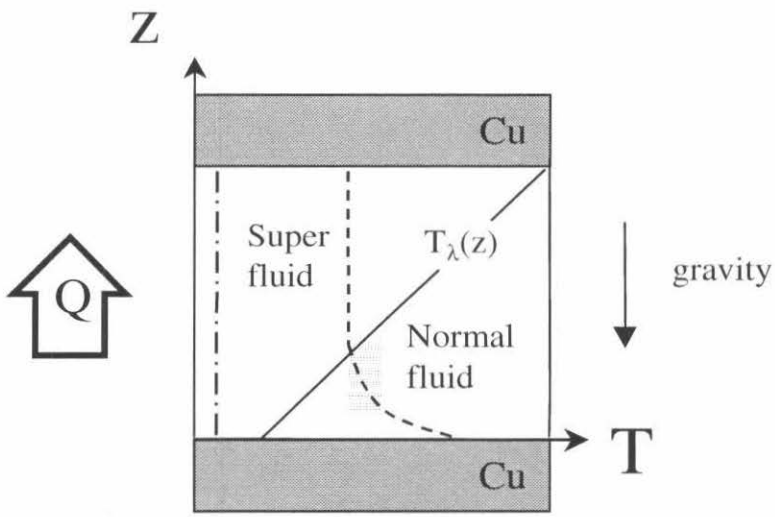

Figure 3.2: Temperature profiles for ^{4}He in a gravitional field and a heat current, Q. A gravitational field causes the transition temperature of ^{4}He to vary as a function of cell height. Solid line: the transition temperature T_λ as a function of cell height, z. Dashed-dotted line: when the temperature of the sample is adjusted so that the temperature at the bottom of the cell is less than the local transition temperature, the temperature will be uniform throughout the cell. Dashed line: if the temperature is tuned so that the center of the cell is at the local transition temperature, then the top of the cell is superfluid and the bottom of the cell is normal fluid. Shaded region: the interfacial region between the superfluid and the normal fluid. [Note: not drawn to scale.]

range of $t \geq 4 \times 10^{-8}$.

Gravity affects our experiment by averaging the heat capacity curve over the temperature range of δt for our particular cell height. This can cause a rather extreme rounding effect, especially in the vicinity of a divergence. Figure 3.3 illustrates the anticipated effects of gravity on heat capacity measurements taken in a 2 mm and a 0.64 mm cell.

(a)

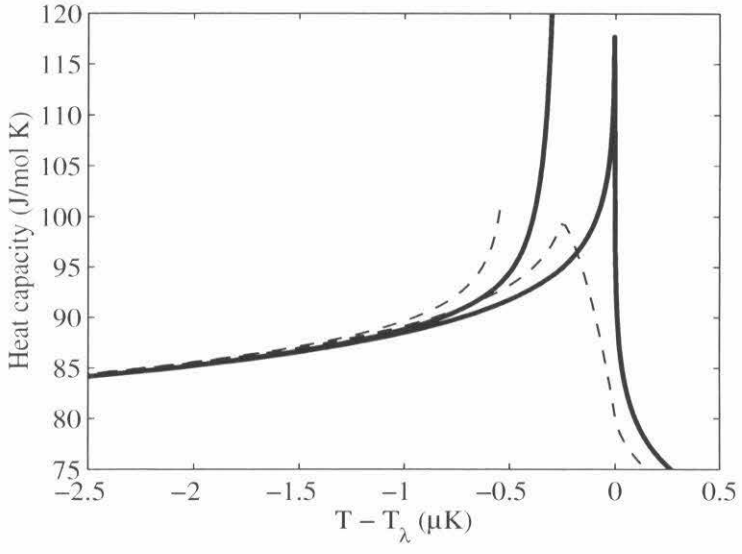

(b)

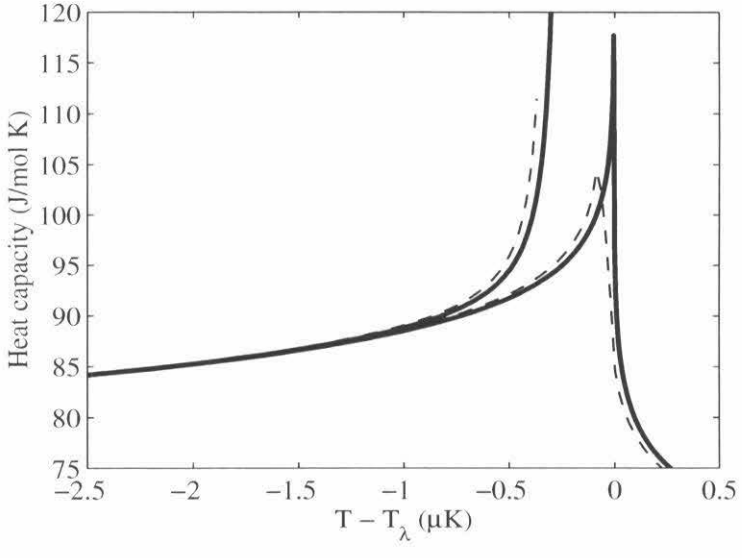

Figure 3.3: Heat capacity curves in a gravitational field in (a) a 2 mm high cell (b) a 0.640 mm high cell. Right thick solid line: a fit to LPE data [2] (at saturated vapor pressure and $Q = 0$). Right thin dashed line: LPE data rounded for gravity. Left thick solid line: Haussmann's theoretical predition for C_Q [18] (at saturated vapor pressure and $Q = 3.5$ μW/cm^2). Right thin dashed line: Haussmann's prediction rounded for gravity. This curve is cut off when the temperature at the bottom of the cell reaches the local value of $T_c(Q)$.

3.1.2 Thermometer placement, specific heat error, and temperature instability: the singular Kapitza resistance

A heat flux, Q, flowing across a solid metal wall into superfluid ^{4}He produces a discontinuity between the temperature of the metal ($T_{\rm Cu}$) and the temperature of the superfluid at the wall (T_W). This temperature jump is linear in Q, and is caused by the acoustic mismatch between the two materials. It is known as the Kapitza boundary resistance.

There is another component to the boundary resistance that has been observed to be weakly singular near the superfluid transition [78, 79] (see Figs. 3.4, 3.6). This singularity comes about because, in a boundary layer within about a correlation length of the endplates, the superfluid/normal fluid conversion rate becomes too slow to support the entire heat flux by counterflow, resulting in a very small temperature gradient near the end-plates (see Fig. 3.4).

The thermal resistance across this boundary, $R_b = \Delta T_b/Q$, where $\Delta T_b = T_W - T_{SF}$ (with T_{SF} the temperature of the bulk helium), is thought to diverge in the $Q \to 0$ limit when T_{SF} approaches T_λ. At the wall where the heat flows into the cell, the temperature in the boundary layer is higher than T_{SF}. The opposite is true at the wall where the heat exits the cell. It is found that the data for R_b at both walls collapse onto a single curve if R_b is expressed as a function of the mean boundary temperature $T_b = (T_{SF} + T_W)/2$ [79]. The plot of R_b vs. T_b is independent of Q.

Measurements taken in the range $10^{-4} > t > 10^{-7}$ indicate that a log-log plot of the singular boundary resistance, R_b, versus the reduced boundary temperature, $t_b = 1 - T_b/T_\lambda$, is nearly a straight line [78, 79], so that

$$\Delta T_b = T_W - T_{SF} = QR_b = Q\beta t_b^{-z_K} \tag{3.2}$$

$$\Rightarrow T_W - T_{SF} = Q\beta \left(1 - \frac{(T_W + T_{SF})}{2T_\lambda}\right)^{-z_K}, \tag{3.3}$$

where β and z_K are fitting parameters to the experimental singular Kapitza resistance.

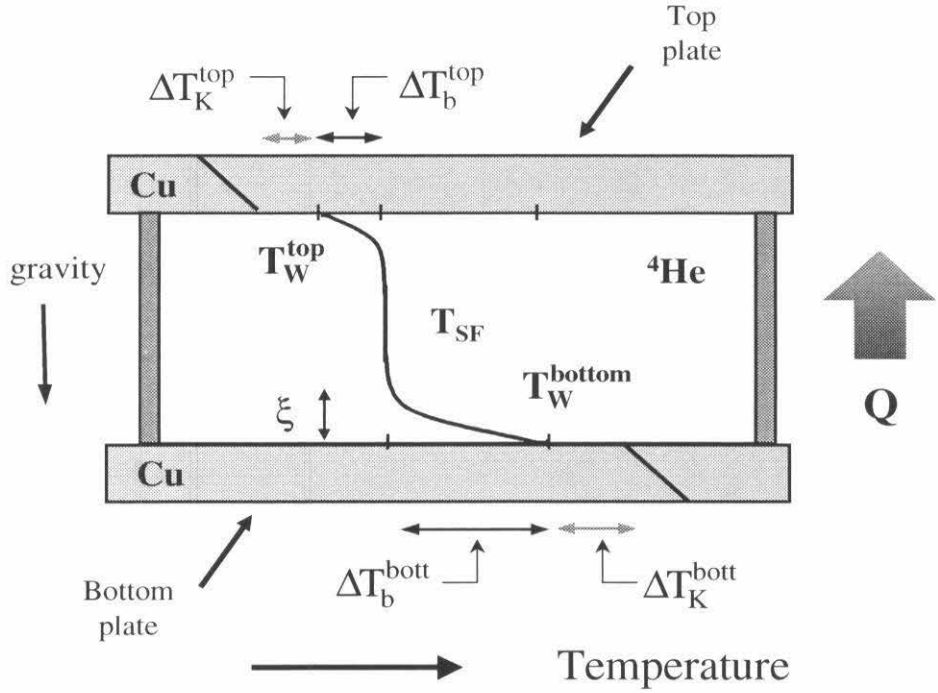

Figure 3.4: Grey arrows: the temperature jump due to the regular Kapitza resistance, $\Delta T_K = T_{\rm Cu} - T_W = QR_K$. Black arrows: the temperature jump due to the singular Kapitza resistance, $\Delta T_b = T_W - T_{SF} = QR_b$. [Note: not drawn to scale.]

The most recent data are shown in Fig. 3.5 [78]. When the fit is performed over the entire temperature range of this plot, $\beta = 4.388 \times 10^{-3}$ K/W, and $z_K = 0.2033$.

The existence of the regular and singular components of the Kapitza resistance, shown in Fig. 3.5, have a number of adverse effects on the execution of our experiment.

Thermometer placement

Both components of the Kapitza resistance influence the temperature readings of thermometers mounted on the cell end-plates. The fact that the singular Kapitza resistance is a function of temperature causes serious complications when using endplate thermometers for a dynamic measurement. This problem can be eliminated by using a thermometer in contact with the midplane of the cell sidewall. The temperature of the sample is then read in a manner analogous to a standard four wire resistance measurement, where the thermal boundary resistances are avoided in the same way that contact resistances are eliminated in the four-wire measurement.

We attempted to build a midplane thermometer into our experiment. Unfortunately, it proved difficult to meet both the stringent height requirements described in Sec. 3.1.1 and to have a functioning mid-plane thermometer. As will be described in future sections, the short cell height caused the midplane thermometer to be thermally linked in a non-trivial way to one of the cell endplates.

Specific heat error: the specific heat of the boundary layer

Because the singular Kapitza resistance is actually in the fluid itself, the heat capacity of the upper and lower boundary layers will be somewhat different than the heat capacity of the bulk. At a reduced temperature of $t = 10^{-7}$, about 2% of the volume of the sample would be within these boundary layers. However, because the temperature of the top boundary layer falls below T_{SF}, while the temperature of the bottom boundary layer falls above T_{SF}, the two different heat capacity effects would partially cancel, and the overall error should be quite small. This is fortunate: since the bulk heat capacity close to $T_c(Q)$ is unknown, it would be impossible to account accurately

(a)

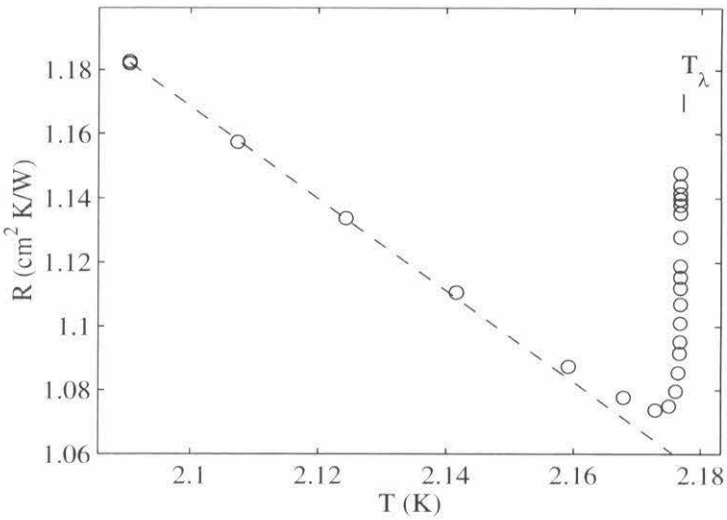

(b)

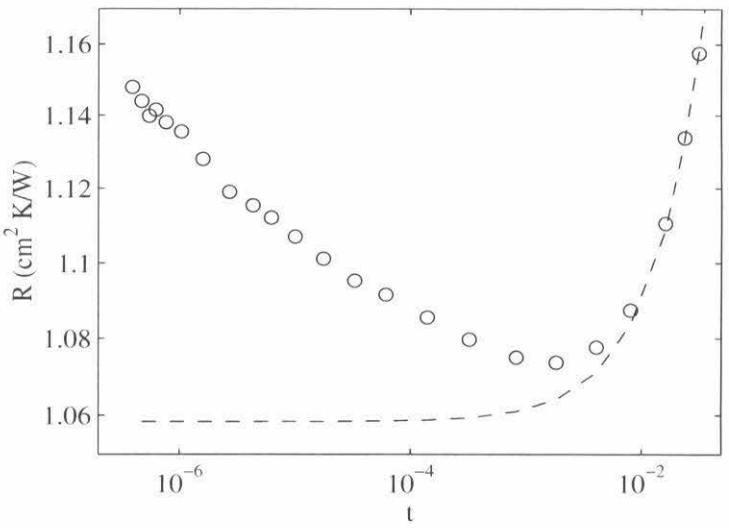

Figure 3.5: (a) Linear plot of the total Kapitza resistance as a function of temperature. Open circles: the total Kapitza resistance $R = R_K + R_b$ as a function of bulk helium temperature T. (From Fu, Baddar, Kuehn, and Ahlers (FBKA) [78], Fig. 2.) (b) Semi-log plot of the total Kapitza resistance as a function of temperature. Open circles: the total Kapitza resistance R as a function of the reduced bulk helium temperature t. Dotted line: a fit to the regular component of the Kapitza resistance, R_K. (From FBKA [78], Fig. 4.)

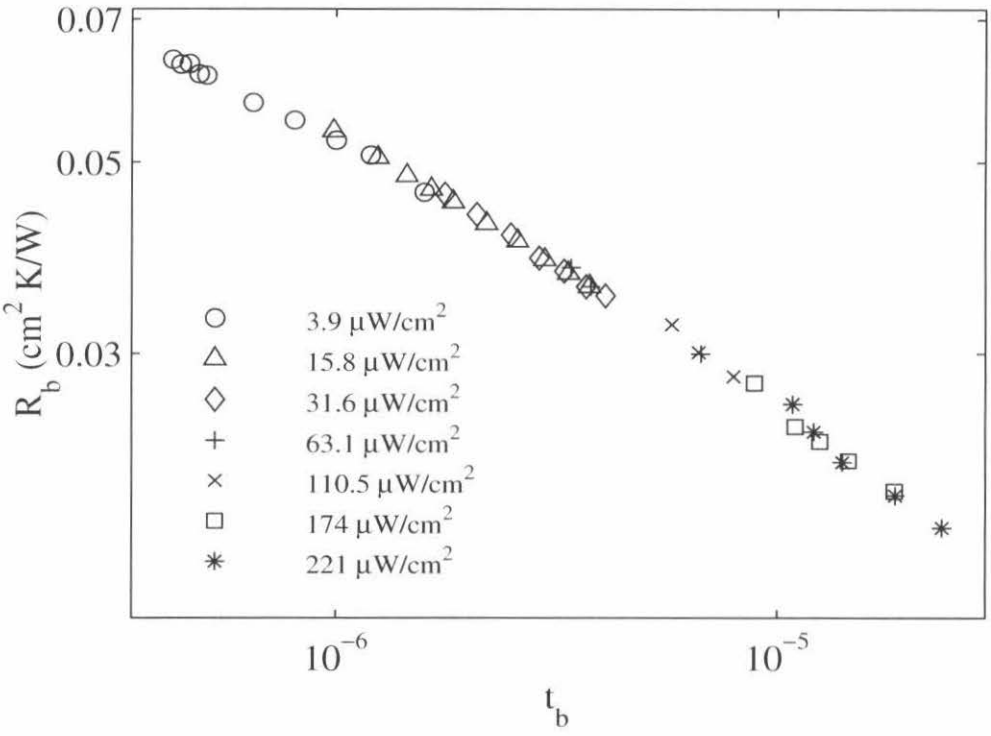

Figure 3.6: Log-log plot of the singular boundary resistance R_b as a function of reduced mean boundary temperature t_b. This plot was obtained by subtracting the dotted line from the open circles on Fig. 3.5 for different heat currents and then adjusting the x-axis to be $t_b = 1 - (T_b/T_\lambda) = 1 - [(T_W + T_{SF})/T_\lambda] = t \pm [QR_b/2T_\lambda]$. (From FBKA [78], Fig. 5.)

for this error. It will therefore be assumed that it is negligible for the analysis of this experiment.

Temperature instability at the boundary[1]

The singular Kapitza resistance might have a considerably more serious impact on the results of this experiment: because the temperature of the helium in contact with the lower wall (in the heat from below configuration) is higher than the temperature of the bulk liquid, the superfluid might become unstable at the boundary before the bulk fluid reaches $T_c(Q)$.

The hypothesis that the experimental superfluid breakdown temperature, $T_{\rm DAS}$, might be due to an effect at the boundary was proposed independently by myself and R.V. Duncan [80]. The argument goes as follows: According to Weichman and Miller, the normal-fluid interface probably emerges continuously from the warmer boundary layer [61]. Suppose that the interface detaches from the endwall more or less when $T_b = T_c(Q)$, where $T_c(Q)$ is the breakdown temperature. For lack of an experimental measurement of $T_c(Q)$, we estimate its value using Haussmann's prediction $t_c = (Q/6571\ \mathrm{W/cm^2})^{0.744}$ [18]. Let T_x be the temperature of the bulk superfluid at this point. If our hypothesis is correct, T_x will be equal to $T_{\rm DAS}$. From (3.2) we have

$$T_W - T_x = Q\beta\, t_c^{-z_K}, \tag{3.4}$$

while

$$T_c = T_b = \frac{T_W + T_x}{2} \;\Rightarrow\; T_W = 2T_c - T_x. \tag{3.5}$$

Substituting this relation into (3.4) we obtain

$$T_c - T_x = \frac{Q\beta}{2}\, t_c^{-z_K} \tag{3.6}$$

$$\Rightarrow\; t_x = t_c + \frac{Q\beta}{2T_\lambda}\, t_c^{-z_K} > t_c. \tag{3.7}$$

[1] Some of the text in this subsection appears in Harter, Lee, Chatto, Wu, Chui, and Goodstein [25].

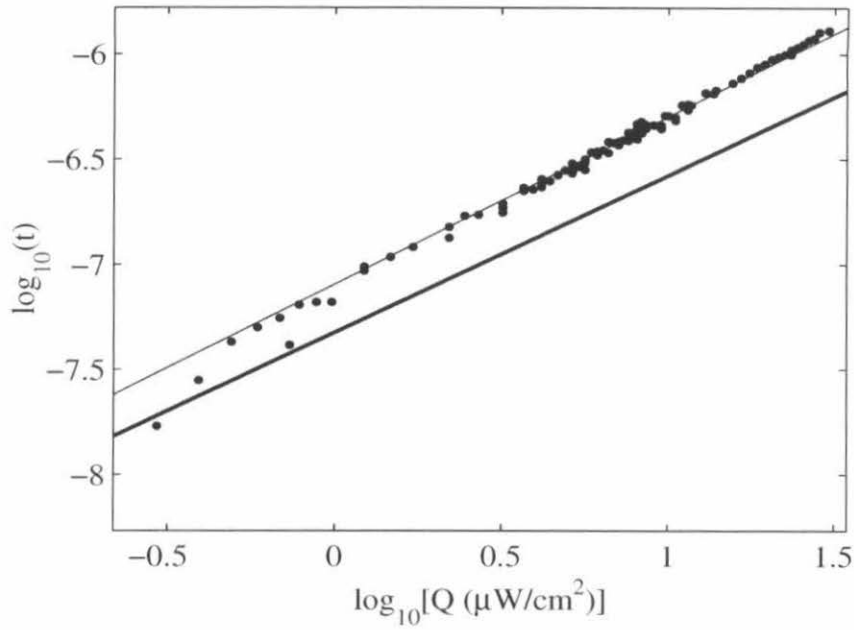

Figure 3.7: A numerical calculation of superfluid breakdown, obtained by setting the boundary temperature T_b equal to the theoretical prediction for T_c. Dots: the DAS data. Thin solid line: the breakdown temperature, t_x, determined numerically from (3.7). Thick solid line: Haussmann's $t_c(Q)$ [18].

The results of substituting the theoretical value of t_c into the above equation are shown in Fig. 3.7 as the thin solid line. The agreement between the DAS data and the numerical simulation is nearly perfect, with *no adjustable parameters.*

The agreement between the numerical calculation and the data is quite compelling. In particular, it seems to explain the disturbing discrepancy between the exponent of the DAS data and the exponent of the theory, which should be quite dependable. The former appears within the fit (3.7) via a *combination* of the theoretical exponent $1/2\nu \simeq 0.744$ and the Kapitza exponent z_K. These results inspired our group to design an experiment to determine if $T_{\rm DAS}(Q)$ was, in fact, due to a boundary effect. This experiment is currently running in our laboratory.

During the course of this investigation, it was discovered that there is yet another

way to reach the conclusion that $T_{\rm DAS}$ is due to the singular Kapitza resistance.[2] Apparently there is an inherent instability built into (3.2) that occurs extremely close to $T_{\rm DAS}$ [25]. The proof does not rely on the theoretical value of $T_c(Q)$, or on *any* theoretical parameters, and therefore eliminates possible errors in the theoretical values from affecting the conclusion that $T_{\rm DAS}$ is a boundary effect.

The proof goes as follows:

Solving (3.3) for T_{SF} as a function of ΔT_b,

$$t_{SF} = \frac{\Delta T_b}{2T_\lambda} + \left(\frac{\Delta T_b}{Q\beta}\right)^{-1/z_K}, \tag{3.8}$$

one sees that there is a *minimum* t_{SF} for which a solution exists. The condition $\partial t_{SF}/\partial \Delta T_b = 0$ for this minimum yields

$$\Delta T_b = \frac{2T_\lambda}{z_K}\left(\frac{\beta z_K Q}{2T_\lambda}\right)^{\frac{1}{z_K+1}}. \tag{3.9}$$

The corresponding value of t_{SF} at this value of ΔT_b (which we will call t_i) is:

$$t_i = \frac{T_\lambda - T_i}{T_\lambda} = \frac{z_K+1}{z_K}\left(\frac{\beta Q z_K}{2T_\lambda}\right)^{\frac{1}{z_K+1}} \equiv \left(\frac{Q}{Q_0}\right)^x. \tag{3.10}$$

From the experimental values of β and z_K one obtains $Q_0 \approx 600$ W/cm^2 and $x = (z_K+1)^{-1} \approx 0.83$. Thus the instability temperature is close to $T_{\rm DAS}$ (2.41). The existence of t_i is really an indication that the linear (in Q) relation (3.2) no longer makes sense when $t_b \to 0$ at fixed finite Q, and $t_i(Q)$ really then defines a boundary of validity of this linear resistance approximation. It is very interesting, though, that this boundary corresponds very closely to the onset of dissipation in the DAS experiment, and presumably to the detachment of the interface from the boundary.

To make a more accurate comparison, we note that the logarithmic plot of the singular boundary resistance data shown in Fig. 3.6 has some curvature, so it cannot be fitted adequately by single values of z_K and β. However, for any t_b, one can do a local linear fit to find accurate values for these parameters. Combining (3.9) and

[2] A. Chatto, private communication (1999).

(3.10) and solving for Q as a function of $t_b = t_{SF} - \Delta T_b/2T_\lambda$, one obtains for a given t_b an instability at $Q = Q_i$ given by

$$Q_i = \frac{2T_{\lambda 0}}{z_K \beta}\, t_b^{z_K+1}. \tag{3.11}$$

We can now proceed directly from the boundary resistance data of FBKA [78] shown in Fig. 3.6 to a prediction of superfluid breakdown. We first find a local fit for β and z_K at a given t_b, then compute Q_i from (3.11) and t_i from (3.10), and finally plot them against each other on the same graph as the DAS data. This is shown in Fig. 3.8. The results predicted from the singular Kapitza resistance data are at higher Q values than the DAS data, but the extrapolated agreement with the DAS data is excellent nevertheless. A fit to our predicted points in the form $t_i = (Q/Q_0)^x$ gives $x = 0.8163 \pm 0.0023$ and $Q_0 = 813 \pm 9$ W/cm^2, which is consistent with the DAS fit.

From the above equations, one can show that $(T_\lambda - T_i)/(T_W - T_i) = (1 + z_K)/2$. Since $z_K < 1$ for all t_b this implies that, when the temperature of the cell becomes unstable at T_i, $T_W > T_\lambda$. One would expect that as $T_W \to T_\lambda$, ΔT_b will depend nonlinearly on Q, and (3.2) will no longer hold true. The instability would therefore enter the cell at a lower temperature than if the temperature drop across the boundary were to remain linear in Q. We would therefore expect the predicted points ($\circ$) shown on Fig. 3.8 to lie slightly lower than an extrapolation of the DAS fit to larger reduced temperatures. For comparison, we have also plotted the reduced temperature of the bulk superfluid when $T_W = T_\lambda$. This shows an even closer match to the DAS results.

We conclude from the previous analyses that the *scaling* of a boundary-driven instability, determined from various criteria [both intrinsic to the singular Kapitza resistance (3.2), and including aspects of $T_c(Q)$ via (3.7)], all appear, with reasonable fitting parameters, to yield decent agreement with $T_{\rm DAS}(Q)$. More experimental data will be required to understand which criterion is the most physically correct one.

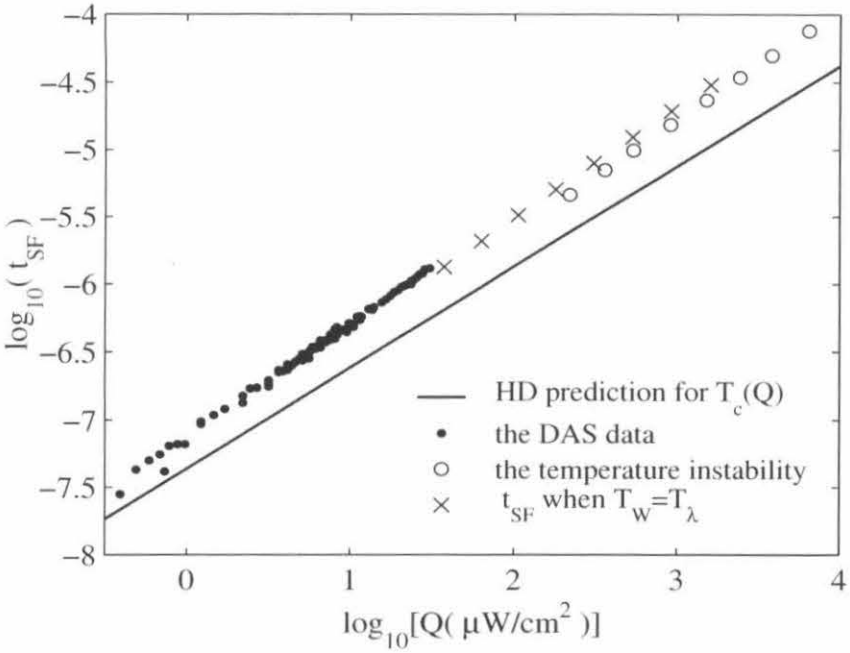

Figure 3.8: The breakdown temperature as a function of Q. (From Harter *et al.* [25], Fig. 2.)

3.2 High resolution thermometers

One of the most important components of our experimental apparatus was the thermometry, since all of our data lies within several μK of T_λ. Fortunately, in the last decade, very high resolution magnetic thermometers (HRTs) [81], have been developed for studies near the lambda transition. The best of these thermometers exhibit low frequency noise on the order of 10^{-9} to 10^{-11} $K/\sqrt{Hz}$.[3]

3.2.1 Design

In thermodynamic terms, a *thermometer* is modeled as a subsystem in contact with a heat reservoir. The *reservoir*, the object whose temperature is to be measured, is

[3]Some of the text in the next few sections appears in Lee, Harter, and Chui [26] and Day, Hahn, Chui, Harter, Rowe and Lipa [22].

assumed to be isothermal and to have infinite heat capacity. The thermometer incorporates an easily measured quantity, like the magnetization of a salt, whose mean value is a function of temperature and can thus be used to infer the reservoir temperature. From statistical mechanics, it is well known that thermodynamic properties undergo continual fluctuations about their mean values. In the case of a magnetic thermometer, this phenomenon leads to magnetization fluctuations over a frequency band from dc to the inverse of a characteristic time constant. If the magnitude of these fluctuations are comparable to the resolution of the thermometer, they appear as noise in the temperature measurement. Another source of fluctuation noise in a thermometer is the temperature variation caused by energy transfer through the thermal link to a reservoir. HRTs are currently limited by this latter form of noise.

Concept

In its basic form, an HRT consists of a paramagnetic salt pill tightly coupled to a superconducting pick-up coil. A superconducting flux tube, surrounding the HRT, is used to trap a very stable DC field ($\sim$ 10 mTesla). The salt is thermally coupled to the helium sample through a grid of high purity (99.999%) copper heat fins. High purity copper is used to maximize the thermal conductivity. The pick-up coil is connected to a superconducting quantum interference device (SQUID), which measures changes in the magnetization of the salt as a function of temperature. Ideally, these thermometers should be operated in a temperature range where the salt pill is in the paramagnetic phase and is close to its Curie temperature, T_c, where its magnetization is highly temperature dependent. In the ferromagnetic phase, discontinuous changes in the flux density due to switching of magnetic domains—the Barkhausen effect [82]—can appear as a significant noise contribution in the thermometer measurements. Most HRTs use salt pills made of crystalline copper ammonium bromide [$Cu(NH_4)_2Br_4 \cdot 2H_2O$] (CAB) which has a T_c of approximately 1.8 K. Recent designs use $GdCl_3$, which is chemically less reactive than CAB and can be grown directly onto the copper fins. In addition, $GdCl_3$ is approximately five times as sensitive as CAB at the superfluid transition temperature, T_λ.

Despite these favorable properties, T_c for $GdCl_3$ lies just above T_λ at 2.2 K, causing the salt to operate in the ferromagnetic phase. In an attempt to overcome this problem, we constructed several thermometers using $GdCl_3$ doped with La3+, a non-magnetic ion. This was done in order to depress the Curie temperature of the salt. $GdCl_3$ and $LaCl_3$ are isomorphous salts. In a solid solution, the diamagnetic La3+ ions substitute for the paramagnetic Gd3+ ions to form crystals in which both ions are present [83]. For a non-magnetic ion such as La3+, the depression in T_c is expected to be approximately linear with doping concentration [84].

Construction

The HRTs in our experiment were constructed and assembled at the Jet Propulsion Laboratory (JPL) and at Caltech by Talso Chui, Richard Lee, and myself.[4] The salt was prepared from 94.5 g of $GdCl_3{\cdot}6H_2O$ and 2.7 g of $LaCl_3$, producing 63.74 g of $Gd_{0.9585}La_{0.0415}Cl_3$. The hydrated $GdCl_3$ was first mixed with $LaCl_3$ and then dehydrated, using a reflux condensing technique with thionyl chloride [86]. The mixture was heated in a dry nitrogen atmosphere until the sample melted. The molten salt was poured into a BeCu capsule, flowing in-between the enclosed copper heat fins, and left to solidify. The assembly was sanded to remove excess salt and sealed, using a BeCu cap and cadmium solder. BeCu was chosen in order to reduce background noise caused by current fluctuations in the capsule wall, while maximizing thermal conduction to the salt pill. Cadmium solder was used because it is not superconducting at 2 K, and would therefore not distort the field trapped by the flux tube.

A superconducting pick-up coil made of 3 mil niobium wire fit tightly around the capsule. Its dimensions were optimized to match the input impedance of the SQUID and to cover the salt sufficiently to ensure maximum energy transfer. The twisted pair leads of the pick-up coil were threaded into a 9 mil i.d. Teflon tube, and then into a 15 mil i.d. niobium-titanium capillary shield. The Teflon tubing was used to prevent shorts between the leads and the Nb-Ti capillary. After the twisted pair

[4]For a detailed description of the HRT construction technique, see the JPL HRT Fabrication and Assembly Report [85].

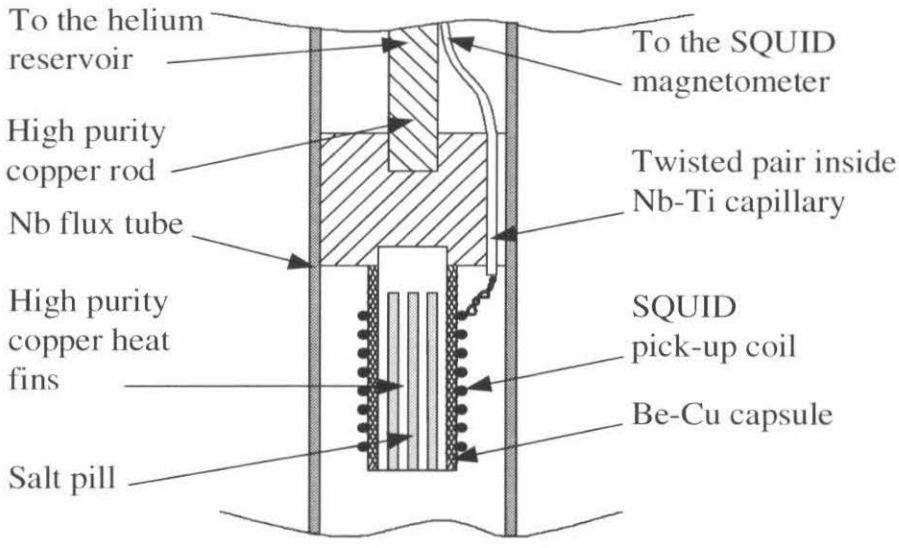

Figure 3.9: Schematic of the HRTs used in our experiment. (From Lee, Harter, and Chui [26], Fig. 1.)

and its casing were inserted, the capillary was injected with grease to prevent noise due to microphonic vibration. Pure niobium can also be used for the capillary, but niobium-titanium has a higher thermal resistance, and is therefore preferred in order to minimize the influence of heat leaks. The capsule was cadmium soldered to an annealed, high purity (99.999%) copper rod that was put into close thermal contact to the object whose temperature was to be measured. (See Fig. 3.9 and the inset of Fig. 3.11.)

3.2.2 Sensitivity

We constructed three HRTs out of $GdCl_3$ doped with lanthanum, and one out of pure $GdCl_3$. The three doped salts were mounted directly on the calorimeter, and the pure $GdCl_3$ salt was mounted on a radiation shield that surrounded the experiment. Sensitivity versus temperature measurements were made for both the pure and doped $GdCl_3$ HRTs by slowly cooling the helium sample and recording the output of the

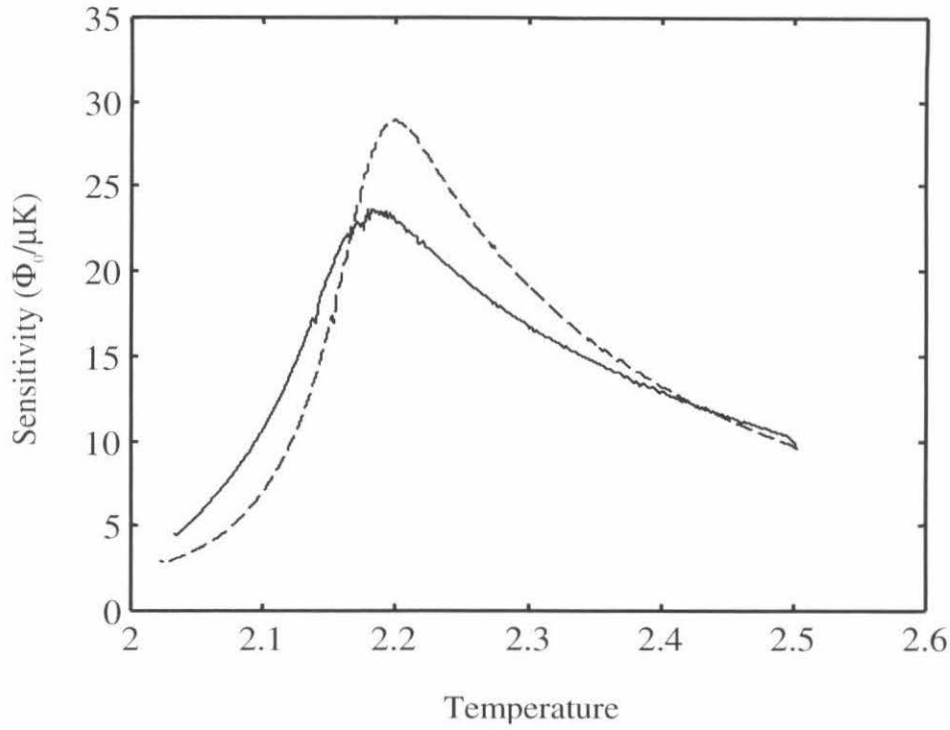

Figure 3.10: Sensitivity vs. temperature for $GdCl_3$ (dashed line) and La doped $GdCl_3$ (solid lines) HRTs, with temperature determined by the calibrated GRTs. (From Lee, Harter, and Chui [26], Fig. 2.)

HRTs along with the measurements of calibrated germanium resistance thermometers (GRTs) mounted close to the HRTs. The sensitivity of each thermometer is plotted versus temperature in Fig. 3.10. The sensitivity is defined as the change in the number of magnetic flux quanta, $\phi_0 \equiv h/2e \approx 2.07 \times 10^{-15}$ Weber, recorded by the SQUID magnetometer over a given change in temperature, as measured by the adjacent GRT.

The pure $GdCl_3$ HRT had a maximum sensitivity of 28.9 ϕ_0/μK at 2.200 K, while the doped HRT had a maximum sensitivity of 23.6 ϕ_0/μK at 2.185 K. This clearly demonstrates that the Curie temperature had been depressed. However, the depression in T_c by 0.7% was smaller than expected for a 4% La concentration [84], and this lower T_c is still above the temperature range for experiments conducted very near to T_λ.[5] This may be due to inhomogeneous doping of the $GdCl_3$ salt due to

[5]These thermometers were, nonetheless, used for our heat capacity experiments. The

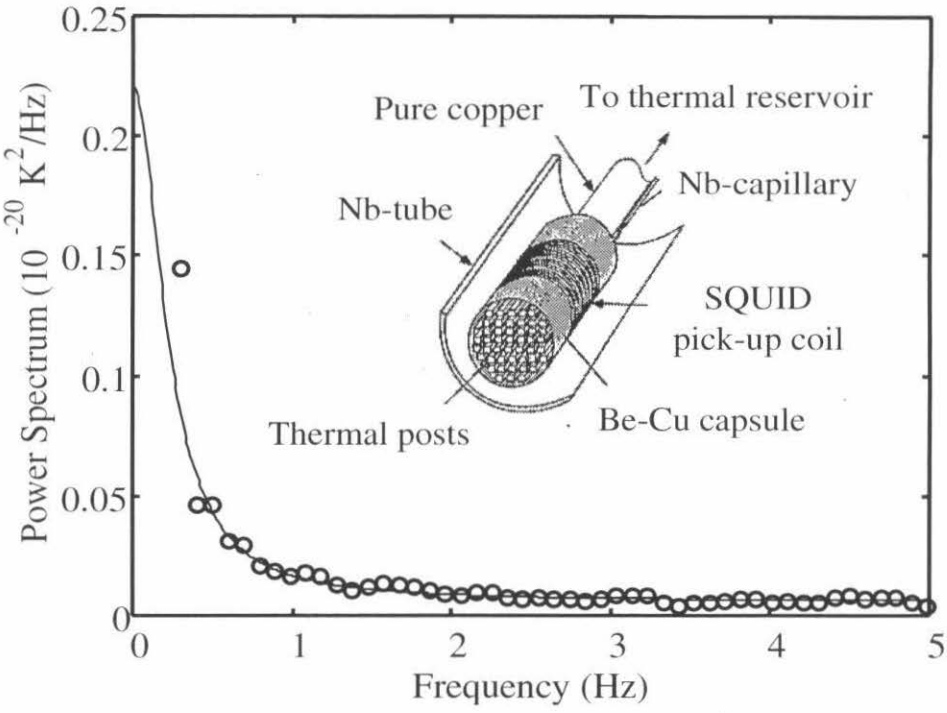

Figure 3.11: Circles: noise spectrum of the La doped $GdCl_3$ thermometer. Solid line: fit to the fluctuation-dissipation theorem (FDT). (From Lee, Harter, and Chui [26], Fig. 3.) Inset: a schematic drawing of an HRT. (From Day *et al.* [22], Fig. 4.)

clustering of the $LaCl_3$ while the salt solidified. $LaCl_3$ has a melting temperature of 860°C compared to 609°C for $GdCl_3$ [87]. The reduction in sensitivity, by 18%, is thought to be due to the anisotropic susceptibility of the $GdCl_3$ crystals that were formed during solidification [88].

3.2.3 Noise

To measure the HRT thermal noise density, the shield temperature was adjusted so that the cooling rate of the calorimeter was less than 0.01 nK/s. Measurements were taken 5 μK below T_λ. The output of the HRT was filtered at 10 Hz, connected to a spectrum analyzer, and the power spectral density (PSD) determined (see Fig. 3.11).

The main source of noise is caused by temperature variation due to energy fluctu-

Barkhaussen effect was far from our limiting noise source.

ations through the thermal link to the reservoir. The fluctuation-dissipation theorem (FDT) predicts a specific relation for this thermal noise density [21, 89]:

$$\left(T^2\right)_{f+} = \frac{4\tau k_B T^2}{C\left(1+4\pi^2\tau^2 f^2\right)}, \tag{3.12}$$

where $(T^2)_{f+}$ is the power spectral density of temperature fluctuations, defined for positive frequencies. Here τ and C represent the thermal relaxation time and heat capacity, respectively, of the salt pill. They are related by $\tau = RC$, where R is the thermal impedance between the salt pill and the helium sample. In the low frequency limit, (3.12) reduces to $\sqrt{4Rk_BT^2}$, indicating that R is the only relevant parameter that can be adjusted in order to reduce noise originating from thermal fluctuations [22].

Agreement with the FDT can be verified by fitting (3.12) to the noise spectrum. This requires knowing the value of τ and C for the salt pill. The heat capacity was measured directly by a heat pulse technique, with the helium reservoir empty. After taking into account the additional heat capacity of the copper reservoir, each salt pill was determined to have $C = 82 \pm 2$ mJ/K. This agreed with an estimate of C calculated using the volume of the salt (0.24 cm^3), the density of $GdCl_3$ (4.52 $\mathrm{g/cm}^3$) [87], and the zero field heat capacity data of Hovi *et al.* [90]. The thermal relaxation time was determined by observing the response of the HRT to a pulse of heat applied to the helium reservoir, when full. This yielded $\tau \approx 1.0$ s which is consistent with the value determined from the fit to the noise spectrum, $\tau = 0.7 \pm 0.1$ s (see Fig. 3.11). This gives an estimate $R = 8.5 \pm 1.5$ K/W for the thermal impedance. At low frequencies, the noise density was 5×10^{-11} K/$\sqrt{\mathrm{Hz}}$, which is equal to the noise density of HRTs made with salt pills of pure $GdCl_3$ [22]. The PSD was found to contain a small but observable background noise due to Johnson current noise in the capsule assembly. This was confirmed from measurements of a 'dummy' capsule, where the salt pill was absent. By disassembling the capsule and taking noise measurements of each component, it was shown that most of the current noise originated from the copper heat fins, and not from the BeCu capsule or the copper thermal

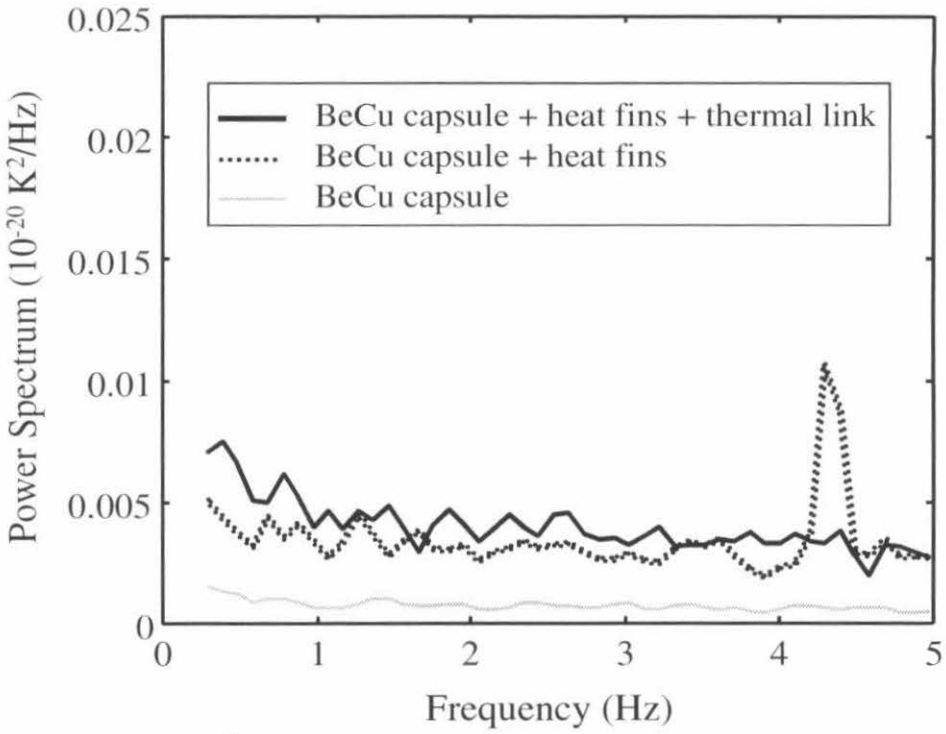

Figure 3.12: The background noise due to Johnson current noise in the components of the capsule assembly.

link. This background noise had a magnitude of approximately $1.8 \times 10^{-4}\ \phi_0/\sqrt{\text{Hz}}$, corresponding to a PSD of 5×10^{-23} K^2/Hz.

3.2.4 Drift rates

All HRTs exhibit small drift rates that must be taken into account when making precise measurements over long periods of time. The origin of this drift is thought to be due either to flux creep in the niobium flux tube, or thermal relaxation of the salt pill that causes changes in its magnetization. It has been observed [91] that, following the initial cool down of the salt pill, the drift rate decays to a constant value over a period of several days. Even small temperature changes 're-energize' the drift, which then decays with a faster time constant back to a steady value.

The drift rates of the doped HRTs were measured for every data run (see a de-

scription of the analysis technique in Sec. 5.1.4). They drifted both up and down in temperature, at rates that ranged from zero to 10^{-5} ϕ_0/sec $\equiv 1.5 \times 10^{-12}$ K/sec. This corresponds to a temperature drift of around $\frac{1}{2}$ nK/hour, and can be accounted for during data analysis. For comparison, the drift rates of pure $GdCl_3$ and CAB HRTs are $\leq 10^{-12}$ K/s and $\leq 10^{-13}$ K/s, respectively [91].

3.2.5 Implementation and calibration

SQUIDs, filters, and computer interface

Each of the HRTs in our experiment was attached to a 220 MHz RF SQUID system that was manufactured by Quantum Design, Inc. (QD). Each SQUID chip was mounted on a sapphire substrate for better thermal conductivity and stability. The SQUIDs themselves were shielded by niobium flux tubes and mounted on a bracket that was separate from all other thermal stages. During the experiment, the bracket was at approximately 4 K and was not thermally controlled. Measurements by other groups indicate that the HRT noise can be somewhat reduced by servoing the SQUID mounting bracket at low temperatures [91].

Each SQUID was interfaced to a 486 computer through a fluxcounter board[6] designed by Peter Day, a postdoc in the lab at the time of my arrival in the group. The fluxcounter board read the unfiltered analog voltage signal from the SQUID controller. If the signal was greater than the voltage equivalent to ~ 0.8 ϕ_0, it sent out a reset signal to the controller, and the analog signal dropped quickly to zero. At the same time, the flux counter was incremented by one, and a timer signal was started that measured the time that had elapsed since the reset signal had been sent to the controller.

The voltage signals were seperately filtered in the SQUID controllers and read directly into a Data Aquisition board (DAQ) manufactured by National Instruments. The signal was filtered to match the Nyquist criterion for our data aquisition rate of 1 Hz. This was accomplished by modifying the filters, shown in Fig. B.1, that were

[6]For a diagram of the fluxcounter board, see the JPL HRT Fabrication and Assembly Report [85].

part of the commercial package to have a cutoff of 0.4 Hz.[7] Diagrams of the modified filters are included in Appendix B.

A LabVIEW program read in the filtered analog voltage values from the DAQ, and added them to the digital counting signal read in from the fluxcounter board. This gave the total temperature, in units of ϕ_0, read by the HRTs. Because there is some delay between the time that the reset signal is received by the SQUID controller and the time that the fluxcounter increments its value, a spike appears in the data at the time of the reset. This can easily be removed during data analysis by throwing away any data points taken in some small window (usually about half a second) after the timer signal had begun counting (see Sec. 5.1.1).

This fluxcounter system could not count faster than approximately 50 ϕ_0/sec. For the sensitivity levels of our experiment, that meant that if the temperature changed at a rate greater than ~ 8 μK/sec, the thermometers would no longer give an accurate reading. Although this was fairly (OK, very) inconvenient, and put a slight restriction on the manner in which experiments were conducted, it was not difficult to avoid passing this threshold. The counting limitation was due to a spike at the output of the QD SQUID. Future iterations of the experiment should consider using another system— the Low Temperature Group at JPL has begun testing a Star Cryo electronic DC SQUID controller, and they have found that it counts up to 1500 ϕ_0/sec [92].

Heat switches

There was one other limitation on the operation of the HRTs. If the magnetization of the HRT salt pills increased significantly during the course of a temperature sweep, the leads of its niobium pick-up coil started to approach critical current, and its temperature reading began to behave inconsistently and inaccurately. To avoid this problem, a heat switch made out of manganin wire with copper-clad niobium-titanium wire leads was wrapped around and GE-varnished to the pickup coil's niobium-titanium

[7] The design of the modified filters was given to us by QD, and we experimentally confirmed the cutoff after the changes were made.

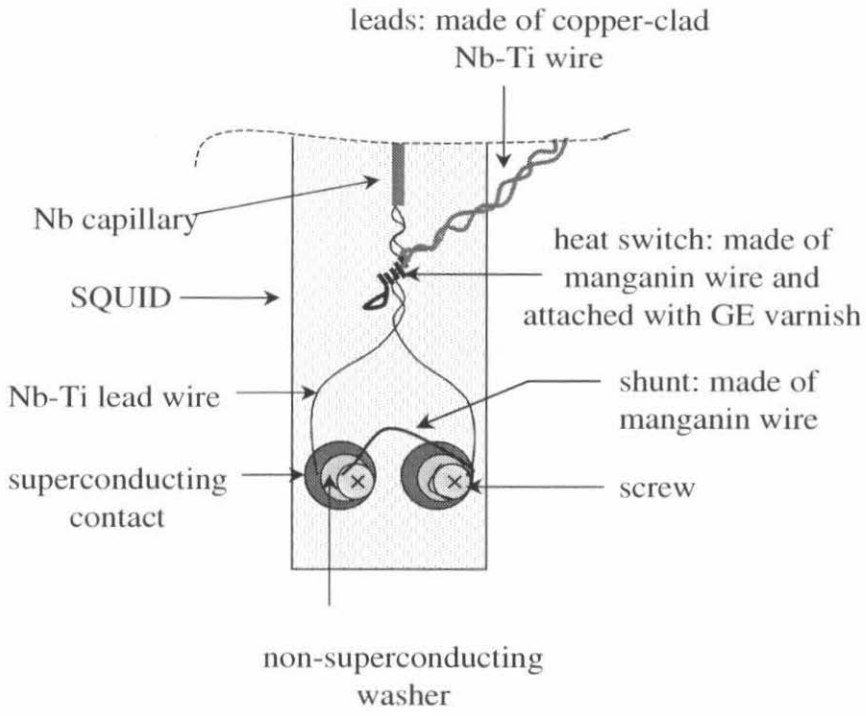

Figure 3.13: Attaching an HRT to a SQUID. The shunt acts as the R in an RC low pass filter formed with the inductance of the superconducting coil. The heat switch is used to drive the Nb lead normal, dumping the current when it becomes near critical.

lead wires (see Fig. 3.13).[8] When a voltage was applied across the heat switch, it heated up, driving the lead wires normal, thereby eliminating their current. In order to ensure that the thermometers had the same calibration from one run to the next, the heat switch for each HRT was fired within a μK of T_λ at the beginning of every experimental run. Because our heat capacity data sweeps covered a temperature range of only several μK, the lead currents never approached their critical values during standard operation.

[8]Niobium lead wires can also be used, although this should be avoided since pure niobium tends to turn brittle and break at low temperatures.

Calibration

The first step in calibrating the HRTs was to trap a magnetic field in the flux tubes. This was done by raising the temperature of the experiment above 9 K, the superconducting temperature of the Nb flux tubes, applying a current to a magnet surrounding the vacuum can to give the desired field value, and then cooling the experiment below 9 K. Because the thermometer sensitivity is proportional to the magnetization of the salts, the higher the magnetic field, the higher the sensitivity (ϕ_0/K) of the HRT. We used fields of approximately 1–100 Gauss for various runs. For the final heat capacity run we applied 0.25 Amps to the magnet leads, which corresponds to a field of approximately 30 Gauss. The precise value of the field used was not measured, since its absolute value was not important — only its relative value as it affected HRT sensitivity.

The next step in calibrating each HRT was to determine its Volt/ϕ_0 ratio. This number is related to the tank circuit of each HRT's SQUID, and is therefore slightly different from one HRT to the next. The easiest way to find this ratio is to servo the shield stage until the temperature of the calorimeter has an extremely slow drift rate. The drift rate should be sufficiently slow that it takes 1-5 minutes for the thermometer to go through the temperature range equivalent to one flux quantum. This slow rate ensures that there are many data points taken per ϕ_0, and that the unfiltered analog signal from the SQUID controller will look more or less like a saw-tooth wave. The amplitude of the triangle wave is the V/ϕ_0 ratio. The approximate value can be determined by fitting lines to the edges of the wave and then extrapolating to get the height. Several more decimal places can be obtained for the fit by plugging in the tentative value to a software simulated flux counter and attempting to make a continuous temperature signal from the data. By zooming in on the regions where the flux count changes, the V/ϕ_0 value can be tweaked until the curve matches on each side of the discontinuity. Once the final V/ϕ_0 value was obtained, it was entered into a LabVIEW program that automatically added the analog signal and the flux count to obtain a temperature reading in units of ϕ_0.

The next step in the calibration process was to determine how many ϕ_0 the flux-counter sweeps through when the HRT salt changes by one Kelvin. This value varies depending on the composition and the amount of the salt used in the HRT, and on the magnitude of the magnetic field that was frozen into the flux tube.

The calibration was performed twice for each run, once over a large temperature range from approximately 1.8 K to approximately 2.5 K (as shown in Fig. 3.10), and once within only ± 2 mK of T_λ. The calibration runs were automated by a LabVIEW program that servoed an upper stage of the experiment, incrementing the servo point every few seconds, until the HRT traversed the entire temperature range of the calibration. For the large range calibration, the LabVIEW program also supplies a voltage pulse from the DAQ to the heat switch of each HRT every 20 minutes, so that the leads never reach critical current. Although this appears as a large spike in the calibration data, it can easily be removed during data analysis. The wide range calibration was only used to map out the wide range sensitivitiy of the HRT. The heat capacity data was analyzed with the narrow range calculation, which did not require heat switches to be fired.

For both calibrations, the total flux reading of the HRT is plotted vs. the temperature reading of a calibrated GRT located in close proximity, where both axes are normalized so that T_λ is equal to zero. For the finer calibration, which is the one used to analyze the heat capacity data, the resulting curve is then fitted to the form:

$$\mathrm{T}\,(\mu\mathrm{K}) = \mathrm{a} + \mathrm{b}\phi + \mathrm{c}\phi^2 + \mathrm{d}\phi^3, \tag{3.13}$$

where $\phi \equiv n\phi_0$ is the number of flux quanta. The values of the coefficients for the HRTs used during our heat capacity data run are listed in Table 3.1. An example calibration run is shown in Fig. 3.14.

As can be seen from the values of the coefficients, the fit in (3.13) is nearly linear over the limited temperature range of our measurements. Therefore, for most purposes, only coefficient 'b' is needed for data analysis, as it gives a very accurate conversion between the number of ϕ_0 in one μK.

	Location	Salt	V/ϕ_0	a	b	c	d
HRT0	cell bottom	$GdCl_3$ doped w/ La	6.309	-2.7437	0.1618	-1.3844×10^{-7}	2.4168×10^{-12}
HRT1	cell top	$GdCl_3$ doped w/ La	6.17	-7.5073	0.1785	-3.9479×10^{-7}	3.3076×10^{-12}
HRT2	shield	pure $GdCl_3$	?	?	?	?	?
HRT3	cell midplane	$GdCl_3$ doped w/ La	6.94	-7.9392	0.1283	-5.2975×10^{-8}	-2.6418×10^{-14}

Table 3.1: HRT specifications. Data is not available for HRT2 because this stage has little heat capacity, making thermal control difficult and calibration challenging. Approximate values derived from the other stages are sufficient for all experimental purposes.

3.3 The calorimeter stage

3.3.1 Dimensions

The calorimeter that we used in our experiment was designed and built by Peter Day soon after my arrival in the group. The top and bottom endplates were built of oxygen free high conductivity (OFHC) copper, and were annealed to further increase their thermal conductance (see Fig. 3.15). The endplates were brazed to a 0.025" thick stainless-steel sidewall. The fact that the endplates were brazed to the sidewall turned out to be quite fortuitous. Although it was not known at the time of construction, any joining technique that leaves a small gap between the sidewall and the copper ledge of the endplate gives a large Q-dependant signal on the endplate thermometers at temperatures near T_λ [93]. This signal varies from one cell to another, and is known as the anomalous Kapitza resistance. Because we were forced to use our top and bottom thermometers to take our data, this effect would have swamped our signal and prevented us from obtaining meaningful measurements.

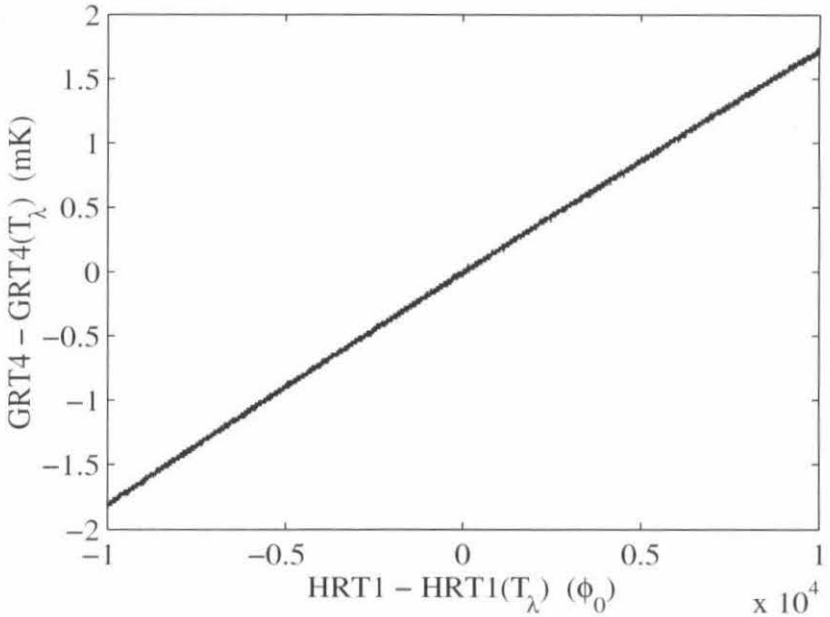

Figure 3.14: A calibration run for HRT1, taken in file 090698.01.

As previously mentioned, the height of the sidewall was made as small as practically possible to avoid the insidious effects of gravity. The diameter of the cell was chosen to be 2.75". This gave the sample a decent amount of total heat capacity (approximately 10 J/K), and therefore a large equilibrium time constant to the shield (approximately 2.4 hours).

The dimensions of the cell are shown in Fig. 3.15. The total volume of the copper parts shown in this figure is approximately 124.33 cm^3. At 2 K, the specific heat of copper is around 0.03 mJ/g K [94], which implies that the heat capacity of the copper portion of our cell should be around 33.567 mJ/K. At the end of the experiment, the heat capacity of the empty cell was measured by injecting a pulse of heat and measuring the height of the resulting temperature discontinuity. This measurement was taken several times at 1.89 K, and the average value was determined to be 0.18 J/K. The remaining heat capacity is due to the heat capacity of the three HRT salts in close thermal contact with the calorimeter stage [26].[9]

[9]The careful reader will notice that the heat capacity of the copper plus three times the heat

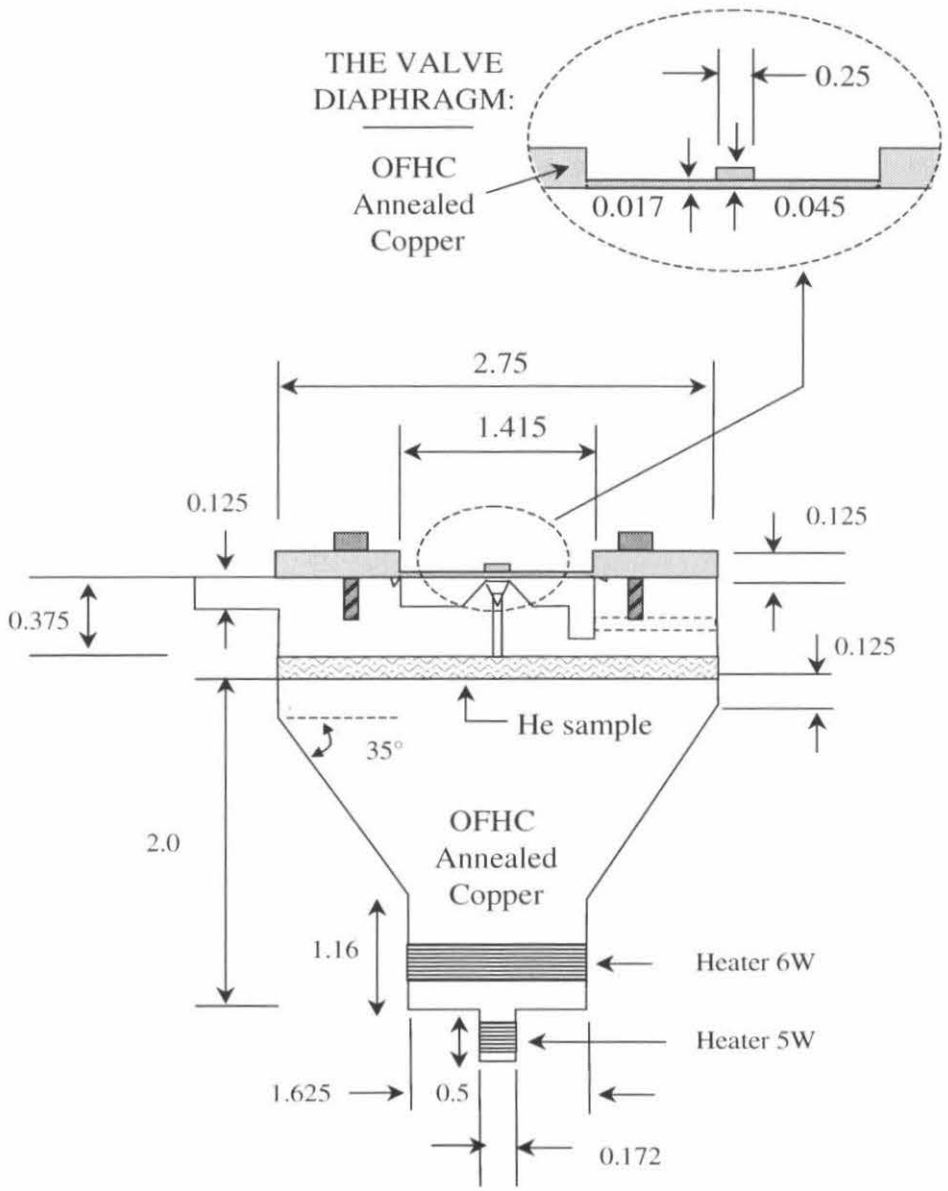

Figure 3.15: The calorimeter dimensions. All numbers are in inches. [Not drawn precisely to scale.]

3.3.2 Valve

Low temperature valves are notoriously tricky. It is difficult to get them to work consistently without leaking. Because the thermal stability of our sample was so essential for the success of our experiment, it was necessary that our valve have an absolutely negligible leak rate, since any helium in the fill line would give a devastating heat leak to the bath. For this reason, we did not use a pressure activated valve that required pressure to close the valve (default open). We feared that the helium gas used to keep the valve shut during the data run might have acted as a short to the bath. We subsequently learned that other groups have used this valve successfully, since the pressure depressed the value of T_λ in the fill line [92].

Our cell used a simple mechanical valve (see Fig. 3.16). A mechanical plunger from room temperature, which was attached to an allen head on the cold end and a fitting for a torque wrench on the warm end, was fed into the vacuum can through an o-ring fitting that allowed the plunger to rotate.[10] The plunger was used to turn a 10-40 screw, which deflected a thin copper diaphragm onto a knife-edge seat machined onto the fill line on the top endplate.[11] A leak tight seal was caused by the plastic deformation of the diaphragm. Before every cool-down a small amount of indium was melted on the bottom of the diaphragm in the location where it makes contact with the knife-edge seat. This allowed the valve to be shut multiple times without leaking. It took ~25 lb-in of torque to shut the diaphram. If the valve had to be shut multiple times on a cooldown, slightly more torque was used each time. After the valve was shut, the fill line was hooked up to a charcoal cryopump to remove any helium that might leak out.[12]

---

capacity value quoted for the HRT salts in Sec. 3.2.3 does not add up to 0.18 J/K. This is not an oversight or a mistake. During the run that we used to characterize the HRTs, a higher magnetic field was used than during the run where we took our heat capacity data, and the heat capacity of the salts is a function of magnetic field. The total heat capacity of the cell during the thermometer characterization run was approximately 0.28 J/K.

[10] When turning the plunger, care had to be taken to avoid lateral motion, or the o-ring would become displaced, and the vacuum can would quickly fill with enough helium to ruin a run.

[11] The top-plate of our cell was annealed, and so after one or two uses the 'knife-edge' became quite blunt. It functioned anyway, but future designs of this valve should either not anneal the copper or use a stainless steel knife edge soldered to the top plate.

[12] As will be described in future chapters, we measured the amount of helium in the cell at the

The advantages of this valve design is its simplicity and effectiveness. Its disadvantage is that the dimensions of the mechanical diaphragm puts constraints on the aspect ratio of the cell in a way that is not ideal for thermal heat flow. For future experiments it would be advantageous to change to a more versatile valve design, such as the one constructed by Richard Packard's group at Berkeley [95] or Yuanming Liu's at the Jet Propulsion Laboratory [96].

3.3.3 Helium cavity

The precise volume of the helium compartment of the cell was determined during the experiment. Although the diameter of the cell could easily be measured directly when the cell was warm, the precise depth was somewhat more difficult to determine. When it was originally built, the distance between the two endplates was intended to be 1 mm. However, between small errors in machining the depth of the sidewall ledge and the sidewall itself, and the sidewall not being flush against the endplate during the braze, the accuracy of this depth was not guaranteed. We measured the actual value of the cell height to great precision by using three techniques:

1. We filled the cell with helium and then measured its heat capacity as a function of temperature (see Fig. 3.17). Since the heat capacity of helium in the absence of a heat current is known to great precision, we could subtract off the heat capacity of the empty cell from our data, and then match it to the known curve by using the number of moles in the sample as an adjustable parameter. Because the width of the cell is known, the density of liquid helium could then be used to derive the height of the cell.

2. At the end of our experiment, we extracted all of the helium in our cell into a calibrated volume, and measured the number of moles in the sample. We verified the number determined by method (1), confirming the estimated value of the cell height.

beginning of the run and several months later right before we warmed up. We found the exact amount of helium as originally present, indicating that our valve did not leak, and the cryopump was an unnecessary precaution.

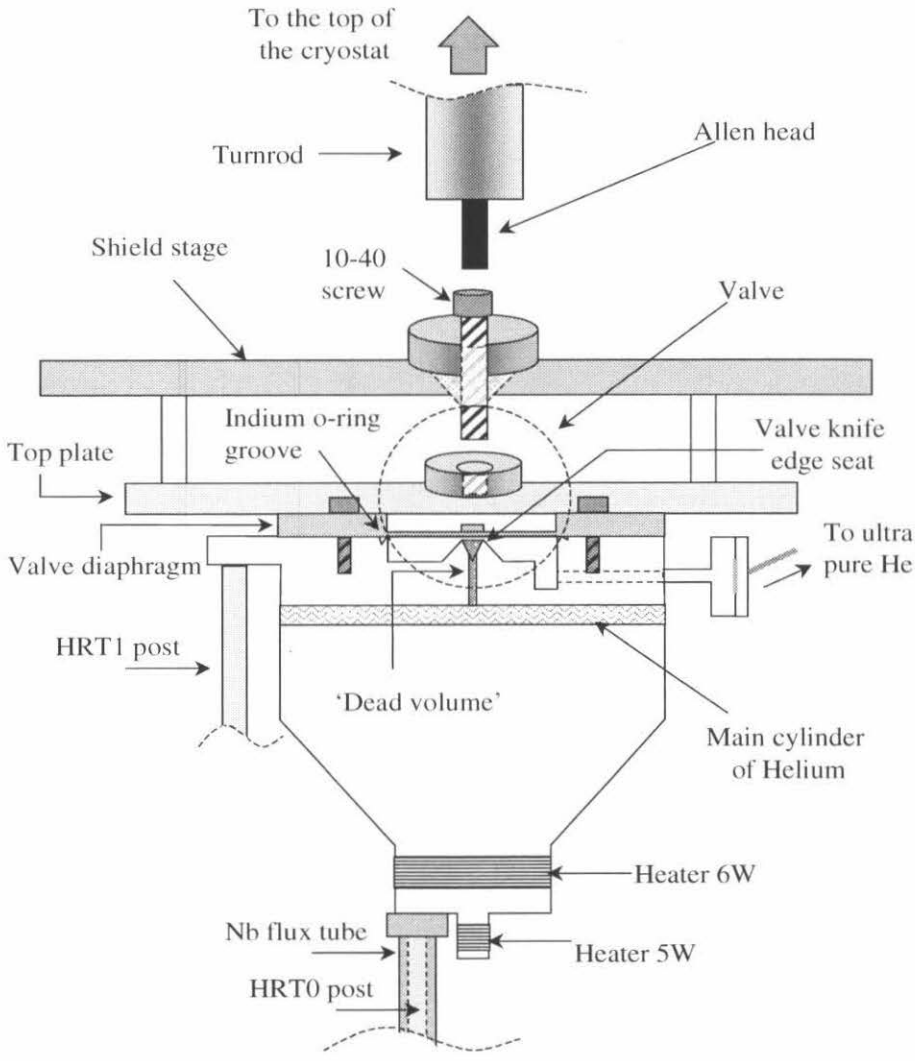

Figure 3.16: A schematic drawing of the valve that seals the helium in the cell. A mechanical turnrod from the top of the cryostat turns a 10-40 screw, that presses down on a thin copper diaphragm, which seals against a knife edge seat. [Not drawn precisely to scale.]

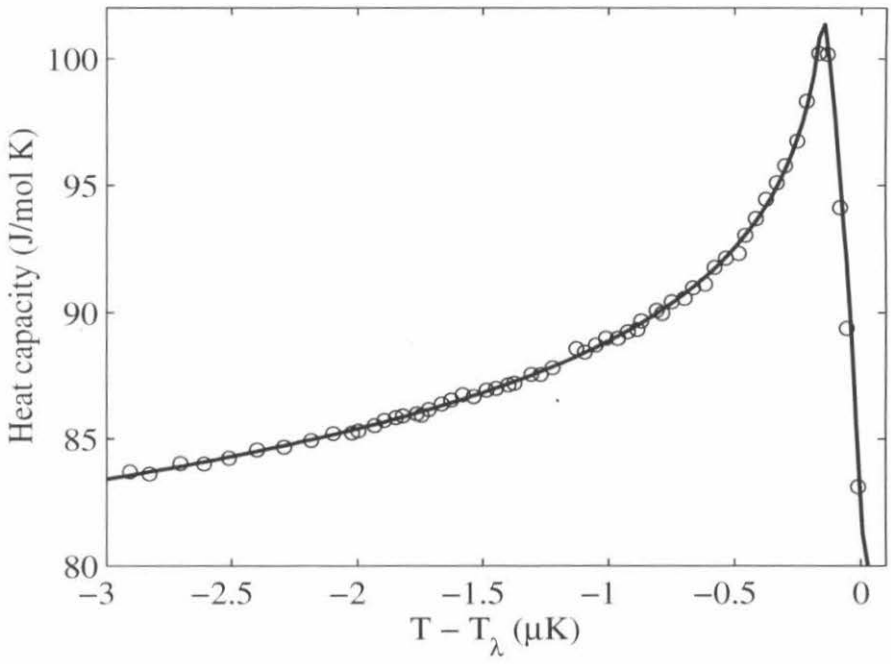

Figure 3.17: Heat capacity curve at zero heat flux. Solid line: fit to the LPE data [2], rounded for the gravity width of a 0.64 mm cell. Open circles: our pulse data taken at zero Q, using the number of moles of helium in the sample as an adjustable parameter. The fit indicates that the height of the cell is $h = 0.64$ mm. The excellent agreement between the gravity rounding of the data and the theoretical curve is also evident.

3. As described in Sec. 3.1.1, gravity creates a hydrostatic pressure gradient that causes the transition temperature to vary as a function of height within the cell. This has the effect of rounding the specific heat over a temperature range determined by the cell height. The deeper the cell, the more the rounding that occurs. The degree of rounding can therefore be used to give a precise cell depth (see Figs. 3.17 and 3.3).

All of these methods indicated that the cell contained 0.0896 moles of helium, had a volume of 2.452 cm^3, and therefore had a height of 0.640 mm.

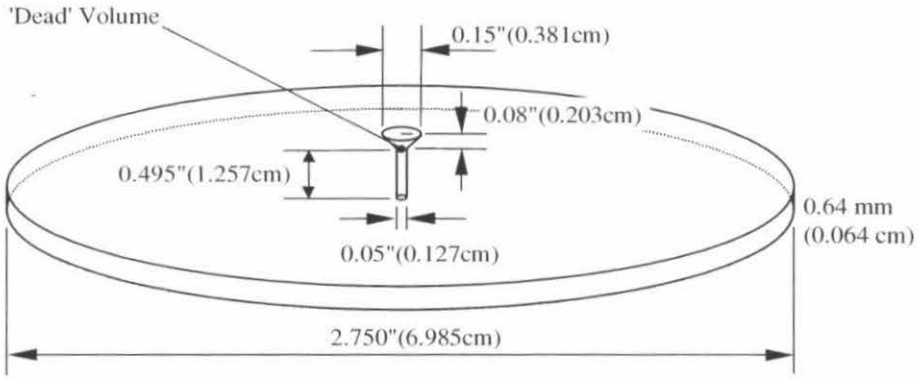

Figure 3.18: Schematic of the cell volume. The 'dead volume' refers to the fill line and valve seat that are outside the main cylinder of helium. Ideally this volume is not filled with liquid helium, but with a bubble of helium vapor.

'Dead volume'

Because of the design of our fill line and valve, our cell contained a certain amount of 'dead volume' that lay outside of the main cylinder of helium. If this volume was filled with superfluid helium, then it would have distorted the uniform heat flow in the sample. In addition, because the heat flow through the thin fill line would be larger than for the rest of the sample, the heat capacity C_Q per mole of the helium in this volume would be enhanced over that of the bulk helium.

Ideally, this 'dead volume' should be made as small as possible when the calorimeter is designed. From Fig. 3.18, it can be calculated that, for our cell, its volume was

$$V_{\mathrm{DV}} = \pi \left(\frac{0.127}{2}\right)^2 \times 1.257 + \frac{1}{3}\pi \left(\frac{0.381}{2}\right)^2 \times 0.203 = 0.0236 \text{ cm}^3. \tag{3.14}$$

Therefore, the percentage of the cell occupied by the 'dead' volume was approximately

$$\frac{V_{\mathrm{DV}}}{V_{\mathrm{TOT}}} \times 100 \approx \frac{0.0236}{2.476} \times 100 = 0.95\ \%. \tag{3.15}$$

In our experiment, we attempted to limit the influence of the dead volume by only

filling the cell with enough helium to occupy the main cylinder. The idea was that the 'dead volume' would then be filled with a 'bubble' of helium vapor. Unfortunately, it is more or less impossible to verify the location of the bubble without going to rather drastic measures (which we did not). In any case, the existance of a 'bubble', regardless of its location, assured that our experiment was performed at constant saturated vapor pressure (SVP), and could therefore be compared to the abundance of theoretical predictions and experimental data derived under these conditions.

3.3.4 Location of heaters and thermometers

There were two heaters located directly on the calorimeter. They were both four wire heaters, constructed out of evanhom wire, counterwound to be non-inductive and GE varnished directly to the copper. They were both located below the helium sample. Heater 6W, which provided the main heat current Q, was 312.51 Ω and located approximately 1.42" below the helium sample. Heater 5W, which provided the calorimetry heat current, $Q_{\rm cal}$, was 36.96 Ω, and was located approximately 2.25" below the helium sample (see Fig. 3.15). Both heaters were crimped at the calorimeter to superconducting niobium-titanium lead wires which were heat-sunk at each progressively colder (higher) stage until reaching the top of the vacuum can (see Fig. 3.16).

There were four thermometers located directly on the calorimeter:

1. HRT0[13] was e-beam welded to the bottom of the calorimeter 2" below the helium sample. The post of HRT0 was approximately 7" long and hung below the calorimeter. The HRT salt, which was 0.95" long, was located at the end of the post.

2. HRT1 was e-beam welded to a tab located on the top endplate of the calorimeter. It was located 0.313" above the helium sample. The post of HRT1 was approximately 10" long. It was bent around the calorimeter, so that the end

[13] A note for those who might actually look at the lab books for this experiment: for some reason that I cannot explain, HRT0 was also referred to as HRT4 at times during the experiment. My apologies for any confusion that this may cause.

of the HRT post and the salt lay parallel to those of HRT0 underneath the calorimeter (see Fig. 3.19).

3. GRT4 was also located 0.313" above the helium sample, so that it would give the same temperature reading as HRT1. It was coated with silicone heat-sinking compound and tightly fitted into a copper foil that was indium soldered to the top-plate of the calorimeter.

4. HRT3 was e-beam welded to a knife-edge ring that was in pressed contact with the stainless-steel sidewall. It was intended to act as a mid-plane thermometer. Figure 3.20 shows why this design was not successful.

3.3.5 Heat flow within the calorimeter

Because there is significant heat flow in this experiment, the cell should ideally have been designed so that the isotherms within the copper are flat in the region between the sample and the thermometers. Duncan and Ahlers [79] performed a numerical simulation using the thermal diffusion equation discretely in cylindrical coordinates, to determine what constraints this requirement puts on the dimensions of a cell. They discovered that in order to ensure flat isotherms at the helium surface, it is necessary to use an endplate with an aspect ratio (diameter/length) of one or less in order to separate the heater from the sample. In other words, in order to ensure that the heat entering our cell was uniform across the width of the cell, the heater (6W) should have been located at least 2.75" below the sample. Likewise, the thermometer (HRT1) should have been located 2.75" above the sample. Unfortunately, the design of the valve made the realization of this second criterion impossible.

To determine the effect that the locations of our heaters and thermometers might have on our experiment, we performed a finite-element analysis on our cell. We discovered that although our design was not ideal, the thermal problems were not too severe. The results of this analysis are shown in Fig. 3.20. The isotherms in the copper near the sample surface and the thermometers are nearly flat. On the

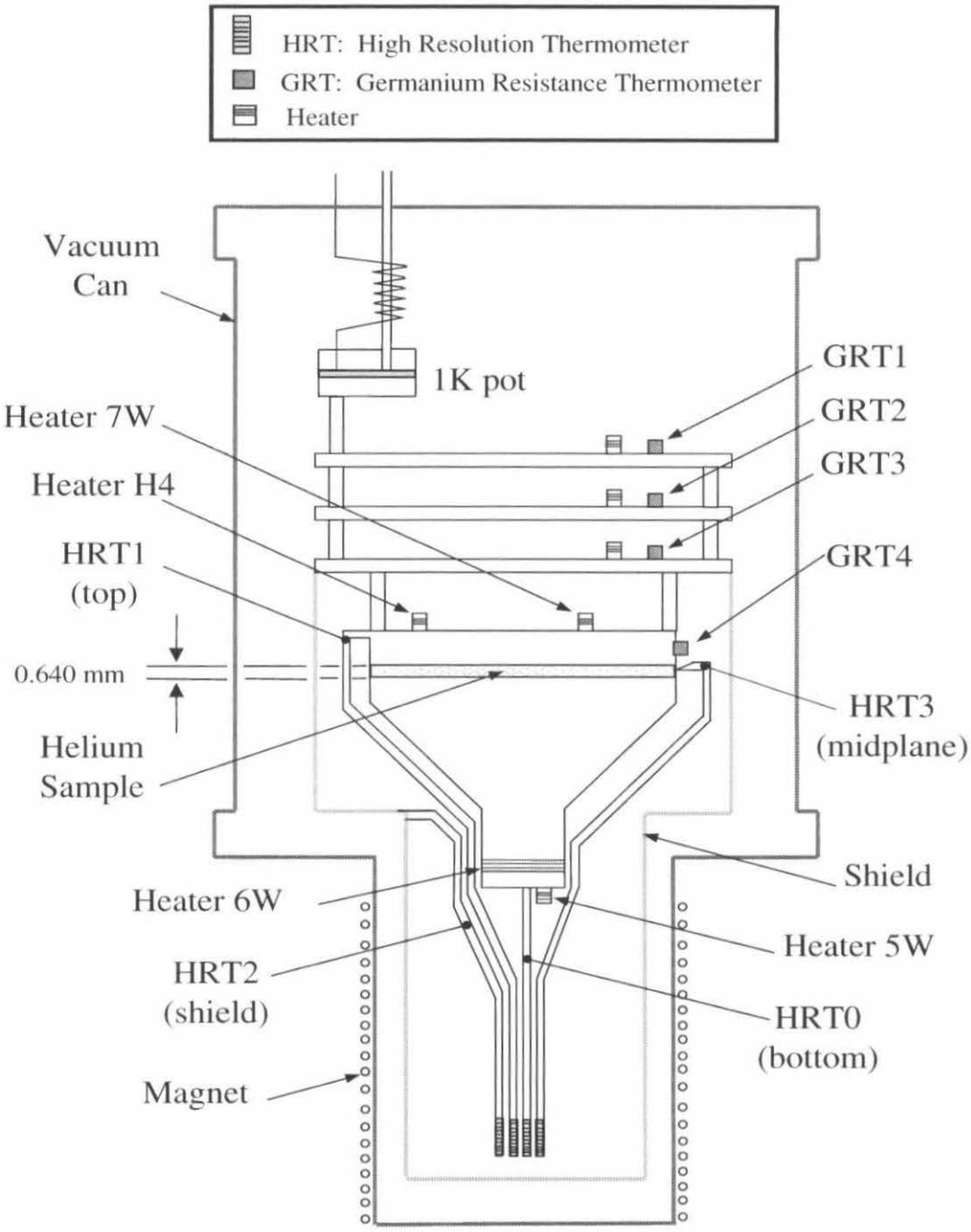

Figure 3.19: Schematic of the apparatus, illustrating the location of all the heaters and thermometers used in the experiment. The heat current Q is applied with heater 6W and the calorimetry heat current $Q_{\rm cal}$ with heater 5W. [Note: not drawn to scale.]

other hand, the isotherms in the vicinity of the midplane thermometer are clearly not flat, indicating that, as suspected, HRT3 did not give a trustworthy indication of the helium temperature.

3.4 Thermal network

Because of the relatively large heat currents and narrow temperature range of our experiment, the thermal network was an important aspect of the design of the apparatus. It was essential that all thermal paths were accounted for, and that the distribution in thermal resistance and heat capacities were designed so that we could both have sufficient thermal control and apply the necessary heat currents and still have the sample be stable when at the lambda temperature.

3.4.1 Three stage thermal isolation system

The calorimeter was mounted on a three stage thermal isolation system. In its basic form, each stage consisted of a 4" copper ring plated in gold, a GRT, and a heater made of evanohm wire non-inductively wound around a copper post also plated in gold.[14] The heaters and GRTs were screwed tightly to the stage ring. The gold plating was to improve the thermal contact between them.

The top stage was connected to a 1 K pot, whose helium feed capillary's impedence was measured[15] to be $Z = 0.2 \times 10^{12}$ cm^{-3}. According to Richardson and McClintock [98], this should have given a base temperature of 1.55 K and a cooling power of 20 mW. The base temperature of our 1 K pot was measured to be 1.68 K. Its behavior was a bit flaky. The pumping power necessary to provide a stable, non-oscillatory, temperature base varied as a function of helium bath level. The temperature would remain stable for approximately 15 hours at a given pumping power, after which it would begin to oscillate wildly. If the valve to the pump was then shut almost all the way down, thereby decreasing the pumping power, the oscillations would stop and

[14] See Appendix B for heater values and GRT calibrations.

[15] The impedence was measured using the technique described in Richardson [97], p. 55.

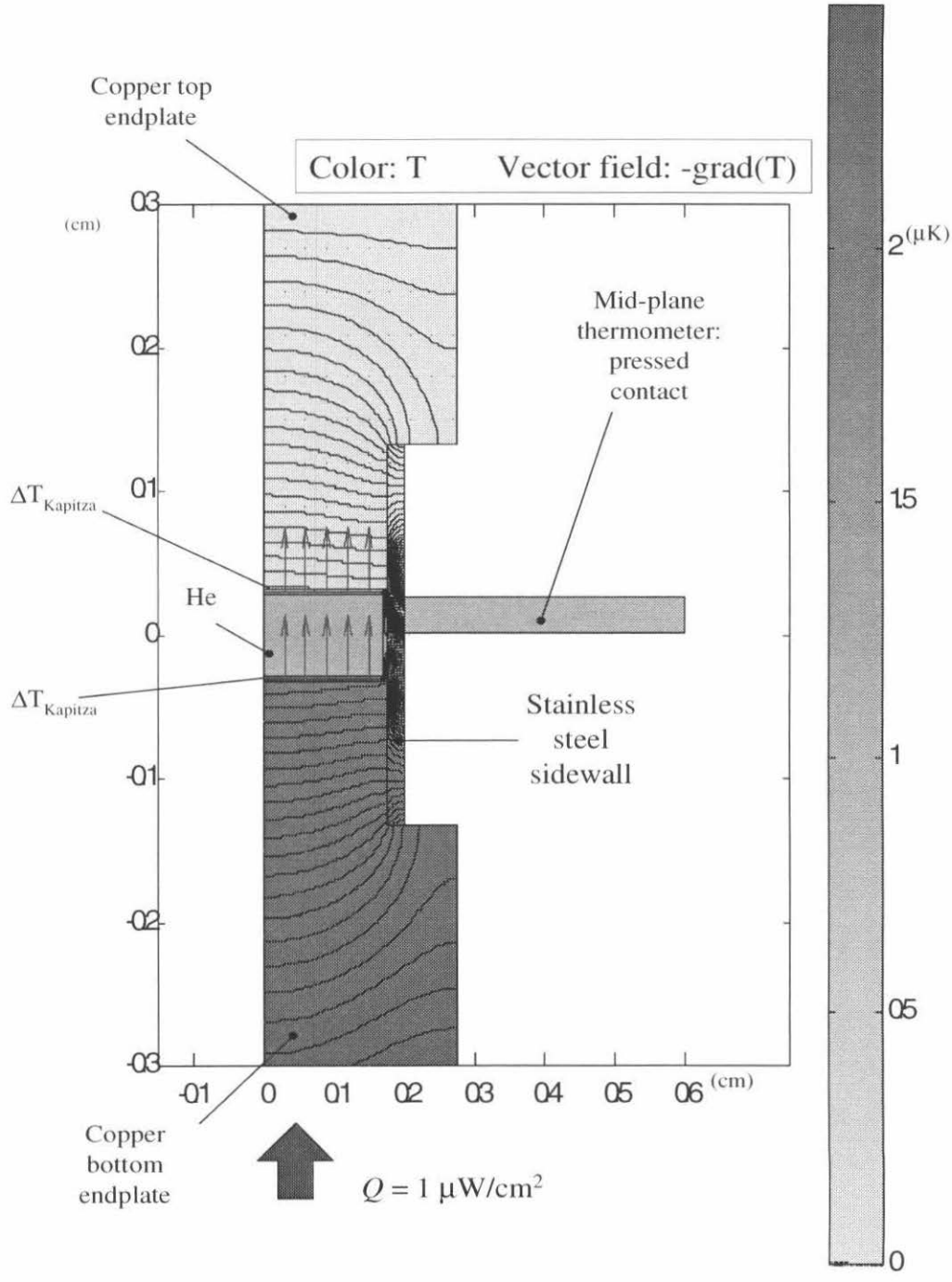

Figure 3.20: A finite element analysis of the thermal profile of the cell. Isotherms are at 10 nK separation. The distorted isotherms near the stainless steel sidewall indicate why the midplane thermometer did not give accurate temperature readings.

the temperature would stabilize for another 15 hours. It was this peculiarity that put a time limit on the length of our experimental runs. The top stage was servoed using the GRT and a QD Resistance Bridge run through LabVIEW. During the periods that the 1 K pot was behaving, it was controlled to within ± 10 μK.

The third stage consisted of a radiation shield that completely surrounded the calorimeter and the HRTs. It was constructed of copper and plated in gold. A copper coil that was pressurized with helium gas while at 77 K, sealed, and soldered shut was attached to the bottom of the shield. This was to increase the heat capacity of this stage, thereby improving its thermal control. Throughout all heat capacity runs it was servoed using an HRT to within about ± 0.2 μK.

All stages were structurally connected by thin wall stainless-steel posts with high thermal resistivity, brazed to the copper rings. They were also linked by a thin wall cupernickel circulator, that was thermally anchored to all of the stages. The circulator was used to cool the experiment from 77 K to 4 K, by applying approximately 3 psi of helium gas at one end of the circulator, and pumping it out the other end. It was evacuated during data runs.

Due to the heat currents used in the experiment, there had to be a fairly strong thermal link between all of the stages—the stainless-steel posts were not nearly sufficient. The various stages were therefore connected using brass rods soldered to copper foils which were then screwed down to the stage rings. Due to the adverse effect that this had on thermal control, the linking resistances were chosen to be as large as possible given the heat currents that we intended to use for our experiment. Measurements of the thermal resistivity of ^{4}He indicate that the fluid begins to exhibit dissipation for heat fluxes larger than 4 μW/cm^2 [23], so we chose this as our upper heat current limit. For our cell, this corresponded to a total power of 153.3 μW. For decent thermal control, it was necessary to servo the top stage temperature slightly above the base temperature of the 1 K pot, and we therefore estimated that optimal data could be obtained if the total resistance between stage one and the calorimeter

was:

$$R = \frac{\Delta T}{Q} \approx \frac{2.1768 \text{ K} - 1.90 \text{ K}}{153.3 \ \mu\text{W}} \approx 1805 \text{ K/W}. \tag{3.16}$$

In addition, it was advantageous to put the largest portion of this resistance between the shield and the calorimeter, so that any thermal noise on the shield stage would have a minimal influence on the sample. The thermal resistances between the stages were measured, and their values are shown in Fig. 3.21. The total resistance turned out to be 1668.76 K/W, close to the desired value. The thermal link between the shield and the calorimeter was composed of three thin brass rods, which were attached at locations separated by 120° near the edge of the calorimeter. This design was to distribute the heat flow as evenly as possible out of the top of the cell.

Sidewall thermal resistance

The thermal network between the sidewall and the HRTs [shown in Fig. 3.22(b)] was also investigated by injecting a heat current of 32.08 nW into the empty cell, and measuring the temperature displacement of the HRTs. This added Q changed the temperature of HRT1 by 30.8 μK, of HRT3 by 33.3 μK, and of HRT0 by 36.4 μK. This implies that the resistance between HRT1 and HRT3 was $R_{\text{SW1}} \approx 75.66$ K/W, and the resistance between HRT3 and HRT0 was $R_{\text{SW2}} \approx 99.03$ K/W. [16] This confirms that our midplane thermometer, HRT3, was biased towards the top plate of the cell.

3.4.2 Contact resistance

The fact that our experiment was sensitive to extremely small changes in temperature meant that we also had to be concerned about the effects of contact resistance. At different times we were plagued by both the thermal and electrical varieties.

[16] This is of the same order of magnitude to the anticipated value. Given that the conductivity of stainless-steel is about 0.002 W/K cm, a 0.025" thick SS sidewall that was 2.75" in diameter and 1 mm high would have an overall resistance of approximately 91 K/W.

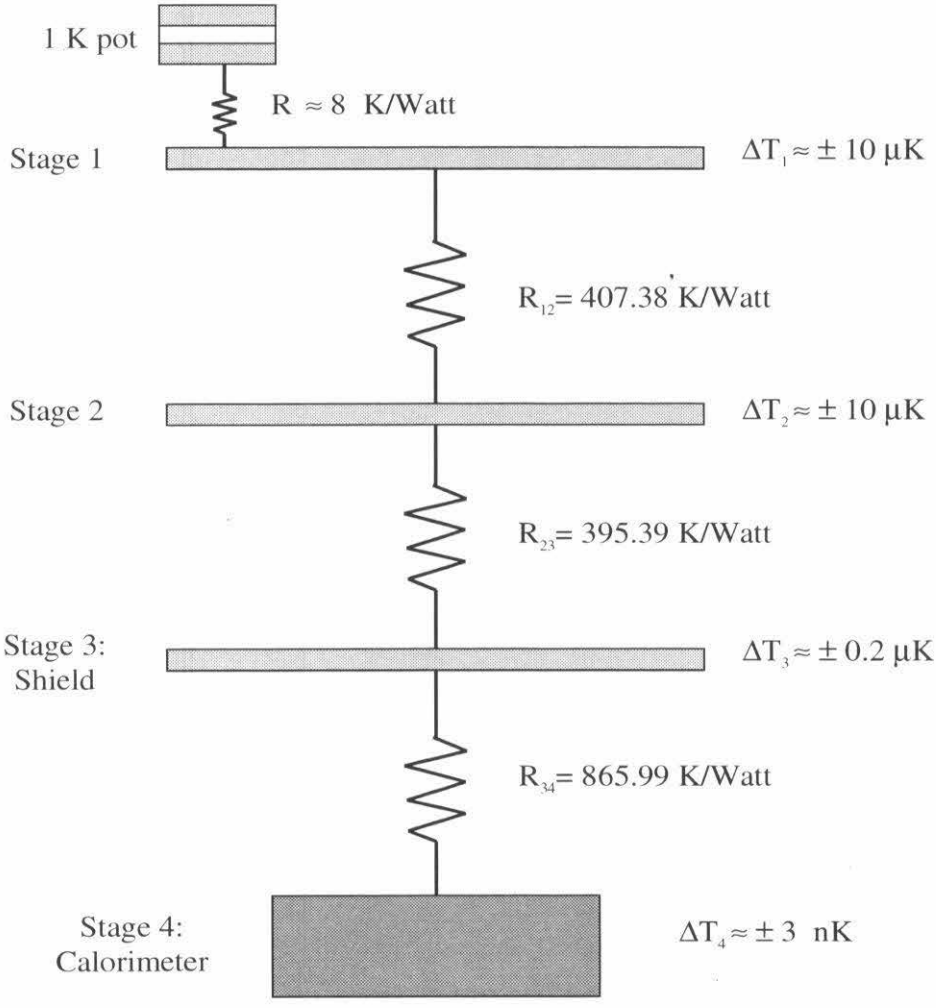

Figure 3.21: Schematic of the thermal network of the apparatus. ΔT_i represents the thermal noise on stage i when stages 1 and 3 are under servo with Q applied.

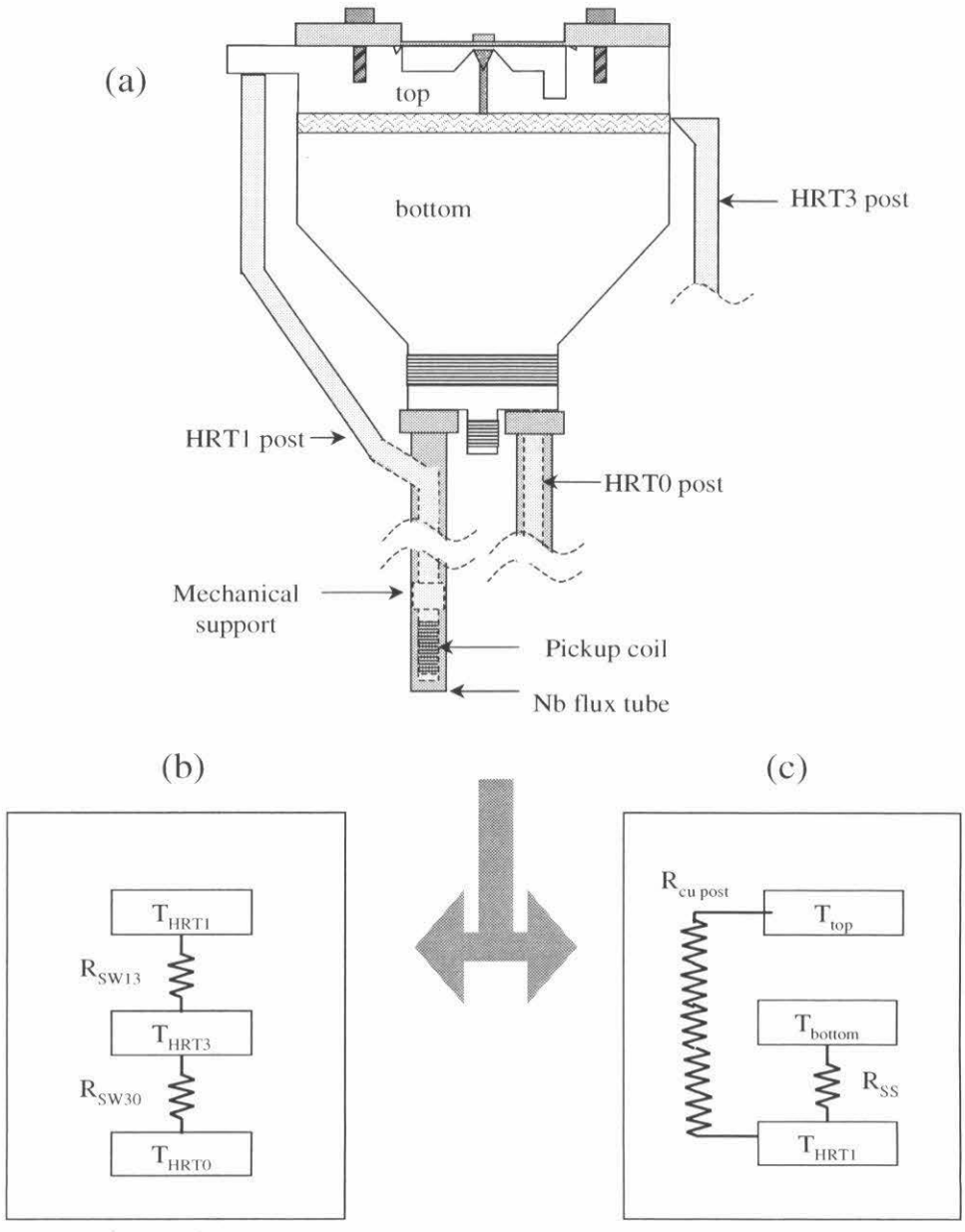

Figure 3.22: (a) Schematic of the cell with HRTs. (b) The thermal network of the stainless-steel sidewall. (c) The thermal network and possible heat leak of the Nb flux tube to the top-plate.

Thermal contact resistance problems

During one of our early runs, we noticed that there was a mysterious variable thermal resistance that would occasionally appear between the top plate and the valve diaphragm of the cell (see Fig. 3.16). It wasn't large, but it was enough to ruin a data run if it changed part way through. We had attached these two joints (and all other joints) with Apiezon grease in order to increase thermal contact. Apparently this was not a wise choice. It seems that Apiezon grease, and most other forms of vacuum grease, fracture at low temperatures, and are not good for thermal joints [99, 100]. During our next warm up, we cleaned off the grease and replaced it with a thin layer of silicone heat sink compound with ZnO_2 (Dow Corning 340). We used this compound when connecting all GRTs, heaters, heat sinking posts, and circulator anchors to the thermal stages, as well as when assembling the various components of the shield and the calorimeter. After that, we never encountered any problem with thermal contact resistance.

Electrical contact resistance problems

During another run, the temperature of our calorimeter stage would occasionally start to drift, even when the shield temperature remained extremely constant. This only happened during runs when Q was applied to the cell. After some preliminary testing, it became clear that the voltage that was being applied to heater 6W to generate Q was changing over time. After a few false starts, we discovered that it was due to problems with contact resistance on the aluminum four pin connectors located on our breakout box. Apparently they had built up a fair amount of oxide, which caused an intermittent contact resistance to be added to the lead resistance. We did two things to cure this problem:

We first replaced all of the aluminum four pin connectors with Deteronix 'military' connectors (Amphenol PT06A-8). These not only have gold plated pins for optimal contact, but they also lock into place, preventing gravity from loosening the connection. This eliminated the problem.

As an extra safety measure, we also attached heaters 6W and 5W to current sources that were supplied by the two DAQ voltage channels. The power generated in the heaters would then be insensitive to the resistances of the leads, contact and otherwise. The current sources that we installed are shown in Fig. 3.23. For constant current operation, R_3/R_1 is set equal to R_4/R_2, so that

$$I_{\text{constant}} = \frac{V_{\text{in}}}{R_2}. \tag{3.17}$$

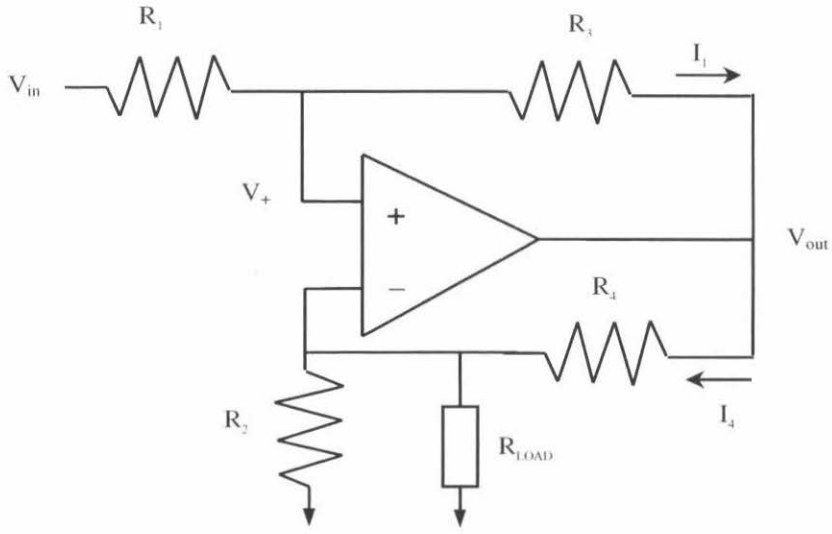

Figure 3.23: The current source used to supply Q and Q_{cal}. V_{in} comes from the output of a DAQ controlled by a LabVIEW Virtual Instrument.

We used only precision ($\pm 0.01\%$) resistors in the construction of the current sources. The resistance values we installed in our two current sources our listed in Table 3.2. They were chosen to give optimal power for our heat current ranges, using the fact that the maximum voltage put out by the DAQ was 10 V.

The design of these current sources were chosen so that if either side of the heater became shorted to ground, the current supplied to the sample would be minimal. This was to prevent ruined runs and exploded cells. For the resistances listed above, the

Heater	R_1	R_2	R_3	R_4	**Max.Current**	**Max.** Q
5W	100 kΩ	100 kΩ	10 kΩ	10 kΩ	100 μA	9.65 nW/cm^2
6W	10 kΩ	10 kΩ	1 kΩ	1 kΩ	1 mA	8.15 μW/cm^2

Table 3.2: Current source specifications.

maximum current supplied in the event of a short would be 4.7 mA, which corresponds to a power of 690 μW. Given our thermal network, this would lead to a change in the temperature of the calorimeter stage of 1.145 K, which would not lead to any problems that could not easily be remedied.

The current sources were tested for a simulated change of 10 Ω in lead resistance. The voltage across the load (the simulated heater) was stable to less than 0.001 mV, giving a percentage voltage error of less than 0.0005%, and a percentage heat current error of less than 0.001%. Because 10 Ω is far larger than any reasonable variability in the lead resistance, actual errors should be far below these values.

3.4.3 Potential heat leaks

For the sample to be thermally stable to the needed tolerance, it was essential to make sure that the thermal resistances between our stages were constant at all times. This meant that all lead wires, niobium capillaries, circulators, and brass resistance bars had to be secured firmly in place, so that they would not change position and intermittently conduct heat to unwanted locations. The lead wires were all heat sunk to every colder (higher) stage by GE-varnishing its twisted pairs around a gold-plated post that was thermally anchored to that stage (see Fig. 3.24). They were therefore immobile, and had constant thermal resistances.

The HRT niobium capillaries were secured in a similar manner. Ten to fifteen strands of copper wire were wrapped around the capillary at the location of the heat sinking, and attached with GE-varnish. The other ends of the copper strands were

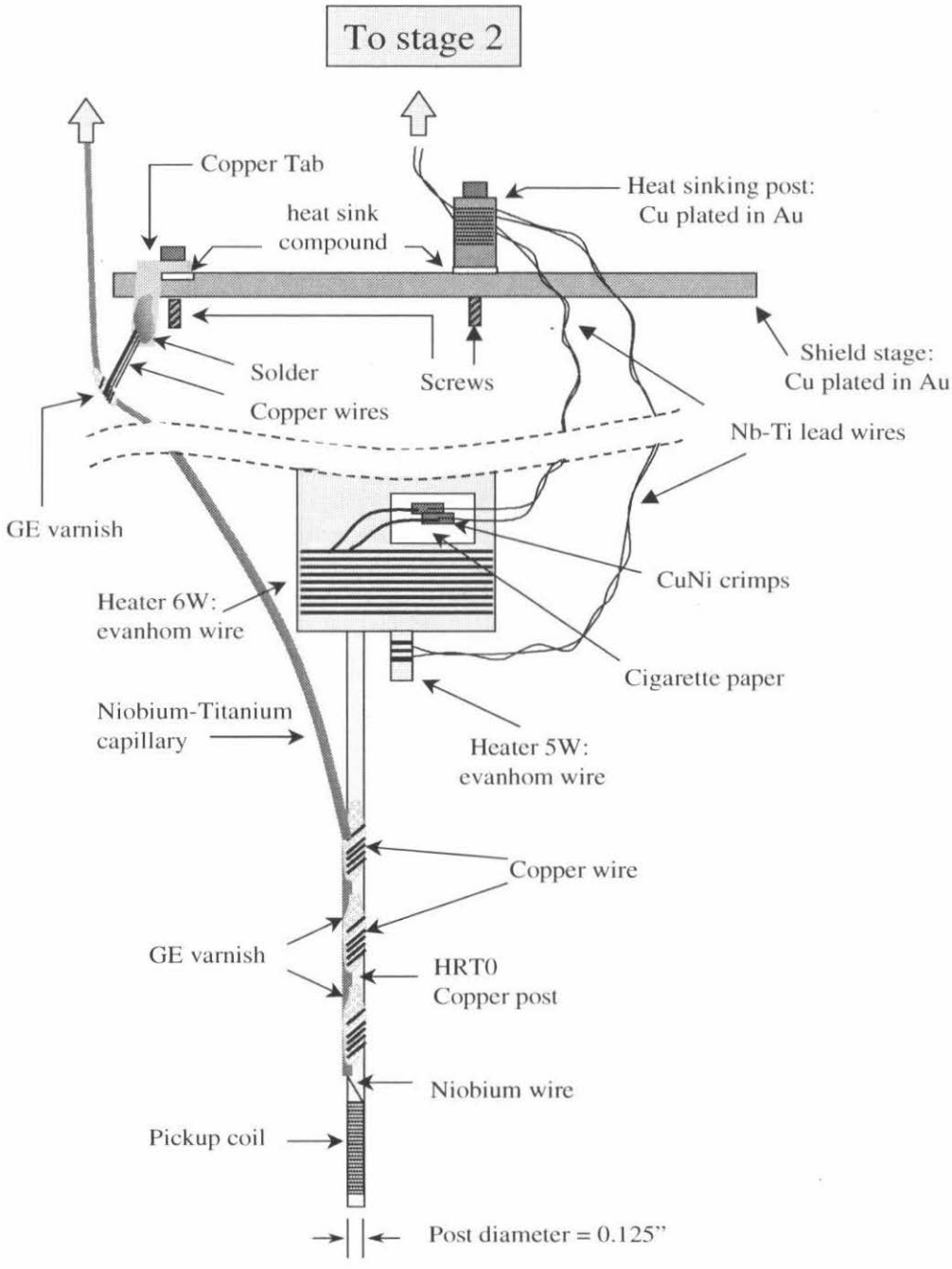

Figure 3.24: Heat sinking the HRT capillary and heater lead wires.

soldered to a copper tab, which was painted with heat sink compound, and firmly secured to the stage.

Niobium HRT capillary

Although this method of securing the niobium capillaries ensured that they would not give an intermittent thermal resistance between stages, it was not clear that the unchanging thermal resistance that they *did* give would not be a problem. After all, the Nb-Ti capillaries were essentially running from the bottom, middle, and top of the cell to colder stages. This would seem to be a perfect path for heat to escape from 6W and 5W and avoid going through the cell of helium. Since the effect that we were trying to measure was strongly dependent on the magnitude of the heat current, it was important to know if this would be a large effect. To make sure that it was not, an analysis was performed on the cell network. An arbitrary heat current of $Q = 3.8\ \mu\mathrm{W/cm}^2$ was chosen for the analysis. The network used is shown in Fig. 3.25.

From Fig. 3.25, we see that:

$$Q_1 - Q_4 - Q_3 = 0 \tag{3.18}$$

$$Q_5 - Q_3 - Q_2 = 0 \tag{3.19}$$

$$Q_4 - Q_7 - Q_6 = 0 \tag{3.20}$$

$$Q_8 - Q_6 - Q_5 = 0 \tag{3.21}$$

Substituting $\Delta T = QR$ (for example, $T_{\mathrm{tep}} - T_{\mathrm{ep}} = Q_5 R_{\mathrm{joint}}$), we used the following estimated values for temperature and resistance values:

$$
\begin{aligned}
T_{\text{shield}} &= 2.049 \text{ K} \\
T_{\text{He}} &= 2.1768 \text{ K} \\
R_{\text{joint}} &= 10 \text{ K/W} \\
R_{\text{SW}} &= 10 \text{ K/W} \\
R_{\text{Kapitza}} &= 20.5 \ \mu\text{K/W} \\
R_{34} &= 866 \text{ K/W} \\
R_{\text{nb}}(1) &= 9.56 \times 10^6 \text{ K/W} \\
R_{\text{nb}}(2) &= 1.19 \times 10^6 \text{ K/W} \\
R_{\text{nb}}(3) &= 5.96 \times 10^6 \text{ K/W} \\
R_{\text{link}} &= 334 \text{ K/W}
\end{aligned}
$$

To obtain these estimates, we used the fact that the thermal resistance of the Nb-Ti capillary is 1 cm K/W, and that it has an outer diameter of 0.660 mm, and an inner diameter of approximately 0.406 mm. Furthermore, $R_{\text{nb}}(1)$ was approximately 8 inches long, $R_{\text{nb}}(2)$ was approximately 1 inch long, and $R_{\text{nb}}(3)$ was approximately half an inch long.

Substituting all of these values into the equations and solving for T_1, T_2, T_{tep}, and T_{ep}, we found:

$$
\begin{aligned}
T_1 &= 2.17679957 \text{ K} \\
T_2 &= 2.17527228 \text{ K} \\
T_{\text{tep}} &= 2.17679999 \text{ K} \\
T_{\text{tp}} &= 2.17534244 \text{ K}
\end{aligned}
$$

From these values, we can determine that the heat flux out of the top of the cell would be 145 μW, or ~ 3.8 μW/cm^2, and that the heat flow out of the sidewall through the niobium capillary is 4.5×10^{-8} μW. Clearly there is no problem with stray heat leaks through the Nb-Ti capillaries.

Niobium flux tube

Another potential source of heat leaks was between the HRTs and the bottom of the cell, through the niobium flux tubes. The flux tubes were both firmly mounted on the

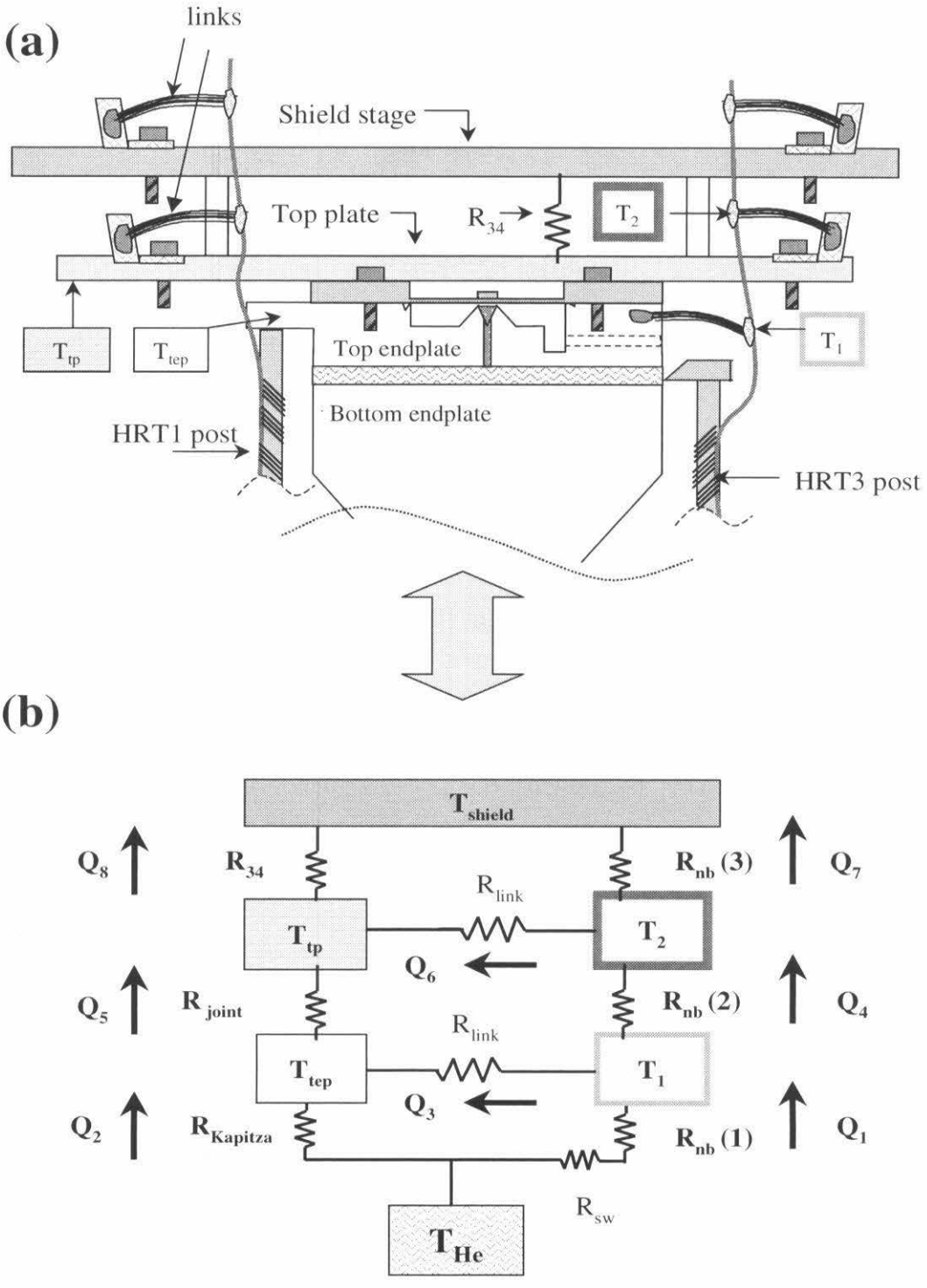

Figure 3.25: Potential heat leak: the Nb HRT capillary.

bottom of the cell and also in solid contact with the mechanical support holders of the HRT copper posts [see Fig. 3.22 (a) and (c)]. If the conductivity of the flux tube was too high, the top-plate and midplane thermometers would be adversely influenced by the hotter temperature of the bottom plate.

A quick calculation shows that the temperature of HRT1 will be equal to:

$$T_{\mathrm{HRT1}} = T_{\mathrm{tp}} + (T_{\mathrm{bp}} - T_{\mathrm{tp}}) \frac{R_{\mathrm{Cu}}}{R_{\mathrm{Cu}} + R_{\mathrm{FT}}}, \tag{3.22}$$

where T_{tp} is the temperature of the top plate, T_{bp} is the temperature of the bottom plate, R_{Cu} is the resistance of the HRT copper post, and R_{FT} is the resistance of the flux tube. At 2 K, annealed copper has a thermal conductivity $\lambda \approx 16$ W/cm K, and both stainless-steel and niobium (the two components of the flux tubes) have a thermal conductivity $\lambda \approx 10^{-3}$ W/cm K. This implies that for the dimensions of the HRT post and the flux tube, $R_{\mathrm{FT}}/R_{\mathrm{Cu}} \approx 14 \times 10^3$. The temperature error is therefore on the order of one part in ten thousand, and extremely negligible.

3.4.4 Thermal stability

In order to test how well we had managed to control the time dependence of the thermal network, and the consistency of other thermal parameters, we did a test of the thermal stability of our system. In the absence of a heat current, we servoed the shield stage so that the helium sample was in the vicinity of T_λ with approximately zero temperature drift rate. We left the shield stage at a constant temperature for about 18 hours, which was about as long as the 1 K pot would allow without acting up. As can be seen in Fig. 3.26, there is no overall time-dependent resistance, and overall stability is within a fraction of a μK.

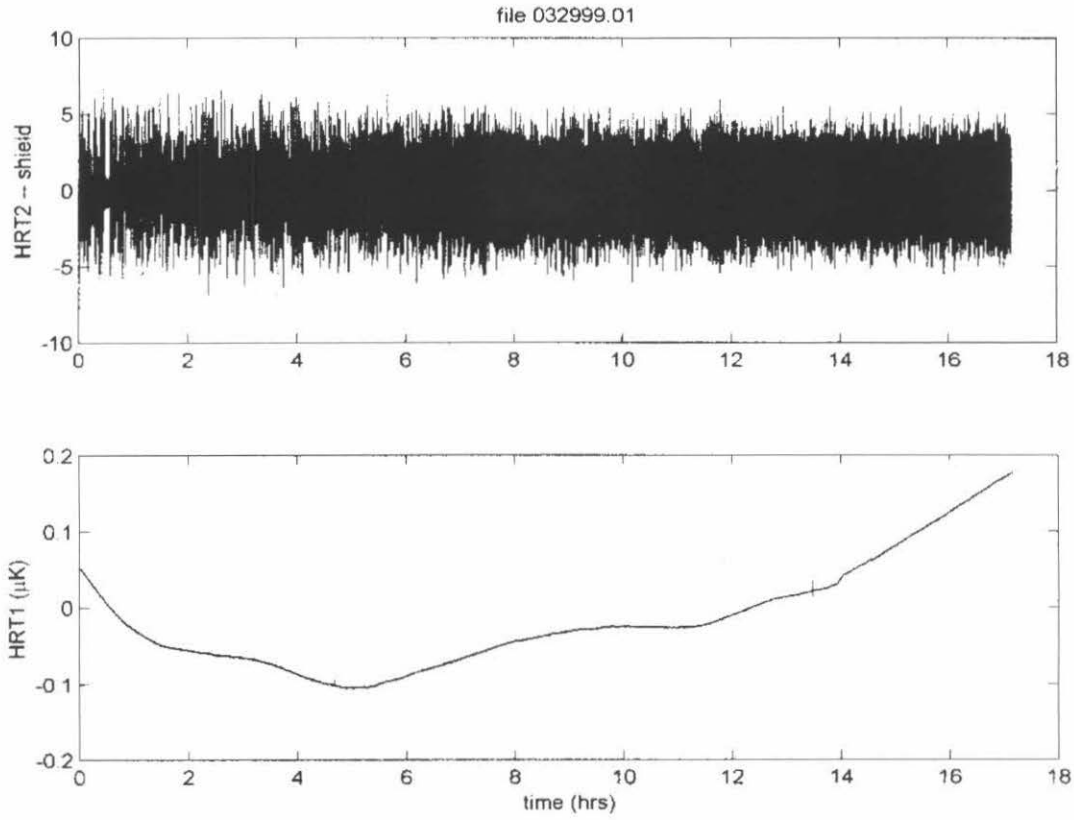

Figure 3.26: The thermal stability of our experimental system. The units of the shield (HRT2) are in ϕ_0.

3.5 Experimental configuration and interface

3.5.1 The cryostat and the computer interface

The calorimeter, shield, and thermal isolation stages were mounted inside of an aluminum vacuum can. Aluminum was used because it is non-magnetic, and therefore had a minimal impact on the functioning of the SQUIDs. A magnet was wound around the bottom of the vacuum can, directly outside the location of the HRT salt pills (see Fig. 3.19). The magnet was wound of AWG #16 copper wire with polythermalyze insulation. It was based on a design by John Lipa's group at Stanford. It was constructed to localize the field in the center of the magnet, and thereby prevent the field from affecting anything but the HRT flux tubes.[17] Because the magnet is only turned on when the field is trapped in the flux tubes, and not for the duration of the entire experiment, it is not important that the copper wires generate a fair amount of heat. The process only takes ten to twenty minutes, and therefore does not boil off a significant amount of helium. The resistance of the magnet wire is 12.5 Ω at room temperature, 2.0 Ω at 77 K, and 0.5 Ω at 4 K. Measuring this resistance was therefore an excellent way to determine the temperature of the outside of the experiment during cool-down.

The vacuum can was mounted on a probe that has stainless-steel support tubes running to a top brass plate (see Fig. 3.27). Also running between the vacuum can and the top plate were: the pumping line for the 1 K pot, the mechanical rod to shut the cell valve, four RF lines for the SQUIDs, the cell fill line, the circulator capillaries, a helium level meter, a charcoal cryopump for the fill line, and approximately 50 twisted pairs of wires used to run the heaters, GRTs, and heat switches. These wires entered the vacuum can through a hermetic Bendix connector.

All of these items were threaded through holes cut into a series of copper radiation baffles, which prevented room temperature radiation from coming down from the top plate of the cryostat. Tinfoil was epoxied around what was left of the openings in these holes to even further protect against radiation and further prolong the helium

[17] The magnet specifications are given in Appendix B.

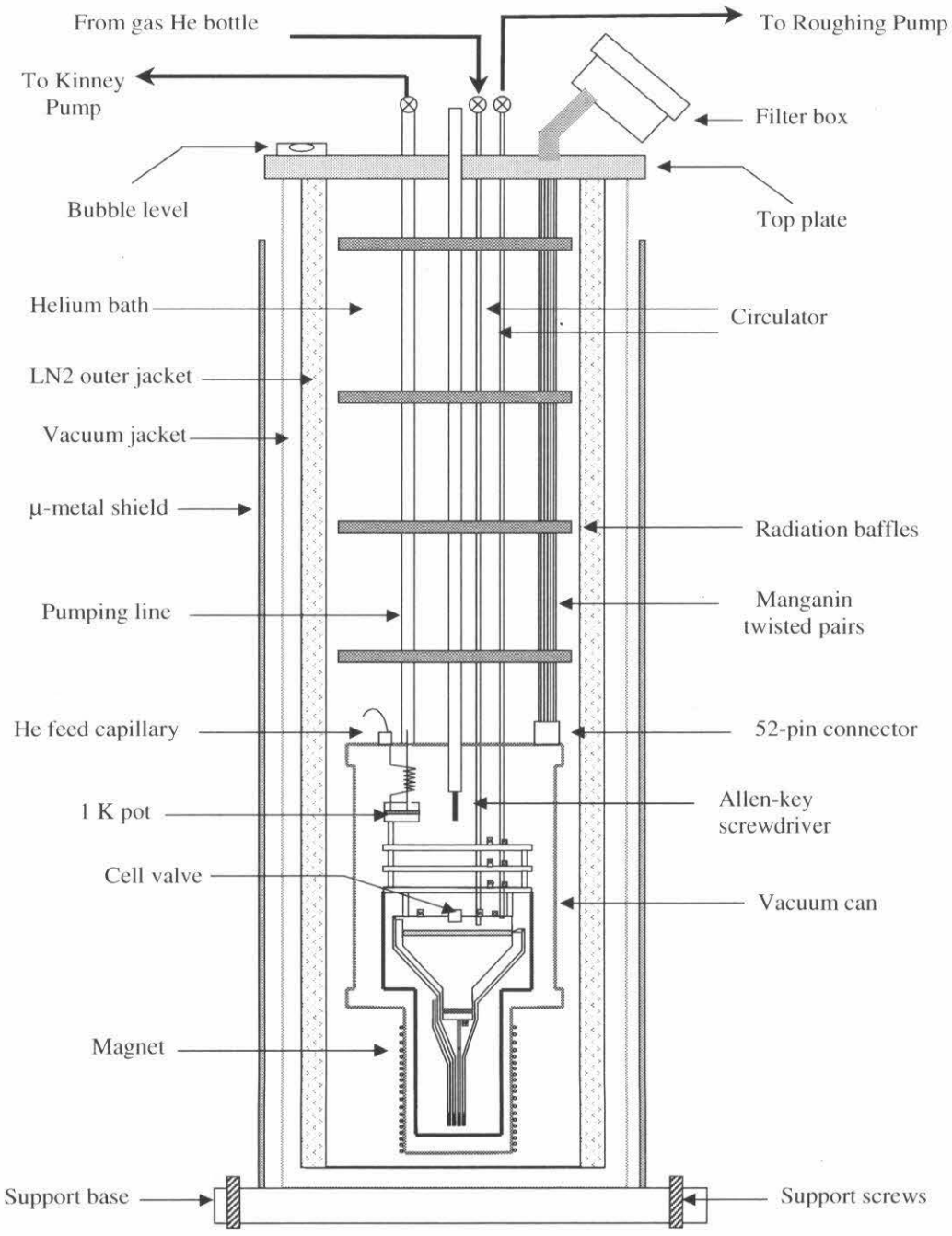

Figure 3.27: A schematic drawing of the cryostat.

bath life. The magnet leads were attached to banana plugs connected to one of the lower radiation baffles. Lead wires were only inserted to turn on the magnetic field and were removed for the remainder of the run, which prevented a strong heat leak to room temperature.

During the experiment, the probe was inserted into a helium dewar that had both an outer liquid nitrogen (LN2) cavity and an outer vacuum jacket to thermally shield the helium bath from room temperature. Surrounding the entire dewar was a double walled μ-metal shield to prevent magnetic fields from affecting the SQUIDs.

The 100 lead wires were attached to an LC filter as they entered and exited the cryostat in order to prevent RF pickup. The resonance of this circuit was 3.5 MHz, and its configuration is shown in Fig. 3.28. After leaving the filterbox, the wires ran to a breakout box. From there the wires for the GRTs and for the heater on stage 1 (H1) were attached to the QD Resistance Bridge. The bridge was attached to a National Instruments GPIB board installed on a 486 computer and controlled through a LabVIEW program. The other heater wires were attached directly to two different DAQ boards that were run from the same computer. At the breakout box, every wire was filtered by another LC filter constructed by wrapping them around a lossy ferride torus and connecting the wires of each twisted pair with a capacitor (see Fig. 3.29). The RF lines were hooked to SQUID contollers that were attached both to the DAQ boards and to the fluxcounter boards mentioned in Sec. 3.2.5.

The pumping line for the 1 K pot went to a Kinney pump located in an adjacent room. This helped to cut down on the vibration present in the room. All other lines leaving the cryostat were attached through a series of valves (shown in Fig. 3.1), and run through $\frac{1}{4}$" copper pipe to a gas handling system (shown in Fig. 3.30) that was used to supply the regular helium gas, ultra-pure helium gas, and roughing pump lines.

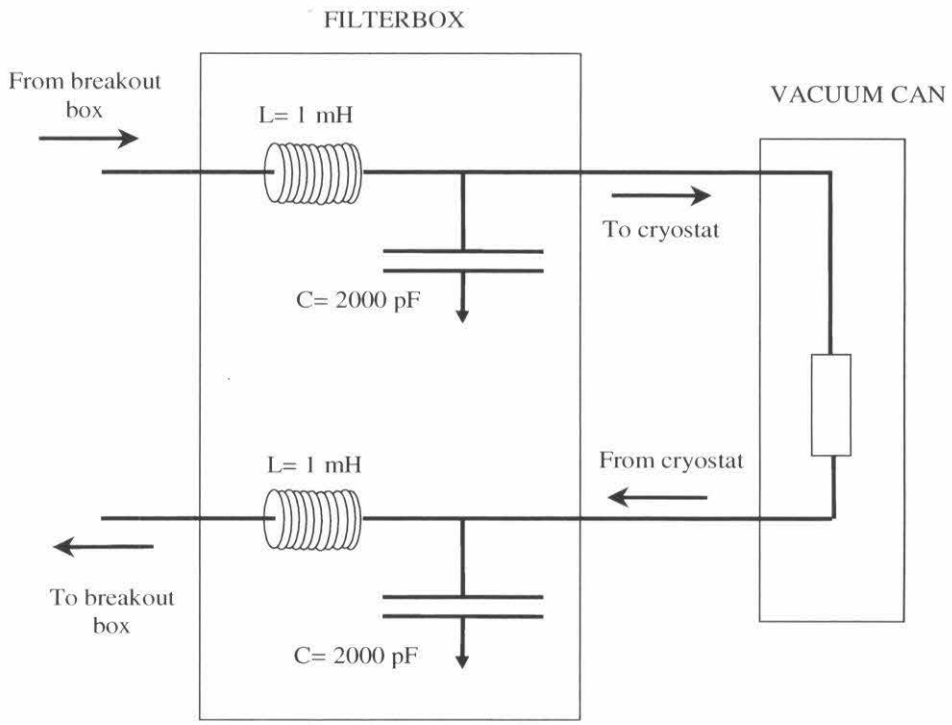

Figure 3.28: The Filterbox at the top of the cryostat. These LC filters are on every wire entering and exiting the cryostat to prevent RF pickup.

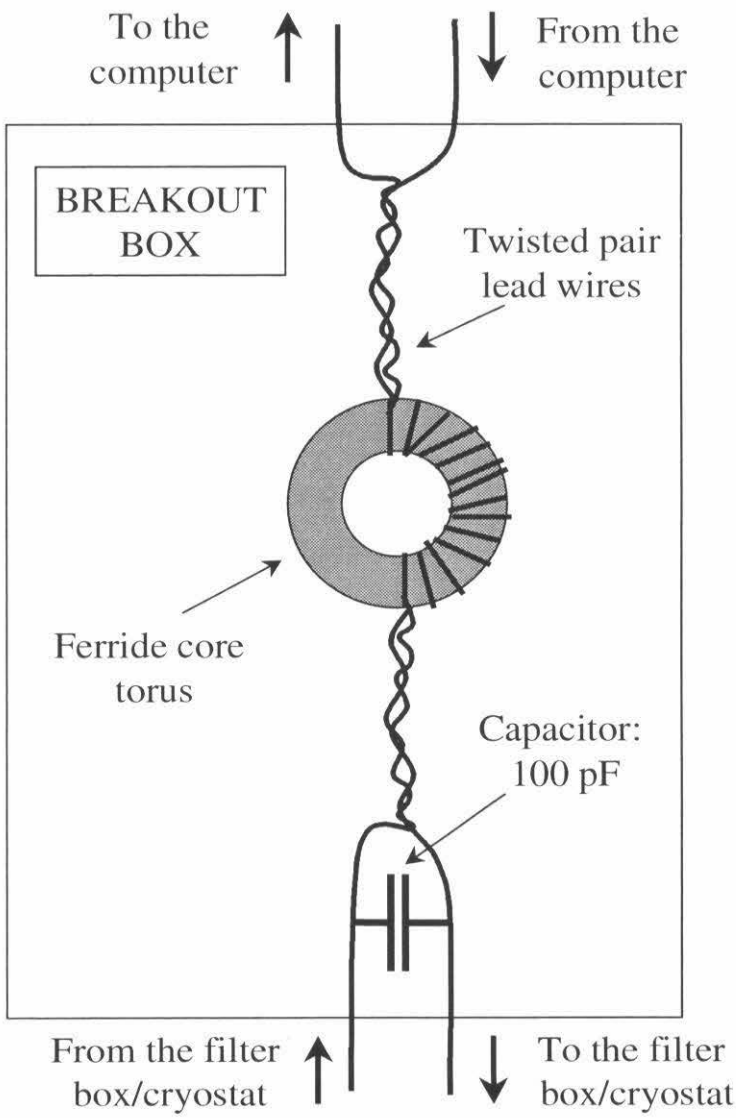

Figure 3.29: The breakout box filters. These LC filters were on every twisted pair of lead wires in the experiment.

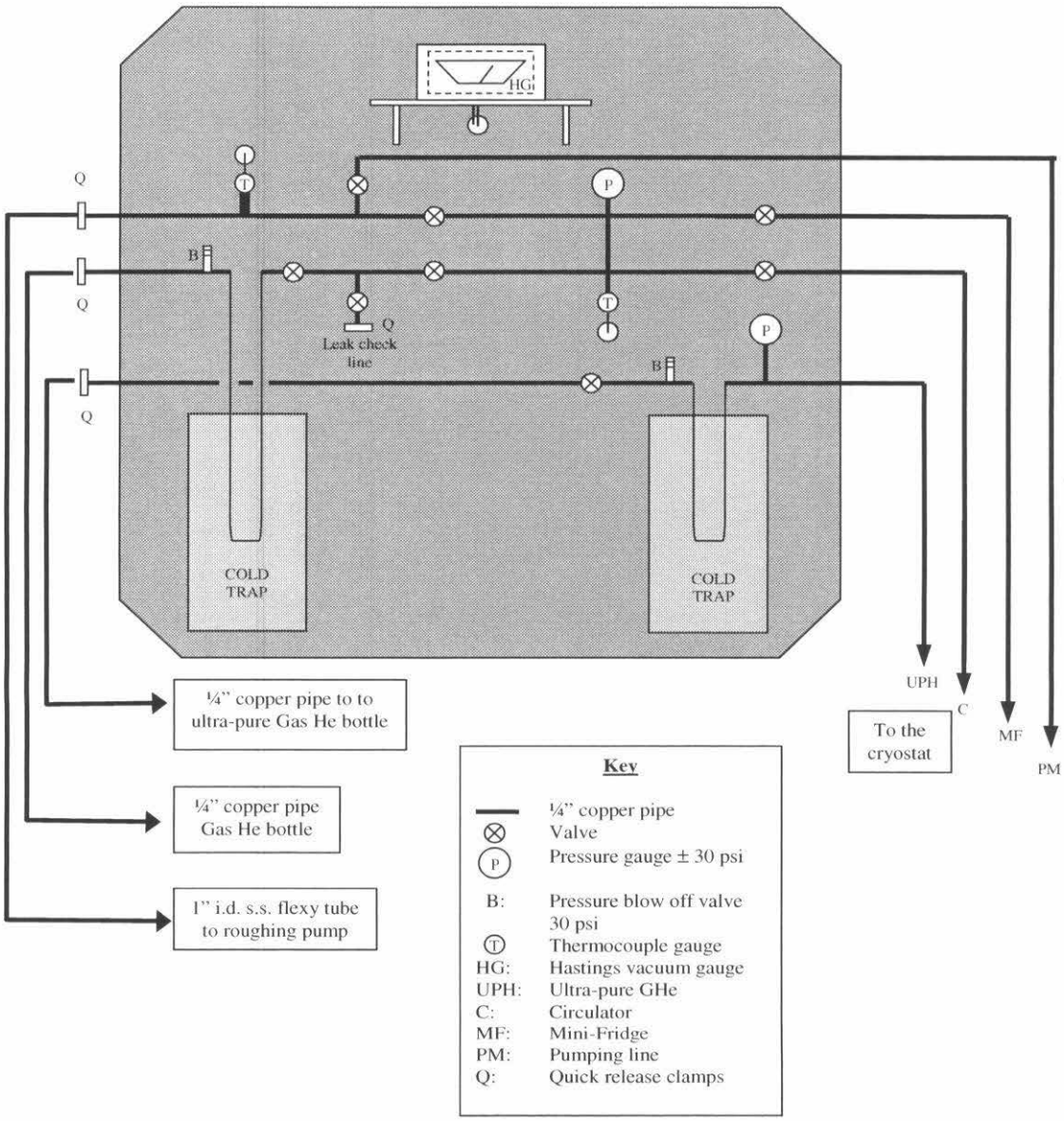

Figure 3.30: A schematic drawing of the gas handling system.

3.5.2 Vibration isolation

The temperature measurements of the HRTs were very sensitive to vibration. The cryostat itself was mounted on a piece of concrete in the sub-sub-basement of the Sloan Laboratory, on a piece of concrete that was separated from the rest of the building. General building vibrations therefore did not affect the experiment.

In-between the cryostat and the gas handling system, the $\frac{1}{4}$" copper pipes were attached to $\frac{1}{2}$" flex-tubes, and run through a large bucket of sand. This damped any vibration from the pumps or from people walking around on the floor next to the cryostat. As an added precaution, the area around the cryostat was roped off during any data runs to cut down on floor vibration.[18]

The final source of vibration came from an unexpected place. The outer LN2 jacket for our cryostat was plugged at the top and had a 2 psi blowoff valve to let out the nitrogen gas boil-off. The slight hissing of this blow-off valve was enough to cause noticeable noise in our data. To cure the problem we took off the cap to the inlet and replaced it with a U-shaped open copper pipe. So long as there was LN2 in the jacket, there was always positive pressure, and the inlet did not ice over and the noise stopped.

[18] We could actually see the noise in our data from people walking in the vicinity of the cryostat. Deliveries of LN2 dewars were particularly devastating.

Chapter 4 Experimental Methods

Three different methods were used to take heat capacity data during the course of this project: AC calorimetry, drift calorimetry, and discrete pulse calorimetry. A full set of LabVIEW programs was written to control the experiment using each method. For all data runs, regardless of method used, the heat current Q was supplied to heater 6W (see Fig. 3.19) by a current source powered by a voltage output from one of the channels of a National Instruments AT-MIO-16X 16-bit DAQ board. The heat used for the calorimetry measurement, $Q_{\rm cal}$, was supplied to heater 5W by another current source powered by a voltage output from a second channel on the same DAQ. The top stage was servoed to approximately ± 10 μK with a QD bridge controlled by LabVIEW through a National Instruments GPIB board. The temperature measurement for this servo was provided by a Lakeshore calibrated germanium resistance thermometer. The shield was servoed to approximately ± 0.2 μK with a PID program written in LabVIEW. HRT2 provided the temperature measurement for this servo, and the heat was supplied by a voltage output by a channel on a National Instruments AT-AO-6 12-bit DAQ across heater H3. The temperature of the helium sample was measured by thermometers HRT3, HRT1, and HRT0. Each experiment was run by a master LabVIEW program that coordinated the various servos, turned off and on the voltages to the heaters, read in the temperatures of all of the stages, and saved the data to disk.

4.1 Heat capacity measurement techniques

4.1.1 AC calorimetry

The first technique that we[1] used was AC calorimetry. This method has a number of advantages over other techniques: it eliminates the adverse effects of stray heat leaks, and it easily permits each data point to be averaged over long periods of time, improving the signal to noise ratio.

In this method, the sample is attached through a known thermal resistance to a bath at constant temperature [101]. For our experiment, the bath is the shield, and the thermal resistance is R_{34}. Heat is applied to the sample through a heater (5W) at the rate of $Q_{\rm cal} = Q_0 \cos\left(\frac{1}{2}\omega t\right)$, and the temperature is measured by a thermometer mounted on the calorimeter (see Figs. 3.19 and 4.1). This thermometer measures

$$T_\theta = T_{\rm shield} + \frac{1}{2} Q_0 \left[R_{34} + \frac{1}{\omega C} \cos\left(\omega t - \alpha\right) \right], \tag{4.1}$$

where $T_{\rm shield}$ is the temperature of the shield, C is the heat capacity of the sample, and α is a phase offset of little importance—so long as the following experimental conditions are met:

1. The heat capacity of the sample is much larger than the heat capacities of the thermometer and the heater;

2. The thermal resistances between the sample and the heater, thermometer, and bath do not change as a function of time;

3. $\omega\tau_s >> 1$, where τ_s is the relaxation time of the sample;

4. The relaxation times of the heater and the thermometer, τ_h and τ_θ, are extremely short compared to the frequency ω.

[1] Although I was the only one who took discrete pulse calorimetry data, at various times during this project, Talso Chui and Richard Lee were involved in the execution of the experimental procedures, and the whole group was involved in making decisions concerning the experiment. I am therefore using the plural for all active and passive experimental actions.

The magnitude of the sinusoidal component of the temperature oscillation is $T_0 = Q_0/(2\omega C)$, so the heat capacity of the sample can be determined by measuring T_0:

$$C = \frac{Q_0}{2\omega T_0}. \tag{4.2}$$

The heat capacity, C, is averaged over the temperature range of the oscillation.

The initial results of our attempt at AC calorimetry gave rather baffling results. The amplitude of the AC temperature signal seemed to indicate that the heat capacity of our cell was significantly different than we expected. It appeared, in fact, to be even smaller than the well-known heat capacity of ^{4}He in the absence of a heat flux. As it would turn out, this strange result was due to the fact that our midplane thermometer was shorted to the top plate of the cell, and was therefore being influenced by the singular Kapitza resistance at the top boundary. Since the magnitude of this resistance changes as a function of temperature, condition (2) of the above experimental requirements was violated, and (4.2) was not an accurate formula for the heat capacity. We would not discover that this was our problem until we tried other calorimetry methods that were somewhat more straightforward to interpret.

4.1.2 Drift calorimetry

We next turned to the drift calorimetry technique. Like the AC method, the drift method also easily allows the data to be averaged over many cycles.

The standard technique

For this technique, the shield temperature is controlled so that the temperature of the helium sample drifts downwards at several nK/sec. The temperature range of the experiment is defined by a minimum temperature, $T_{\rm min}$, and a maximum temperature, $T_{\rm max}$.

The temperature is permitted to drift down until it reaches $T_{\rm min}$. When it falls below $T_{\rm min}$, another heat current, $Q_{\rm cal}$, is supplied to the sample. The magnitude of $Q_{\rm cal}$ is chosen so that when it is applied, the temperature of the helium drifts

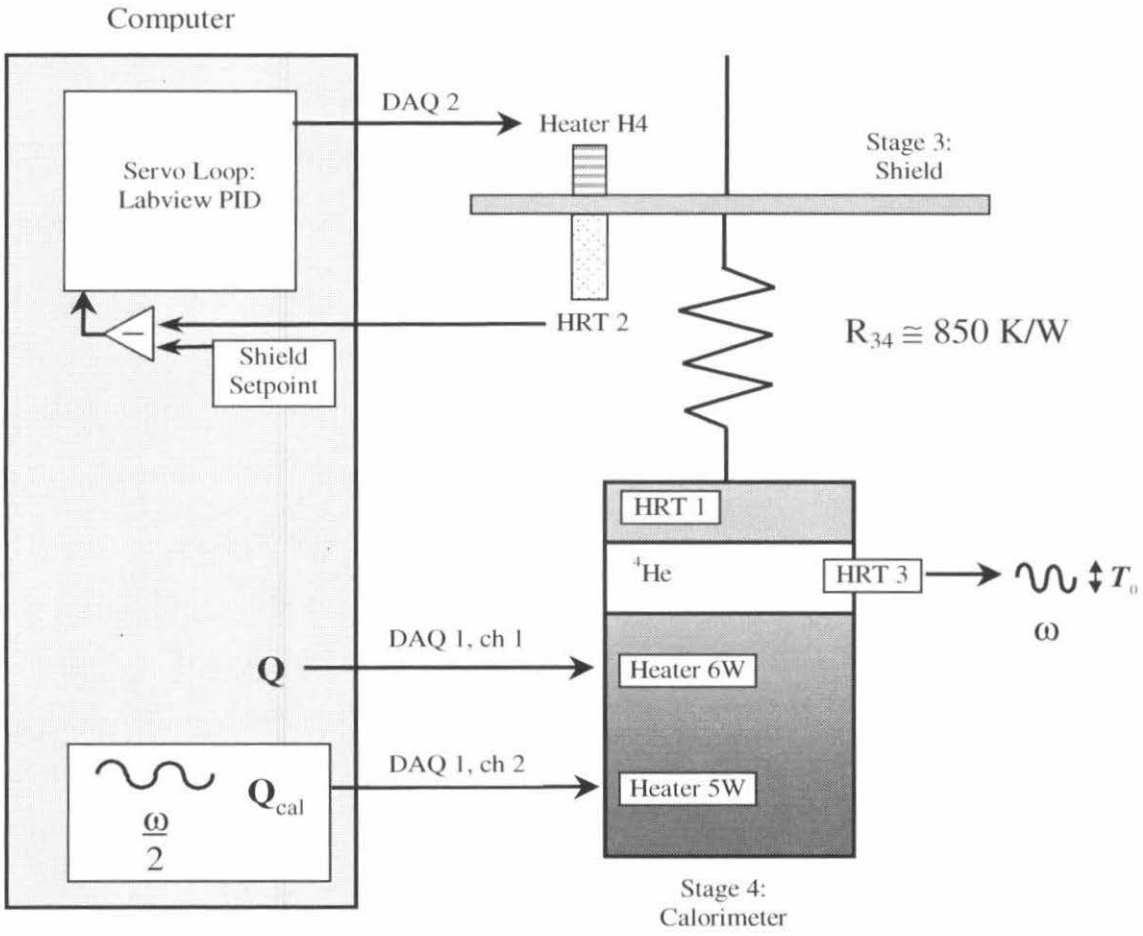

Figure 4.1: Schematic of the AC method of heat capacity measurement. A heat flux, Q, is supplied to the bottom of the cell. The temperature of the shield is controlled to ± 0.2 μK. A sinusoidal heat current, $Q_{\rm cal} = Q_0 \cos\left(\frac{1}{2}\omega t\right)$, is supplied to the bottom of the cell, causing the sample temperature to oscillate with frequency ω. The amplitude of the oscillation, T_0, is inversely proportional to the heat capacity C.

upwards at several nK/sec. It is allowed to drift upwards until it reaches $T_{\max}$. At that point, $Q_{\rm cal}$ is turned off, and the temperature once again drifts down to $T_{\min}$. This process is repeated 5-10 times so that the data can be binned and averaged. The shield temperature remains unchanged throughout the measurement. (See Figs. 4.2 and 4.3.)

The heat capacity can be easily derived. On the downward ramp, when only Q is applied to the bottom of the cell,

$$Q = \frac{T - T_{\rm shield}}{R} + C(T)\left(\frac{dT}{dt}\right)_{\rm down}, \tag{4.3}$$

where T is the temperature of the sample, $T_{\rm shield}$ is the temperature of the shield, R is the thermal resistance between the top of the calorimeter and the shield (in our case $R = R_{34}$), and $C(T)$ is the heat capacity of the sample. On the upward ramp, when $Q_{\rm cal}$ is also turned on,

$$Q + Q_{\rm cal} = \frac{T - T_{\rm shield}}{R} + C(T)\left(\frac{dT}{dt}\right)_{\rm up}. \tag{4.4}$$

Since the shield temperature is kept constant throughout the measurement, the heat capacity is found by subtracting (4.3) from (4.4),

$$C(T) = \frac{Q_{\rm cal}}{(dT/dt)_{\rm up} - (dT/dt)_{\rm down}}. \tag{4.5}$$

A variation on the standard technique

For our experiment, $T_{\min}$ and $T_{\max}$ were chosen in relation to $T_{\rm DAS}(Q)$. $T_{\min}$ was chosen to be 3-5 μK below $T_{\rm DAS}(Q)$, and $T_{\max}$ was chosen to be just above $T_{\rm DAS}(Q)$. A heat current Q was applied to heater 6W at the very beginning of the experiment. One up-down ramp sequence was taken with Q applied.

In order to compare the specific heat at constant heat flux with the well-known static specific heat, Q was slowly turned off at the end of the first ramp, and another ramp sequence was taken in the absence of a heat flux. Q was turned off and on in between every up-down ramp sequence (see Fig. 4.3). It was this particular technique

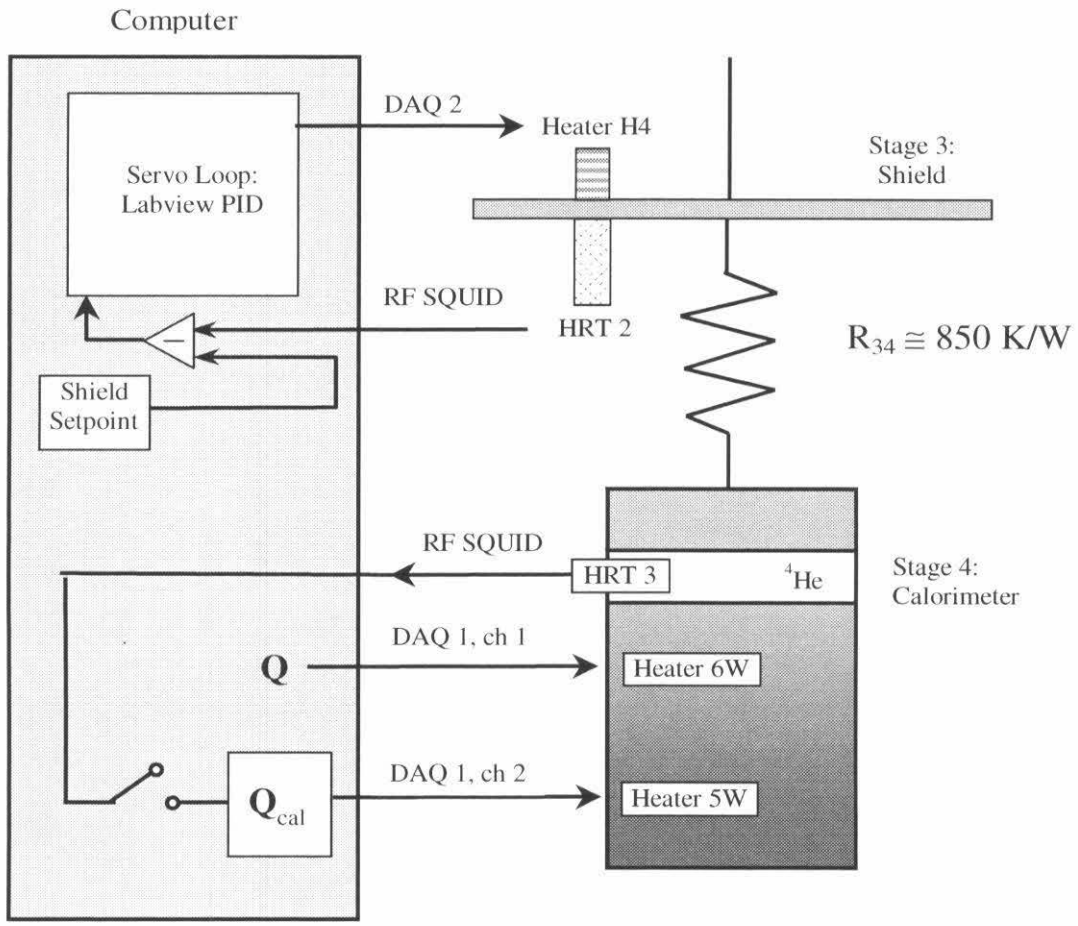

Figure 4.2: Schematic of the drift method of heat capacity measurement. A heat flux, Q, is supplied to the bottom of the cell. The temperature of the shield is controlled to ± 0.2 μK at a temperature chosen so that, with Q applied, the temperature of the sample is within several μK of $T_{\rm DAS}(Q)$ and drifts downwards at ~ 5 nK/sec. Once the temperature reaches a fixed temperature $T_{\rm min}$, located ~ 5 μK below $T_{\rm DAS}(Q)$, a second heat current, $Q_{\rm cal}$, is supplied to the bottom of the cell. The magnitude of $Q_{\rm cal}$ is chosen so that the temperature of the sample drifts upwards at ~ 5 nK/sec. When the sample temperature reaches a fixed temperature, $T_{\rm max} \sim 1$ μK above $T_{\rm DAS}(Q)$, $Q_{\rm cal}$ is turned off. The temperature of the sample then once more drifts downwards, and the process is repeated indefinitely.

that uncovered the fact that the mid-plane thermometer was shorted to the top plate. The specific heat measurements taken at zero heat flux were in excellent agreement with measurements in the literature [2]. However, when a heat flux was applied, the temperature scale appeared to shift relative to the temperature scale for the $Q = 0$ measurements (see Fig. 4.4). It was, in fact, shifted as a direct result of the Kapitza resistance between HRT3 and the sample.

If the temperature shift were due only to the uniform offset of the regular component of the Kapitza resistance, we could have continued to use the drift method to pursue heat capacity results. In that case, the heat capacity data would have been accurate, only shifted in temperature. The singular component of the Kapitza resistance, however, is a function of temperature. Therefore:

$$\frac{dT_\theta}{dt} = \frac{dT_{\mathrm{He}}}{dt} + \left(\frac{d\Delta T_b}{dT_b}\right)\left(\frac{dT_b}{dt}\right), \tag{4.6}$$

where T_θ is the temperature measured by HRT3, T_{He} is the helium temperature, ΔT_b is the temperature drop due to the singular Kapitza resistance, and T_b is the boundary temperature described in Sec. 3.1.2. Extracting dT_{He}/dt from the measurement of T_θ to determine the heat capacity of the sample from the data is extraordinarily difficult, if not impossible.

4.1.3 Discrete pulse calorimetry

With this discovery, we finally we abandoned our so-called 'mid-plane' thermometer and turned to the discrete pulse calorimetry method. This method is extremely simple. A single heat pulse, ΔQ_{cal}, is injected into the sample, and the resulting discontinuity in the temperature, ΔT, gives the heat capacity:

$$C = \frac{\Delta Q_{\mathrm{cal}}}{\Delta T}. \tag{4.7}$$

Stray heat leaks can cause some error, but this effect can be minimized by extrapolating the temperature trajectories both before and after the discontinuity to the

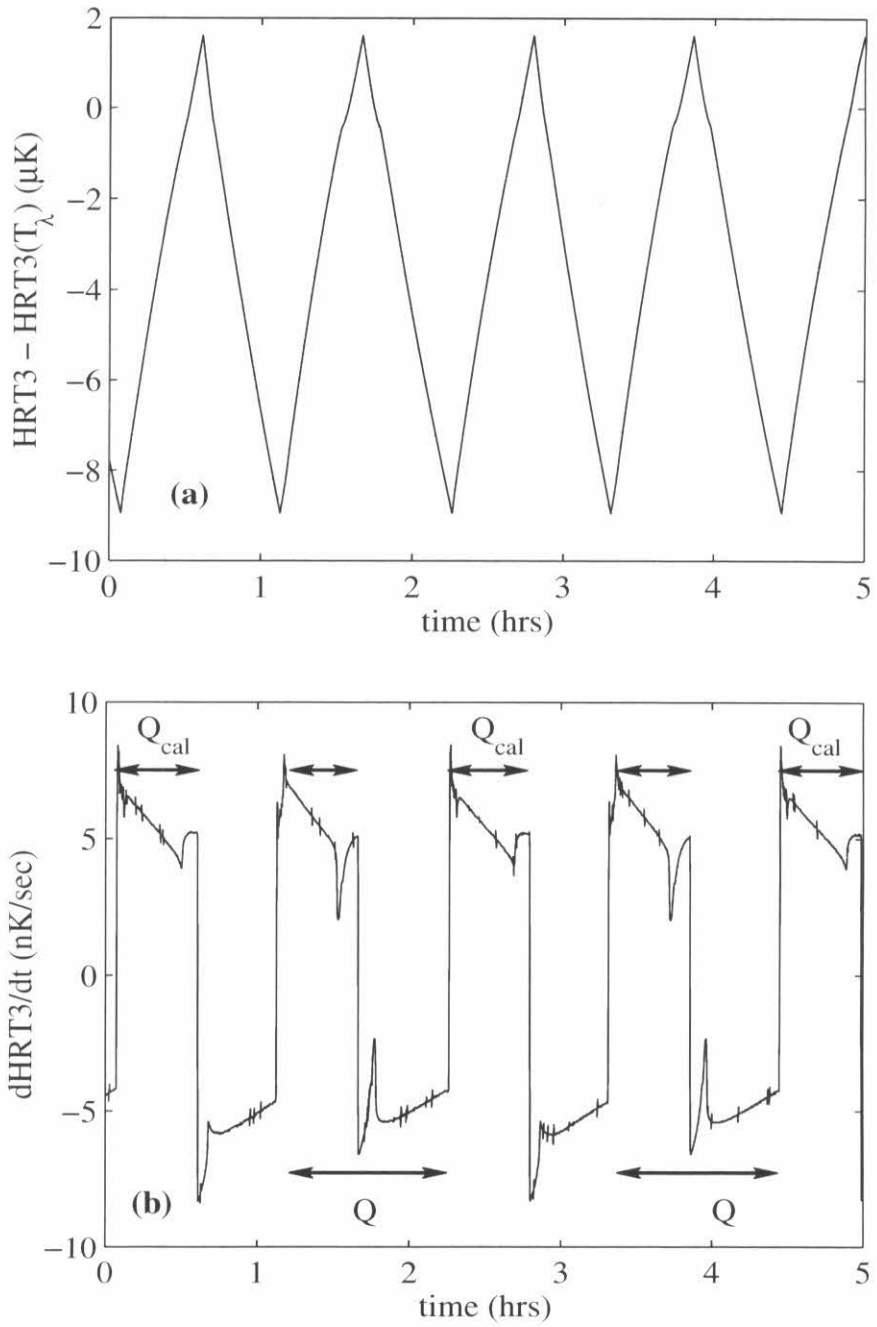

Figure 4.3: Data taken with the drift calorimetry method at $Q = 0.243\ \mu\mathrm{W/cm}^2$ (from file 011498.01). (a) The temperature read by HRT3. (b) The derivative of HRT3. The range of data over which Q and Q_{cal} are applied are marked by arrows and labeled. The small spikes are due to electronic noise, and were removed during the final data analysis. The procedure used to clean the data will be described in Sec. 5.1.3.

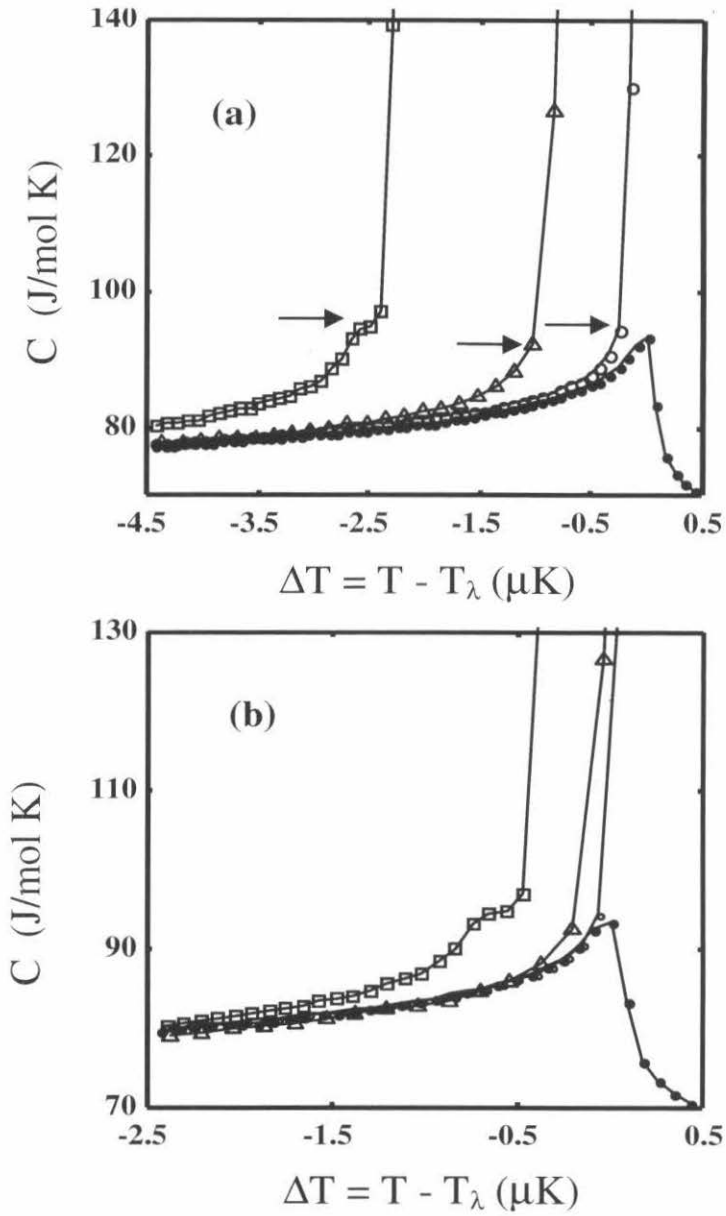

Figure 4.4: Specific heat data taken with the drift method. The data are taken with the mid-plane thermometer. Files at non-zero Q are affected by a Kapitza resistance and do not give valid readings. Solid circles: no heat flux. Open circles: $Q = 0.243\ \mu\mathrm{W/cm^2}$. Triangles: $Q = 1.12\ \mu\mathrm{W/cm^2}$. Squares: $Q = 3.58\ \mu\mathrm{W/cm^2}$. (a) Unshifted data. Arrows indicate where dissipative fluid enters the cell. (b) The data shifted in temperature to adjust for boundary resistance. (A version of this figure was published in Harter, Lee, Chui, and Goodstein [102], Fig. 2.)

middle of the pulse. The error will be negligible if:

1. The temperature of the sample has minimal drift before the pulse;

2. The time constant of the system is extremely long, so that the temperature drift after the pulse is also small.

Both of these conditions were easily met for our experiment. We not only had excellent thermal control to satisfy condition (1), but the time constant of our sample was $\tau = RC \approx 8,640$ sec $= 2.4$ hrs, which clearly satisfies condition (2).

As in the AC technique, the heat capacity value expressed in (4.7) is averaged over the temperature range of ΔT. The magnitude of ΔQ should therefore be chosen so that the resulting ΔT is much smaller than the temperature range of any expected features in the data. However, for a decent signal to noise ratio, ΔT also needs to be significantly larger than the noise of the thermometers. These problems were not significant for our experimental system: the noise of our thermometers was extremely low, and we were trying to observe a strong divergence—not subtle details in the data.

We applied a pulse of approximately 20 μAmps across a 36.963 Ω resistor (heater 5W) for 500 msec. This injected ~ 0.7 μJ into the sample, resulting in a temperature step of $\sim$ 100 nK. In retrospect, this was slightly larger than ideal. Since it was performed on earth, our experiment had an intrinsic rounding due to gravity. For our cell, this averaging was over the temperature range $\delta T \sim 1.27$ μK/cm $\times$ 0.064 cm $=$ 81 nK. If we had matched the rounding due to $\Delta Q_{\rm cal}$ to the rounding due to gravity, then minimal information would have been lost.

4.1.4 Modified discrete pulse calorimetry

Because of the large time constant of our system, the difference in the temperature drift rates on either side of a single heat pulse was extremely small [see Fig. 5.6(a)]. However, after multiple pulses, the system became noticeably out of equilibrium, and the drift rates before and after the pulses increased accordingly. To combat

this problem, we did not keep the shield temperature constant throughout the entire temperature range of our measurement.

The initial shield setpoint was chosen so that, with Q applied, the temperature of the sample was $\sim 3-5$ μK below $T_{\rm DAS}(Q)$, and had a drift rate less than 0.1 nK/sec. After this drift rate was established, the cell temperature was measured for one to two minutes. The first heat pulse was then applied, and the temperature was measured for another one to two minutes without changing the shield temperature. At the end of the two minutes, the shield temperature was adjusted to null the drift rate of the sample [see Fig. 5.6(b)]. When the drift rate was measured to be anomalously large as compared to a pre-defined cutoff value, the shield correction was not executed. This prevented the control program from dumping alot of heat into the system after reading a flux jump[2] (or jumps), caused by electronic noise, and averted thermal disaster.

The heat flow equations imply that the correct amount to raise the shield temperature to null the drift rate is:

$$\Delta T_{\rm shield} = \Delta T_{\rm He} - RC\left(\frac{dT_{\rm He}}{dt}\right), \tag{4.8}$$

where $\Delta T_{\rm He}$ is the temperature step height due to the pulse, R is the thermal resistance between the sample and the shield (R_{34}), and C is the heat capacity of the sample. However, because $\tau = RC$ is so large for our system, the first term can be ignored. Therefore, the shield temperature should be raised by

$$\Delta\Phi_{\rm shield} = f\,\overline{\frac{d\Phi_{\rm He}}{dt}}, \tag{4.9}$$

where $\overline{d\Phi_{\rm He}/dt}$ was the average drift rate before adjustment, measured in ϕ/sec. Therefore, $f \simeq R_{34}C\cdot(\kappa_{\rm shield}/\kappa_{\rm He})$, where $\kappa_{\rm shield}$ is the conversion rate of the shield thermometer, HRT2, in ϕ_0/K, and $\kappa_{\rm He}$ is the conversion rate of whichever HRT was

[2]Flux jumps will be discussed in more depth in the data analysis chapter. They are essentially unitary jumps in the count of the flux counter board that are caused by RF noise. They can be easily removed in data analysis, but are more difficult to account for when corrections are done in real time.

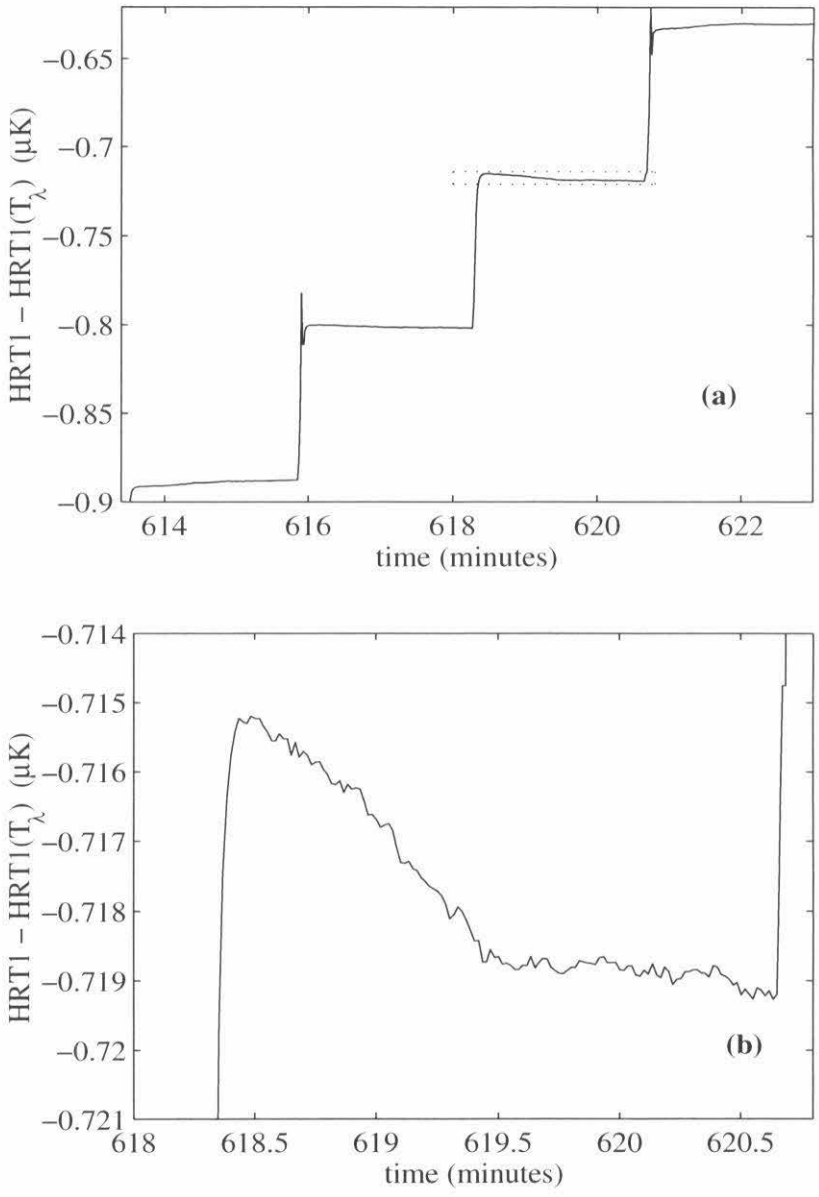

Figure 4.5: Data taken with the discrete pulse calorimetry method at $Q = 3.7\ \mu\mathrm{W/cm^2}$ (from file 022399.01). (a) A sequence of three pulses. (b) One pulse. This plot is the area enclosed by the box in (a). This pulse had an unusually large drift rate after the pulse, and therefore illustrates how changing the shield temperature after the pulse is very effective in nulling the sample drift rate. It should also be noted that although the after pulse drift rate looks quite steep on the scale of plot (b), it is still very small compared to the pulse height, as can be seen on the scale of plot (a).

used to measure the drift rate of the helium temperature (for most runs HRT3 was used). Although all of the HRT conversion factors remain more of less constant over the range of several μK, they vary significantly over a range of one or two mK. The calorimeter stage HRT conversion factor, κ_{He}, was therefore the same for all runs. However, since the shield setpoint temperature was altered in proportion to Q, the shield conversion factor, κ_{shield}, changed significantly from one run to the next. Therefore, f was different for all runs taken at a distinct values of Q, and was empirically determined for each data run.

After the shield was adjusted to null the drift rate, the temperature was measured for another two minutes, and the process began again. The entire sequence, illustrated in Figs. 4.7 and 5.6 was:

1. Take temperature data for two minutes;
2. Inject a heat pulse into the sample;
3. Take data for another two minutes, holding the shield temperature at the same setpoint as it was before the pulse;
4. Adjust the shield setpoint to null the drift rate;
5. Return to step (1) and repeat until the cell temperature is above $T_{\mathrm{DAS}}(Q)$.

One of the disadvantages of the discrete pulse method is that the technique does not easily permit averaging. In order to combat this problem, we repeated the sequence listed above 5-10 times per run. After the temperature of the sample, T_{He}, went above $T_{\mathrm{DAS}}(Q)$, the shield temperature was lowered so that T_{He} began to cool at a rate of 0.1-1 nK/sec. This slow rate ensured that the thermometers would stay within calibration. Because we were also limited to 15 hour data runs, and we wanted to average as many times as possible, we did not switch Q off and on during the discrete pulse data runs. Instead, we measured the $Q = 0$ heat capacity data on separate runs several times throughout the cooldown (see Appendix C). All $Q = 0$ files were

in excellent agreement with one another (and with previously published measurements [2]), indicating that none of the relevant experimental parameters changed significantly over the course of the run.

4.2 Cooldown details

The first step for every cooldown was the same as for every other low-temperature physics experiment: get the sample to 4 K without vacuum can leaks, electical shorts, or plugged capillaries. When this was ultimately accomplished, the next step was to characterize the experimental system. We:

1. Determined the thermal network of the system. This was done by applying various heat currents to the system with heater 6W and measuring the resulting changes in temperatures of the various stages;

2. Measured the attributes of the 1 K pot. We determined both its base temperature and total cooling power. This indicated the maximum heat current that could be passed through the system while the cell temperature was near T_λ;

3. Measured the heat capacity of the empty cell. This was done using the standard discrete pulse technique.

4.2.1 Calibrating the HRTs and filling the cell

Once the general characteristics of the system were determined, the next step was to put in the magnetic field and then calibrate the thermometers, as was described in Sec. 3.2.5. This had to be done before the cell was filled, since freezing the magnetic field into the flux tubes required raising the temperature of the system above 9 K, the transition temperature of niobium. A closed cell of helium tends to react poorly (or more precisely, explosively) to these sorts of temperatures.

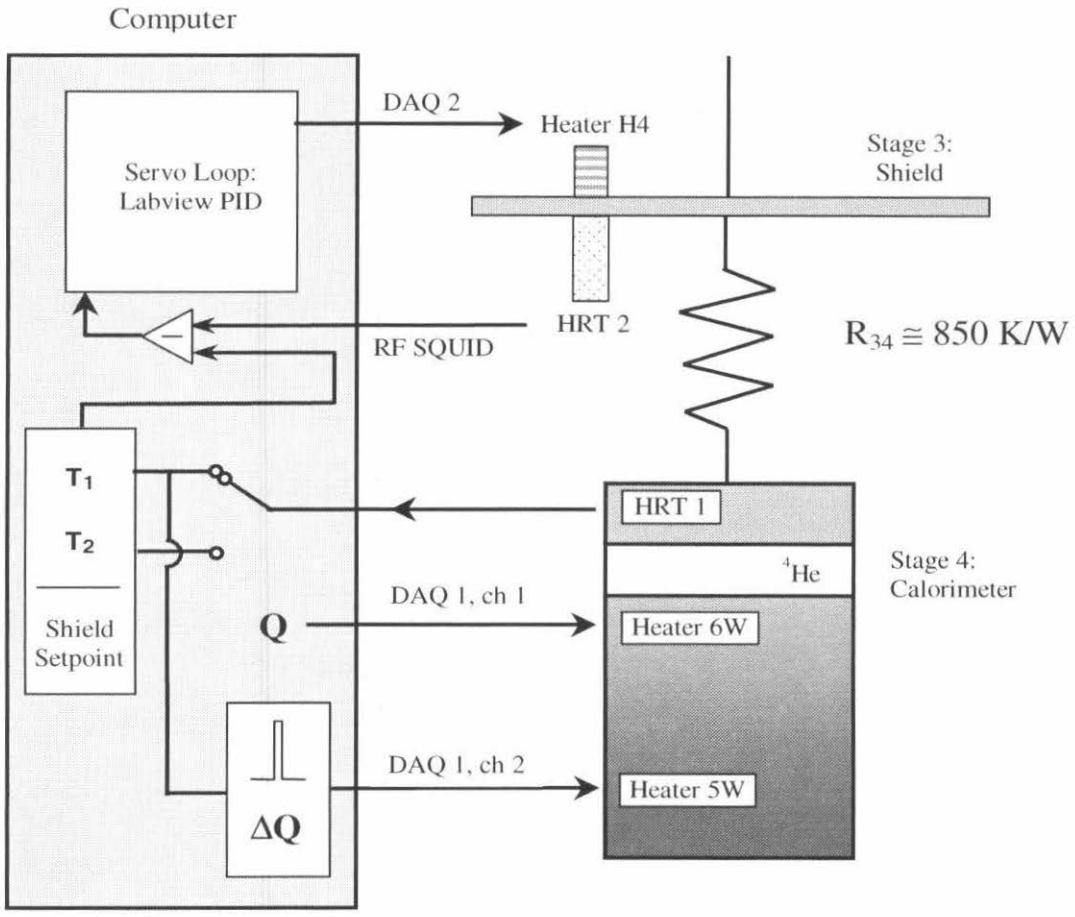

Figure 4.6: Schematic of the discrete pulse heat capacity measurement used in our experiment. A heat flux, Q, is supplied to heater 6W. The temperature of the shield is controlled to within ± 0.2 μK of a temperature T_1, a temperature chosen so that the temperature of the sample is approximately $3-4$ μK below $T_{\mathrm{DAS}}(Q)$ with a drift rate less than 10^{-11} K/sec. A pulse train is supplied to heater 5W. Once the temperature reaches a fixed temperature T_{max} located approximately 1 μK above $T_{\mathrm{DAS}}(Q)$, the pulse train is discontinued, and the shield temperature setpoint is lowered to a temperature T_2, chosen so that the helium cools at a rate of $5-10$ nK/sec. When the temperature reaches the initial temperature of the measurement, the shield setpoint is returned to its original value, and the pulse train is resumed. This process is repeated a number of times for every run.

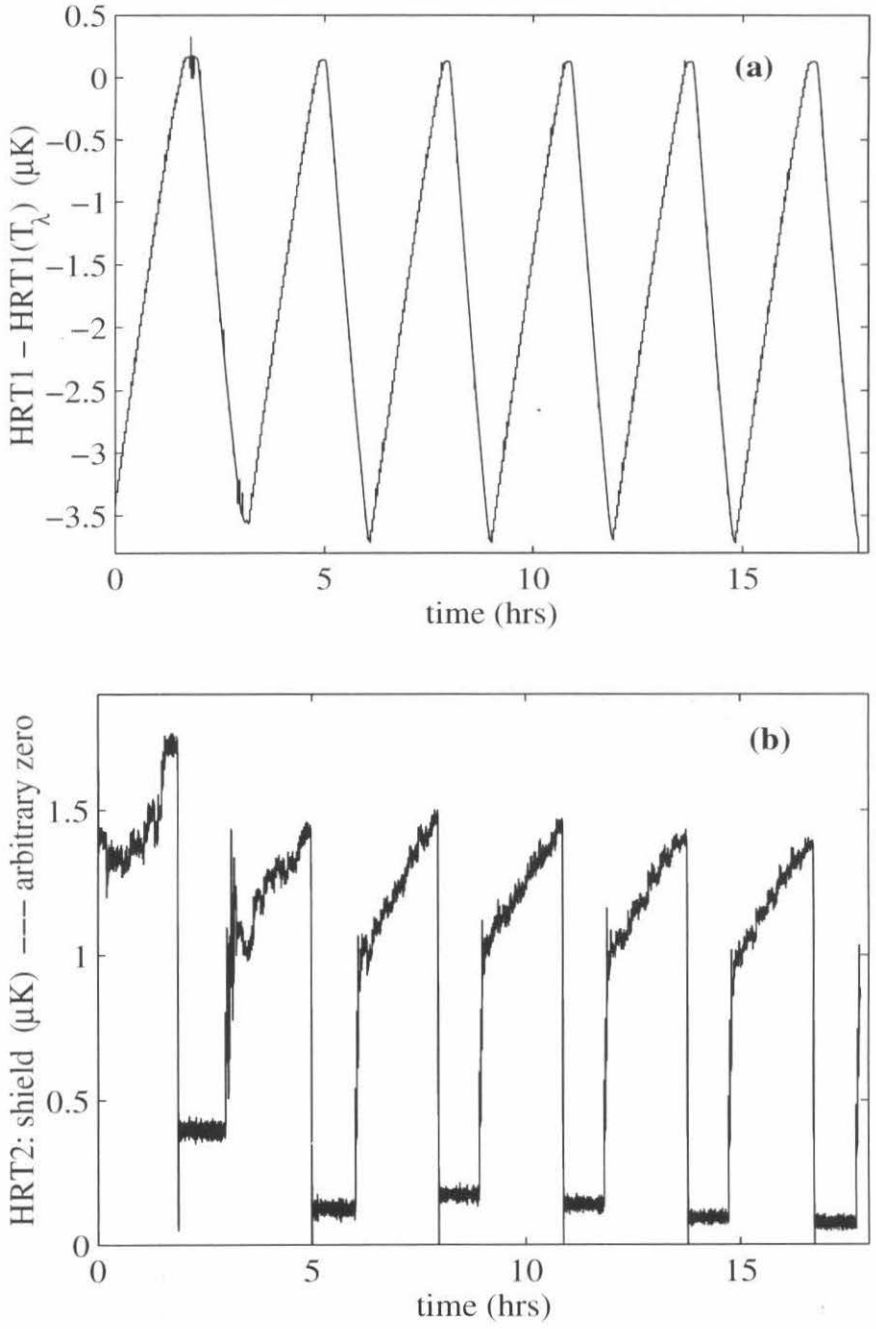

Figure 4.7: Data taken with the discrete pulse calorimetry method at $Q = 3.7\ \mu\mathrm{W/cm^2}$ (from file 022399.01). (a) The entire run measured by the top thermometer, HRT1. (b) The shield temperature throughout the run. The uneveness of the shield adjustment on the first two ramps occurred when electronic noise caused flux jumps in the thermometers. This problem will be discussed further in the next chapter.

Filling the cell

After the HRTs were satisfactorily calibrated, the calorimeter was filled with isotopically pure ^{4}He, with a ^{3}He concentration of only 0.07 parts per billion ($X = [^3\text{He}]/[^4\text{He}] = 7 \times 10^{-11}$). Although the effect of ^{3}He contamination on $T_c(Q)$ is not known, its effect on T_λ has been measured [103] to be $dT_\lambda/dX = -1.4$ K. If the effect on $T_c(Q)$ is of comparable magnitude, a concentration of $X = 0.07$ ppb would not affect our results. In fact, it can be argued that, in our range of Q, t and X, the effect of the heat flux would be to sweep the ^{3}He out of the cell, producing a film of less than a single monolayer at the cooler endplate. Therefore, with respect to ^{3}He impurities, the heat flux may actually improve the precision of the measurement, making isotropically pure helium unnecessary. However, it never hurts to be over-cautious, so we used it anyway.

Before filling the cell, we flushed the room temperature pipe work three times with ultra-pure ^{4}He to make sure there were no lingering contaminants. We then opened the regulator (valve 7 in Fig. 4.8[3]) to 3 psi, and then opened the valve at the top of the cryostat (valve 2). We wanted to make sure that our measurements were at saturated vapor pressure (SVP), so we had to make sure to fill the cell with just enough helium so that it would be nearly, but not completely, filled at the lambda temperature. Because the molar volume of helium decreases with increasing temperature in the superfluid region, this requirement would be met so long as we filled the cell at a temperature above T_λ. Since a large bubble would distort the heat flow, we also wanted to make sure that we didn't put in too little helium. Ideally, we wanted to fill the cell with just enough helium so that the bubble would completely occupy the 'dead volume' of the cell. From the curve of molar volume versus temperature [104], we found that if we filled the calorimeter at 2.67 K, we would have a bubble filling 0.1% of the cell volume at T_λ. We aimed below the 'dead volume' percentage of 0.95% since we knew that the action of the mechanical plunger would heat up the cell, forcing some of the helium into the fill line, and decreasing the helium fill factor

[3]For the remainder of this chapter, valve numbers will refer to the valve numbers labeled in Fig. 4.8.

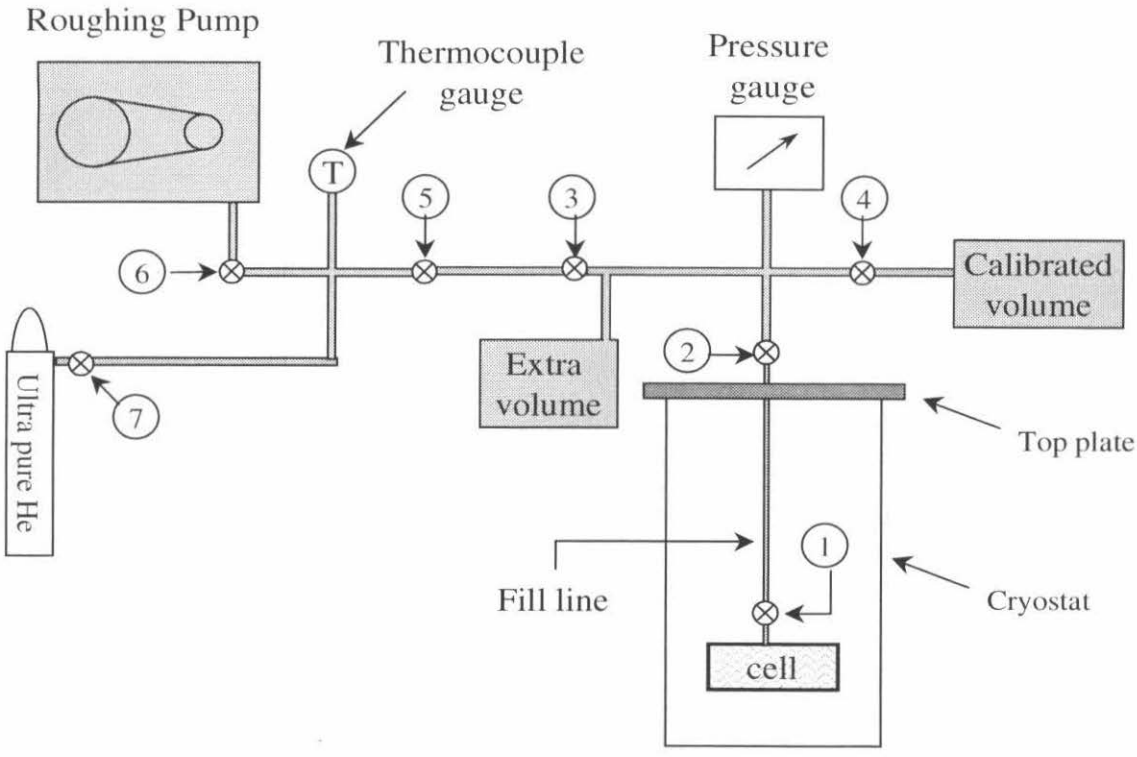

Figure 4.8: The cryostat configuration used to fill the cell before the run and extract the helium after the run. The 'calibrated volume' and 'extra volume' were only present during helium extraction.

below the 'target'.

While the fill line was open to the ultra-pure bottle of helium, we servoed the cell temperature to 2.67 K. When we had confirmed that the cell was filled by checking that the pressure of the fill line no longer dropped when the valve to the helium bottle (valve 7) was closed off, we shut the valve at the top of the cryostat (valve 2) to prevent helium from escaping when we closed the cell valve (valve 1). We then shut the valve to the cell by rotating the turnrod with 25 lb-in of torque. This mechanical action raised the temperature of the cell to 4.34 K, forcing some fraction of the helium in the cell into the fill-line. We pumped out the fill-line until it no longer gave a detectable reading on the leak-detector. We then opened it up to a charcoal cryopump for the duration of the run, where it maintained a pressure less than 10^{-3} torr.

The bubble hunt

In order to determine exactly how much helium we had in our cell, we followed a procedure very similar to that used in the HRT calibration, which we affectionatly termed 'the bubble hunt'. We used a LabVIEW program to slowly ramp the temperature of the cell from 2.7 K to 1.8 K over a 20 hour period (an average rate of 12.5 μK/sec or 1.08 K/day). We hooked up the HRT heat switches (described in Sec. 3.2.5) to a DAQ, and automatically fired them every 20 minutes.

The molar volume of helium has a minimum at approximately 6 mK above T_λ, causing the volume occupied by the helium to change as a function of temperature. Therefore, as the liquid is heated above the transition, if the bubble is small enough, it will eventually disappear, filling the entire cell with helium. At this point, the heat capacity of the sample changes from C_{SVP} to C_{V}, and the heating rate of the helium also changes. Therefore, the temperature drift rate will exhibit a slope change when the bubble disappears (see Fig. 4.9). When the sample is cooled as opposed to heated, in addition to the slope change, there will also be an actual jump in the temperature due to the heat released when the bubble is formed. By observing at what temperature this discontinuity occurs, and matching it with the appropriate molar volume, it is possible to determine how much helium is in the cell, and therefore how large a bubble will exist at T_λ during the measurements.

The temperature discontinuity during our bubble hunt occurred at 2.371 K. The molar volume of helium, V_m, at this temperature is approximately 27.530 cm^3/mol, indicating that during our experiment, the bubble size would be:

$$\frac{V_{\mathrm{bubble}}}{V_{\mathrm{cell}}} \approx 1 - \frac{V_m\,(2.1768\ \mathrm{K})}{V_m\,(2.371\ \mathrm{K})} = 1 - \frac{27.530}{27.287} \approx 0.005. \tag{4.10}$$

Therefore, our bubble would occupy approximately 0.5% of the cell, or slightly less than the 'dead volume'.

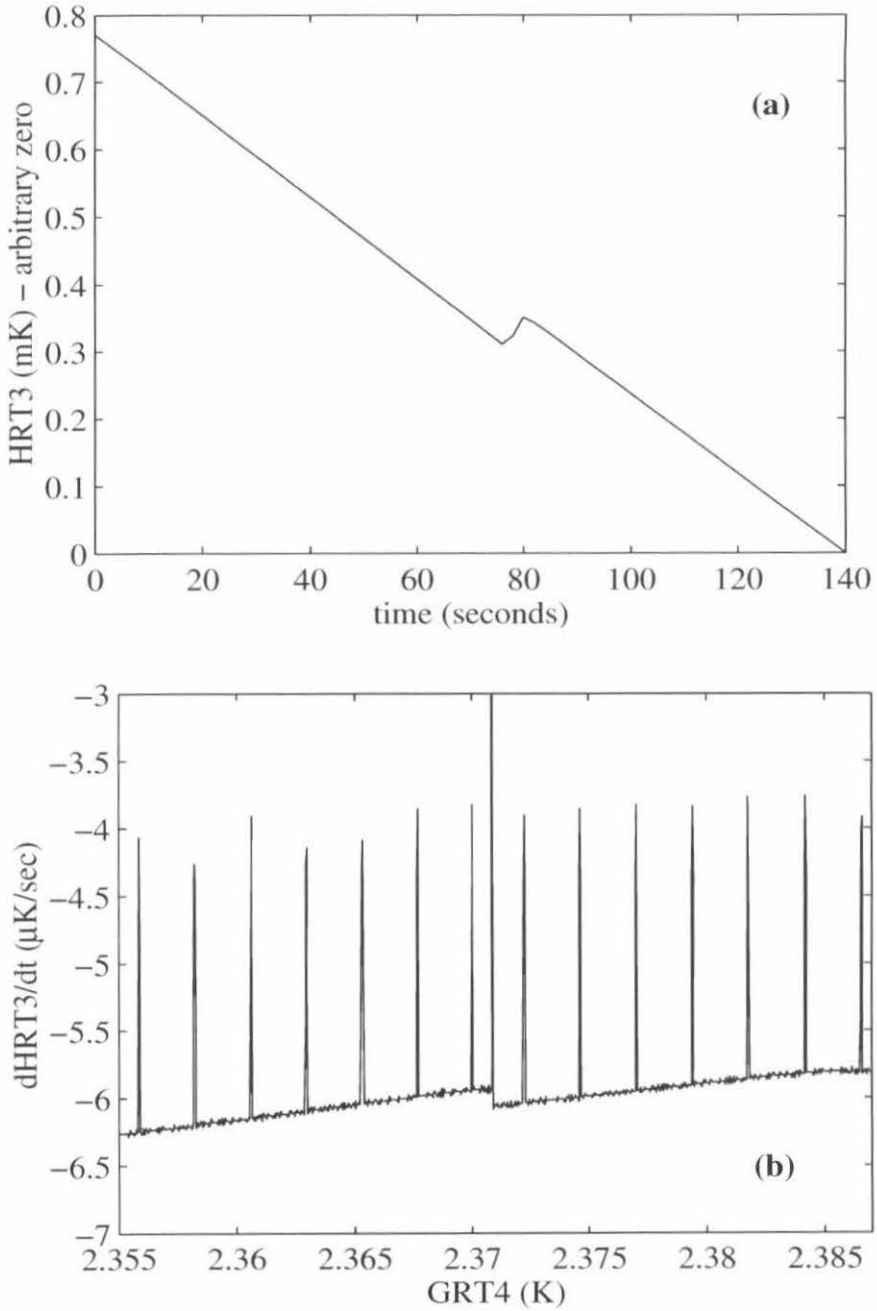

Figure 4.9: The bubble hunt: determining the helium fill factor (from File 090298.02). (a) The discontinuity in temperature that results from bubble formation (b) The derivative of (a), plotted versus GRT temperature. The derivative clearly indicates the discontinuity in slope that results as the curve switches from C_V to C_{SVP}. The other spikes are a result of the heat switch firing at regular intervals.

4.2.2 Taking data

Leveling the dewar

At the beginning of every data run, we leveled the experimental cell to minimize the effects of gravity on our data. We used a fairly crude technique to do this. Before cooling down, we leveled the cell with respect to the top-plate of our cryostat. We built a platform that was attached to the cell and put a 2-d bubble level on both the platform and the top-plate, and adjusted the vacuum can supports until the bubble-levels both indicated that the two surfaces were horizontal and parallel. Once cold, we then adjusted the support screws of the dewar until a 2-d bubble-level indicated that the top-plate was horizontal (see Fig. 3.27).

Using sheets of paper, a micrometer, and a sine-bar, we performed a test to see what sort of resolution we had during this leveling process. We determined that by leveling the 2-d bubble-level by eye, we could resolve up to $\pm 0.03°$. If we assume maximum error, this corresponds to a tilt of approximately 36.5 μm to our 6.985 cm diameter cell. Although small in absolute terms, our cell was only 0.064 cm tall, so this corresponds to a height error of nearly 5%.

Fortunately our data are not all *that* sensitive to gravity. Although a 5% leveling error would slightly increase the heat capacity enhancement, it would certainly not change it qualitatively. For any experiment in which it is essential that the cell be level, such as those performed by Day *et al.* [58, 59], more care should be taken. An excellent technique was developed by R.V. Duncan's group, and is described in detail in [59].

The data sets

After leveling the cell, we began taking data. We first applied Q to heater 6W, brought Stage 1 into servo using GRT1 and the QD bridge, located $T_{\mathrm{DAS}}(Q)$, and then chose the setpoint of the shield servo so that the temperature of the calorimeter was several μK below $T_{\mathrm{DAS}}(Q)$ with a low drift rate. We then waited for the system to come sufficiently into equilibrium that the drift rate of the sample was less than

6×10^{-4} ϕ_0/sec $\approx$ 0.1 nK/sec. We then started the LabVIEW program that executed the modified discrete pulse calorimetry method described in Sec. 4.1.4, and shown in Fig. 4.7. We then left everything alone for the next 15-20 hours.[4] When the run was over, we measured the currents we had applied to both heaters 5W and 6W by measuring the voltage drop across precision resistors that were in series with the heaters. We then adjusted the 1 K pot to eliminate any oscillations, transferred helium if needed, re-leveled the cell, and began again.

It became clear early on in the cooldown that we were not getting much of a distinguishable signal for heat currents less than 1 μW/cm^2. We therefore concentrated our efforts in the heat current range 1 μW/cm^2 $\leq$ Q $\leq$ 4 μW/cm^2. We took 20 successful data sets in all. Their distribution as a function of Q is shown in Fig. 4.10, and their file names and details are given in Appendix C.

4.3 Warming up

After all the data runs were finished, there were a few things left to do before warming up the cell. We remeasured the thermal network to make sure that it hadn't changed during our run due to bad thermal contacts, heat leaks, gas in the vacuum can, etc. Fortunately, it hadn't. We also performed another 'bubble hunt' in order to determine whether we had lost and helium during the course of the run due to a leaky valve. The temperature jump once again occurred at 2.37 K, indicating that the amount of helium in our cell also had not changed during the cooldown.[5] We then used a Philips PM 6672 high resolution timer/counter (1 GHz) to measure the consistency of the pulses output by our DAQ board. We found that the error in the pulse width was $\pm$0.1 μsec, or 2×10^{-5} %.

Before warming up, the final step was to extract the helium from the cell and directly measure the number of moles that we had used in our experiment. We set

[4]The more alone we left it, the better the data. The quality of the data taken overnight was significantly better than the data taken during the day. The only drawback was a large spike that appeared in the data at approximately 6 am when the campus came to life. This could always be removed later during data analysis.

[5]All of the pulse data runs were taken in a single cooldown.

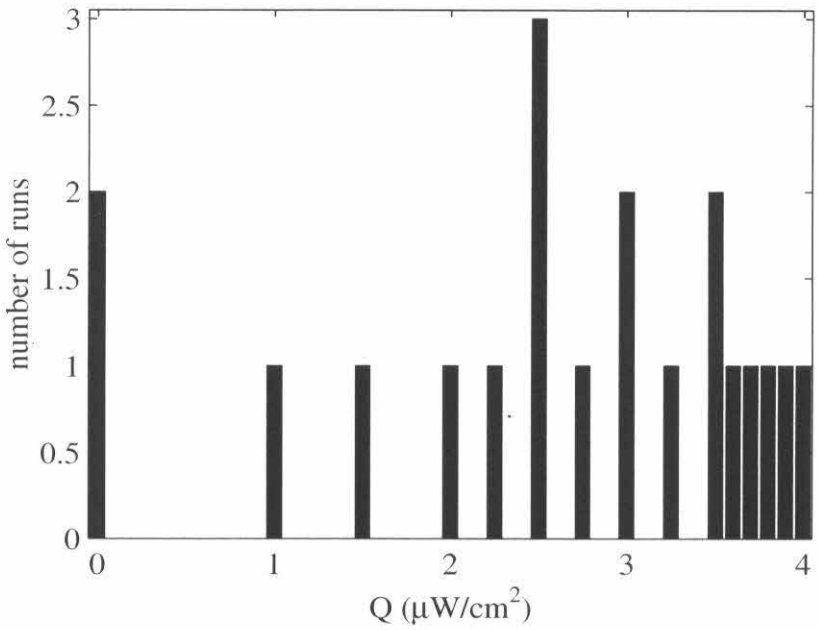

Figure 4.10: The number of data runs taken as a function of Q. We concentrated on the larger values of Q since this was the range where the largest heat capacity enhancement was observed.

up the cryostat in the configuration shown in Fig. 4.8. We used a Paroscientific, Inc. Digiquartz quartz-crystal pressure gauge that had an accuracy of 0.01% and a resolution of 0.0001%. It could withstand a maximum pressure of approximately 1.2 bar. Our calibrated volume was 398.329 cm^3. If all of the liquid helium in our cell were to expand into the gas phase, it would occupy approximately 2.3 liters at RTP. We therefore added an extra volume to the system so that the maximum possible pressure that the gauge would see during the extraction was around 1 bar.

With the valve to the cryostat (valve 2) closed, we put helium gas into the room temperature system and calibrated the volume of the pipework and of the 'extra volume'. We found that, together, they occupied 2.447 liters. We then extracted the helium in five steps, taking out successively smaller amounts, until we were down to the resolution of our pressure gauge. In total, we measured that there were 0.08918 moles of helium in our cell.

During a previous run (one of the drift calorimetry runs), we had overfilled the

cell.[6] Because the compressiblility of liquid helium is extremely small, we would expect that the number of moles in the cell during that run would be close to the total number of moles that could fit in the cell while at SVP. At the end of that run, we extracted 0.08962 moles. The percent change was therefore:

$$\frac{0.08962 - 0.08918}{0.08962} \times 100 = 0.491\%, \tag{4.11}$$

which is in excellent agreement with our measured bubble size.

After the helium was extracted, we once again measured the heat capacity of the empty cell, and then warmed up the experiment.

It was time to begin analyzing the data ...

[6] In other words, filled it to a pressure above the SVP.

Chapter 5 Data Analysis

This chapter will describe the methods used to analyze the final specific heat data. In general, the discrete pulse method has a rather simple data analysis procedure. The main complications specific to our experiment were:

1. Eliminating electronic noise and HRT drift;
2. Determining the absolute temperature scale;
3. Correcting the endplate temperature measurements for the singular Kapitza resistance.

After these things were accomplished, finding the heat capacity was then only a matter of fitting lines to the slope in temperature on the sides of each pulse, and then extrapolating these lines to find the difference in height in the middle of each pulse.

5.1 Eliminating electronic noise and other error sources

There were a number of things we had to do to clean up our data before using it to determine the heat capacity. Because the effect that we were looking for was supposed to be fairly small, eliminating spurious signals meant the difference between having the heat capacity enhancement lost in the noise and having it be clearly distinguishable.

5.1.1 SQUID timer resets

As described in Sec. 3.2.5, if the analog part of the signal is taken immediately after the flux counter is incremented (and a reset is sent to the controller), its value is not valid, because it has not yet had time to settle. The settling time is determined by

the analog filter used to condition the signal (see Appendix B.3). As a result, a spike appears in the data at the time of the reset. These spikes can be seen in Fig. 5.1 every time the data counts a multiple of ϕ_0.

These spikes can easily be removed during data analysis. When the fluxcounter sends a reset signal to the SQUID controller, it also starts a timer that is recorded by the computer. This timer signal can be used to eliminate any data points taken in the vicinity of the reset signal. The size of the window needed to completely eliminate the spike varies depending on the temperature drift rate and the filter settings of the SQUID controllers. The drift data shown in Fig. 5.1 were filtered by a filter[1] with a cutoff of 0.4 Hz, and had a fairly large drift rate of 5 nK/sec. We had to throw out data in a window of 1 second after the reset to eliminate the spikes. For the pulse data, where the drift rate on the pulse ledge (the data taken in between subsequent pulses) was extremely minimal, a 100 msec window was sufficient.

5.1.2 Flux jumps

Radio Frequency (RF) noise interfered with the electronics on the fluxcounter board, and caused the flux count to jump discontinuously by an integral number of flux quanta. When we first set up the experiment, we experienced around one flux jump per minute. We eliminated some of the problem by putting low pass filters on all inputs and outputs of the fluxcounter board. Although this made the experiment robust against turning on and off light switches in adjacent rooms, it was still sensitive to soldering iron switches, flickering flourescent lights, drills, and other unusually high RF noise sources. During a normal run, we got an average of 1-3 flux jumps per hour. Occasionally, when contractors were working nearby, or an overhead flourescent bulb started to die out, we would get considerably more. One of the more afflicted runs is shown in Fig. 5.2.

Although a nuisance, these flux jumps could easily be accounted for during data analysis. It was simply a matter of finding the location of the jumps, and then

[1]The filter specifications are given in Appendix B.

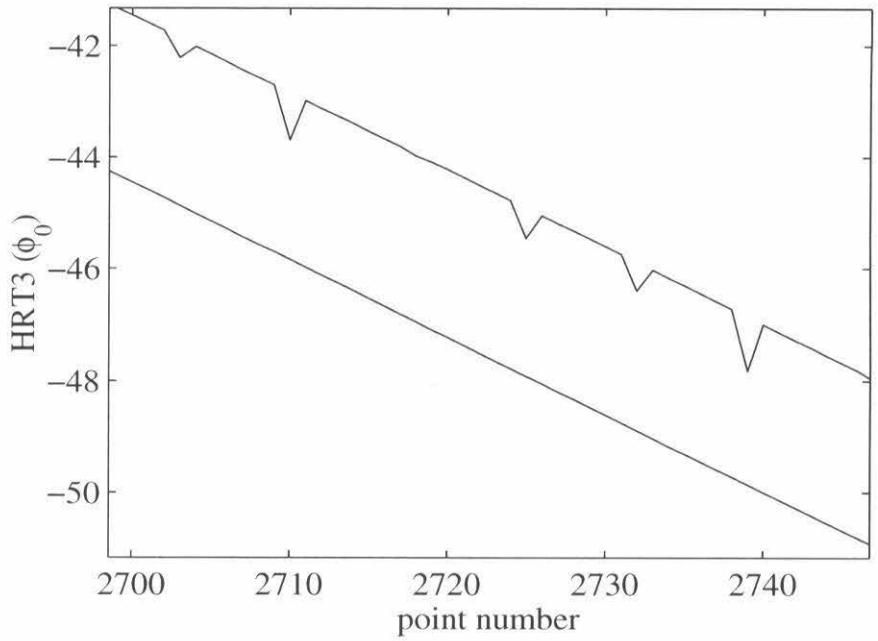

Figure 5.1: Correcting for flux-counting reset errors. A drift calorimetry file at $Q = 0.243\ \mu\mathrm{W/cm}^2$ (file 011498.01). Top line: The data before correction for SQUID timer resets. Bottom line: the data after SQUID timer correction, shifted down by 3 ϕ_0. Data points were taken approximately once a second, filtered at 0.4 Hz, and cleaned by eliminating the data taken within one second after the reset signal was received.

subtracting the appropriate number of quanta from the flux count for all subsequent data points. This process was automated by a program[2] that took the difference between the HRT data of adjacent points,

$$\Delta = \mathrm{HRT(n+1)} - \mathrm{HRT(n)}, \tag{5.1}$$

and then plotted them as a function of point number, n. The program then scanned Δ to see if it was within certain cutoff values. These cutoff values were determined by the pulse height and the drift rate down for the discrete pulse calorimetry data. Typically, the pulse height was around 0.6 ϕ_0, and the drift rate on the downward ramps was -5-6$\times 10^{-3}$ ϕ_0/sec. Therefore we usually set the cutoff values so that we

[2]The program is written in Matlab and is called 'clean_flux2.m'.

would count:

$$+1\ \phi_0 \quad \begin{cases} \Delta \geq 0.6\ \phi_0 \\ \Delta \geq 0.2\ \phi_0 \text{ and } \dfrac{1}{20} \displaystyle\sum_{\mathrm{i=n-10}}^{\mathrm{n+10}} \dfrac{\mathrm{dHRT}}{\mathrm{dt}}\,(\mathrm{n}) \leq -5 \times 10^{-3}\ \phi_0/\mathrm{sec} \end{cases}$$

$$-1\ \phi_0 \quad \{\ \Delta \leq -0.4\ \phi_0$$

where the first $+\phi_0$ condition is to account for positive flux jumps on the upward ramps, the second $+\phi_0$ condition is to account for positive flux jumps on the downward ramps, and the $-\phi_0$ condition takes care of both upwards and downward ramps. This technique was extremely effective, and allowed us to adjust for runs that had as many as several hundred flux jumps, such as the one shown in Fig. 5.2.

The one place that this technique failed was when a flux jump occurred on HRT0 right on a pulse on the normal fluid side. As can be observed in Fig. 5.6(b), HRT0 pulse heights in this region were considerably larger than one ϕ_0. The program was therefore not run on the HRT0 pulse data above the transition. Instead, flux jumps were found by plotting the HRT0 data versus the HRT1 data and looking for discontinuous offsets of multiples of ϕ_0 between the different ramps.

5.1.3 Microflux jumps

The final type of electronic noise we had to eliminate were the microflux jumps. 'Microflux jumps' is a bit of a misnomer. The microflux jumps were neither $10^{-6}\ \phi_0$ in magnitude, nor a true jump. They were more of a blip [see Fig. 5.3(a)] that resembled the timer resets discussed in Sec. 5.1.1. The origin of the name is a complete mystery. But the name once given, stuck. Since it appears throughout the lab books, I will not change it here. Like its name, the precise origin of the microflux jumps themselves is not known. They clearly do not represent thermal properties of the system, and appear to be due to some sort of electronic noise.

As with the flux jumps, it was easy to eliminate the microflux jumps during data

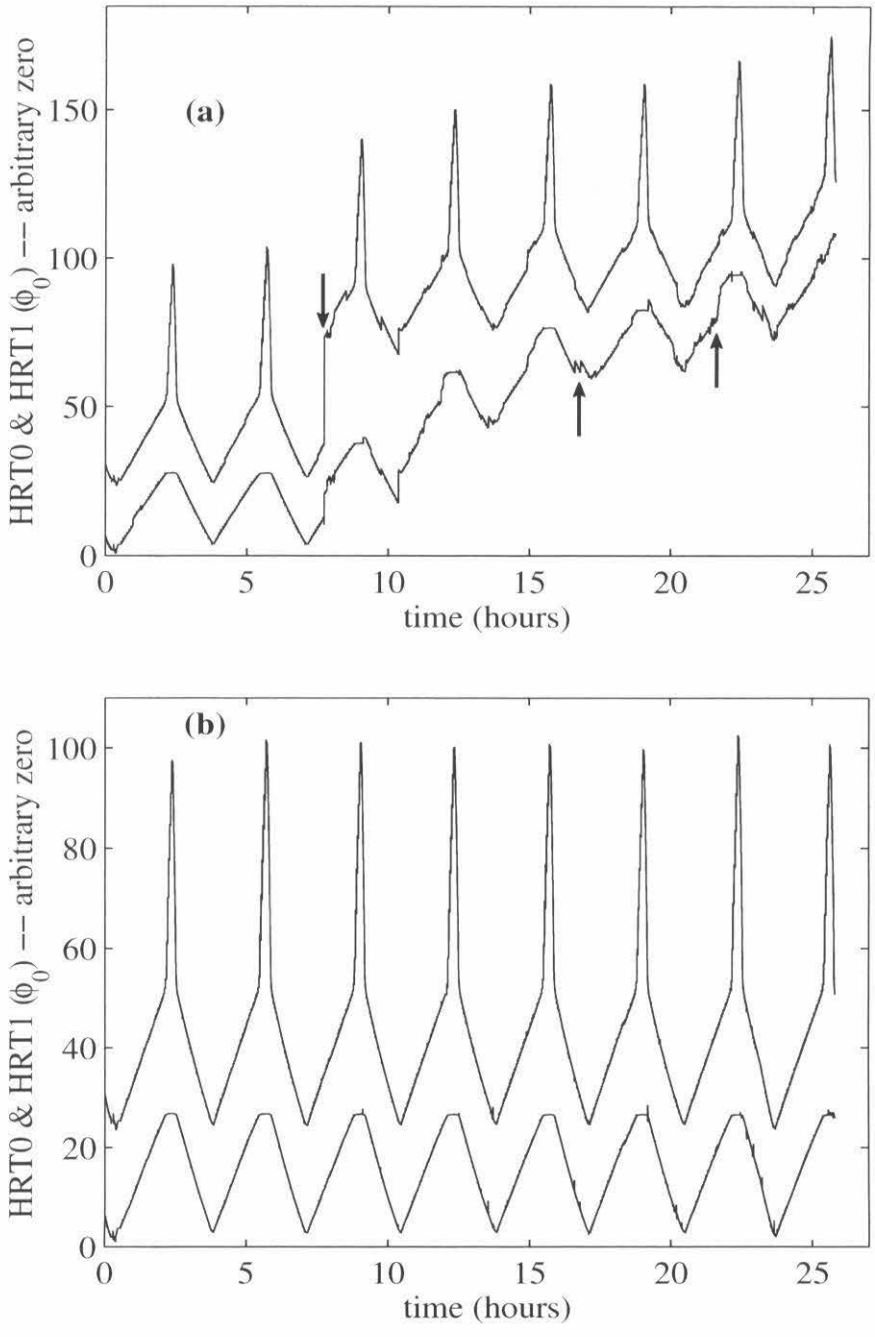

Figure 5.2: Correcting for flux jumps. A discrete pulse calorimetry file at $Q = 3.26\ \mu\mathrm{W/cm}^2$ (file 030699.01). (a) The data before it is corrected. This file has many more flux jumps than usual. The top curve is HRT0 and the bottom curve is HRT1. Three of the larger flux jumps are indicated by arrows. (b) The data after the flux jumps are removed.

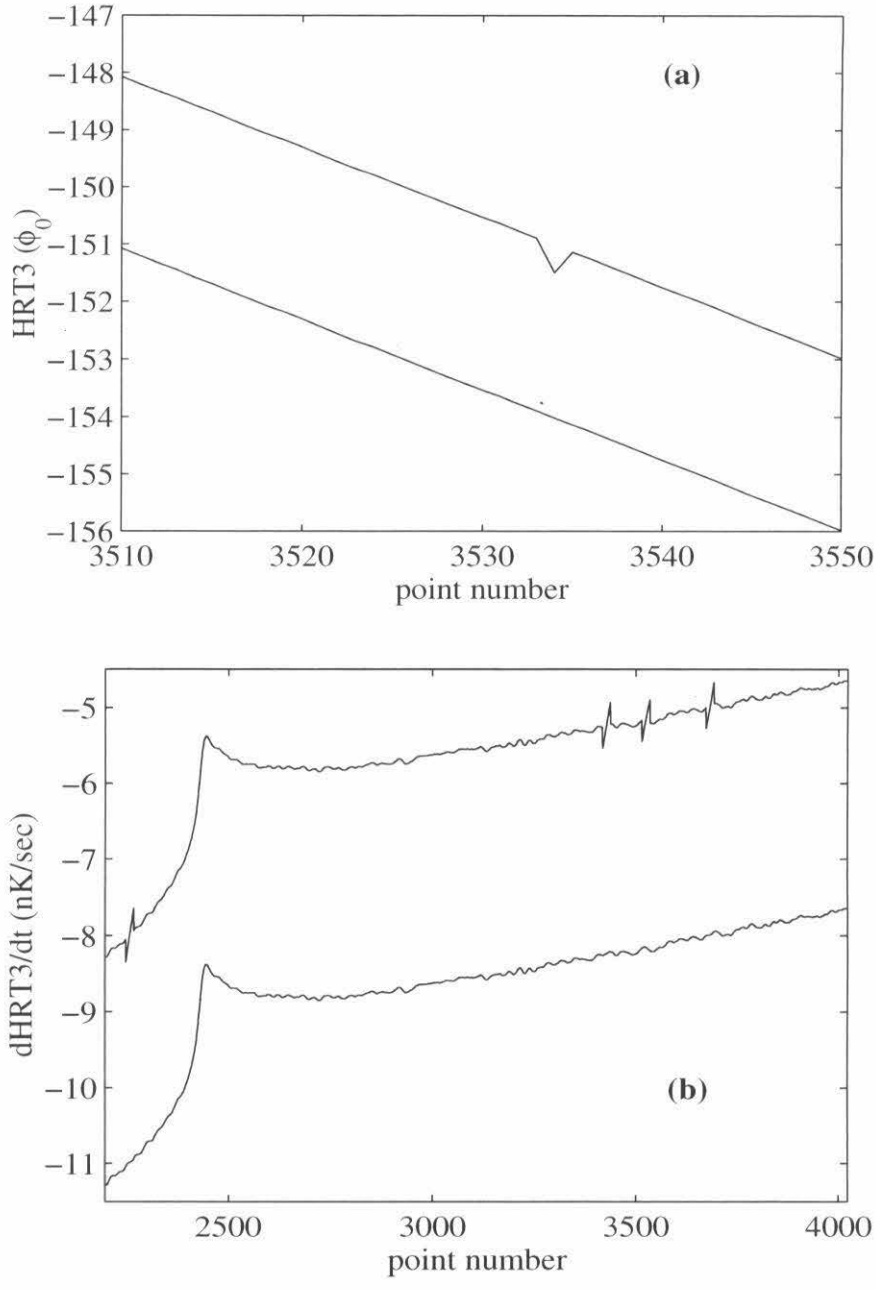

Figure 5.3: Eliminating microflux jumps. A drift calorimetry file at $Q = 0.243\ \mu\mathrm{W/cm}^2$ (file 011498.01). (a) A microflux jump on HRT3. The top curve is before correction. The bottom curve is after correction, and is shifted down by 3 ϕ_0. (b) The derivative of HRT3. The top curve is before correction. There are four microflux jumps in this range. The bottom curve is after correction, and is shifted down by 3 nK/sec.

analysis. This procedure was automated by a program[3] that also took the 2-point difference defined in (5.1), and scanned Δ for a negative spike closely coupled to a positive spike. When it found this signature at point n, it replaced HRT(n) with [HRT(n+1) + HRT(n-1)]/2. This effectively eliminated the microflux jumps [see Fig. 5.3(b)].

5.1.4 HRT drift

As was described in Sec. 3.2.4, all HRTs exhibit small drift rates. These drift rates must be taken into account when making precise measurements over long periods of time. The HRT drift rates are not the same from run to run, and must be measured empirically for every data file. The drift rates were usually more or less constant over the length of one file, although occasionally they would exhibit small changes from one part of a file to another. We found that the drift rates of HRT1 (top thermometer) were usually slightly higher than those of HRT0 (bottom thermometer), and both were on the order of several $\mu\phi_0$/sec, or approximately 15 nK/day.

The drift rate of the thermometers can be determined by plotting the temperature reading of HRT1 vs. the temperature reading of HRT0[4] for each file. Because HRT1 and HRT0 are thermometers adjusted to read the temperature of the same object, this plot should be a straight line, whose slope is the ratio of κ_{HRT1} to κ_{HRT0}, where κ is the number of ϕ_0/K for each thermometer. However, if HRT1 drifts relative to HRT0, this straight line will move for each subsequent ramp (see Figs. 5.4 and 5.7). When the drift rates are constant, they can be more or less determined by finding out what values of f_1 and f_0 used in a plot of [HRT1 + $f_1 \cdot t$] vs. [HRT0 + $f_0 \cdot t$], where t is time, cause all data points to collapse onto a single curve. It is easiest to observe the drift rates on the downward ramps, because they contain data points that are continuous in temperature (see Fig. 5.4). However, they also have considerably more noise than the data on the pulse ledges.

[3] This program was also written in Matlab and is called 'clean_microflux.m'.

[4] Both HRT1 and HRT0 should first be adjusted for the singular Kapitza resistance by the method described in Sec. 5.3 so that they both read the temperature of the helium sample.

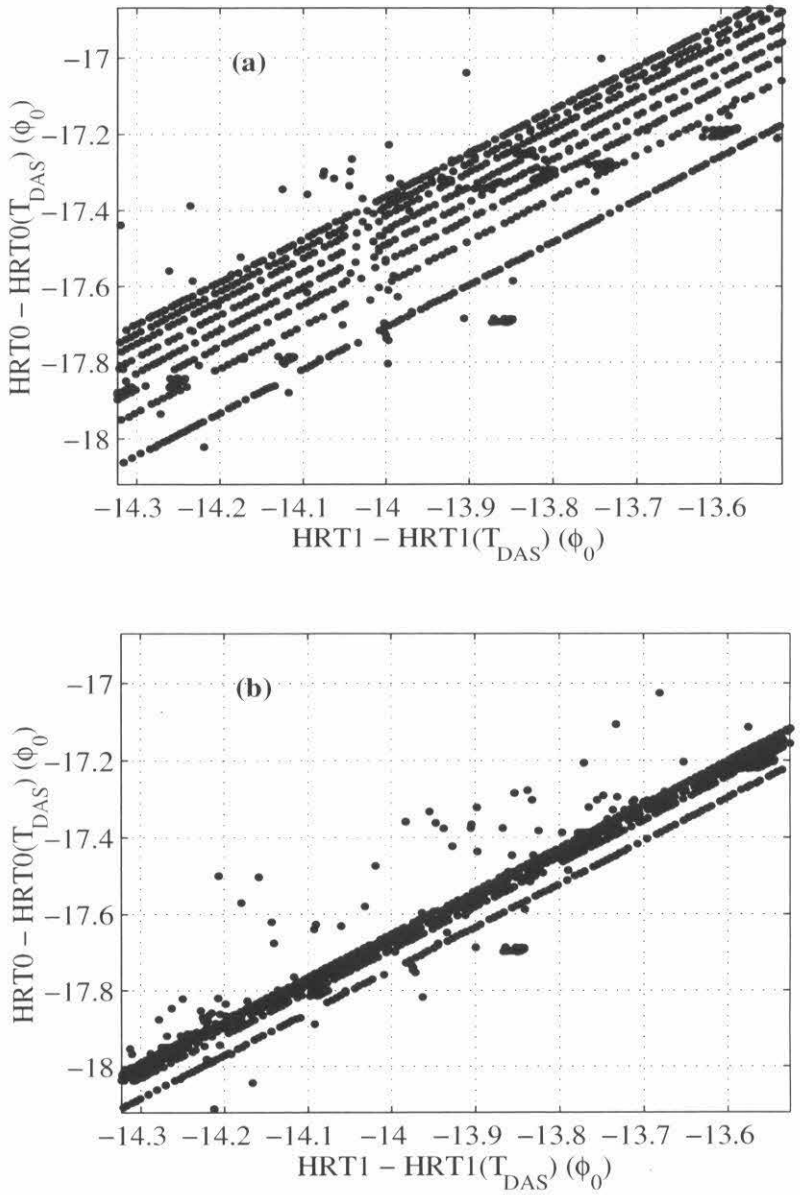

Figure 5.4: Correcting for HRT drift on a $Q = 3.6\ \mu\mathrm{W/cm}^2$ file (030999.01). HRT1 vs. HRT0— the whole file. The small clumps of points [like the ones at (-13.7, -17.2) and (-13.75,-17.3)] are the upward pulse ledges. The continuous lines are the downward ramps. The scattered points that do not lie on the lines are due to the spikes immediately following a pulse (an example of which can be observed in Fig. 5.13) that are caused by SQUID timer resets (see Sec. 5.1.1). (a) Before drift correction. (b) After most of the drift is corrected. On this file, one of the ramps has a slightly different drift rate than the others.

Using the pulse ledges

In order to fine-tune f_1 and f_0, we therefore used the data from the pulse ledges. We found the temperatures $\mathrm{HRT1}_{\mathrm{ledge}}$ and $\mathrm{HRT0}_{\mathrm{ledge}}$ in the middle of each pulse ledge, and plotted them against one another (see Fig. 5.4). This was also an automated process.[5] Once again, the program first found the 2-point difference, Δ, and then located the pulses by sorting for all points where $\Delta \geq 0.15\ \phi_0$ (see Fig. 5.5). It saved the point numbers of the pulses as the set $\{P\}$. Because there is one data point on each pulse's rising edge, the number $0.15\ \phi_0$ was chosen because it was a little less than half of the smallest pulse's total height. It then recorded the HRT value halfway in between each pulse (see Fig. 5.6) as $\mathrm{HRT}_{\mathrm{ledge}}$. By adjusting f_1 and f_0 on the plot of $\mathrm{HRT1}_{\mathrm{ledge}} + f_1 \cdot t$ vs. $\mathrm{HRT0}_{\mathrm{ledge}} + f_0 \cdot t$, the drift rates could be more accurately determined (see Fig. 5.7).

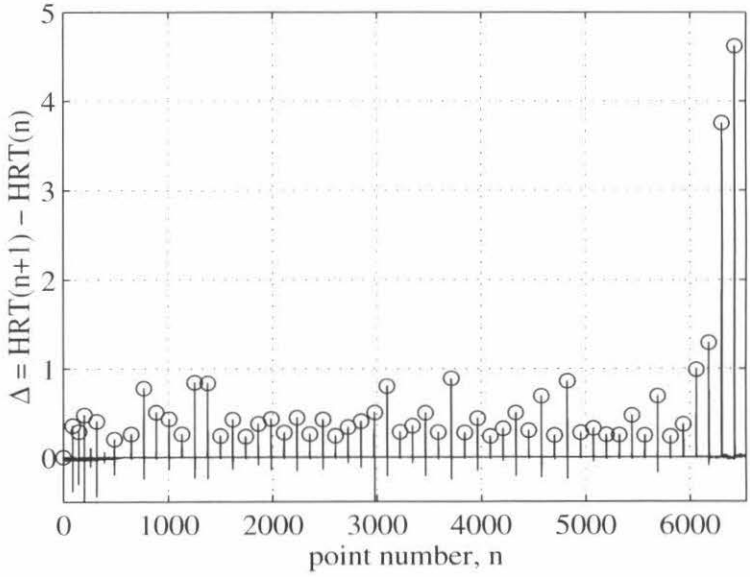

Figure 5.5: Finding the pulses. The y-axis is the 2-point difference of HRT0 on a $Q = 3.6\ \mu\mathrm{W/cm}^2$ file (030999.01): Δ = HRT0(n+1) - HRT0(n). The program finds all the points with $\Delta \geq 0.15\ \phi_0$ and saves them in the variable P. These are indicated by circles ($\circ$). Note that the noise at $\Delta = 0$ (the data on the pulse ledges) increases when dissipative fluid is in the cell for $n > 6000$ and $n < 500$.

[5]This process was written into a Matlab program, 'temps_pulse_time.m'

Using the derivative of the pulse ledges

For some files, it was difficult to independently guess f_1 and f_0 to make the various ramps collapse. For these cases, we came up with a method that examines the drift of each thermometer separately. This method works best on drift calorimetry files, but could also be used on discrete pulse files. We first took the time derivative of $\mathrm{HRT}_{\mathrm{ledge}}$, and then plotted $\mathrm{HRT}_{\mathrm{ledge}}$ vs. $\mathrm{dHRT}_{\mathrm{ledge}}/\mathrm{dt}$ (see Fig. 5.8). Because there were a number of ramps, for non-drifting thermometers, this curve should retrace itself many times. A constant drift rate, on the other hand, would change $\mathrm{dHRT}_{\mathrm{ledge}}/\mathrm{dt}$ by a constant offset, and cause $\mathrm{HRT}_{\mathrm{ledge}}$ to move over time. By measuring the total distance between $\mathrm{HRT}_{\mathrm{ledge}}$ on the first ramp and the last ramp, and then dividing this number by the total time of the file, an approximate drift rate can be determined for that particular thermometer.

For most files, we used all of these methods. We first separately found the drift rates for HRT1 and HRT0 using the derivative method; we then confirmed that these were correct by plotting HRT1 vs. HRT0 and looking at the downward ramps. We then fine-tuned the rates by plotting $\mathrm{HRT1}_{\mathrm{ledge}}$ vs. $\mathrm{HRT0}_{\mathrm{ledge}}$.

For some files, the drift rate did not remain constant throughout the run. For example, the file plotted in Figs. 5.4 and 5.7 had a different drift rate between the first ramp and the rest of the file. On files like this one, we had two options. If the differing data was only on one ramp, we often would throw away the anomalous ramp, and only analyze the remaining data. If, however, there were several ramps that did not behave, we found that we could make the data collapse by adjusting each deviating ramp by a fixed amount. This analysis showed that most of the thermometer drift took place during the downward portions of the data files.

5.2 Fixing the temperature scale

HRTs are secondary thermometers, and do not give a reading of the absolute temperature. It was therefore necessary to fix the temperature scale for each run by

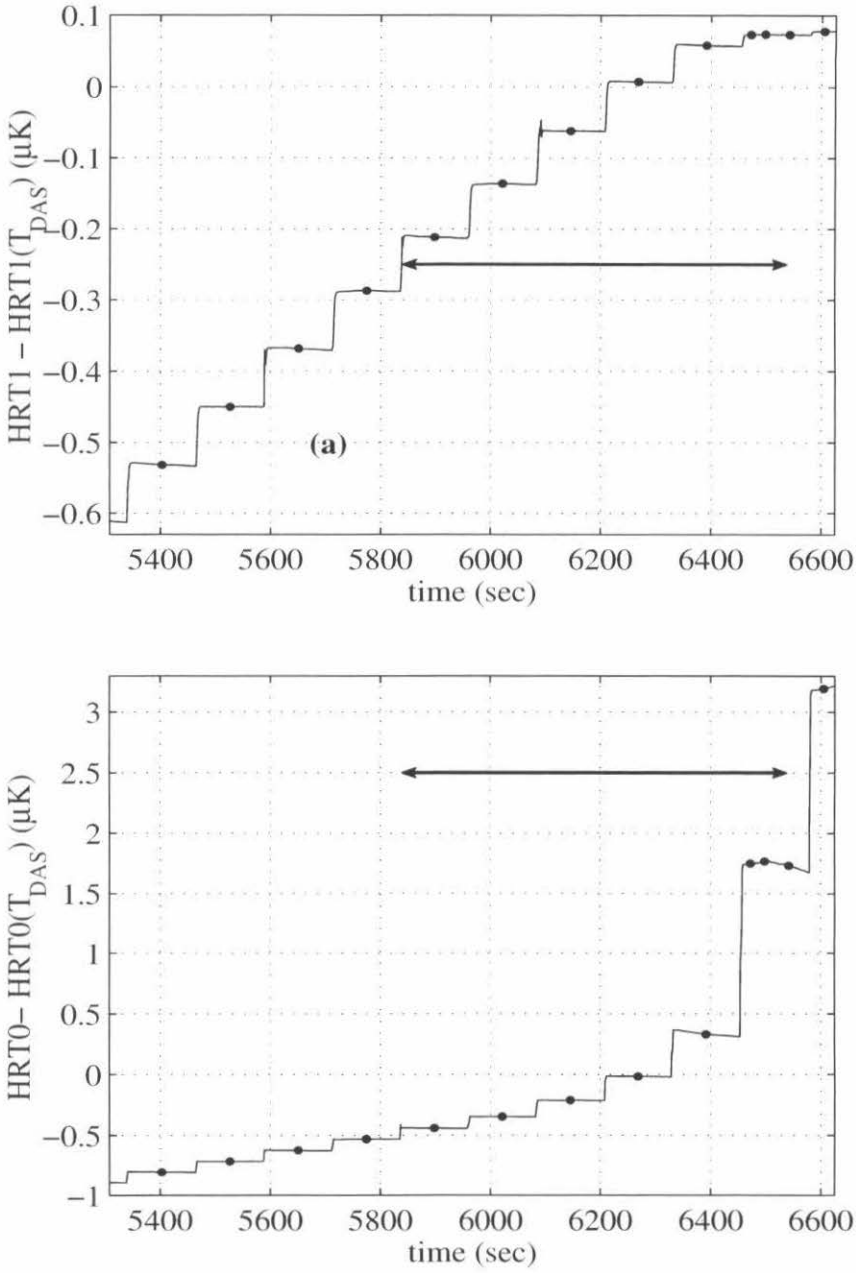

Figure 5.6: Finding the middle of the pulse ledge on a $Q = 3.6\ \mu\mathrm{W/cm^2}$ file (030999.01). Midway between the spikes found on Fig. 5.5, we locate the pulse ledges. The arrows indicate the points plotted in Fig. 5.9. Dissipative fluid enters the cell around point 6300. Note that the HRT0 pulse heights begin to increase at this point, as the bottom layer of fluid begins to heat up. Soon after this point, the HRT1 pulse heights begin to decrease, since the heat starts going into heating up the bottom layer of normal fluid.

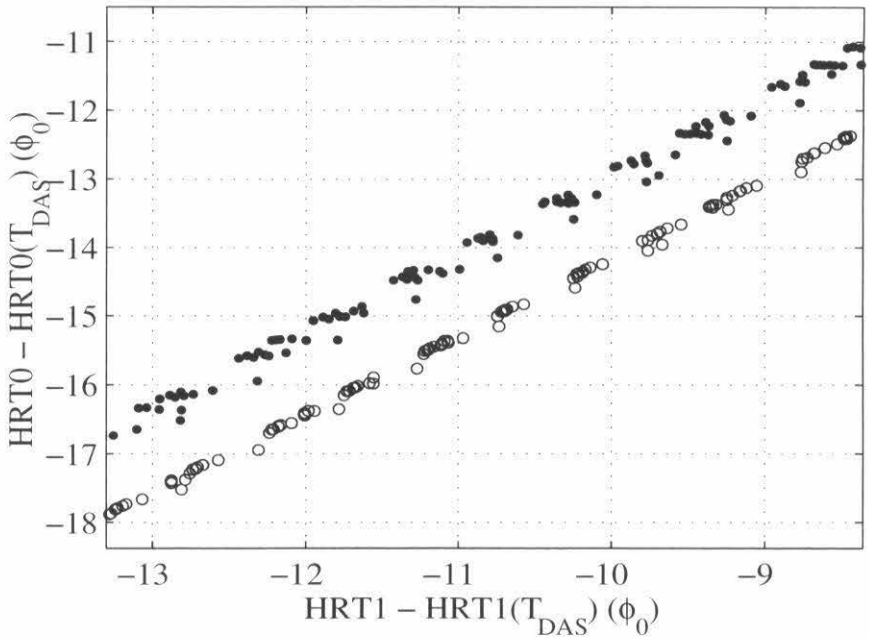

Figure 5.7: Correcting for HRT drift on a $Q = 3.6\ \mu\mathrm{W/cm^2}$ file (030999.01). HRT1 vs. HRT0 'middle of the ledge' points. Solid dots: before drift correction. Open circles: after most of the drift is corrected. On this file, one of the ramps has a slightly different drift rate than the rest of the file. The points in each cluster of 10 or so points are from various ramps.

matching a feature in our data with a previously measured quantity. We did this by correlating the temperature at which superfluid turned to dissipative fluid in our cell with $T_{DAS}(Q)$ [19].

This point was determined by first observing on which temperature pulse ledge the noise of the bottom thermometer suddenly increased (see Fig. 5.9) during the upward ramp. This set an upper limit (the temperature of the first noisy ledge), as well as a lower limit (the temperature of the previous ledge) for $T_{\mathrm{DAS}}(Q)$. To get a more precise location, we then looked at the downward ramp (see Fig. 5.10) and picked out the temperature where the bottom thermometer became less noisy and changed the most rapidly. We then fixed the temperature scale of the top and bottom thermometers by setting their temperatures at this point equal to $T_{DAS}(Q) \pm Q \cdot R_b$,

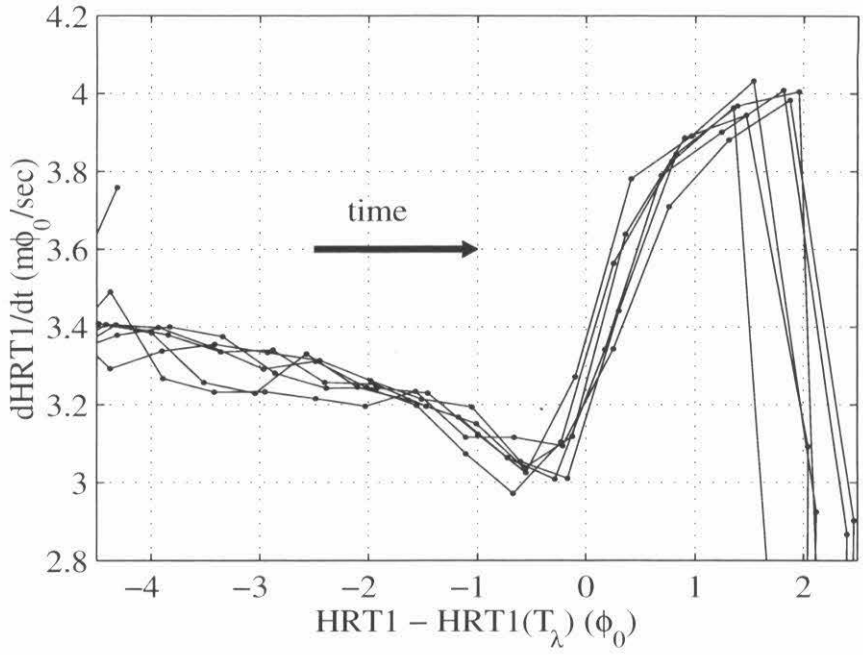

Figure 5.8: Correcting for HRT drift on a $Q = 0$ file (021699.01). HRT1 vs. dHRT1/dt, where HRT1 is composed of the 'middle of the ledge' points. Because there are many ramps, this curve should retrace itself many times. Any HRT drift will be observed as a width in the x-axis spread of the various curves. On this file, the spread in HRT1 is approximately 0.5 ϕ_0. Since the file is approximately 25.5 hours long, this corresponds to a drift rate of $\approx 5.4\ \mu\phi_0$/sec.

where R_b was the singular boundary resistance discussed in Sec. 3.1.2. In other words, if $\mathrm{n_{DAS}}$ was the point number at which $T_{\mathrm{DAS}}(Q)$ was observed, we set

$$\mathrm{T1 = HRT1 - HRT1(n_{DAS}) + T_{DAS}(Q) - \Delta T^{c}[T_{DAS}(Q)]}, \tag{5.2}$$

and

$$\mathrm{T0 = HRT0 - HRT1(n_{DAS}) + T_{DAS}(Q) + \Delta T^{h}[T_{DAS}(Q)] + \delta_0}, \tag{5.3}$$

where $\Delta T^c = Q \cdot R_b^h$ and $\Delta T^h = Q \cdot R_b^c$ are equal to the temperature drop across the hotter and colder boundary layers, respectively; R_b^h and R_b^c are the singular boundary resistances of the hotter and colder boundary layer as a function of *superfluid temperature* instead of *boundary layer temperature*; and δ_0 is a constant offset that

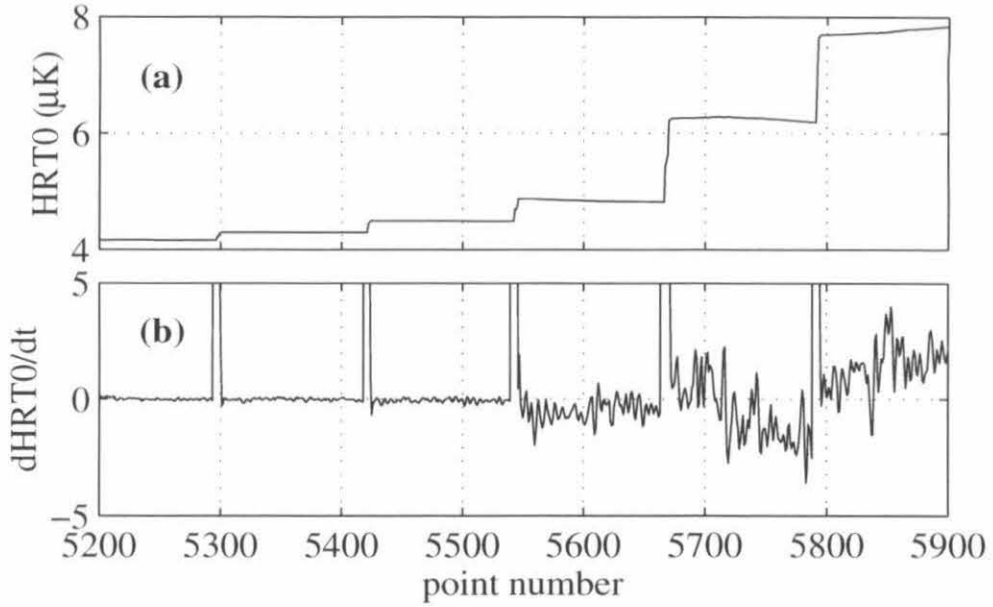

Figure 5.9: Finding T_{DAS} on a $Q = 3.6\ \mu\mathrm{W/cm^2}$ file (030999.01) on the upward ramp. (a) HRT0 in μK, arbitrary zero. (b) dHRT0/dt (nK/sec). By observing when the derivative of the bottom thermometer becomes noisy, one can determine when dissipative fluid enters the cell. As soon as this happens, the temperature of the bottom boundary layer begins to heat up, absorbing an ever greater fraction of the heat, as compared to the bulk, and the pulse height measured by the bottom thermometer starts to increase.

will be explained further below. T_1 and T_0 are set to be equal to the temperatures at the wall (T_W) at the top and bottom of the cell, respectively. In the superfluid phase they therefore differ by the total temperature drop across the top and bottom boundaries.

We found ΔT^c by plotting $t_{\mathrm{SF}}^{\mathrm{top}}$ vs. $\Delta T^c \equiv Q \cdot R_b(Q, t_b)$, where

$$t_{\mathrm{SF}}^{\mathrm{top}} = t_b + \frac{Q \cdot R_b(Q, t_b)}{2T_\lambda}, \tag{5.4}$$

t_b and R_b are the boundary temperature and resistance measured by FBKA [78], Q is the heat current used in the measurement being corrected, and $t_{\mathrm{SF}}^{\mathrm{top}}$ is the inferred reduced helium temperature at the top wall (with respect to the lambda transition temperature at the top of the cell, T_λ^{top}). We then interpolated from this graph to

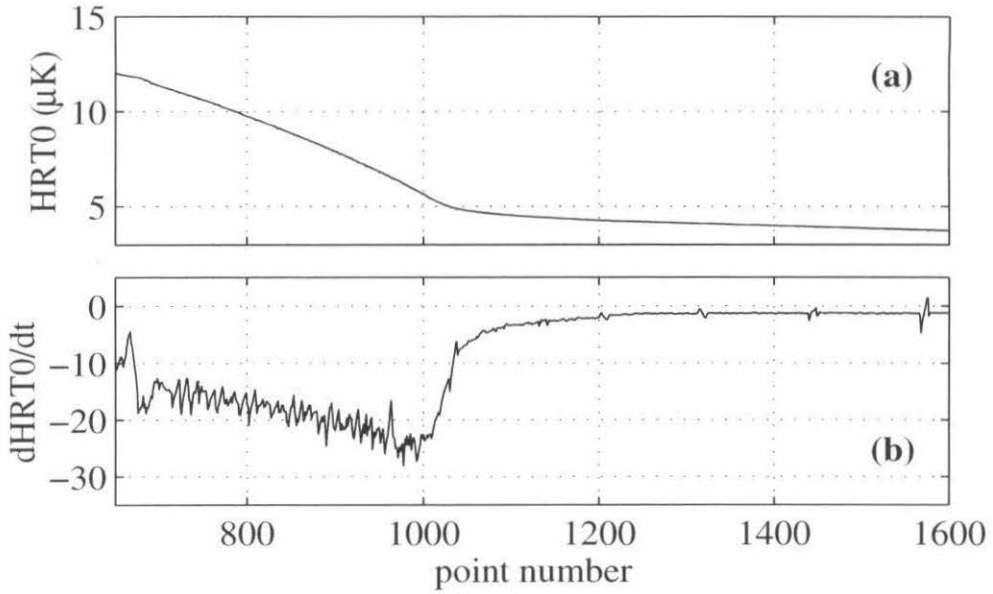

Figure 5.10: Finding $T_{\rm DAS}$ on a $Q = 3.6\ \mu$W/cm^2 file (030999.01) on the downward ramp. (a) HRT0 in μK, arbitrary zero. (b) dHRT0/dt (nK/sec). By observing when the derivative of the bottom thermometer becomes quiet, one can determine when dissipative fluid leaves the cell. The temperature at which this occurs on the downward ramp should be in-between the last quiet temperature pulse ledge and the first noisy temperature pulse ledge on the upward ramp.

find the value of $\Delta T^c = Q \cdot R_b$ at $T_{\rm DAS}(Q)$. Similarly, we found ΔT^h by plotting R_b versus the reduced helium temperature at the bottom wall (with respect to the lambda transition temperature at the bottom of the cell, $T_\lambda^{\rm bottom}$):

$$t_{\rm SF}^{\rm bott} = t_b - \frac{Q \cdot R_b(Q, t_b)}{2T_\lambda} + \frac{\alpha l}{T_\lambda}, \tag{5.5}$$

where $\alpha = 1.2744248 \times 10^{-6}$ K/cm is the slope of the transition temperature in gravity, and $l = 0.064$ cm is the height of our cell. The two curves described by (5.4) and (5.5) are shown in Fig. 5.11.

It was not necessary to adjust the temperature scale by the regular component of the Kapitza resistance because it is not a strong function of temperature over the range of our data. Therefore, our thermometers were adjusted to read the temperature of the superfluid right next to the wall, T_W.

5.3 Correcting the endplate temperature readings for the singular Kapitza resistance

The next data analysis step was to correct the readings of HRT1 and HRT0 for the singular Kapitza resistance, in order to obtain readings of the temperature of the helium sample. We used the data of FBKA [78] to plot R_b vs. the endplate temperatures [6] $t_{\rm top}$ and $t_{\rm bott}$, and then interpolated these curves to find the correction for each point of $T0$ and $T1$ defined in (5.2) and (5.3).

There were a number of points that we could not directly adjust in this way, since our data came considerably closer to the lambda transition than the FBKA data. In order to correct these points, we extrapolated the FBKA data to lower reduced temperatures. We altered the way this extrapolation was performed until we could verify that it was correct. We did this by first defining three different measurements of the superfluid temperature:

$$\begin{aligned} T^1_{\rm SF} &= \frac{T1+T0}{2} - \epsilon = \frac{T1+T0}{2} - \left(\frac{\Delta T^h - \Delta T^c}{2}\right) \\ &= \frac{T^2_{\rm SF} + T^3_{\rm SF}}{2} \qquad (5.6) \\ T^2_{\rm SF} &= T1 + \Delta T^c \qquad (5.7) \\ T^3_{\rm SF} &= T0 - \Delta T^h, \qquad (5.8) \end{aligned}$$

where ΔT^h and ΔT^c are the temperature drops across the hotter and colder boundaries over the temperature range of *both* the FBKA data and its extension. If we compute the heat capacity from the data using these three expressions for the superfluid temperature, we expect to get three different curves that will agree *only* if

1. The singular Kapitza resistance of our cell agrees with the data of FBKA, and

[6] The endplate temperatures are: $t_{\rm top} = t_b + (Q \cdot R_b/2T_\lambda)$ and $t_{\rm bott} = t_b - (Q \cdot R_b/2T_\lambda)$.

2. The singular Kapitza resistance of our cell at lower reduced temperatures is the same as our extension of the FBKA data.

We found that far away from T_λ the three heat capacity curves almost always agreed, indicating that (1) was generally satisfied. For the highest temperatures (lowest reduced temperatures) of the FBKA data, the three heat capacity curves did not quite overlap (see Fig. 5.12), indicating that there was a small range where the singular Kapitza resistance of our cell did not agree with that of FBKA. In order to make the curves agree in the temperature range closest to the transition, we had to adjust the way in which we did the extension. We ultimately found that if we extended the data by performing a first order fit to the curve $[\log_{10}(t_b), \log_{10}(R_b)]$ to get

$$\log_{10}[R_b(\mathrm{cm^2K/W})] = -0.1610 \cdot \log_{10}(\mathrm{t_b}) - 2.119, \tag{5.9}$$

we could make the three heat capacity curves agree quite well. This extrapolation is shown as triangles ($\triangle$) and circles ($\circ$) in Fig. 5.11. It is, in fact, an indirect measurement of the singular Kapitza resistance at lower reduced temperatures.

5.4 Measuring the heat capacity

5.4.1 Determining the size of the temperature discontinuity

After the Kapitza correction was made, it was time to calculate the heat capacity using the temperature expressions T^1_{SF}, T^2_{SF}, and T^3_{SF}. For each pulse, the height of the temperature discontinuity, ΔT^i_{SF}, was measured by

1. Fitting a line to the temperature data points composing half of the ledge before the pulse, and a line to the temperature data points composing half of the ledge after the pulse [see Fig. 5.13(a)]. In order to make sure that the fit did not contain any of the points on the pulse itself or too close to the shield temperature adjustment, the fit on the ledge, before the kth pulse at point $\mathrm{P}(k)$,

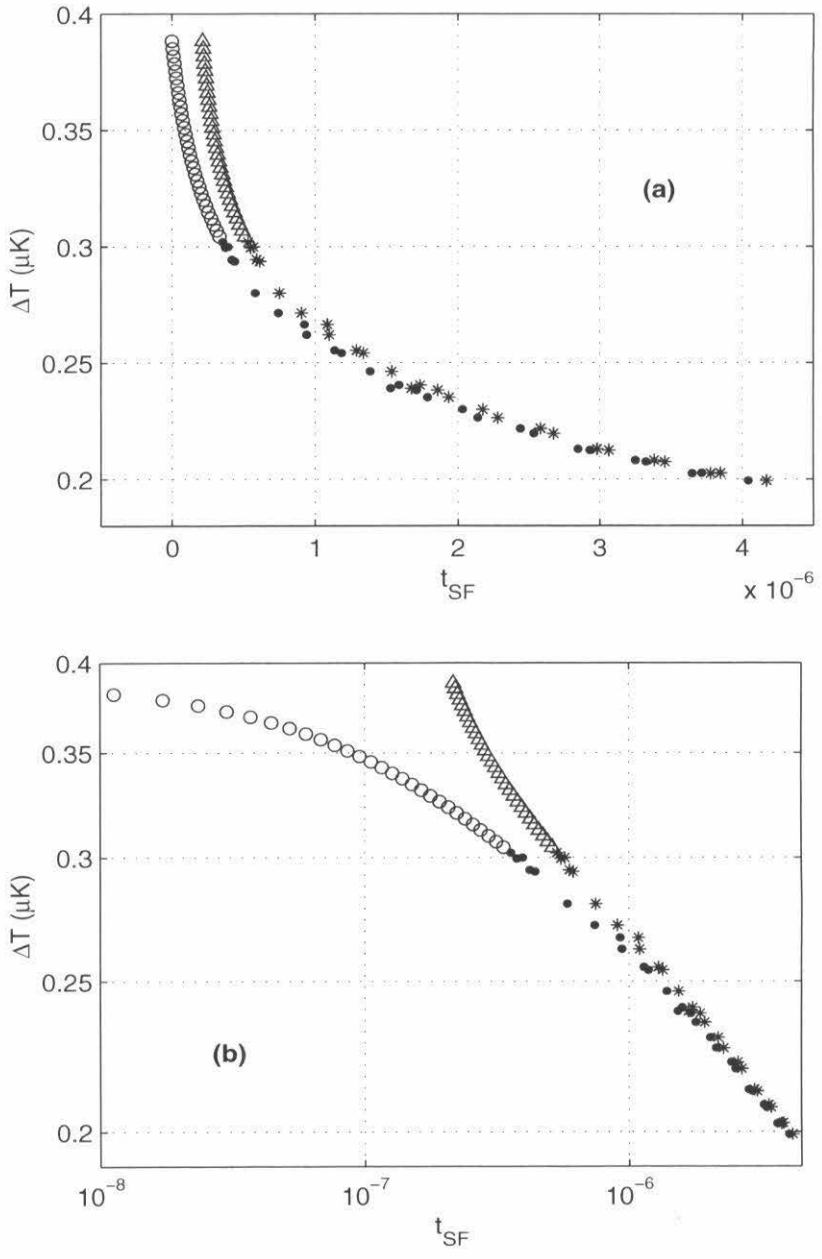

Figure 5.11: The singular Kapitza resistance as a function of superfluid temperature, for $Q = 3.6$ μW/cm^2. Dots ($\bullet$): the temperature drop across the cooler boundary (FBKA [78] data). Stars ($*$): the temperature drop across the hotter boundary (FBKA). Open circles ($\circ$): the temperature drop across the cooler boundary (extension of the FBKA data). Triangles ($\triangle$): the temperature drop across the hotter boundary (extension of the FBKA data). (a) Linear plot. (b) Log-log plot. The curvature is due to using $t_{\rm SF}$ vs. t_b.

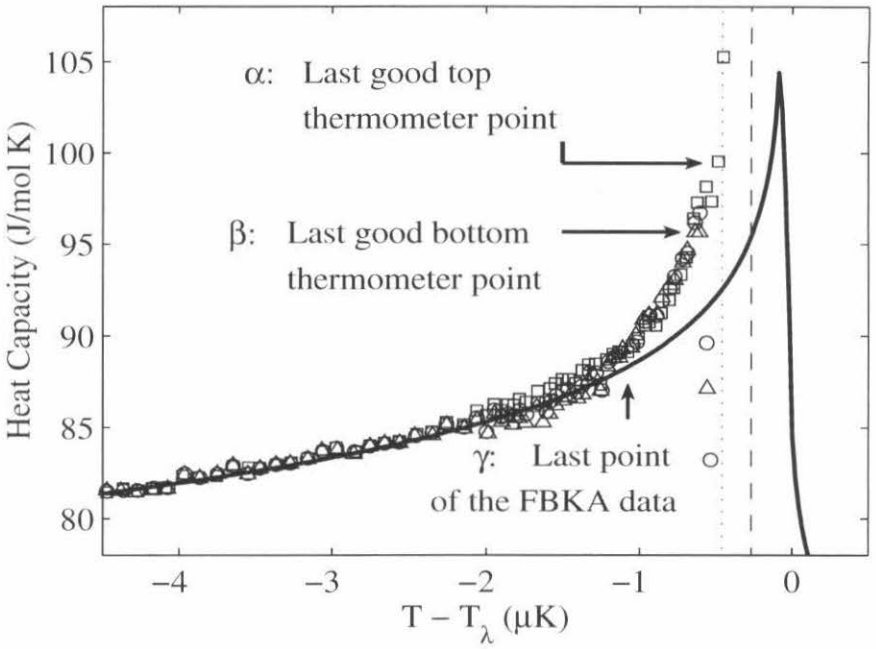

Figure 5.12: Binned heat capacity data at $Q = 2.26\ \mu\mathrm{W/cm}^2$ (file 030499.02) using three different measurements of the superfluid temperature. Solid line: $Q = 0$ data (fit to the LPE data, rounded for gravity). Open circles: using the average of the top and bottom thermometers, T_{SF}^1. Squares: using the top thermometer, T_{SF}^2. Triangles: using the bottom thermometer, T_{SF}^3. Dotted line: $T_{\mathrm{DAS}}(Q)$ [19]. Dashed line: Haussmann's $T_c(Q)$ [18]. Note that there is a small amount of disagreement at $T - T_\lambda \approx -1.5\ \mu\mathrm{K} \Rightarrow t_{\mathrm{SF}} \approx 0.689 \times 10^{-6}$. As can be observed on Fig. 5.11, this disagreement occurs at the very lowest reduced temperatures of the FBKA data, indicating that for this range the singular Kapitza resistance of our cell did not agree with their results.

is performed from point

$$\mathrm{min1} = \mathrm{P(k-1)} + \frac{\mathrm{length1}}{2} + 7$$

to point

$$\mathrm{max1} = \mathrm{P(k)} - 7,$$

and the fit on the ledge after the pulse is performed from point

$$\mathrm{min2} = \mathrm{P(k)} + 7$$

to point

$$\mathrm{max2} = \mathrm{P(k)} - \frac{\mathrm{length2}}{2} - 5,$$

where P(k) is the set of point numbers of the pulses illustrated in Fig. 5.5; length1 = P(k) − P(k − 1) is the number of points on the first ledge; and length2 = P(k + 1) − P(k) is the number of points on the second ledge (see Fig. 5.13b);

2. Extrapolating these two lines to the pulse point, P(k);

3. Calculating the height difference between the extrapolated lines at the point P(k). This difference is equal to ΔT^i_{SF}.

5.4.2 Calculating the heat capacity

The specific heat (per mole) of the helium sample was then calculated three different ways, using the various temperature measurements ΔT^i_{SF}:

$$\mathrm{SHC_{He}} = \left(\frac{\Delta \mathrm{Q_{cal}}}{\Delta \mathrm{T^i_{SF}}} - \mathrm{HC_{cell}} \right) / \mathrm{N}, \tag{5.10}$$

where $\mathrm{HC_{cell}} = 0.20675$ J/K is the heat capacity of the empty cell, and $N = 0.08918$ is the number of moles of helium in the sample.

The temperature range of the heat capacity measurements

We would expect that all of the data taken at temperatures less than $T_{\mathrm{DAS}}(Q)$ should give good heat capacity results. At higher temperatures, the fluid in the bottom of the cell becomes dissipative, and some of the heat from Q and Q_{cal} begins to heat

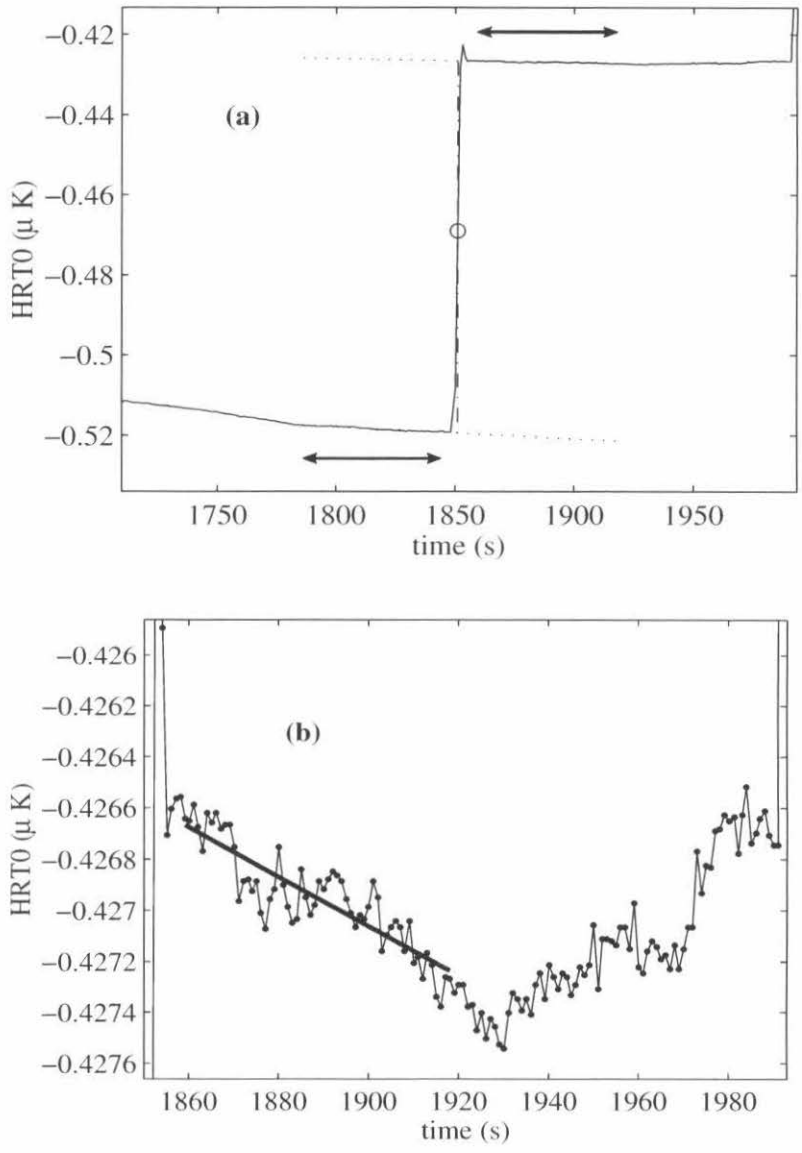

Figure 5.13: The points used for a temperature fit on a $Q = 3.7\ \mu\mathrm{W/cm}^2$ file (022399.01). (a) An entire pulse. The open circle is the point chosen as the 'pulse location,' P(k), found in Fig. 5.5. The arrows indicate the points used to fit the temperature drift before and after the pulse. Dotted lines: the extrapolation of the fitted lines. Dash-dotted line: the height, ΔT. (b) The fit to the upper ledge of the pulse shown in (a). The thick line is the fit, and it is only drawn over the range of the fit. The error estimate for this fit was $9.65 \times 10^{-5}\ \mu$K [see (5.11) to explain this quantity]. For both plots, the y-axis has an arbitrary zero. The minimum at $t = 1930$ s is where the shield temperature adjustment was made.

up this layer. As can be observed in Fig. 5.6, this causes the bottom thermometer to shoot up, and the apparent 'heat capacity' [the quantity calculated in (5.10)] to plummet. On the other hand, less heat now goes through the top of the cell, so the pulse sizes measured by the top thermometer begin to decrease, and the apparent 'heat capacity' begins to rise rapidly.

Although this behavior is just what we observe for the top thermometer (see point α in Fig. 5.12), we found that the temperature steps measured by the bottom thermometer suddenly became larger than those measured by the top thermometer at a temperature below $T_{\rm DAS}(Q)$ (see point β in Fig. 5.12). A careful examination of the drift data indicates that a distinct kink in the drift rate of the bottom thermometer can be clearly observed at this temperature (see Fig. 5.14). This phenomenon occurred at roughly the same value of T_W at the bottom surface for all values of Q used in the experiment. This value of T_W corresponds to a local coherence length, ξ, of a few micrometers, which we believe to be of the same order as the surface roughness of the wall. When ξ becomes larger than the surface roughness, the effective area through which heat passes from the interface into the bulk helium is reduced, thereby increasing the apparent R_b. A simple check indicates that the coherence length at the top surface should never become as large as the surface roughness before dissipation enters the cell.

The fact that the bottom thermometer begins to misbehave at $T_\beta(Q) < T_{\rm DAS}(Q)$ has several implications for our experiment. For one, we need to take this behavior into account when fixing the absolute temperature of the HRT0, the bottom thermometer. To adjust for the apparent increase in ΔT^h near the transition, we added an offset δ_0 to the temperature T_0 defined at $T_{\rm DAS}(Q)$ in (5.3). This phenomenon also means that we cannot really trust our heat capacity data for temperatures greater than T_β. We therefore were not able to get as close to the transition as we had originally hoped.

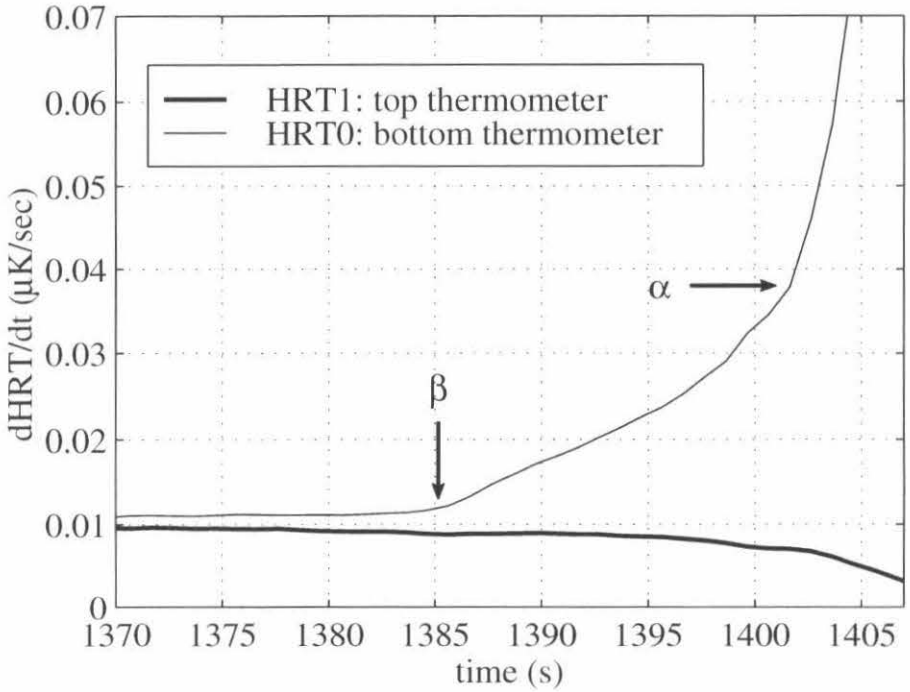

Figure 5.14: A drift data file (101098.01) taken at $Q = 2.907\ \mu\mathrm{W/cm^2}$. The two thermometers are not corrected for the Kapitza resistance. Since the singular Kapitza resistance is a function of temperature, their derivatives are not identical, even in the superfluid. Point β points to a kink in the derivative in HRT0, where we believe the coherence length ξ becomes larger than the surface roughness. Note that nothing happens in HRT1 at this temperature. Point α indicates another kink in the derivative of HRT0. This is the point where dissipation enters the cell, and corresponds to T_{DAS}. A decrease in the drift rate of HRT1 also occurs at α.

5.4.3 Improving the noise of the data

Throwing out noisy pulses

In order to improve the noise of our heat capacity measurement, we only used the pulses that had low error estimates to the lines fit to the data on both the trailing and following ledges. Most of this noise was due to the instability of the 1 K pot as a function of bath level. The fit to the data points on each ledge was performed using the least-squares fit function ('polyfit.m') in Matlab. The error estimate for each point, σ_y, was evaluated by this function. If, for a given line fit to N data points

on a pulse ledge,

$$\sqrt{\frac{1}{N}\sum_{i=1}^{N}\sigma_{yi}^2} \leq 2\times 10^{-4}\ \mu\mathrm{K}, \tag{5.11}$$

we would count the pulse towards the heat capacity measurement. Otherwise, we would throw out the data derived from that pulse. In Fig. 5.15, two fits are shown—the first one has an acceptable fit error, while the second one lies just outside the acceptable range, and was therefore not counted for the heat capacity measurement. Figure 5.16(a) shows a run where the first couple ramps had a high rejection rate due to the oscillating 1 K pot. Figure 5.16(b) shows the second of these upward ramps, where approximately one third of the pulses were rejected due to high error estimates. This technique ensured that only data taken with low thermal noise would count towards the heat capacity measurement.

Binning the data

The other thing we did to lower the noise of the heat capacity measurement was to average the data. As described in Sec. 4.1.4, each ramping sequence was repeated 5-10 times per run. In order to perform the data averaging, we defined a number of temperature bins, and then averaged both the temperature and the heat capactity over the points that fell within each bin.

Far away from the transition, the heat capacity data are fairly flat, and the bin sizes could be chosen to be quite large without losing any information. However, as the temperature approached $T_c(Q)$, the slope of the heat capacity data began to rise steeply. In this range, a higher density of bins was therefore required. For temperatures less than 2 μK below T_λ, we defined 10 bins/μK, and for higher temperatures, we defined 25 bins/μK. An example of the number of points per bin is shown in Fig. 5.17.

(a)

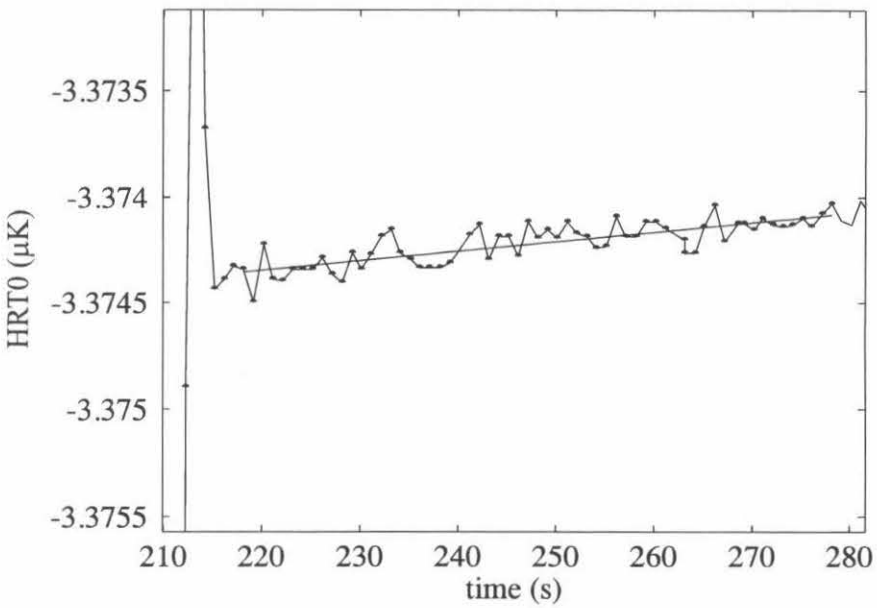

(b)

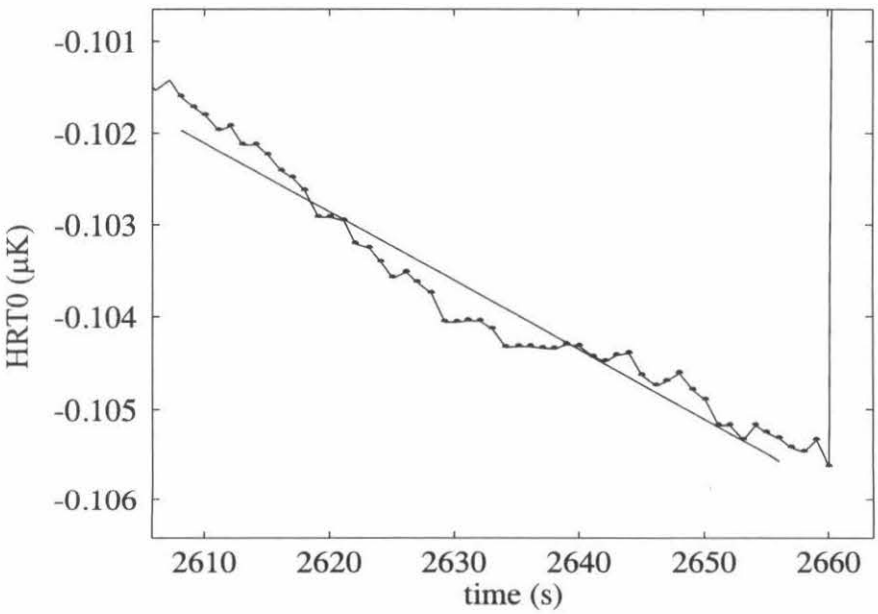

Figure 5.15: Fitting the temperature drift on a $Q = 3.7\ \mu\mathrm{W/cm}^2$ file (022399.01). (a) A pulse whose fit had an error estimate equal to $6.42 \times 10^{-5}\ \mu$K. (b) A pulse whose fit had an error estimate equal to $2.54 \times 10^{-4}\ \mu$K. This pulse would not have been selected. For both plots, the y-axis has an arbitrary zero.

(a)

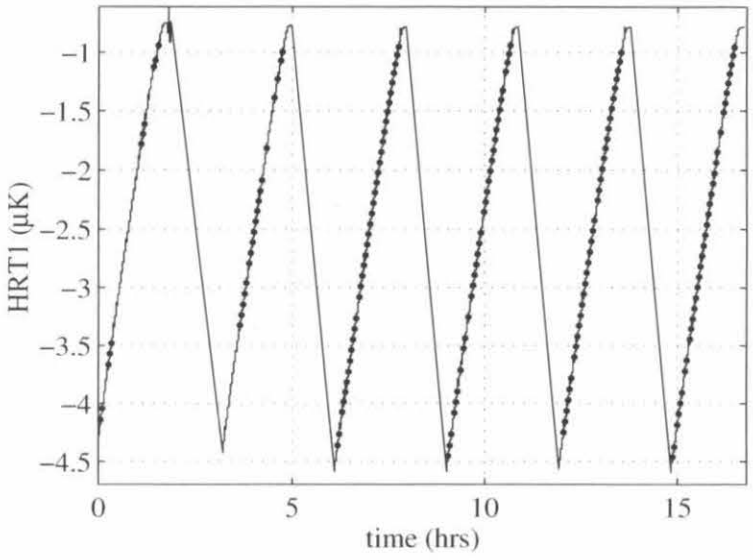

(b)

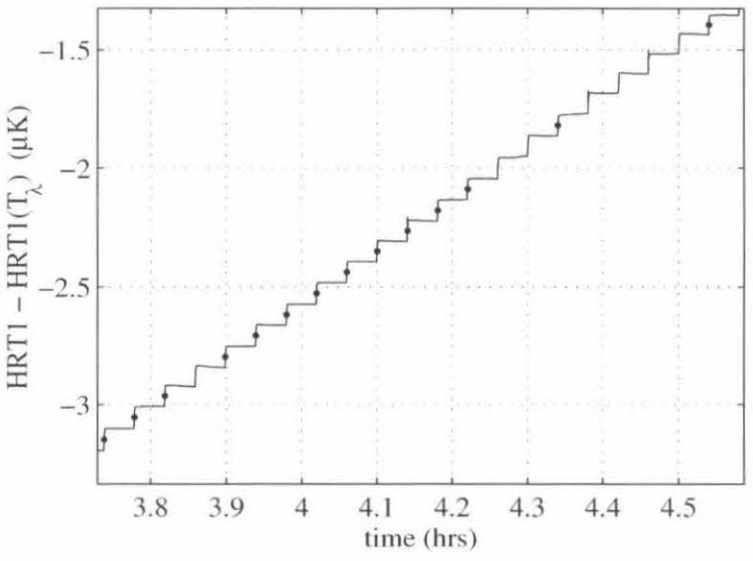

Figure 5.16: Pulse selection on a $Q = 3.7\ \mu\mathrm{W/cm}^2$ file (022399.01). The pulses that were selected to use for the heat capacity data are marked with a dot on the upward temperature rise. The other pulses were rejected because their error estimates were above the cutoff. (a) The whole file. This file was taken immediately after a helium transfer, and so the noise at the beginning of the file was particularly high. As a result, more points were thrown away during the first two ramps. The points thrown away on the later ramps were rejected because of bad servo response. (b) A portion of the second ramp, where the 1K pot was beginning to settle down.

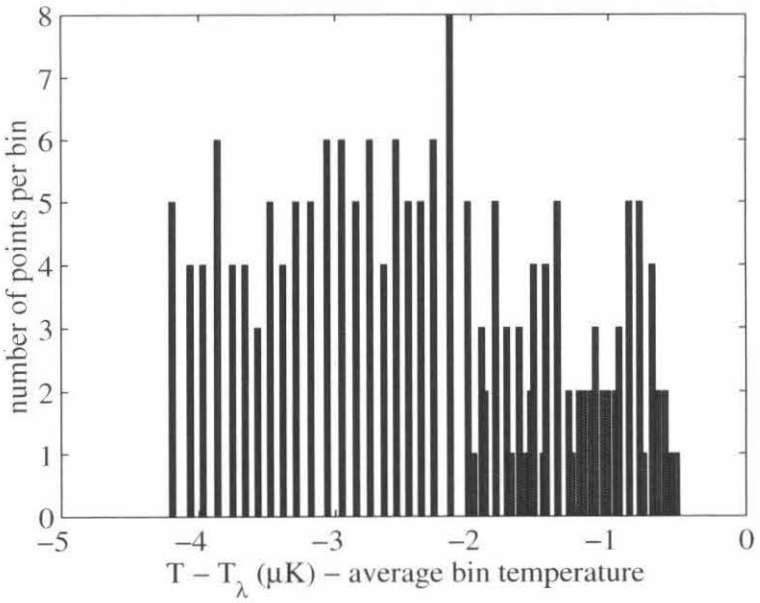

Figure 5.17: The distribution of points within the bins of a $Q = 3.71\ \mu\mathrm{W/cm}^2$ file (022399.01) for the average of the two thermometers. On this file, there were 404 accepted pulses. There were 18 bins for $T - T_\lambda < -2\ \mu$K, and 43 bins for $-2\ \mu\mathrm{K} < T - T_\lambda < T_{\mathrm{DAS}}(Q) - T_\lambda$.

5.5 The heat capacity data at various values of Q

As observed in Fig. 5.18, our various measurements of C_Q agree well with the heat capacity at $Q = 0$ for all temperatures lower than about 1 μK below T_λ. Between 1 μK and 0.5 μK below T_λ, a significant increase of the heat capacity is observed. This is the first direct experimental evidence for the increase in C_Q near $T_c(Q)$. The magnitude of the heat capacity enhancement increases with Q. These results will be compared with current theoretical predictions in Chapter 6.

5.6 Checking the accuracy of the data analysis

Before comparing how our results measure up to theory, it is worth taking a little time to ensure that the possible errors due to our method of data analysis are relatively small.

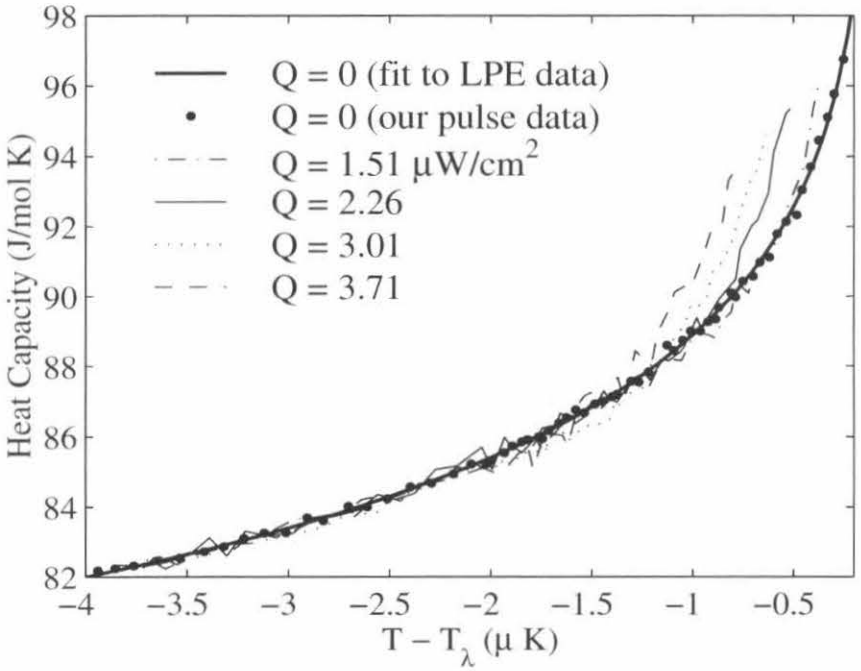

Figure 5.18: Representative heat capacity data at various Q. The C_Q curves are terminated at $T_\beta(Q)$, the temperature marked by β in Fig. 5.12.

5.6.1 The potential error in fixing the temperature scale

The accuracy of our data analysis technique is strongly dependent on whether or not the point number of $T_{\rm DAS}(Q)$ was chosen correctly. If the wrong temperature was chosen, then the singular Kapitza adjustment would be done at the wrong temperature values, and the heat capacity calculation would not be correct. Fortunately, there are several checks that can be performed to verify that the right value of $T_{\rm DAS}(Q)$ was selected:

1. The heat capacity at all non-zero Q values should agree with the the heat capacity curves taken at $Q = 0$, for temperatures lower than about 1 μK below T_λ.

2. The heat capacity measured with $T^1_{\rm SF}$, $T^2_{\rm SF}$, and $T^3_{\rm SF}$ should give identical results.

3. Far from the transition temperature, $(T_0 - T_1)/2$ should be approximately equal

to the FBKA measurement of $\Delta T = Q \cdot R_b(Q)$. In this temperature range, there should be little difference between ΔT^h and ΔT^c. In addition, close to the transition temperature, $(T_0 - T_1)/2$ should lie half way in-between ΔT^c and ΔT^h (see Fig. 5.19).

All of these checks confirm that our method of choosing $T_{\mathrm{DAS}}(Q)$ was quite accurate. Nonetheless, in future experiments, it would be worth attempting to ramp Q off and on for every run, so that the temperature scale can be definitively determined by the location of T_λ at $Q = 0$. As previously mentioned, we were unable to do this during our cooldown because of time limits set by a bath level dependant oscillating 1 K pot and a fluxcounter that would lose count for fast temperature scans. However, having T_λ as a marker would have been extremely useful and saved many headaches during data analysis.

5.6.2 The error due to choosing the incorrect point on the pulse at which to calculate ΔT

For the pulse method, the heat capacity C should be calculated along the temperature trajectory in such a way that:

$$\Delta Q_{\mathrm{cal}} = \int_{\mathrm{pulse}} C \frac{dT}{dt}\, dt. \tag{5.12}$$

If we simplify the process by calculating $C = \Delta Q_{\mathrm{cal}}/\Delta T$, we will obtain the exact same result so long as ΔT, the height difference between the two extrapolated line fits, is measured at the data point at which Area 1 and Area 2, shown in Fig. 5.20, are equal.

The amount of error in the heat capacity measurement caused if the point at which ΔT is calculated is chosen incorrectly, will depend on the difference between the slopes of the temperature ledges preceding and following the heat pulse. If there is no difference between the two slopes, then ΔT will be independent of what point is chosen [see Fig. 5.20(a)]. However, if there is a large difference between the slopes,

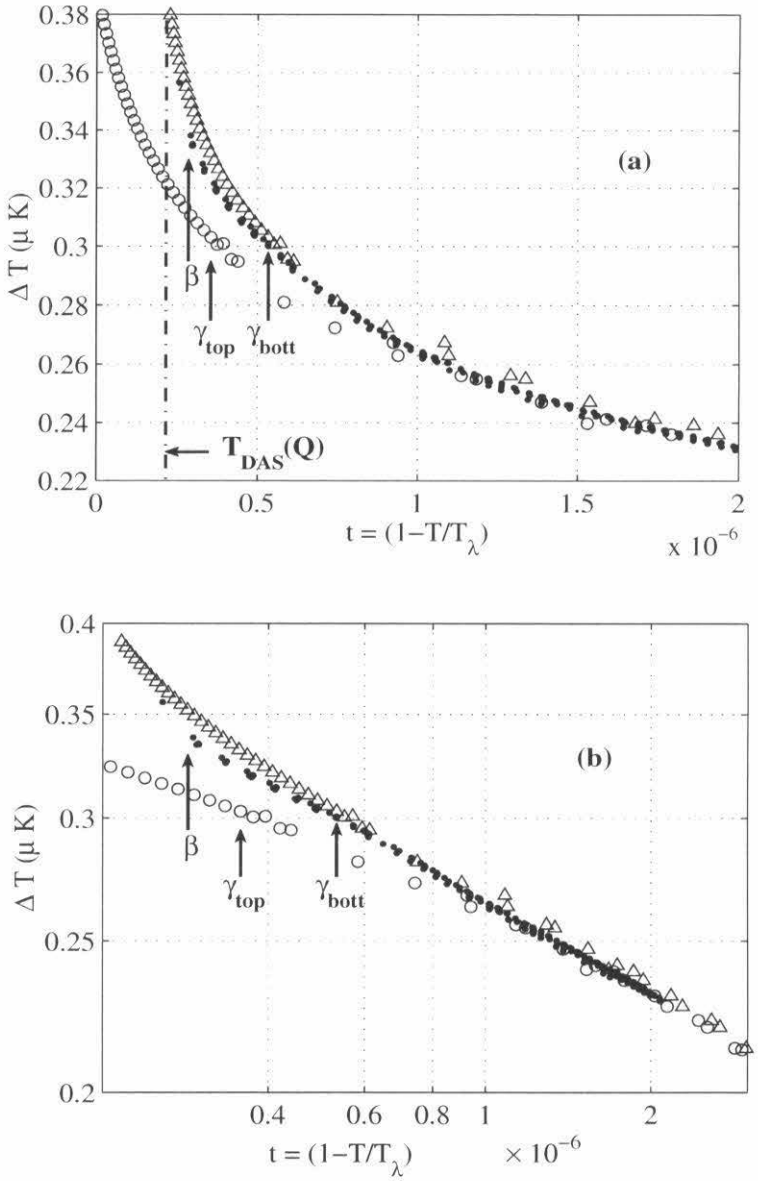

Figure 5.19: The experimental singular Kapitza resistance on the last six ramps of a $Q = 3.6$ μW/cm^2 file (030999.01). Open circles ($\circ$): ΔT^c, the temperature drop across the cooler boundary (both the FBKA data and its extension); triangles ($\triangle$): ΔT^h, the temperature drop across the hotter boundary (both the FBKA data and its extension); solid dots ($\bullet$): the measured singular Kapitza resistance, found by plotting $(\mathrm{HRT0_{ledge}} + \mathrm{HRT1_{ledge}})/2$ vs. $(\mathrm{HRT0_{ledge}} - \mathrm{HRT1_{ledge}})/2$; β: the temperature at which the bottom thermometer begins to misbehave; γ_{top}: the lowest temperature of the FBKA data for ΔT^c; γ_{bott}: the lowest temperature of the FBKA data for ΔT^h. (a) Linear plot. (b) Log-log plot. The pulse data should agree with the FBKA data far away from T_λ, and be halfway in between ΔT^c and ΔT^h close to the transition.

ΔT will be a strong function of which point is chosen [see Fig. 5.20(b)].

We can make some estimate of what the possible error in our heat capacity measurement due to this effect might be. The pulses on a typical file[7] had an average difference of 3×10^{-5} μK/sec between the slopes of the preceding and following ledges. The error in choosing at what point ΔT should be calculated is at most two points, which corresponds to approximately two seconds. Therefore, the error in calculating ΔT is around $\delta(\Delta T) = 6\times10^{-5}$ μK. Since, for our data, $\Delta T \approx 0.1$ μK, this represents an error of approximately:

$$\frac{\delta\left(\Delta T\right)}{\Delta T} \times 100 \approx \frac{6 \times 10^{-5}}{0.1} \times 100 = 0.06\%, \tag{5.13}$$

which is around ten times smaller than the noise of our data.

[7] We used file 022399.01 for this calculation.

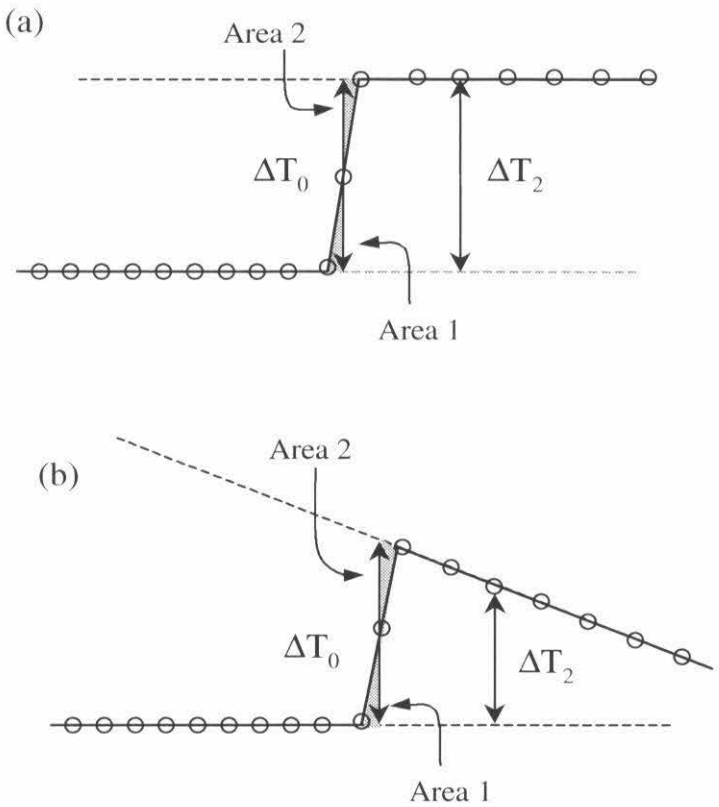

Figure 5.20: A schematic drawing of the error due to choosing the wrong point when the ledges before and after a pulse have different slopes. Open circles: data points. Dashed line: the fit to the data points. The correct point to calculate ΔT is chosen when Area 1 = Area 2. (a) No difference between the slopes of the preceding and following ledges. Shaded triangles: the area between the actual data (the sloped line) and the ideal line used to calculate the heat capacity (vertical line) (b) A large difference between the slopes of the preceding and following ledges.

Chapter 6 Results and Conclusions

In Chapter 1, we demonstrated that the heat capacity of superfluid ^{4}He at constant heat flux, C_Q, is predicted to diverge at a Q-dependent transition temperature. In Chapter 5, we showed that the first measurements of the heat capacity indicate that C_Q is, indeed, enhanced as a function of Q. The question remains, however, whether the theoretical prediction for C_Q and the experimental results share more than general qualitative agreement.

6.1 Comparing our data to theoretical predictions

Our heat capacity data show a considerably larger enhancement than predicted by current theories. This is clearly illustrated in Fig. 6.1, where a heat capacity curve taken at $Q = 3.5\ \mu\mathrm{W/cm}^2$ is shown along with the theories of Haussmann [18] and HD [6, 8]. To determine the extent of the disagreement, we need to examine how our data compares to the theory at various limits. All theories predict[1] that the enhancement should obey scaling of the form

$$\Delta C_Q = t^{-\alpha} f_{J_s}\left(\varrho^2\right), \tag{6.1}$$

where $f_{J_s}(x)$ is a universal scaling function and $\varrho = Q/Q_c$. Since we know that ΔC_Q is analytic at small Q for $t \neq 0$, this implies that

$$\Delta C_Q\, t^{\alpha} = A\varrho^2 + B\varrho^4 + C\varrho^6 + \ldots \tag{6.2}$$

The first term of (6.2) would be the exact result for $\Delta C_Q\, t^{\alpha}$ if ρ_s were not depressed by W— in Sec. 1.6.3 we saw that this was true in the MFT limit. It is easy to show

[1] A short proof of why $\Delta C_Q t^{\alpha}$ must scale in this way is given in Appendix A.

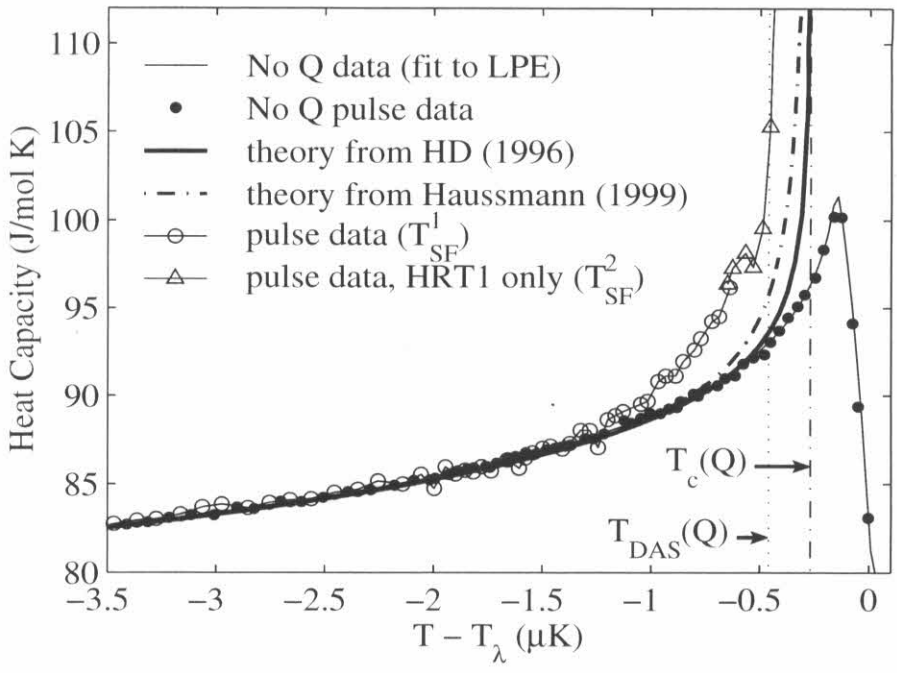

Figure 6.1: Comparing theoretical predictions and experimental measurements for C_Q, for $Q = 3.5$ μW/cm^2 (file 030799.01). The $T_c(Q)$ indicated is that calculated by Haussmann [18]. For all temperatures less than T_β (the point where the symbols switch from $\circ$ to $\triangle$), the theory of HD is nearly identical to the result when ρ_s is not depressed by W.

that this must be true in general[2]

We begin with the free energy differential (recall that $q = Q/ST$):

$$d\Phi = -sdT - Wdq = -sdT - \frac{q}{\rho_s}dq \tag{6.3}$$

$$\Rightarrow \left(\frac{\partial \Phi}{\partial q^2}\right)_{T,q=0} = -\frac{1}{2\rho_s} \tag{6.4}$$

Since

$$C_q = -TV\left(\frac{\partial^2 \Phi}{\partial T^2}\right)_q \Rightarrow \left(\frac{\partial C_q}{\partial q^2}\right)_T = TV\left(\frac{\partial^2}{\partial T^2}\frac{1}{2\rho_s}\right)_{q=0} \tag{6.5}$$

[2]D. L. Goodstein, private communication (1999).

Therefore,

$$C_q = C_0 + A'q^2 + \ldots \tag{6.6}$$

where the coefficient of q^2 is:

$$A' = TV\left(\frac{\partial^2}{\partial T^2}\frac{1}{2\rho_s}\right)_{q^2=0}, \tag{6.7}$$

where $A = A'(Q_c/ST)^2$. Since A' depends only on the equilibrium $\rho_s(q=0,T)$, it is completely determined by the two fluid model.

From (6.2), we can thus define four different limits:

1. When ϱ^2 is sufficiently small, $\Delta C_Q \approx 0$, and $C_Q = C_0$, the heat capacity at zero Q.

2. When only the leading order term matters, the magnitude of ΔC_Q does not depend on the way in which ρ_s is depressed by W. In this region, the physics of the heat capacity enhancement is entirely due to the two-fluid model.

3. When $\varrho^2 \lesssim 1$, ΔC_Q shows a divergence that depends on the depression of ρ_s with W.

4. When $\varrho^2 > 1$, the helium is dissipative fluid, and C_Q is not defined.

As we have already noted, the data show excellent agreement with theory in limit (1), where no enhancement is expected. Very close to the transition, in limit (3), the prediction for C_Q is not very reliable, since it is heavily dependent on the form of $\rho_s(W)$, of which little is known. However, we have not yet examined the intermediate region (2), $\varrho^2 < 1$, where the two-fluid model should dominate the physics. We would expect the agreement between our data and the prediction in this region to be fairly good, since the two-fluid model is quite dependable.

To determine what part of our data falls within this limit, we recall that:

$$t_c(Q) = \frac{T_\lambda - T_c(Q)}{T_\lambda} = \left(\frac{Q}{Q_0}\right)^x, \tag{6.8}$$

where $x = 1/2\nu$, and

$$Q_c(t) = Q_0\, t^{2\nu}. \tag{6.9}$$

This expression allows us to express ϱ as a function of t when the data is taken at fixed Q:

$$\varrho = \frac{Q}{Q_c} = \frac{Q}{Q_0}\, t^{-2\nu}. \tag{6.10}$$

For the data shown in Fig. 6.1, taken at $Q = 3.6\ \mu\mathrm{W/cm}^2$, this gives $\varrho = 5.48 \times 10^{-10}\, t^{-1.3}$, where we have used the most recent value for Q_0 [18]. If we set the intermediate ϱ^2 limit (2) to be defined as those temperatures for which $0.01 \leq \varrho^2 \leq 0.1$, we find that we should expect the two-fluid model to dominate the physics when $1.82 \times 10^{-7} \leq t \leq 4.41 \times 10^{-7}$, or when $-0.96\ \mu\mathrm{K} \leq T - T_\lambda \leq -0.396\ \mu\mathrm{K}$. Therefore, most of the data below T_β where an enhancement is observed is in the intermediate ϱ^2 limit.

Thus, if one believes that the theoretical value of Q_0 is correct, the disagreement between our data and the theoretical curve is rather disturbing.

6.2 Scaling

The extent of the discrepancy between theory and experiment can be further elucidated by actually plotting the data in scaled form.

Figure 6.2 shows the scaling functions $f_{J_s}(\varrho^2)$ for Haussmann's theory [18], for HD theory [6], and for the case when ρ_s is not depressed by a counterflow.

Figure 6.3 shows our heat capacity data plotted in scaled form. The data are taken at constant Q, changing Q_c by changing T, as was shown in (6.9). They are measured with the average of the top and bottom thermometers (T_{SF}^1), and are therefore terminated at point β marked in Fig. 5.12. The most recent theoretical value of Q_0 [18] is used to scale the data.

The data agree well with the scaling prediction for all but the lowest heat cur-

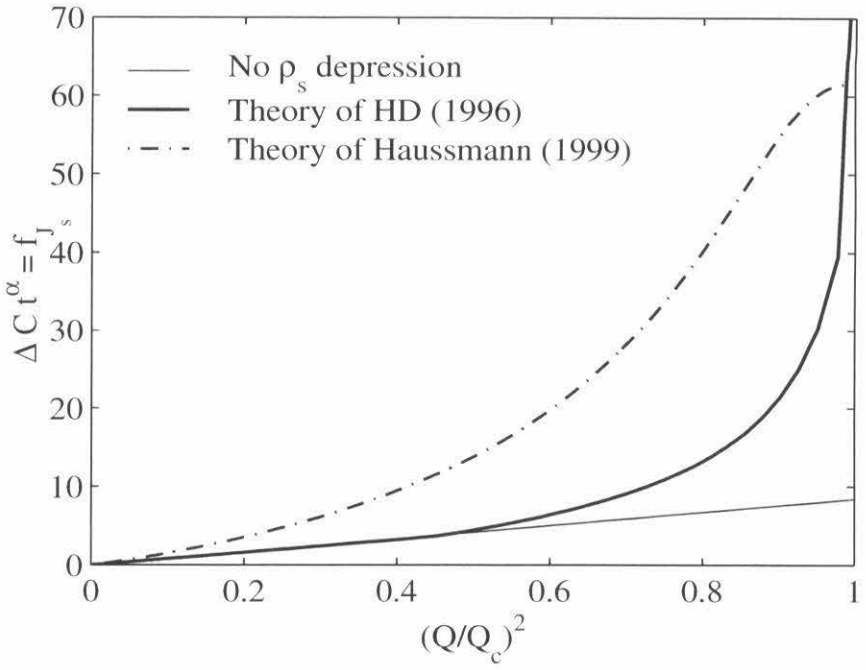

Figure 6.2: The theoretical scaling functions, f_{J_s}. The theory of HD was calculated in Refs. [8, 9]. The theory of Haussmann was calculated in Ref. [18]. These two theories are scaled by their own values of Q_c.

rents[3]— they fall on a single curve, as anticipated. They end when $(Q/Q_c)^2 \approx 0.1$, or $(Q/Q_c) \approx 0.3$, and therefore lie within the intermediate ϱ^2 limit. We would thus expect f_{J_s} to be proportional to ϱ^2. As shown in Fig. 6.3, neither of the theories depart much from linearity in this region. We do find that our data for $2\ \mu\mathrm{W/cm}^2 \leq Q \leq 4\ \mu\mathrm{W/cm}^2$ can be represented in the form

$$f_{J_s} = \Delta C_Q\, t^\alpha = A\varrho^2, \tag{6.11}$$

where $A = 69\ \pm\ 4$ J/mol K. However, the theoretical expression for the first order term given in (6.7) gives a value of $A = A'(Q_c/ST)^2$ almost exactly ten times less than

[3]One possible explanation for why the data of the lowest heat current files do not conform is that their enhancements are expected to occur at lower reduced temperatures. They therefore rely the most on the singular Kapitza resistance correction. If there is any error with our extension of the FBKA data, these files will be influenced the most. More experimental data, preferably with a midplane thermometer, is needed before the final verdict can be issued.

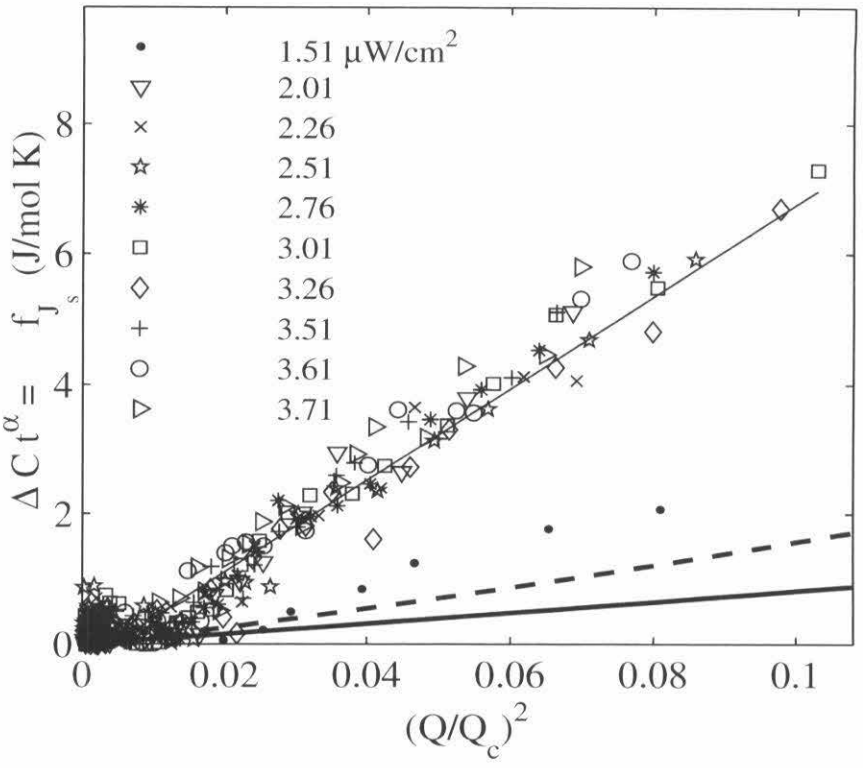

Figure 6.3: The scaled heat capacity data compared to the theoretical scaling functions, f_{J_s}. Each theory is scaled by its own value of Q_c, and the experimental data is scaled by Haussmann's Q_c. Thin solid line: the fit to the data expressed in (6.11). Thick solid line: theory of Chui *et al.* [8] based on HD theory [6]. Dashed line: theory of Haussmann [18].

this experimentally measured value. Thus, if the theoretical value of Q_0 is correct, the two-fluid model (with ρ_s independent of ϱ) cannot explain our result.

One way to test whether the theoretical value of Q_0 is correct is to see if we truly are in the intermediate ϱ^2 range, where only the first order term in (6.2) matters. To do this, we first divide both sides of (6.2) by $Q^2\, t^{-2\nu}$ to obtain:

$$\frac{\Delta C_Q\, t^{\nu+2}}{Q^2} = A_0 + B_0 \left(Q^2\, t^{-4\nu}\right) + C_0 \left(Q^2\, t^{-4\nu}\right)^2 + \ldots, \tag{6.12}$$

where

$$A_0 = \frac{A}{Q_0^2} = \frac{\nu(\nu+1)V}{2\rho_0 S^2 T_\lambda^3} = 1.6075 \times 10^{-7}. \tag{6.13}$$

Haussmann and Dohm's theory [6] calculated $A_0 = 1.14 \times 10^{-7}$, and Haussmann's theory [18] calculated $A_0 = 2.24 \times 10^{-7}$ [105]. We then plot $Q^2\, t^{-4\nu}$ vs. $\Delta C_Q\, t^{\nu+2} Q^{-2}$ to see whether the data have any curvature at all (implying that they are influenced by higher order terms), or whether they fall on a straight horizontal line (implying that they are dominated by the leading order term). Plotting it in this way also eliminates any dependance on the theoretical value of Q_0. As can be seen in Fig. 6.4, the data are scattered about a constant value that is *exactly* ten times larger than the value expected if ρ_s were not depressed by W.

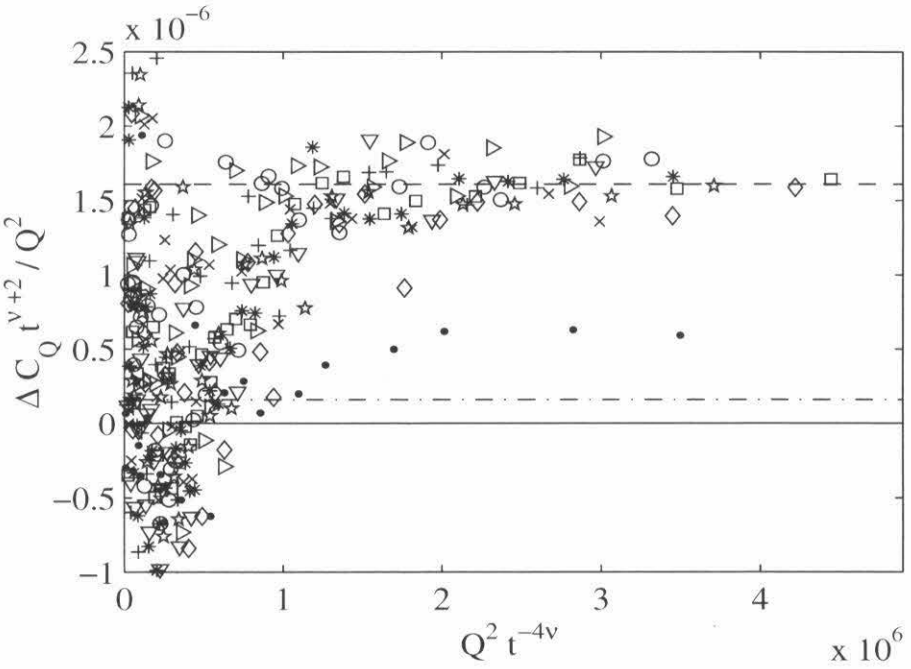

Figure 6.4: A plot to determine the linearity of the scaling data. The data symbols are the same as those used in Fig. 6.3. Q is in units of W/cm^2. The units of the y-axis are (J/mol K)/(W/cm^2)^2, and the units of the x-axis are (W/cm^2)^2. Solid line: $y = 0$. Dotted-dashed line: $y = 1.6075 \times 10^{-7}$. Dashed line: $y = 1.6075 \times 10^{-6}$.

6.3 Rescaling

One possible (and optimistic) explanation for the discrepancy between the theoretical curves and the experimental measurements is that our data are not, in fact, in the low ϱ^2 limit. Although it certainly appears that our data scale to a linear function, it is possible that the scatter in our data simply obscures the underlying curvature. In other words, perhaps the theories are producing reasonable estimates for the universal scaling function $f_{J_s}(\varrho^2)$, but that the nonuniversal amplitude Q_0, defined by (6.8), is estimated less accurately. This would not be *all that* surprising, since the calculation of Q_0 depends on detailed properties of the ^{4}He system and is considerably more difficult to compute [4] than $f_{J_s}(\varrho^2)$. As illustrated in Fig. 6.5(a), the choice $Q_0 = 3460$ W/cm^2 places the experimental data on top of Haussmann's theoretical curve [18].[5] With this choice, $T_c(Q)$ lies just above $T_{\rm DAS}(Q)$ in the temperature range of the experimental data (see the dashed-dotted line in Fig. 6.6). A somewhat smaller choice for Q_0 would provide an equally good fit to the earlier theory [6].

Unfortunately, all of the data, even rescaled in this manner, lie at $\varrho^2 \lesssim 0.3$ (or $Q/Q_c \lesssim 0.6$) where the scaling function has little structure. In this range, the scaling function—like our data—is essentially indistinguishable from linear within the scatter of the data. A true test of the rescaling hypothesis would require data in the regime $(Q/Q_c)^2 \to 1$ where the scaling function diverges.

For completeness, we also show in Fig. 6.5(b) an equally good scaling collapse based on the assumption that $T_c(Q) \approx T_{\rm DAS}(Q)$. For this plot, we have used $Q_c(T)$ derived from (6.8) with $x = 0.813$ (i.e., effectively $\nu = 0.615$) and $Q_0 = 650$ W/cm^2 (optimally chosen within the error bars quoted in [19]). Since $T_{\rm DAS}(Q)$ places a lower bound on $T_c(Q)$, the sharpest conclusion we can make at this stage is that the data are consistent with the scaling hypothesis for a fairly broad range of experimentally and theoretically motivated parameter choices, and that more data closer to $T_c(Q)$ will be required for a critical test of the theory.

[4] P. B. Weichman, private communication (2000).

[5] This value is in fact within the estimated margin of error for the amplitude calculation. The uncertainty of the theory is a factor < 2 [R. Haussmann, private communication (1999)], while the adjustment here is $\simeq 1.9$.

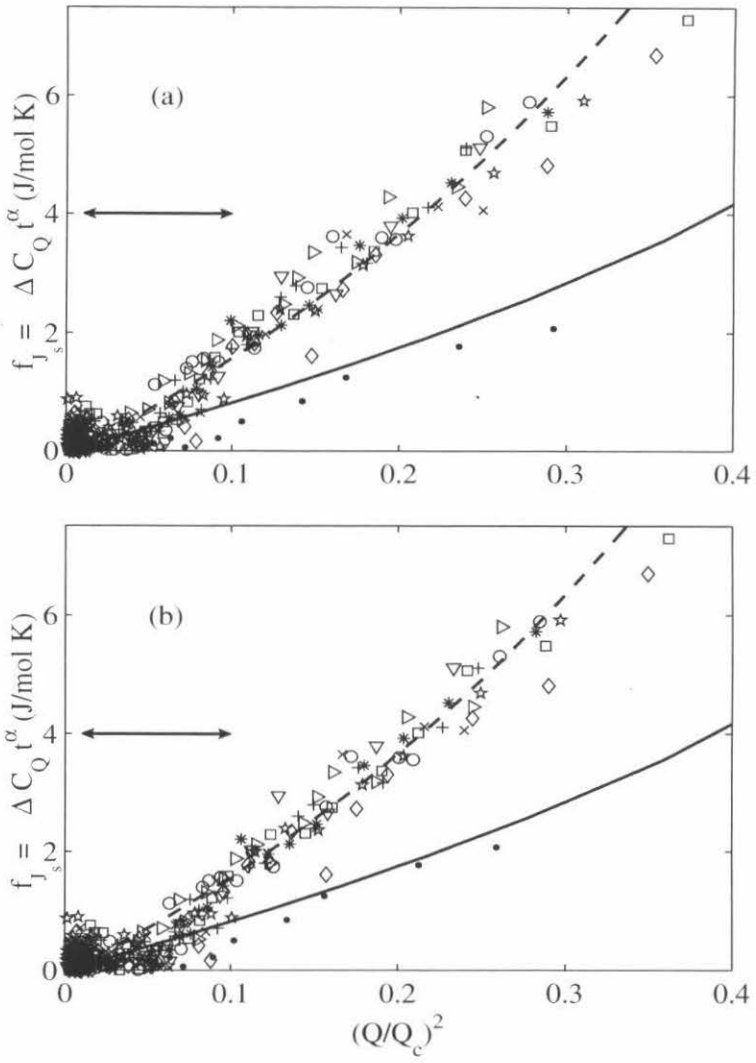

Figure 6.5: Alternative scaling plot of the heat capacity measurements for various values of Q [25]. The data symbols are the same as those used in Fig. 6.3. The experimental data are scaled using $Q_c(T)$ derived from (6.8) by (a) using the theoretical exponent value $x = 1/2\nu = 0.746$, but amplitude $Q_0 = 3460$ W/cm^2 chosen to best match the theoretical scaling function; and by (b) assuming that $T_c(Q) \approx T_{DAS}(Q)$ with $Q_0 = 650$ W/cm^2 and $x = 0.813$. For the Q-range of the experimental data, the two analyses are basically identical, with the lines completely overlapping to well within experimental resolution. Only for higher Q data would the two fits become distinguishable. Solid line: theoretical prediction neglecting dissipation [8, 9]. Dashed line: theoretical prediction including dissipation [18]. Arrows: the intermediate $\varrho^2 = (Q/Q_c)^2$ region, where the first coefficient of the expansion in (6.7) dominates.

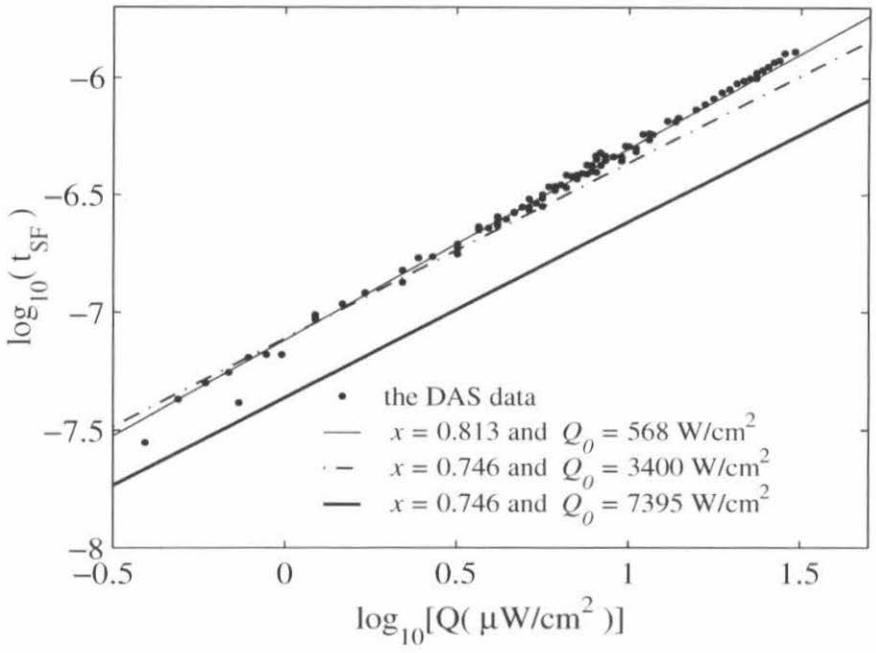

Figure 6.6: Thick solid line: $T_c(Q)$, the theoretically predicted temperature of superfluid breakdown [6]; thin solid line: $T_{\rm DAS}(Q)$, where the exponent x and amplitude Q_0 are chosen to best fit to the observed temperature of superfluid breakdown represented by the data points [19]; dashed-dotted line: the value of Q_0 that, along with the theoretical value $x = 1/2\nu$, makes the experimental heat capacity data match the more recent theoretical prediction for the scaling function [18] (see Fig. 6.5).

6.4 Conclusions

Our data give the first conclusive evidence that C_Q, the heat capacity of ^{4}He at fixed Q, is enhanced as a function of Q. In addition, C_Q scales with $\varrho^2 = (Q/Q_c)^2$, as predicted. However, *either*:

1. ΔC_Q is considerably larger than theoretically predicted *or*

2. $T_c(Q)$ is much closer to $T_{\rm DAS}$ than current theory predicts, and our data are therefore strongly influenced by the beginning of the divergence at $T_c(Q)$.

Data lying closer to $T_c(Q)$ are needed to determine which of these two options is correct, or if there is yet another unexplored possibility that explains our results.

The answer should illuminate the way that ρ_s is depressed by Q as well as the actual value of $T_c(Q)$.

Appendix A A proof for why $\Delta C_Q\, t^{-\alpha}$ scales with $(Q/Q_c)^2$

According to (1.26), the change in the free energy due to a constant heat flux, Q, is

$$\Delta\Phi = -\int_0^q W\, dq, \tag{A.1}$$

where $q = \rho_s W$.

We now define the scaling variable ϱ by the equation

$$\varrho \equiv q/q_c, \tag{A.2}$$

where $q_c = Q_c/ST = (Q_0/ST)\, t^{2\nu}$. We now show that if $\rho_s(T,Q)$ scales in the form

$$\rho_s(T,Q) = \frac{\rho_s(T,0)}{g(\varrho)} = \frac{\rho_0\, t^{\zeta}}{g(\varrho)}, \tag{A.3}$$

then the specific heat C_Q will scale as well. Here $\zeta = \nu$, and $g(\varrho) = 1/f(\kappa)$ [see (1.29)] is a smooth universal scaling function, with $g(0) = 1$, that suppresses ρ_s as ϱ is increased. Substituting this expression into (A.1), we find

$$\Delta\Phi = -\frac{q_c^2}{\rho_0\, t^{\zeta}} G(\varrho),\ G(\varrho) \equiv \int_0^{\varrho} x g(x)\, dx, \tag{A.4}$$

with universal scaling function $G(\varrho) \approx \varrho^2/2$ for small ϱ, equivalent to the two fluid result $\Delta\Phi \approx q^2/2\rho_s(T,0)$.

From (A.2), $\varrho = (Q/Q_0)\, t^{-2\nu}$, and

$$\left(\frac{\partial \varrho}{\partial t}\right)_Q = \frac{2\nu}{T_\lambda}\left(\frac{Q}{Q_0}\right) t^{-2\nu-1} = \frac{2\nu}{T_\lambda}\varrho\, t^{-1}. \tag{A.5}$$

From (A.4),

$$\Delta\Phi = -\frac{Q_0^2}{S^2 T_\lambda^2 \rho_0} t^{2-\alpha}\, G(\varrho), \tag{A.6}$$

where the specific heat exponent is $\alpha = 2 - 3\nu$ (the usual hyperscaling relation in $d = 3$ dimensions), and it is permissible to replace T by T_λ in the prefactor in the critical region. This demonstrates explicitly that the free energy increment scales with the expected exponent.

Proceeding now to the specific heat, we have

$$-\frac{\rho_0 S^2 T_\lambda^2}{Q_0^2}\left(\frac{\partial\Delta\Phi}{\partial T}\right)_Q = \frac{1}{T_\lambda} t^{1-\alpha} H_Q(\varrho),\ H_Q(\varrho) \equiv -3\nu G(\varrho) + 2\nu\varrho G'(\varrho), \tag{A.7}$$

and

$$-\frac{\rho_0 S^2 T_\lambda^2}{Q_0^2}\left(\frac{\partial^2\Delta\Phi}{\partial T^2}\right)_Q = \frac{1}{T_\lambda^2} t^{-\alpha} f_{J_s}(\varrho),\ f_{J_s}(\varrho) \equiv (1-3\nu) H_Q(\varrho) + 2\nu\varrho H_Q'(\varrho). \tag{A.8}$$

The specific heat enhancement obeys the requisite scaling form:

$$\Delta C_Q = -TV\left(\frac{\partial^2\Delta\Phi}{\partial T^2}\right)_Q = C_0 t^{-\alpha}\, f_{J_s}(\varrho), \tag{A.9}$$

where the amplitude is given $C_0 = VQ_0^2/\rho_0 S^2 T_\lambda^3$, and the universal scaling function obeys $f_{J_s}(\varrho) \approx \nu(\nu+1)\varrho^2/2$ for small ϱ, equivalent to (1.36).

Appendix B Experimental Details

This Appendix contains very specific details about the equipment used during this experiment. It will probably be of little interest to anybody except for Xinkai Wu, Andrew Chatto, and other future inheritors of my experiment. It is intended to limit the amount of time that they are forced to spend digging through my numerous lab books, sorting through endless descriptions of leak checking and cooldown procedures in order to find essential descriptions of lab equipment and calibrations. I have tried to include all of the information that I had to hunt for at one time or another during my run.

B.1 The heaters

Heater	location	resistance	# of wires	purpose
H1	Stage 1	235.3 Ω	2	servo S1
H2	Stage 2	270.7 Ω	2	servo S2
H3	Stage 3 (shield)	240.3 Ω	2	servo shield
H4	Calorimeter (top)	92.4459 Ω	4	hold/switch Q to the top
7W	Calorimeter (top)	49.546 Ω	4	hold/switch Q to the top
6W	Calorimeter (bottom)	312.514 Ω	4	apply Q
5W	Calorimeter (bottom)	36.963 Ω	4	apply Q_{cal}

Table B.1: Heater values. The listed 2-wire resistance values include the lead resistances. Without the lead wires, these heaters were approximately 50 Ω each.

B.2 The germanium resistance thermometers (GRTs)

	location	**serial number**	**R vs. T calibration curves taken by:**
GRT1	Stage 1	25770	Lakeshore
GRT2	Stage 2	26294	P.K. Day
GRT3	Stage 3	26293	P.K. Day
GRT4	Calorimeter	25771	Lakeshore
GRT5	SQUID holding bracket	26295	P. K. Day

Table B.2: GRT locations.

The GRT calibrations are fit to an equation of the form:

$$\ln T = a_0 + a_1 \ln R + a_2 (\ln R)^2 + ... \tag{B.1}$$

and

$$\ln R = b_0 + b_1 \ln T + b_2 (\ln T)^2 + ... \tag{B.2}$$

	$1.4 < T < 2.7$	$2.7 < T < 4.5$	$1.4 < T < 5.0$
a_0	6.2091449	2.0064398	4.5429196
a_1	-0.90147248	0.59865212	-0.35487907
a_2	0.041739325	-0.13665641	-0.017659023
a_3	-0.00076388126	0.0063042152	0.0013741778
b_0	12.339725	12.641712	12.350092
b_1	-4.4024999	-5.2370130	-4.4608890
b_2	0.95767928	1.7394952	1.0596051
b_3	-0.12858632	-0.37923448	-0.18374704

Table B.3: GRT1 (GRT25770) calibrations for three different temperature ranges.

	$1.4 < T < 2.7$	$2.7 < T < 4.5$	$1.4 < T < 5.0$	$5 < T < 20$
a_0	6.4799551	2.4105263	4.9350023	5.7171536
a_1	-0.99598763	0.44799897	-0.49672422	-1.3259221
a_2	0.051851284	-0.11910656	-0.0016523896	0.18678894
a_3	-0.0011143260	0.0056380441	0.00078669171	-0.011455714
b_0	12.292549	12.613498	12.303673	?
b_1	-4.3835491	-5.2727602	-4.4477334	?
b_2	0.91638015	1.7574867	1.0308806	?
b_3	-0.10776608	-0.38211452	-0.17106898	?

Table B.4: GRT4 (GRT25771) calibrations for four different temperature ranges.

B.3 The SQUID filters

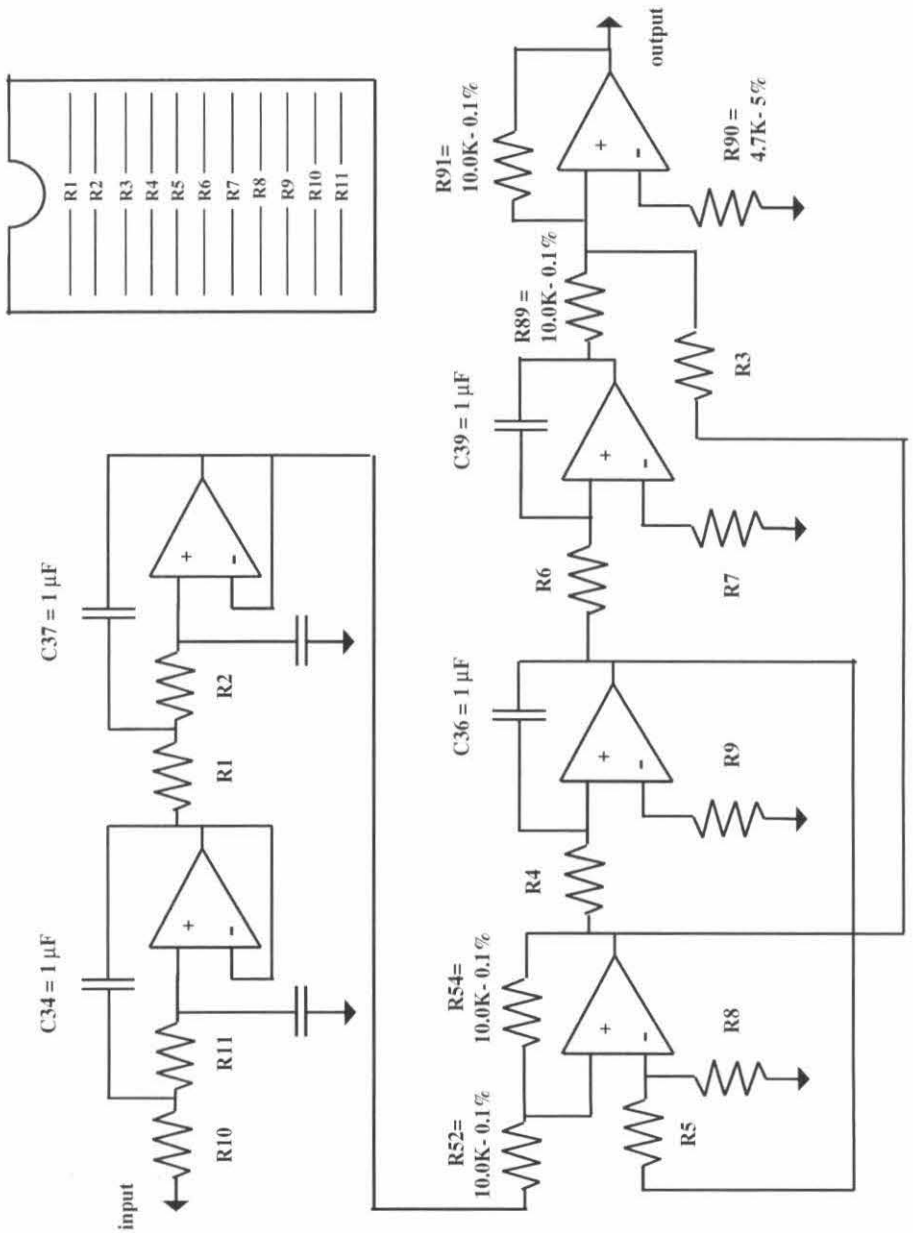

Figure B.1: The SQUID filters. See Table B.5 for resistor values before and after modification.

SQUID filter resistor numbers	Original resistor value	Modified resistor value
R1	5.62KΩ	5.62KΩ
R2	5.62KΩ	5.62KΩ
R3	22.6KΩ	22.6KΩ
R4	3.92KΩ	570KΩ
R5	24.3KΩ	24.3KΩ
R6	3.92KΩ	570KΩ
R7	3.9KΩ	249KΩ
R8	4.99KΩ	49.9KΩ
R9	3.9KΩ	249KΩ
R10	13.0KΩ	13.0KΩ
R11	2.43KΩ	2.43KΩ

Table B.5: SQUID filter resistor values, before and after modification.

B.4 The magnet

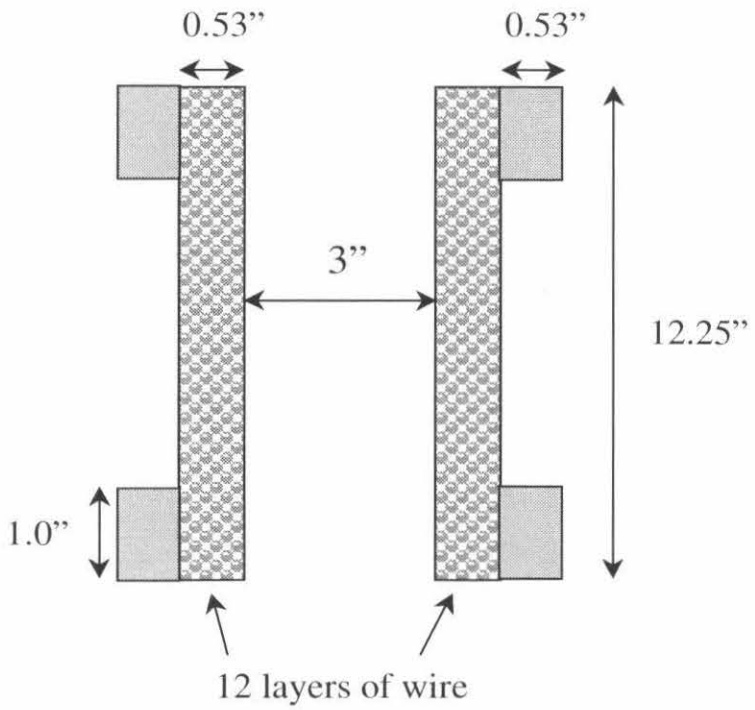

Figure B.2: The dimensions of the magnet solenoid.

Wire:	AWG #16 copper wire, polythermaleze insulated, 2671 ft. long.
Weight:	21 pounds (30.6 pounds with the vacuum can)
Resistance:	12.5 Ω at room temperature 2.0 Ω at 77 K 0.5 Ω at 4 K
dH/dI:	110.71 G/A

B.5 The vacuum can lid

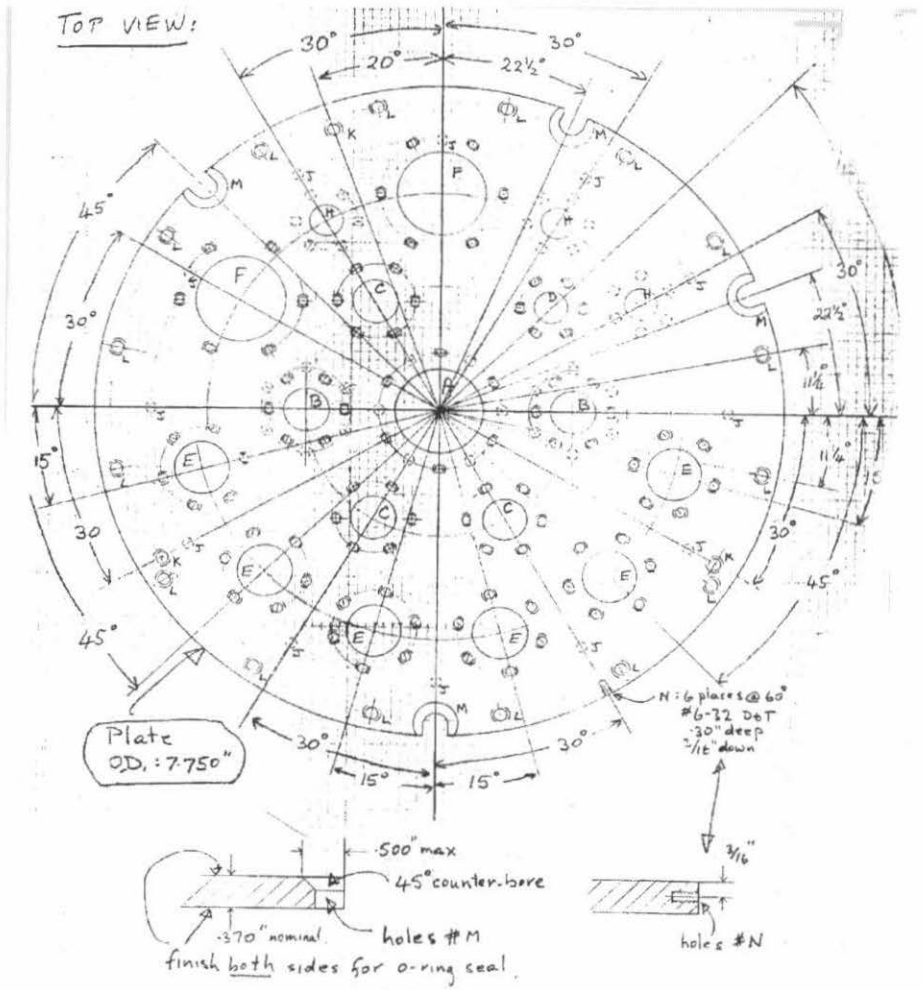

Figure B.3: The vacuum can lid.

Hole type	# of holes	Hole diameter	Radius from plate cntr	Top Bolt Circle (BC)	Bottom BC	comments
A	1	1.000"	0.0	1.350"	1.350"	
B	2	0.500"	1.500"	0.850"	0.975"	
C	3	0.500"	1.500"	. 0.850"	-	
D	1	0.375"	1.750"	0.725"	-	
E	6	0.625"	2.750"	0.975""	-	
F	2	1.000"	2.600"	1.350"	-	
H	3	0.375"	2.600"	-	0.725"	
J	12	6-32	-	-	6.500"	BCO
K	3	10-24	-	7.200"	-	BCO
L	16	10-24	-	7.400"	-	BCO
M	4	9/32"	3.740"	-	-	BCO
N	6	6-32	3.875"	-	-	BCO

Table B.6: Vacuum can lid holes and bolt circles. BCO: Bolt circle only.

Notes: 1) Type N holes are radial holes around the rim of the plate

2) All bolt holes are #6-32 D+T, 6 places at 60°, 0.30" deep blind holes except type K and L, which are #10-24. Type L is a thru-hole, but type K is blind.

Appendix C Catalog of Data Runs

This Appendix lists the files taken with the discrete pulse calorimetry method that gave satisfactory data. The first table comments on the noise of the files, and the second table gives the parameters used during data analysis.

File name	Q	**Comments**
021099.01	3	Very quiet data. Flux jumps in the shield make the downward drift rate change.
021199.01 021199.02	2.76	Combine the 2 ramps from 021199.01 and the first 3 from 021199.02 for very good noise. The last 2 ramps of 021199.02 ruined by 1 K pot oscillations.
021399.01	2	The last 2 ramps of 021199.02 ruined by 1 K pot oscillations.
021499.01	1	Good noise on all ramps. Can't resolve enhancement of C_Q.
021699.01	0	Good noise on all ramps.
021899.01	0	Fairly good noise.
022199.01	3	Noise is fair. Repeats the results of 021099.01 well.
022299.01	3.5	Very few flux jumps. Ramps 2-5 have very low noise.
022399.01	3.7	Very good noise. Very few flux jumps until the contractors arrive in the morning.
030199.01	2.5	Flux jumps on the shield cause some problems, but with a tight sorting cutoff, noise is decent.
030399.01	1.5	Excellent noise throughout 25 hr file.
030499.02	2.26	Excellent noise throughout 22 hr file.

—This table is continued on the next page—

File name	Q	Comments
030599.01	2.5	Very good noise throughout 20 hr file.
030699.01	3.26	Literally **hundreds** of flux jumps. After they are cleaned up, the noise is decent.
030799.01	3.5	Not many flux jumps. Fairly good noise. First ramp has a different drift rate.
030999.01	3.6	Noise is good for the whole file. First ramp has a different drift rate.
031199.01 031599.01	3.8	A large range file that goes well into the normal fluid side so that we can plot HRT0 vs. HRT0.
31899.01	0	Test to see if BNC measuring voltage applied to $Q_{\rm cal}$ makes a difference to the data. First 4 ramps the BNC is plugged in. Last 3 the BNC is not plugged in. (It didn't make a difference.)

Table C.1: A catalog of the data runs, their approximate heat currents, and comments on their noise. For more precise values of Q, see Table C.2.

The next table gives the parameters used during the data analysis process described in Chapter 5. The column headings (that aren't completely obvious) are:

$I_{\rm cal}$: The magnitude of the current applied to heater 5W during the heat pulse. This quantity is measured by measuring the voltage drop across a 100 kΩ precision resistor.[1] The power applied to the cell is $P = I_{\rm cal}^2 R_{\rm 5W} = I_{\rm cal}^2 \times 36.963\ \Omega$.

Drift Rate: The temperature drift rate of the HRTs as a function of time. This drift rate is thought to be due to either flux creep in the niobium flux tubes or thermal relaxation of the salt pills. For the drift method it is determined by tracking the movement of T_λ or $T_{\rm DAS}$ for subsequent ramps. For the pulse method, it is determined by both that and by plotting HRT1 vs. HRT0.

Offset in HRT0: This is an empirically determined number that should be equal to the temperature shift in HRT0 due to the offset at the bottom at point β (as described in Sec. 5.4.2).

[1] This voltage V = 100 kΩ · $I_{\rm cal}$ is the voltage requested by the Matlab analysis program 'calc_hc2.m'.

Q	**File name**	**# of ramps**	**Offset in HRT0 (μK)**	**Point # of $T_{\mathrm{DAS}}(Q)$**	I_{cal} **(μA)**	**Drift rate of HRT1 ($\mu\phi_0$/sec)**	**Drift rate of HRT0 ($\mu\phi_0$/sec)**
3.00853	021099.01	5	0.132	17,660	20.082	-1.2	-8
2.758272	021199.01 02119902	2 5	0.129	18,600	20.083	5 2	0 0
2.00707	021399.01	7	0.157	16,110	20.083	0	-1.5
1.00488	021499.01	7	0.01	18,625	20.080	3	-0.5
0	021699.01	7	0	9,402	20.079	-5	-2.7
0	021899.01	7	0	6,828	20.076	0	0
3.010287	022199.01	6	0.085	20,620	20.084	1	-2
3.51205	022299.01	6	0.215	18,950	20.092	5	-0.5
3.71249	022399.01	6	0.28	17,850	20.091	8	0
2.508546	030199.01	5	0.11	57,974	-	0	0
1.5072	030399.01	9.5	0.05	8,600	20.090	-0.5	0
2.259107	030499.02	9	0.07	69,080	20.088	1.3	-1.4
2.5097	030599.01	7	0.056	16,930	20.090	5.4	-3
3.26124	030699.01	8	0.027	8,850	20.089	2	-2
3.511845	030799.01	7	0.08	26,310	20.091	0.7	-2
3.61212	030999.01	8	0.16	18,700	20.090	2.5	-1
3.81278	031199.01	4	—	2,282	20.094	2	-0.5
0	031899.01	7	0	5,514	20.092	10	8

Table C.2: A catalog of the data runs and their analysis parameters.

Appendix D Heat Capacity of a Current Carrying Superconductor

The physics of ^{4}He under a heat flow can be applied to the case of a superconductor carrying a constant electric current. This was described in an article by David Goodstein, Talso Chui, and myself that appeared in *Physics Letters A* [106]. This Appendix consists of the text of that article.

Abstract

We present an analysis of the heat capacity of a superconductor carrying a constant applied electric current. We find that the heat capacity diverges with an exponent of 0.5 at a depressed transition temperature. This result is similar to a recent calculation of the heat capacity of superfluid helium under an applied heat current.

The Ginzburg-Landau (GL) equations [107] give a remarkably accurate description of superconductors in the vicinity of the superconducting transition. It is well known that the GL equations predict that superconductivity will break down at a critical current that occurs when the velocity of the Cooper pairs, ν_s, is [108]

$$\nu_{s,c} = \frac{1}{\sqrt{3}} \frac{\Delta}{p_F} \tag{D.1}$$

where Δ is the energy gap and p_F the Fermi momentum. It does not seem to have been noticed, however, that in a current-biased sample, the same physics leads to a divergent heat capacity. The argument is as follows:

The free energy density of a uniform sample is given by GL as

$$f = f_0 + \alpha|\psi|^2 + \frac{\beta}{2}|\psi|^4 + \gamma|\nabla\psi|^2 \tag{D.2}$$

where f_0 pertains to the normal state. If the sample carries a uniform current, the order parameter is given by

$$\psi = \psi_0 e^{i\vec{k}\cdot\vec{r}} \tag{D.3}$$

where ψ_0 and $\vec{k}$ are constant. Then, minimizing f with respect to ψ^* yields

$$f = f_0 - \frac{(\alpha + \gamma k^2)^2}{2\beta} \tag{D.4}$$

where, according to the usual GL arguments, β is a constant,

$$\alpha = -a_0(T_c - T) \tag{D.5}$$

where a_0 is a positive constant,

$$\gamma k^2 = \frac{1}{2} m^* \nu_s^2 \tag{D.6}$$

where m^* is the mass of a Cooper pair, and the number density of Cooper pairs is given by

$$n_s = -\left(\frac{\alpha + \gamma k^2}{\beta}\right). \tag{D.7}$$

The super current is then given by

$$J_s = n_s e^* \nu_s \tag{D.8}$$

where e^* is the charge on a Cooper pair. It follows that,

$$\left(\frac{\partial J_s}{\partial \nu_s}\right)_T \sim -(\alpha + 3\gamma k^2). \tag{D.9}$$

At small k [or ν_s, which is equivalent to k according to (D.6)] this derivative is positive and nearly constant, but because n_s is reduced by increasing k according to (D.7), the derivative is driven to zero at a critical value of k, and the super current

becomes unstable along a curve in the $T-k$ plane given by

$$\alpha + 3\gamma k^2 = 0. \tag{D.10}$$

Equation D.10 reduces to (D.1) if we recognize that $(-\alpha/\gamma)^{\frac{1}{2}} = \Delta/\hbar\nu_F$ where ν_F is the Fermi velocity.

It follows from (D.4) that the entropy density in the $T-k$ plane is given by

$$s = s_0 + \frac{a_0}{\beta}(\alpha + \gamma k^2). \tag{D.11}$$

At any constant value of k, this gives rise to the usual finite step in the heat capacity,

$$C_s = C_n + \frac{a_0^2 T}{\beta}, \tag{D.12}$$

where C_s and C_n are the superconducting and normal heat capacities. However, if instead of holding k constant we hold J_s constant (as in a current-biased sample), then

$$C_{J_s} = C_n + \frac{a_0^2 T}{\beta} + \frac{2a_0\gamma k}{\beta}\left(\frac{\partial k}{\partial T}\right)_{J_s}. \tag{D.13}$$

But, using (D.7) and (D.8),

$$\left(\frac{\partial k}{\partial T}\right)_{J_s} = -\frac{a_0 k}{\alpha + 3\gamma k^2}. \tag{D.14}$$

It follows that C_{J_s} diverges along the critical current curve given by (D.10). If we write the solution of (D.10) as a curve in the T-k plane, $T_c(k)$, then it is easily shown that [8] the singular contribution is proportional to $(T_c(k) - T)^{-1/2}$.

Behavior analogous to this has been predicted to occur in superfluid helium in a constant heat flux [8]. However, in the case of superfluidity, this kind of mean field theory in not dependable. The phenomenon is particularly interesting in the case of superconductivity, because in this case the GL equations are thought to be valid without correction for thermal fluctuations, and because the heat capacity at constant

current is relevant to device applications such as transition-edge bolometers [109]. We know of no other instance in which a mean field theory predicts a power-law divergence in the heat capacity. It should also be noted that the same analysis leads one to expect that the mean-square velocity fluctuations, $\langle \nu_s^2 \rangle$, should also diverge along $T_c(k)$.

Bibliography

[1] J. A. Lipa, in *Near Zero*, edited by J. D. Fairbanks, J. B. S. Deaver, C. W. F. Everitt, and P. F. Michelson (W.H. Freeman and Company, New York, 1988), p. 190.

[2] J. A. Lipa *et al.*, Phys. Rev. Lett. **76**, 944 (1996).

[3] R. J. Mikeska, Phys. Rev. **179**, 166 (1969).

[4] A. Onuki, J. Low Temp. Phys. **50**, 433 (1983).

[5] A. Onuki, J. Low Temp. Phys. **55**, 309 (1984).

[6] R. Haussmann and V. Dohm, Phys. Rev. B **46**, 6361 (1992).

[7] D. L. Goodstein, T. C. P. Chui, and A. W. Harter, Phys. Rev. Lett. **77**, 979 (1996).

[8] T. C. P. Chui, D. L. Goodstein, A. W. Harter, and R. Mukhopadhyay, Phys. Rev. Lett. **77**, 1793 (1996).

[9] R. Haussmann and V. Dohm, Czech. J. Phys. **46-S1**, 171 (1996).

[10] A. Onuki, Jpn. J. Appl. Phys. **26**, 365 (1987).

[11] R. Haussmann and V. Dohm, Z. Phys. B **87**, 229 (1992).

[12] V. Dohm and R. Haussmann, Phys. Rev. Lett. **72**, 3060 (1994).

[13] V. Dohm and R. Haussmann, Physica B **197**, 215 (1994).

[14] A. Onuki, J. Low Temp. Phys. **104**, 133 (1996).

[15] A. Onuki and Y. Yamazaki, J. Low Temp. Phys. **103**, 131 (1996).

[16] R. Haussmann, J. Low Temp. Phys. **107**, 21 (1997).

[17] R. Haussmann, J. Low Temp. Phys. **114**, 1 (1999).

[18] R. Haussmann, Phys. Rev. B **60**, 12349 (1999).

[19] R. V. Duncan, G. Ahlers, and V. Steinberg, Phys. Rev. Lett. **60**, 1522 (1988).

[20] T. C. P. Chui *et al.*, in *Temperature: its Measurement and Control in Science and Industry*, edited by J. F. Schooly (American Institute of Physics, N.Y, 1992), Vol. 6, p. 817.

[21] T. C. P. Chui *et al.*, Phys. Rev. Lett. **69**, 3005 (1992).

[22] P. Day *et al.*, J. Low Temp. Phys. **107**, 359 (1997).

[23] H. Baddar, G. Ahlers, K. Kuehn, and H. Fu, J. Low Temp. Phys. **119**, 1 (2000).

[24] C. J. Gorter and J. H. Mellink, Physica **15**, 285 (1949).

[25] A. W. Harter *et al.*, Phys. Rev. Lett. **84**, 2195 (2000).

[26] R. A. M. Lee, A. W. Harter, and T. C. P. Chui, in *ICEC 17*, edited by D. Dew-Hughes, R. Scurlock, and J. Watson (Inst. of Physics Publishing, Bristol and Philadelphia, 1998), p. 817.

[27] R. J. Donnelly, Physics Today **48**, 30 (1995).

[28] Z. M. Galasiewicz, *Helium 4* (Pergamon Press, Oxford, 1971).

[29] F. London, Nature **141**, 643 (1938).

[30] R. J. Donnelly and C. F. Barenghi, J. Phys. Chem. Ref. Data **27**, 1217 (1998).

[31] J. Wilks and D. S. Betts, *An Introduction to Liquid Helium* (Clarendon Press, Oxford, 1987).

[32] M. J. Buckingham and W. M. Fairbank, in *Progress in Low Temperature Physics, Volume 3*, edited by C. J. Gorter (North-Holland, Amsterdam, 1961).

[33] L. Tisza, Nature **141**, 913 (1938).

[34] Landau, L.D. 1941, USSR **5**, 71. [English translation: 1965, *Collected Papers of L.D. Landau*, D. ter Haar, editor, (Gordon and Breach, New York), p. 301.

[35] L. D. Landau, J. Phys. (Moscow) **11**, 91 (1947).

[36] E. L. Andronikashvili, Zh. eksp. theor. Fiz **16**, 780 (1946).

[37] R. J. Donnelly, *Experimental Superfluidity* (The University of Chicago Press, Chicago and London, 1967).

[38] H. Palevsky, K. Otnes, and K. E. Larsson, Phys. Rev. **112**, 11 (1958).

[39] J. L. Yarnell, G. P. Arnold, P. J. Bendt, and E. C. Kerr, Phys. Rev. **113**, 1379 (1959).

[40] D. G. Henshaw and A. D. B. Woods, Phys. Rev. **121**, 1266 (1961).

[41] D. R. Tilley and J. Tilley, *Superfluidity and Superconductivity* (Adam Hilger, Bristol, UK, 1990).

[42] N. N. Bogoliubov, J. Phys. U.S.S.R. **11**, 23 (1947).

[43] E. C. Svensson, in *Proc. 75th Jubilee Conf. on Helium-4 (St. Andrews)*, edited by J. G. M. Armitage (World Scientific, Singapore, 1984).

[44] L. D. Landau and E. M. Lifshitz, *Statistical Physics, 3rd Ed., Part 1* (Pergamon Press, Oxford, 1980).

[45] G. B. Hess, Phys. Rev. Lett. **40**, 119 (1978).

[46] I. M. Khalatnikov, *Introduction to the Theory of Superfluidity* (Benjamin, New York, 1965).

[47] V. K. Mishra and K. S. Bedell, Phys. Rev. B **29**, 5171 (1984).

[48] V. L. Ginzburg and L. P. Pitaevskii, Sov. Phys. JETP **7**, 858 (1958).

[49] See, for example, D. L. Goodstein, *States of Matter* (Dover, New York, 1985), p. 30.

[50] D. R. Swanson, T. C. P. Chui, and J. A. Lipa, Phys. Rev. B **46**, 9043 (1992).

[51] L. S. Goldner, N. Mulders, and G. Ahlers, J. Low Temp. Phys. **93**, 131 (1992).

[52] V. L. Ginzburg and A. Sobyanin, J. Low Temp. Phys. **49**, 507 (1982).

[53] W. Y. Tam and G. Ahlers, Phys. Rev. B **33**, 183 (1985).

[54] D. Greywall and G. Ahlers, Phys. Rev. A **7**, 2145 (1973).

[55] R. K. Pathria, *Statistical Mechanics* (Butterworth Heinemann, Oxford, 1996).

[56] P. B. Weichman, A. W. Harter, and D. L. Goodstein, submitted to Reviews of Modern Physics (2000).

[57] F.-C. Liu and G. Ahlers, Phys. Rev. Lett. **76**, 1300 (1996).

[58] W. A. Moeur *et al.*, Phys. Rev. Lett. **78**, 2421 (1997).

[59] P. K. Day *et al.*, Phys. Rev. Lett. **81**, 2474 (1998).

[60] P. B. Weichman, A. Prasad, R. Mukhopadhyay, and J. Miller, Phys. Rev. Lett. **80**, 4923 (1998).

[61] P. B. Weichman and J. Miller, J. Low Temp. Phys. **119**, 155 (2000).

[62] P. Muzikar and N. Giordano, Physica A **157**, 742 (1989).

[63] P. C. Hohenberg and P. C. Martin, Ann. Phys. (N.Y.). **34**, 291 (1965).

[64] J. S. Langer and M. E. Fisher, Phys. Rev. Lett. **19**, 560 (1967).

[65] M. E. Fisher, Proc. Nobel Symp. **24**, 16 (1973).

[66] M. E. Fisher, in *Scaling, universality and renormalization group theory in Critical Phenomena, Lecture Notes in Physics*, edited by F. J. W. Hahn (Springer-Verlag, Berlin, 1983), Vol. 186, p. 1.

[67] P. Pfeuty, D. Jasnow, and M. E. Fisher, Phys. Rev. B **10**, 2088 (1974).

[68] L. S. Goldner and G. Ahlers, Phys. Rev. B. **45**, 13129 (1992).

[69] P. C. Hohenberg, A. Aharony, B. I. Halperin, and E. D. Siggia, Phys. Rev. B **13**, 2986 (1976).

[70] P. C. Hohenberg and B. I. Halperin, Rev. Mod. Phys. **49**, 435 (1977).

[71] M. Dingus, F. Zhong, and H. Meyer, J. Low Temp. Phys. **65**, 185 (1986).

[72] R. Haussmann and V. Dohm, Phys. Rev. Lett. **67**, 3404 (1991).

[73] T. C. P. Chui, P. B. Weichman, R. Galletly, D. Elliott, K. Aaron and D. L. Goodstein, 1997, *DYNAMX vibration requirement*, DYNAMX Design File #27 (DX-DF-27).

[74] P. Bak, C. Tang, and K. Wiesenfeld, Phys. Rev. A **38**, 364 (1988).

[75] J. Machta, D. Candela, and R. B. Hallock, Phys. Rev. B **47**, 4581 (1993).

[76] G. Ahlers and F.-C. Liu, J. Low Temp. Phys. **105**, 255 (1996).

[77] J. R. Clow and J. D. Reppy, Phys. Rev. A **5**, 424 (1972).

[78] H. Fu, H. Baddar, K. Kuehn, and G. Ahlers, Low Temp. Phys. **24**, 69 (1998).

[79] R. V. Duncan and G. Ahlers, Phys. Rev. B **43**, 7707 (1991).

[80] R.V. Duncan, 1998, *An expansion from the 1998 NASA Taskbook Entry for Critical Dynamics in Microgravity (DYNAMX).*

[81] D. R. Swanson *et al.*, J. Spacecraft and Rockets **33**, 154 (1996).

[82] K. Schroeder and J. C. McClure, CRC Critical Reviews of Solid State Science **6**, 45 (1976).

[83] C. A. Hutchison and E. Wong, The Journal of Chemical Physics **29**, 754 (1958).

[84] R. M. Bozorth, *Ferromagnetism* (Van Nostrand, New York, 1958).

[85] T. Chui, P. Day, I. Hahn, A. Nash, D. Strayer, M. Lysek, and J. Lipa, Jan. 10, 1995, *High Resolution Thermometer Fabrication and Test Report.*

[86] J. H. Freeman and M. L. Smith, J. Inorg. Nucl. Chem. **7**, 224 (1958).

[87] *CRC Handbook of Chemistry and Physics, 52nd edition*, edited by R. C. Weast (The Chemical Rubber Co., Cleveland, Ohio, 1971), pp. B–91.

[88] W. P. Wolf, M. J. M. Leask, B. Mangum, and A. F. G. Wyatt, J. Phys. Soc. Japan **17 B-1**, 487 (1961).

[89] H. B. Callen and T. A. Welton, Phys. Rev. **83**, 34 (1951).

[90] V. Hovi, R. Vuola, and L. Salmenpera, J. Low Temp. Phys. **2**, 383 (1970).

[91] P. Day and Y. Mukharsky, private communication, (1998).

[92] T. C. P. Chui, private communication, (2000).

[93] D. Murphy and H. Meyer, J. Low Temp. Phys. **97**, 489 (1994).

[94] E. Gopal, *Specific Heats at Low Temperatures* (Plenum Press, New York, 1966).

[95] N. Bruckner, S. Backhaus, and R. Packard, Czech. J. Phys. **46**, 2741 (1996).

[96] *Low Temperature Valve for BEST*, LTMPF e-library at the Jet Propulsion Laboratory, September 27, 1999.

[97] R. C. Richardson and E. N. Smith, *Experimental Techniques in Condensed Matter Physics at Low Temperatures* (Addison Wesley Publishing Company, Inc., Redwood City, California, 1988).

[98] L. J. Richardson and P. V. E. McClintock, Cryogenics (1978).

[99] M. Larson, *A Review of Published Work on Pressed Contacts.*

[100] L. Salerno, P. Kittel, and A. Spivak, Cryogenics **34**, 649 (1994).

[101] P. Sullivan and G. Seidel, Physical Review **173**, 679 (1968).

[102] A. W. Harter, R. A. M. Lee, T. C. P. Chui, and D. L. Goodstein, J. of Low Temp. Phys. **113**, 549 (1998).

[103] S. Sydoriak and T. Roberts, Phys. Rev. **118**, 901 (1960).

[104] E. Kerr and R. Taylor, Annals of Physics **26**, 292 (1964).

[105] R. Haussmann, private communication, (1999).

[106] D. L. Goodstein, A. W. Harter, and T. C. P. Chui, Phys. Lett. A **245**, 477 (1998).

[107] V. L. Ginzburg and L. Landau, Zh. Eksperim. I. Teor. Fiz. **20**, 1064 (1950).

[108] M. Tinkham, *Introduction to Superconductivity* (McGraw-Hill, New York, 1996).

[109] B. Cabrera, private communication (1998).